ISSN
2712-8172

Magazine of Civil Engineering

103(3), 2021

Федеральное государственное автономное образовательное учреждение высшего образования
Санкт-Петербургский политехнический университет Петра Великого

ПОЛИТЕХ
Санкт-Петербургский политехнический университет Петра Великого

Инженерно-строительный институт
Центр дополнительных профессиональных программ

195251, г. Санкт-Петербург, Политехническая ул., 29, тел/факс: 552-94-60, www.stroikursi.spbstu.ru, stroikursi@mail.ru

Приглашает специалистов организаций, вступающих в СРО, на курсы повышения квалификации (72 часа)

Код	Наименование программы	Виды работ*
	Курсы по строительству	
БС-01-04	«Безопасность и качество выполнения общестроительных работ»	**п.1,2, 3, 5, 6, 7, 9, 10, 11, 12, 13, 14**
БС-01	«Безопасность и качество выполнения геодезических, подготовительных и земляных работ, устройства оснований и фундаментов»	**1,2,3,5**
БС-02	«Безопасность и качество возведения бетонных и железобетонных конструкций»	**6,7**
БС-03	«Безопасность и качество возведения металлических, каменных и деревянных конструкций»	**9,10,11**
БС-04	«Безопасность и качество выполнения фасадных работ, устройства кровель, защиты строительных конструкций, трубопроводов и оборудования»	**12,13,14**
БС-05	«Безопасность и качество устройства инженерных сетей и систем»	**15,16,17,18,19**
БС-06	«Безопасность и качество устройства электрических сетей и линий связи»	**20,21**
БС-08	«Безопасность и качество выполнения монтажных и пусконаладочных работ»	**23,24**
БС-12	«Безопасность и качество устройства мостов, эстакад и путепроводов»	**29**
БС-13	«Безопасность и качество выполнения гидротехнических, водолазных работ»	**30**
БС-14	«Безопасность и качество устройства промышленных печей и дымовых труб»	**31**
БС-15	«Осуществление строительного контроля»	**32**
БС-16	«Организация строительства, реконструкции и капитального ремонта. Выполнение функций технического заказчика и генерального подрядчика»	**33**
	Курсы по проектированию	
БП-01	«Разработка схемы планировочной организации земельного участка, архитектурных решений, мероприятий по обеспечению доступа маломобильных групп населения»	**1,2,11**
БП-02	«Разработка конструктивных и объемно-планировочных решений зданий и сооружений»	**3**
БП-03	«Проектирование внутренних сетей инженерно-технического обеспечения»	**4**
БП-04	«Проектирование наружных сетей инженерно-технического обеспечения»	**5**
БП-05	«Разработка технологических решений при проектировании зданий и сооружений»	**6**
БП-06	«Разработка специальных разделов проектной документации»	**7**
БП-07	«Разработка проектов организации строительства»	**8**
БП-08	«Проектные решения по охране окружающей среды»	**9**
БП-09	«Проектные решения по обеспечению пожарной безопасности»	**10**
БП-10	«Обследование строительных конструкций и грунтов основания зданий и сооружений»	**12**
БП-11	«Организация проектных работ. Выполнение функций генерального проектировщика»	**13**
Э-01	«Проведение энергетических обследований с целью повышения энергетической эффективности и энергосбережения»	
	Курсы по инженерным изысканиям	
И-01	«Инженерно-геодезические изыскания в строительстве»	**1**
И-02	«Инженерно-геологические изыскания в строительстве»	**2,5**
И-03	«Инженерно-гидрометеорологические изыскания в строительстве»	**3**
И-04	«Инженерно-экологические изыскания в строительстве»	**4**
И-05	«Организация работ по инженерным изысканиям»	**7**

***(согласно приказам Минрегионразвития РФ N 624 от 30 декабря 2009 г.)**

По окончании курса слушателю выдается удостоверение о краткосрочном повышении квалификации установленного образца (72 ак. часа)

Для регистрации на курс необходимо выслать заявку на участие, и копию диплома об образовании по телефону/факсу: 8(812) 552-94-60, 535-79-92, , e-mail: stroikursi@mail.ru.

Magazine of Civil Engineering
SCHOLAR JOURNAL

ISSN 2712-8172

Свидетельство о государственной регистрации:
Эл № ФС77-77906 от 19.02.2020,
выдано Роскомнадзором

Специализированный научный журнал.

Выходит с 09.2008.

Включен в Перечень ВАК РФ

Индексируется в БД Scopus

Периодичность: 8 раз в год

Учредитель и издатель:

Санкт-Петербургский политехнический университет Петра Великого

Адрес редакции:

195251, СПб, ул. Политехническая, д. 29

Главный редактор:
Екатерина Александровна Линник

Научный редактор:
Виталий Владимирович Сергеев

Заместитель главного научного редактора:
Галина Леонидовна Козинец

Редакционная коллегия:
PhD, проф. Т. Аввад;
д.т.н., проф. М.И. Бальзанников
д.т.н., проф. А.И. Белостоцкий;
к.т.н., проф. А.И. Боровков;
д.т.н., проф. А. Бородинец;
PhD, проф. М. Велькович;
PhD, проф. Р.Д. Гарг;
PhD, М.Р. Гарифуллин;
Dr.-Ing, проф. Т. Грис;
д.т.н., проф. Т.А. Дацюк;
д.т.н., проф. В.В. Елистратов;
Dr.-Ing., проф. Т. Кэрки;
д.т.н., проф. Д.В. Козлов;
д.т.н., доцент С.В. Корниенко;
д.т.н., проф. Ю.Г. Лазарев;
д.т.н., проф. М.М. Мухаммадиев;
Dr.-Ing. Habil., проф. Х. Пастернак;
Dr.-Ing., проф. Ф. Рёгинер;
д.т.н., проф. Т.З. Султанов;
д.т.н., проф. М.Г. Тягунов;
акад. РАН, д.т.н., проф. М.П. Федоров;
Dr.-Ing., проф. Д. Хецк;
д.г.-м.н. А.Г. Шашкин;
д.т.н. В.Б. Штильман

Дата выхода: 23.04.2021

© ФГАОУ ВО СПбПУ, 2021
© Иллюстрация на обложке: Илья Смагин

Magazine of Civil Engineering
SCHOLAR JOURNAL

ISSN 2712-8172

Peer-reviewed scientific journal

Start date: 2008/09

8 issues per year

Publisher:

Peter the Great St. Petersburg Polytechnic University

Indexing:

Scopus, Russian Science Citation Index (WoS), Compendex, EBSCO, Google Academia, Index Copernicus, ProQuest, Ulrich's Serials Analysis System, CNKI

Corresponding address:

29 Polytechnicheskaya st., Saint-Petersburg, 195251, Russia

Editor-in-chief:

Ekaterina A. Linnik

Science editor:

Vitaly V. Sergeev

Deputy chief science editor:

Galina L. Kozinetc

Editorial board:

T. Awwad, PhD, professor
M.I. Balzannikov, D.Sc., professor
A.I. Belostotsky, D.Sc., professor
A.I. Borovkov, PhD, professor
A. Borodinecs, Dr.Sc.Ing., professor
M. Veljkovic, PhD, professor
R.D. Garg, PhD, professor
M. Garifullin, PhD, postdoctorant
T. Gries, Dr.-Ing., professor
T.A. Datsyuk, D.Sc., professor
V.V. Elistratov, D.Sc., professor
T. Kärki, Dr.-Ing., professor
D.V. Kozlov, D.Sc., professor
S.V. Korniyenko, D.Sc., professor
Yu.G. Lazarev, D.Sc., professor
M.M. Muhammadiev, D.Sc., professor
H. Pasternak, Dr.-Ing.habil., professor
F. Rögener, Dr.-Ing., professor
T.Z. Sultanov, D.Sc., professor
M.G. Tyagunov, D.Sc., professor
M.P. Fedorov, D.Sc., professor
D. Heck, Dr.-Ing., professor
A.G. Shashkin, D.Sc.
V.B. Shtilman, D.Sc.

Date of issue: 23.04.2021

© Peter the Great St. Petersburg Polytechnic University. All rights reserved.
© Coverpicture – Ilya Smagin

Contacts:
E-mail: mce@spbstu.ru
Web: http://www.engstroy.spbstu.ru

Contents

Gumenyuk, V.I., Kuzmin, A.A., Romanov, N.N., Permiakov, A.A., Gumenyuk, O.V., Dmitriev, I.I. Porous inorganic materials for fire protection of industrial structures 10301

Zhakipbekov, Sh.K., Aruova, L.B., Toleubayeva Sh.T., Ahmetganov, T.B., Utkelbaeva, A.O. The features of the hydration and structure formation process of modified low-clinker binders 10302

Frolov, N.V., Smolyago, G.A. Reinforced concrete beams strength under power and environmental influences. 10303

Garedew, G. Cement and animal bone powder on rheological characteristics of bitumen 10304

Marozau, A., Tran Duc, H., Kamluk, A., Parmon, V., Striganova, M. Pump-hose systems with universal fire barrels for extinguishing buildings 10305

Alekseytsev, A.V. Mechanical safety of reinforced concrete frames under complex emergency actions 10306

Strokova, V.V., Le Saout, G., Nelubova, V.V., Ogurtsova, Y.N. Composition and properties of cement system with glutaraldehyde 10307

Tiraturyan, A.N., Uglova, E.V., Nikolenko, D.A., Nikolenko, M.A. Model for determining the elastic moduli of road pavement layers 10308

Jahami, A., Temsah, Y., Khatib, J., Baalbaki, O., Kenai, S. The behavior of CFRP strengthened RC beams subjected to blast loading 10309

Pinto, V., Cunha, M., Martins, K., Rocha, L., Dos Santos, E., Isoldi, L. Bending of stiffened plates considering different stiffeners orientations 10310

Vu, K.D., Bazhenova, S.I. Modeling the influence of input factors on foam concrete properties 10311

Samarin, O.D. Thermal mode of a room with integrated regulation of cooling systems 10312

Lukpanov, R.E., Dyussembinov, D.S., Utepov, Ye.B., Bazarbayev, D.O., Tsygulyov, D.V., Yenkebayev, S.B., Shakhmov, Zh.A. Homogeneous pore distribution in foam concrete by two-stage foaming 10313

Usanova, K., Barabanshchikov, Yu.G., Krasova, A.V., Akimov, S.V., Belyaeva, S.V. Plastic shrinkage of concrete modified by metakaolin 10314

Magazine of Civil Engineering

ISSN 2712-8172

journal homepage: http://engstroy.spbstu.ru/

DOI: 10.34910/MCE.103.1

Porous inorganic materials for fire protection of industrial structures

V.I. Gumenyuk[a]*, A.A. Kuzmin[b], N.N. Romanov[b], A.A. Permiakov[b], O.V. Gumenyuk[a], I.I. Dmitriev[c]

[a] Peter the Great St. Petersburg Polytechnic University, St. Petersburg, Russia

[b] Saint-Petersburg University of State Fire Service of EMERCOM of Russia, St. Petersburg, Russia

[c] Graz University of Technology, Graz, Austria

** E-mail: gumenyuk.vi@yandex.ru*

Keywords: fire, fire protective materials, thermo inductivity, convections, thermal radiation, porous materials, expanded vermiculite, perlite

Abstract. The necessity to study the thermophysical properties of porous inorganic materials is due to the wide use of thin-walled structures, the fire protective coating of which is performed when use porous materials. One of the most dangerous physical influence, leading to the destruction of thin-walled constructions in a fire, is a rapid increase in the temperatures of the combustion products in the fire zone. For a fire fencing, just 20÷30 minutes after its start, the temperature of the products in the combustion zone can reach 800÷900 °C, while the temperature can increase under more favorable conditions for the combustion process of air exchange. For open fires, when the air exchange conditions are not limited, the temperature of the combustion products can quickly reach 1100 °C of more. In the article, analyzing the effect on the porous materials of high-temperature combustion products, high humidity, direct exposure to water, as well as the process of phase of phase transitions of moisture contained in capillaries and its possible consequences. Presented and analyzing the influence of the process of thermal radiation inside gas-filled cellular structures on the heat-conducting properties of porous material based on perlite and expanded vermiculite. The results of an experiment to study the dependence of the thermal conductivity coefficient of expanded vermiculite on the specific particle size density and pressure suggest that with an increase in the temperature of the combustion products a thin-walled fire protection layer made of fibrous materials (for example, perlite and expanded vermiculite) with a decrease in the size of the solid fraction, the thermal conductivity coefficient of expanded vermiculite increases to a greater extent than of perlite, nab a certain tendency is observed to increase the share of the convective component in the thermal conductivity of expanded fire-protective materials as the particle sizes of their solid fraction decrease.

1. Introduction

The object of the present research is the heat and physical properties of porous inorganic materials used for fire protection of building structures. This article used the analysis data of M.V. Gravit et al. On the possible use of components of external substances in improving the fire safety of buildings [1–5], fire protection of high-rise buildings [6, 7, 8, 9], as well as options for increasing strength properties of concrete under fire conditions, which were considered in [10–13] by V.I. Korsun et.al., and concrete protection methods studied in the works [14, 15, 16, 17] of N.I. Vatin et.al.

The relevance of research is due to the fact that the current state of development of modern industrial technologies suggest supporting the required level of fire safety of building and structures since the consequences of their collapse as a result of a fire can lead to significant material losses, personal injury and even death [18].

In the construction of industrial facilities, there is a wide use of reinforced concrete reinforced concrete reinforced cement fiber-reinforced concrete and metal constructions, the value of the fire resistance limit of which usually did not exceed the values of 30-40 minutes [19, 20]. To slow down the

Gumenyuk, V.I., Kuzmin, A.A., Romanov, N.N., Permiakov, A.A., Gumenyuk, O.V., Dmitriev, I.I. Porous inorganic materials for fire protection of industrial structures. Magazine of Civil Engineering. 2021. 103(3). Article No. 10301. DOI: 10.34910/MCE.103.1

This work is licensed under a CC BY-NC 4.0

heating of such structures allows the use of various fire-retardant coating based on the use of relatively inexpensive materials, primary perlite and expanded vermiculite [21–28].

The aim of the research is to assess the possibility of using porous inorganic materials to increase the level of fire protection of building structures, the achievement of which involves solving the following tasks.

- analysis of the process of heating porous inorganic materials in a fire and assessment of the ratio between different types of heat exchange;
- dependence identification between heat-conducting properties of porous inorganic materials and grain sizes;
- studying of the effect on the heat-conducting properties of porous inorganic materials of moisture, accumulated during fire fighting.

2. Methods

For scientific research, experimental data were collected and analyzed from domestic and foreign literary sources, as well as experimental studies of the thermal conductivity of composite materials made on the basis of expanded vermiculite in a temperature range of 50-400 °C. The temperature dependences of the thermal conductivity of these materials were obtained by using the IT-λ-400 meter, which is based on the method of monotonous heating. The thermal circuit of the applied method is shown in Fig. 1.

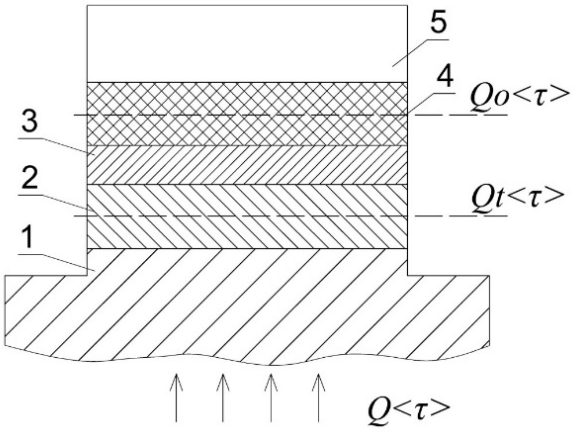

Figure 1. Thermal circuit: 1 – base; 2 – plate; 3 – contact plate; 4 – sample; 5 – core.

The heat flux Q coming from the base 1 passes through the cross section of the plate 2, is partially absorbed by it, and then goes on the monotonous heating of the plate 3, sample 4 Q and rod 5. The lateral surfaces of the rod, sample, and plates 2 and 3 also are thermally insulated.

The rod and contact plate are made of a material with a high thermal conductivity, so the temperature differences on them are insignificant.

The geometric parameters of the system are chosen so that the flows accumulated by the sample and plate are an order of magnitude smaller than those absorbed by the rod. In this case, the temperature field of sample 4 and plate 2 are close to linear and stationary. The theoretical justification of the applied method for measuring thermal conductivity is described in detail in the literature [29].

3. Results and Discussion

The initial stage of the process of passing through the mass of fire during the fire is characterized by its non-stationary nature, while the characteristics of the temperature field of the thin-walled structure are a function of not only spatial coordinates but also time.

The magnitude of the heating rate of such a structure is determined by the ability of its material to conduct heat, which is characterized by the coefficient of thermal conductivity of the material λ (W/(M°C)) and its temperature coefficient of thermal conductivity β (W/(M°C^2)), the effect of which is significant at a fire temperatures. In addition, the heating rate of a thin-walled structure will depend on the ability of the material to accumulate thermal energy, which can be characterized by the heat capacity of the entire material of the structure C (kJ/°C), which is numerically equal to the product of the material ρ (kg/m^3) by the specific (mass) heat capacity of c (kJ/(kg°C)).Thus, effective fire protection of thin-walled structures in

a fire is possible when using materials with a relatively small coefficient of thermal conductivity, the value of which is determined by a large number of factors, such as the average density of the material, its true porosity, size and shape of these pores, moisture content of the material. In addition, the composition and radiative ability of the grains of the material, and of course the average temperature of heating the material, are significant factors.

In the process of heat transfer in an array of porous materials used for fire protection of thin-walled structures in a fire, several components are involved:

- The process of thermal conductivity with direct contact of the structural particles of the solid phase of the porous material.
- The process of free (natural) convention when moving gas molecules in the free space between the structural particles of the solid phase of a porous material.
- The process of radiant heat exchange between the internal surfaces of the structural particles of the solid phase of a porous material [20, 26].

The intensity of heat transfer processes in an array of porous material for fire protection of thin-walled structures is largely determined by the presence of moisture located in the pores of the material, which is caused by both atmospheric conditions (to less extent) and water ingress during the supply of trunks during fire fighting (to greater extent). If the temperature reaches the boiling point of water under the given atmospheric conditions on the heated surface of the fire-retardant layer, then in the capillaries of the array of porous material a phase transition from a liquid to a vapor begins to occur.

Part of the heat of fire heat is used for this, proportional to the specific heat of vaporization of water, equal to 2200 kJ/kg. As the fireproof layer of the porous material warms up, moisture diffuses in the direction of the heated surface, while moisture drops in the depth of the material array, and a dry surface zone forms near the heated surface. Considering that the steam flow during the movement in the opposite direction of heat as it warms up will absorb part of the energy, fire, the heating process of a thin-walled structure can slow down [23, 28]. In this case, the vapor formed in the array of the fire-retardant layer can cause delamination of this layer from the surface of the protected thin-walled structure, which can be identified as a destructive effect.

However, for flame retardant materials such as perlite and expanded vermiculite, the high porosity provides them with good heat-insulating ability. The dependence of the thermal conductivity coefficient of various types of expanded vermiculite on the composition of the fraction is shown in Fig. 2 [19].

The dependence of the coefficient of thermal conductivity of expanded vermiculite on the fractional composition:

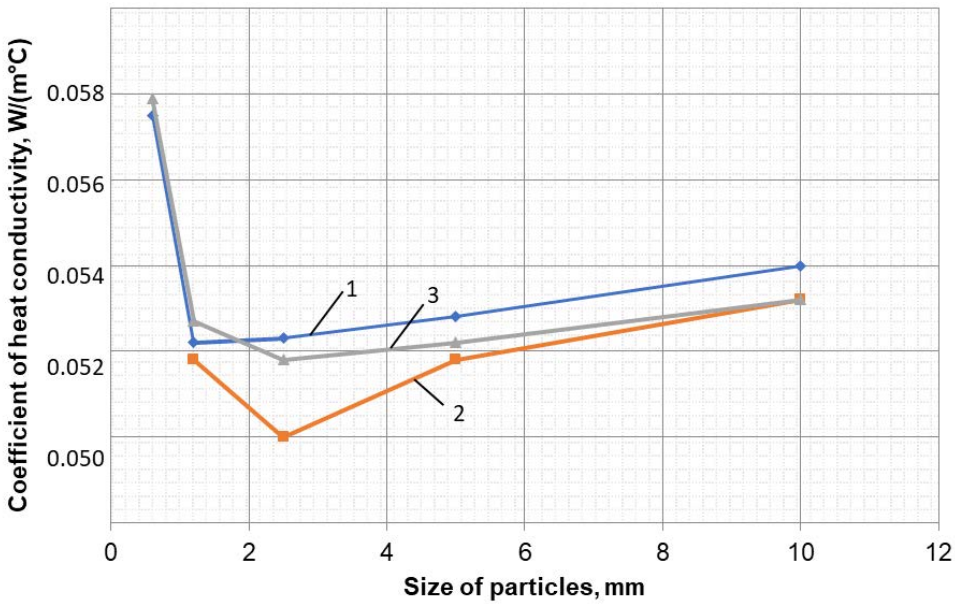

Figure 2. Dependence of expanded vermiculite heat conductivity coefficient from fractional composition: 1. Kovdor hydrophlogopite , sample 1; 2. Kovdor hydrophlogopite , sample 2; 3. Inaglinsky vermiculite.

For the provided samples of fireproof porous materials, the values of the thermal conductivity coefficient fluctuate in the range of 4÷8 %, which follows their analysis of the graphic dependences in Fig. 2

and Fig. 3. A slight increase in the coefficient of thermal conductivity with an increase in the size of structural particles can be explained by the intensification of the process of convective heat transfer in the free space between the structural particles of the solid phase of the porous material associated with the transaction from a free convention in thin layers to a free convention in a large volume. With linear particle sizes less than 0.6 mm, the proportion of gangue decreases, the density of the porous fire-retardant material increases, and the proportion of heat transfer increases due to the process of heat conduction in a solid body.

The shape of the particles making up the porous fire retardant material is also important.

The measurements give reason to argue that the heat-conducting properties of porous materials formed on the basis of lamellar particles are slightly less than those properties of materials whose properties of materials whose particles are closer to the circulations may be the one-sided orientation of lamellar particles, which determines the nature of their contact and the heat flux propagates in vermiculite backfill perpendicular to the sintering plane of lamellar particles.

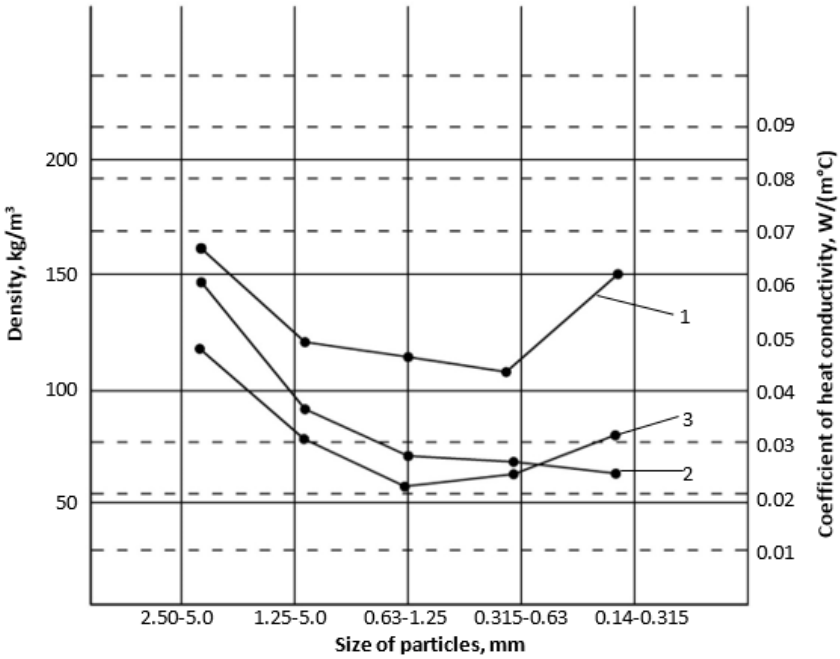

Figure 3. The dependence of the coefficient of thermal conductivity (1) and density and expanded vermiculite (2) and perlite (3) on the particle size.

Graphical Content Analysis the thermal conductivity coefficient and the density and density of expanded vermiculite and perlite on the particle size shown in Fig. 3 make it possible to conclude that the particle size of the solid formation affects the value of the thermal conductivity of perlite.

The experimental data on the thermal conductivity coefficients of porous fire-retardant materials given in [19, 21, 25, 28] are not unambiguous, since the measurements were carried out by different methods, as well as under different atmospheric conditions, for different sizes of solid grains and different characteristics of porosity. This is due to the different nature of heat transfer in the space between the structural particles of the solid phase of the porous material.

It is generally considered that for a porous material its heat-conducting properties of air, since for the solid components of porous materials their thermal conductivity coefficients usually exceed such values for gases, including air.

This statement follows from then proposal that the linear pore sizes of flame retardant materials significantly exceed the mean free path of air molecules under normal conditions. However, in a fire, the thermodynamic parameters in the space between the structural particles of the solid phase of the porous material differ significantly from normal conditions. In this case, for a finely dispersed porous material, the value of its thermal conductivity coefficient can be even less than the thermal conductivity coefficient of air at the same temperature.

Table 1 shows the experimental date obtained for the thermal conductivity of a foreign material, which is silicic acids reduced to a porous state with linear pore sizes of $18 \cdot 10^{-8}$ mm and solid grain sizes of $2.5 \cdot 10^{-8}$ mm.

The values of the thermal conductivity of the domestic material “White Soot BS-280” measured at various temperatures are also given, with the average free path of air molecules for normal atmospheric conditions being assumed to be $10000 \cdot 10^{-8}$ mm.

Table 1. Heat conductivity coefficients of finely dispersed materials depending on temperature.

Material	Heat conductivity coefficient, W/(m°C)	
	At temperature 0 °C	At temperature 50 °C
Santosel	0.0209	0.0239
White soot BS-280	0.01	0.02
Air at normal pressure	0.0237	0.0270

The experiments with silica aerogel with different dispersion characteristics made it possible to prove that the value of the thermal conductivity can decrease to 0.0032 W/(m°C), which is about 10 times less than the thermal conductivity of air measured for normal atmospheric pressure [8].

Increased porosity of flame retardant materials can be achieved by using some features of the shape and structural particles. From the number of thin-walled structure of porous materials is a conglomerate of relatively small ball formation with a diameter of 5÷20 nm. Such materials include silicic acid airgel, white carbon black, “Aerosila” material.

Perlite and expanded vermiculite, the structure of which is cellular in nature, can be attributed to another group, and an empirical equation (1) is proposed to determine the value of the thermal conductivity of such materials:

$$\lambda = \lambda_v \left[1 + \left(\frac{3}{2}(1-P) + 11(1-P)^4 \right) - \frac{1}{2.69 + 0.31 \, \lambda_m / \lambda_v} \right], \quad (1)$$

P is the fraction of the volume of voids between particles of solid reck.

λ_v is air conductivity coefficient

λ_m is thermal conductivity of solid particles.

One of the most important indicators of the fire-retardant properties of porous materials such as perlite and expanded vermiculite is the thermal conductivity coefficient, so when choosing the right material for fire protection of thin-walled structures, it is necessary to take into account the dependence of the thermal conductivity coefficient of the average heating temperature.

Such experiments were carried out in the work for a temperature range of 200÷600 °C.

Measurements showed that the greatest dependence of the thermal conductivity on temperature is observed in the foam asbestos M-25, which is an ultra-light heat-insulating material: the value of the coefficient of thermal conductivity during heating increased 6 times. For expanded M-150 vermiculite, this dependence is not so pronounced: the values of the thermal conductivity coefficient only doubled [27].

As applied to the properties of foam asbestos, such a significant increase in the coefficient of thermal conductivity can be explained by the presence of significant number of large communicative gaps, in which there are conditions for the development of convective flows of the air. Almost all fibrous heat-insulating materials have a similar structure, therefore, as the temperature of the combustion products increases, which is typical for the initial stage of a fire, therefore, fire protection made of foam asbestos is less effective than fire protection made of perlite and expanded vermiculite. The surface of the expanded vermiculite has a characteristic golden color, which reduces the emissivity of this fire protection material to approximately $C \approx 0.6$ Wt/(m^{2}K^4), which is significantly less than the emissivity of the AHT C_0 = 5.67/ Wt/(m^{2}K^4), which can explain the relatively weaker dependence of the thermal conductivity of this material from temperature [20].

A relatively small fraction of the radiation component in the effective heat conductivity of fire retardant thin-walled structures expanding coatings is due to the presence of many tiny thermal screens that formed by porous structure of the substance. They weaken the radiation component of the heat flux aimed at thin-walled structure heating. Therefore, it is desirable to use materials with a small emitting and high reflectivity for fire protection.

They measured reflection coefficients of the surfaces of perlite and expanded vermiculite by a spectrophotometer to evaluate emission factors, and then calculated emissivity value assuming that there is no transmittance.

In case of open fires combustion products temperature can quickly reach 1100 °C and higher, so the fire protection material surface reflectance should be measured for the visible spectrum of the heat fire radiation (λ = 400÷700 nm).

The measuring results of the reflection coefficients of the surfaces of clean and painted black expanded perlite and expanded vermiculite for the visible range of heat radiation of fire are shown on Fig. 4 [23].

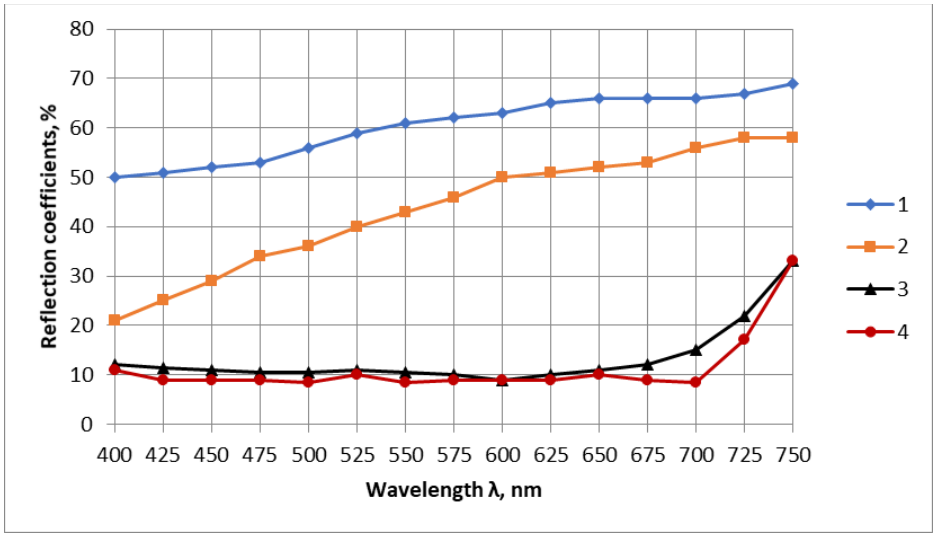

Figure 4. Dependence of reflection coefficient of vermiculite (perlite) from wavelength: 1 – expanded vermiculite, 2 – expanded perlite, 3 – "black" expanded vermiculite, 4 – "black" expanded perlite.

On the basis of measurements results of expanded vermiculite heat conductivity coefficient in Table 2 it is possible to conclude that there is an unambiguous dependence between color of material, condition of its external surface relief (value of reflection coefficient) and value of heat conductivity coefficient of the studied material [20].

Table 2. Coefficients of heat conductivity of black and golden expanded vermiculite.

Color of vermiculite	Fraction size, mm	Density, kg/m^3	Coefficient of heat conductivity, W/(m°C)	
			Probe method	Bicalorimeter
golden	2.5÷5.0	145	0.073	0.080
black			0.085	0.086
golden	1.25÷2.5	175	0.066	0.080
black			0.076	0.085
golden	0.63÷1.25	200	0.072	0.079
black			0.080	0.088

The procedure for detecting the convective component in the thermal conductivity of a porous material is based on determining the difference in values at normal pressure and in vacuum, however, if this deforms the structure of the material cells, this can significantly affect the error, and in the case of significant deformations, such measurements are useless. The fraction of the convective component in the coefficient of the thermal conductivity of the porous materials in % can be calculated using equation (2).

$$\Delta\lambda = \frac{\lambda - \lambda_{vac}}{\lambda} \times 100, \quad (2)$$

where λ is heat conductivity coefficients of material at atmospheric pressure, W/(m°C);

λ_{vac} is heat conductivity of material in vacuum, W/(m°C),

Table 3 presents the dependences of the thermal conductivity of the expanded aggregates on the bulk density, grain size and color, and air pressure [27].

Table 3. Dependence of the coefficient of thermal conductivity of expanded perlite on the bulk density of particle size and air pressure.

Parameters	Size of solid fraction, mm			
	1.25÷2.5	0.63÷1.25	0.315÷0.63	0.16÷0.315
Poured density, kg/m^3	87	70	65	125
Heat conductivity coefficient at atmospheric pressure, W/(m°C)	0.058	0.054	0.049	0.072
Heat conductivity coefficient in vacuum, W/(m°C)	0.043	0.033	0.025	0.029

The proportion of the convective component of the heat transfer process in the body of expanded fire-retardant materials having a porosity in the body of expanded fire-retardant materials having a porosity in the range 82÷97.5 % can vary in a significant range of perlite: 25.9÷63.5 % and 6.7÷37.1 % of vermiculite, Table 4 [25].

Table 4. The proportion of convective component in the heat transfer of expanded fire-retardant materials.

Material	Particle size of solid fraction, mm			
	1.25÷2.5	0.63÷1.25	6.315÷0.63	0.14÷0.315
Expanded vermiculite	6.7	16.8	16.2	37.1
Expanded perlite	25.9	39.4	40.9	63.5

Increasing of fire resistance of LSTC elements can be carried out not only by using additional fire protection, but also by selecting products that are already part of this construction. As a study of the temperature dependence of the thermal conductivity of composite materials made on the basis of expanded vermiculite, the samples presented in Table 5 were considered and are demonstrated in Table 5.

Table 5. Test samples.

No. sample's	Structure	Density, kg/m^3
1	Vermiculite,	360
2	wollastonite,	540
3	liquid glass	700

When researching the temperature dependence of thermal conductivity, an IT-λ-400 thermal conductivity gauge was used in the monotonous heating mode.

It was suggested that the oxides in the composition of vermiculite in the temperature range from 0 °C to 400 °C have a decreasing dependence, then it is possible that the thermal conductivity of the material will decrease with increasing temperature. Table 6 and Fig. 5 show the results of studies of the temperature dependence of the thermal conductivity of composite materials, made on the basis of expanded vermiculite, obtained using a thermal conductivity meter. IT-λ-400, in monotonous mode.

Table 6. The dependence of the thermal conductivity of the composite material on temperature and density.

t,°C	λ, W/(m°C)		
	Material No.1	Material No.2	Material No.3
50	0.291	0.304	0.352
75	0.289	0.302	0.349
100	0.288	0.301	0.346
125	0.287	0.300	0.346
150	0.288	0.301	0.346
175	0.290	0.303	0.347
200	0.293	0.308	0.348
225	0.296	0.312	0.352
250	0.300	0.316	0.356
275	0.304	0.327	0.362
300	0.310	0.335	0.368
325	0.316	0.346	0.375
350	0.322	0.353	0.384
375	0.328	0.366	0.394
400	0.331	0.379	0.404

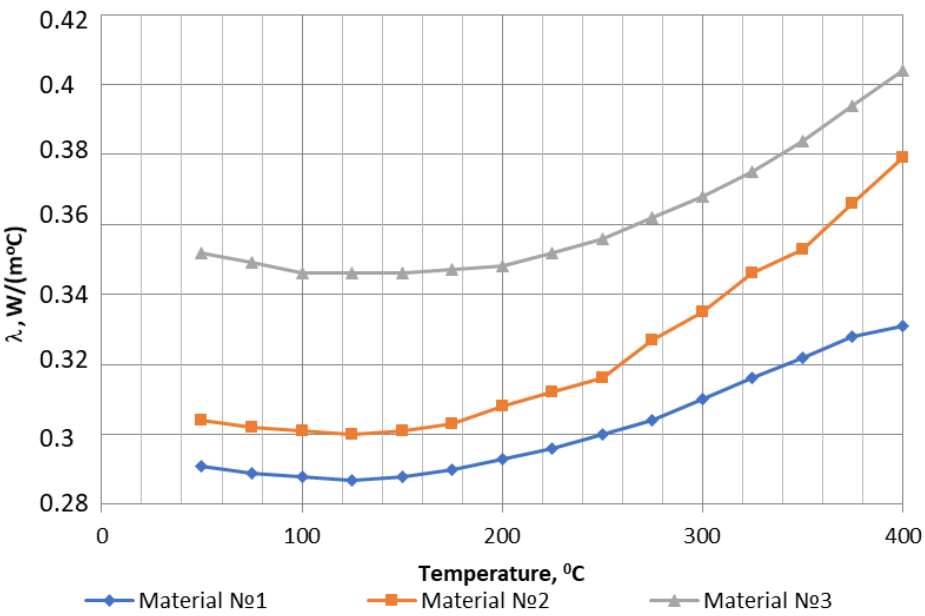

Figure 5 The dependence of the thermal conductivity of vermiculite products on temperature and density.

The experiment showed that the expected results coincide with those expected in the temperature range from 50 °C to 170 °C. Then the thermal conductivity increases monotonically. The distortion of the results can be explained by the radiant component of the thermal conductivity, which begins to increase sharply from 170 °C. With an increase in the density of materials, the thermal conductivity increases.

4. Conclusions

The problem of the working out and research of flame retardants with increased heat-protective properties, as you know, is very relevant. In the light of this problem, the low density and thermal conductivity of intumescent and fire-retardant compositions allow them to be classified as promising materials in the manufacture of heat-resistant and fire-retardant insulation.

In the framework of the presented work, a study was made of the temperature dependence of the thermal conductivity of a composer based on vermiculite, and the studies of domestic and foreign experts in this field were analyzed.

The results of the study confirm the legitimacy of the use of fire-retardant intumescent coating, since with an increase in the temperature of the combustion products the thin-walled fire protection layer made of fibrous materials does not work as effectively as fire protection from porous materials (for example, perlite or expanded vermiculite), as well as, that:

- With a decrease in the size of the solid fraction, the thermal conductivity coefficient of expanded vermiculite increases to a greater extent than that of perlite.
- There is a certain tendency towards an increase in the share of the convective component in the thermal conductivity of expanded fire-retardant materials as the particle sizes of their solid fraction decrease.

References

1. Gravit, M.V., Nedryshkin, O.V., Zhuravlyov, A.V. Negative use of finishing materials on Sorel's cement. MATEC Web of Conference. 2017. 106(2). 03029. DOI: 10.1051/matecconf/201710603029
2. Shevchenko, N., Manucharyan, R, Gravit, M., Geraskin, Y. Programs for calculating the explosion resistance of buildings and structures. IOP Conference Series: Earth and Environmental Science. 2017. 90. 012192. DOI: 10.1088/1755-1315/90/1/012192.
3. Gravit, M.V., Zybina, O., Vaitizkiy, A., Kopytova, A.V. Problems of magnesium oxide wallboard usage in construction. IOP Conference Series: Earth and Environmental Science. 90. 012103. DOI: 10.1088/1755-1315/90/1/012103.
4. Nedryshkin, O., Gravit, M.V., Mukhamedzhanova, O.V. Use of components of external substances in fire putties. IOP Conference Series:Earth and Enviromental Science 19. Cer "Energy Management of Municipal Transportation Facilities and Transport, EMMFT 2017"2017.C.012186.
5. Gravit, M., Mikhailov, E., Svintzov, S., Kolobzarov, A., Popovich, I. Fire and explosion protection of high-rise building by means of plastic composition. Material Science Forum. 2016. Vol. 871. Pp. 138–145.
6. Akimov, L.I., Ilenko, N., Mizharyov, E., Cherkashin, A., Vatin, N.I., Chumadova, L.I. Composite concrete to modify and its effect on the strong characteristics of concrete. MATEC Web of Conference. 2016. 01022.

7. Korniyenko, S.V., Vatin, N.I., Gorshkov, A.S. Thermophysical field testing of residential buildings made of autoclaved aerated concrete blocks. Magazine of Civil Engineering. 2016. 64(4). Pp. 10–25. DOI: 10.5862/MCE.64.2
8. Korsun, V.I., Kalmykov, Yu., Makarenko, S.Yu. Failute criteria modification option for flat concrete. Key Engineering Materials 2017. Vol. 755. Pp. 300–321.
9. Korsun, V., Korsun, A., Vatin, N., Nemova, D. Heterogeneous shrinkage of high-strength concrete in the volume of large-sized structural elemenets. Applied Mechanics and Materials. 2015. Vol. 723. Pp. 445–450.
10. Korsun, V., Korsun, A. The effect of precompression on the strength and deformation properties of concrete under the influence of elevated temperatures. Applied Mechanics and Materials. 2015. Vol. 725–726. Pp. 469–474.
11. Korsun, V., Korsun, A., Mashtaler, S. Determination of the critical duration of the first heating of heavy concrete by the criterion of maximum strength reduction. Applied Mechanics and Materials. 2015. Vol. 725–726. Pp. 566–571.
12. Gravit, M., Dmitriev, I., Ishkov, A. Quality control of fire retardant coating for reinforced concrete structures. IOP Conference Series: Earth and Environmental Science (Electronic resource) 2017.012226.
13. Drinberg, A.S., Gravit, M.V., Zybina, O.A. Ognezashchita konstruktsiy intumestsentnymi lakokrasochnymi materialami pri uglevodorodnom rezhime pozhara [Fire protection with intumescent coatings under the hydrocarbon fire conditions]. Russian Coatings Journal. 2018. No. 1-2. Pp. 44–49. (rus)
14. Akimov, L.I., Ilenko, N., Mizharyov, R., Cherkashin, A., Vatin, N.I., Chumadova, L.I. Composite concrete modifier and its effect on the strength characteristics of concrete MATEC Web of Conference 2016. Vol. 8. No. 53.
15. Bonic, Z., Curcc, G.T., Trivukic, M., Davidovich, N., Vatin, N.I. Some methods of protection of concrete and reinforcement of reinforced-concrete foundations exposed to environmental impacts. Procedia Engineering. 2015. DOI: 10.1016/j.proeng.2015.08.189
16. Gravit, M.V. Nedryshkin, O.V., Vaititzky, A.A., Shpakova, A.M., Nigmattulina, D.G. Fire and Technical characteristics of building materials in European and Russian regulatory documents. Problems of harmonization of research methods and classification. Fire and explosion safety. 2016. Vol. 25. No. 10. Pp. 16–29. DOI: 10.18322/PVB.2016.25.10.16-29 (rus)
17. Gravit, M.V., Svintzov, S.A., Ardeeva, A.A., Kolobzarov, A.E. Zashchita konstruktsiy vysotnykh zdaniy ot pozhara i vzryva shtukaturnymi sostavami [Protection of structures of high buildings from fire and explosion by plaster compositions]. Rostovsky Scientific journal. 2017. No. 5. Pp. 613–628. (rus)
18. Information about accidents that occurred at enterprises controlled by the territorial bodies of the Federal Service for Ecological, Technological Nuclear Supervision. (Electronic source) http/www.rostehnadzor.ru/chronicle.htm (appliance date 21.04.2018)
19. Zarichnyak, Yu.P., Emirov, S.N., Ramazanova, A.E. Evaluation of the role of thermal radiation in the measurement of thermal conductivity of rock samples. Monitoring. Science and technology. 2012. No. 3. Pp. 93–96. (rus)
20. Volkov, D.P., Romanov, N.N., Fedorov, A.V. Thermophysical properties of composites based on vermiculite. Natural and Technological Risks (physics-mathematical and applied aspects). 2013. No. 3(7). Pp. 30–37. (rus)
21. Volkov, D.P., Zarichnyak, Yu.P., Romanov, N.N. Heat conduction of fibrous thermal protection materials. Experimental study. Natural and Technological Risks (physics-mathematical and applied aspects). 2013. No. 4(8). Pp. 37–42. (rus)
22. Heat protection construction from mineral fibers (Electronic source) http://www.b-composites.net/78.html (appliance date 18/01/2013)
23. Strakhov, V.L., Krutov, A.M., Davidkin, N.F. Ognezashchita stroitel'nykh konstruktsiy [Fire protection of building construction] (edited by Yu.A. Koshmarov). Moscow: Information-Publication center “TIMP”, 2000. 433 p. (rus)
24. Zav'Yalov, D.E., Zybina, O.A., Chernova, N.S., Varlamov, A.V., Mnatsakanov, S.S. Fire intumescent compositions based on the intercalated graphite. Russian Journal of Applied Chemistry. 2010. T. 83. № 9. C. 1679-1682.
25. Dubenetzky, K.N., Pozhnin, A.P. Vermikulit (Svoystva, tekhnologiya i primeneniye v str-ve) [Vermiculite (quality, technology, and use in construction)]. Construction Literature Edition, 1971. 176 p. (rus)
26. Nizhegorodov, A.I. Vermikulit i vermikulitovyye tekhnologii: issledovaniya, proizvodstvo, primeneniye [Vermiculite and vermiculitous technologies: researches, production, use]. Irkutsk: Business-Stroy, 2008. 96 p. (rus)
27. Roytman, V.M., Gabdulin, R.S., Scherbina, S.V. Mekhanizatsiya formirovaniya ognezashchitnogo effekta vspuchivayushchikhsya pokrytiy zhelezobetonnykh konstruktsiy pri ikh nagreve [The mechanism of formation of fireproof effect for foam coverings of reinforced concrete structures by heating]. Nauka i Bezopasnost'. 2012. No. 4. Pp. 40–48. (rus)
28. Roytman V.M., Gabdulin, R.S. Ensuring of the reinforced concrete constructions durability against spalling under fire by thin layer intumescent fire retardant coating. Fire and emergencies: prevention, elimination. 2013. No. 2. Pp. 11–16. (rus)
29. Peletskii, V.E., Shur, B.A. Experimental study of the thermal conductivity of heat insulation materials based on expanded vermiculite. Refractories and Industrial Ceramics. 2007. 48(5). Pp. 356–358. DOI: 10.1007/s11148-007-0094-5

Contacts:

Vasiliy Gumenyuk, gumenyuk.vi@yandex.ru

Anatoliy Kuzmin, kaa47@mail.ru

Nikolai Romanov, nik57nik@mail.ru

Alexey Permiakov, jouker2005@yandex.ru

Oksana Gumenyuk, gumenyuk_ov@spbstu.ru

Ivan Dmitriev, i.i.dmitriev@yandex.ru

© Gumenyuk, V.I., Kuzmin, A.A., Romanov, N.N., Permiakov, A.A., Gumenyuk, O.V., Dmitriev, I.I., 2021

Magazine of Civil Engineering

ISSN 2712-8172

journal homepage: http://engstroy.spbstu.ru/

DOI: 10.34910/MCE.103.2

The features of the hydration and structure formation process of modified low-clinker binders

Sh.K. Zhakipbekov[a], L.B. Aruova[b]*, Sh.T. Toleubayeva[c], T.B. Ahmetganov[c], A.O. Utkelbaeva[d]

[a] *Future expansion project of Tengizchevroil, Atyrau, Republic of Kazakhstan*

[b] *Eurasian National University named after L.N. Gumilyov, Astana, Republic of Kazakhstan*

[c] *Karaganda State Technical University, Karaganda, Republic of Kazakhstan*

[d] *Kyzylorda State University, Kyzylorda, Republic of Kazakhstan*

** E-mail: ecoeducation@mail.ru*

Keywords: modified binder, hydration processes, calcium hydro silicates, binder composition, complex modifying additive, physical and chemical studies

Abstract. The effect of a complex additive consisting of silica fume and enrichment waste from the Karagailinsky mining and processing plant on the hydration and structure formation processes of cement systems is investigated. It was established that the introduction of a complex modifying additive consisting of silica fume and enrichment waste from the Karagailinsky mining and processing plant into the cement composition CEM I 42.5 N SR increases the compressive strength at the age of 28 days by 15.7–28 %. It was revealed that the studied complex additives contribute to an increase in the amount of chemically bound water. The processes of hydration and hardening of multicomponent modified binders were investigated. It is shown that the high strength of cement stone on a modified binder is due to the formation of stable low-base hydro silicates. The source of the formation of low-base calcium hydro silicates is the pozzolanic reaction, which proceeds with the binding of the clinker minerals released during hydration, portlandite silica complex additive. It is shown that purposefully changing the composition of the binder and hydration conditions, it is possible to improve the phase composition, morphology of hydrates and influence its final properties.

1. Introduction

Objective: to study the effect of a complex additive consisting of silica fume and enrichment waste from the Karagaila mining and processing plant on the hydration and structure formation of cement systems.

To achieve this goal, the following scientific problems are formulated and solved in this work:

- analysis of scientific research on the effects of various active mineral and finely dispersed additives on the properties of concrete;
- substantiation of scientific and practical aspects of the use of complex modifiers and fine industrial wastes in concrete technology;
- study of the effect of a complex additive consisting of silica fume and enrichment waste from the Karagailinsky mining and processing plant on the composition and morphology of hydrated neoplasms, as well as the hardening processes of cement systems.

The production of high-performance binders of the new generation today is accompanied by the use of complex compositions of components in order to obtain high-strength concrete of different functional purposes with high construction and operational properties [1–3]. It is known [4] that the addition of tripoli dolomite, limestone, slag, and calcined marl during grinding of Portland cement clinker accelerates cement hydration.

V.V. Timashev developed a quick-hardening binder containing 3–7 % alumina cement and 25–30 % active mineral additives (tripoli or diatomite). The reason for hardening acceleration is the formation of calcium hydrosulfoaluminate [5].

Zhakipbekov, Sh.K., Aruova, L.B., Toleubayeva Sh.T., Ahmetganov, T.B., Utkelbaeva, A.O. The features of the hydration and structure formation process of modified low-clinker binders. Magazine of Civil Engineering. 2021. 103(3). Article No. 10302. DOI: 10.34910/MCE.103.2

This work is licensed under a CC BY-NC 4.0

As an active mineral additive to cement, W.A. Ayapov used the flask of the Aisar deposit. Cement with an active mineral additive was activated by complex catalysts – gypsum and ROH, where R-Na, K. According to the authors, the presence of an active mineral additive containing amorphous silica in the cement contributes to an equal increase in the rate of catalytic reactions [7].

Vlasov V.K. investigated the role of active mineral additives in ultra-hardening cements. These cements, including the rapidly hydrating $C_{11}A_7COX$ (where X is fluorine or chlorine) and C3S, are characterized in some cases by strength drops caused by internal stresses, especially at the boundaries of hydro aluminates, which crystallize completely in 6–10 hours of hydration. To reduce the level of internal stresses of ultra-hardening cement, pozzolan type materials (ground volcanic ashes, tuffs, slopes, soot, diatomite, tripoli, calcined clay or slate, blast furnace slag) were introduced into its composition [8].

V.V. Timashev and V.M. Kolbasov established that the introduction of 5–10 % of active mineral additives favors the formation of a strong structure of cement stone by 28 days. The stabilizing role of active mineral additives for ettringite in cement stone and for moisture redistribution presses during cement hydration was confirmed.

The basis for the creation of modified low-linker binders is based on the principle of purposeful management of the technology at all its stages: the use of active components, the development of optimal compositions, the use of chemical modifiers and some other techniques [5, 6].

The introduction of active mineral additives into the cement composition reduces the likelihood of false setting, due to a reduction in the excess of $Ca(OH)_2$ in the liquid phase of the test and the adsorption of R_2O from it, and also hindering the formation of continuous aluminate aggregates with cement grains in the first minutes of hydration. In addition, active additives accelerate the movement of material through the mill, reduce the likelihood of grinding and “steaming” the mixture, disaggregate cement and prevent undesirable surface reactions.

The most important tasks of science in the field of construction: simplification of structures, acceleration and reduction in cost of technological processes, in particular, reducing the duration of heat and moisture treatment of products, increasing the corrosion resistance of concrete can be solved only by giving special properties to cements [8–10]. The way to solve this problem is through the expansion of the nomenclature of hardening modifiers [11–13]. The use of non-ferrous metallurgy waste as additives to cement will significantly expand the raw material base of the cement industry and meets modern requirements to ensure an increase in the demand for raw materials and materials due to their economy and more complete use of secondary raw materials, slags and other wastes [14, 15].

The basis for the creation of modified low-clinker binders is the principle of targeted technology management at all its stages: the use of active components, the development of optimal compositions, the use of chemical modifiers and some other techniques [16, 17].

According to this principle, a multicomponent binder containing up to 45 % of non-ferrous metallurgy waste and chemical additives was obtained [18]. At the same time, the improvement of the submicroscopic structure with a slight increase in the size of the effective radius of micropores from 10.5 to 10.8 nm was determined, which may be associated with the filling of large pores (more than 100 nm) with calcium hydro silicates [19].

As shown in [20], the applied complex additives based on enrichment waste do not increase the normal density of the dough, does not slow down as usual, but accelerate the rate of hydration of the binder. In combination with the use of plasticizing additives, these low-linker binders can be used for the manufacture of concrete and reinforced concrete products under optimal hardening conditions.

2. Research methods

An X-ray diffraction study of the materials was carried out on an URS-50I X-ray diffractometer. Radiographs were taken from flat powdered samples rotating in the plane of the axis of the goniometer at a speed of 25 rev/m, in the range of angles from 20º to 61º. X-ray mode: X-ray radiation ScKº – filter Ni; 14 microns thick, anode current of the X-ray tube 11.5 mA, counter slit 0.25×8 mm, slit limiting the primary beam 1×5 mm, recording constant Rº – IV, recording range of intensities D-1000 imp /c, speed movement of the chart tape 360 mm/hour.

Differential thermal studies were carried out on a MOM-1000 derivatograph system F. Poulik, I. Powlik and L. Erdey (Germany) in the temperature range 25–1000 ºC in an air stream. The rate of temperature rise is 7.5 deg/min. Thermal transformations were determined from the curves of mass loss (TG), differential mass loss (DTA) and the change in differential temperature (DTA).

1. Spectral analysis of cement stone was carried out on a Spekord two-channel spectrophotometer. Using electron microscopes REM-200 and EVM-100 BR, the shapes, sizes, arrangement, and type of crystals

were investigated, volumetric images were obtained, and the composition of individual sections of cement stone was determined.

2. The studies were carried out by the powder method. Samples prepared for REM-200 and EVM-100 BR studies were dried to constant weight and crushed to a specific surface of 480.0 m^2/kg [21, 22].

The optimal content of complex modifying additives was determined based on the greatest compressive strength of cement stone by testing 4×4×16 cm (mortar) after normal hardening according to Russian State Standard GOST 310.4-81 “Cements. Methods for determining the tensile strength in bending and compression" [23]. For a comparative analysis of the effect of complex additives on the compressive strength (Table 1), concrete samples based on cement CEM I 42.5 N SR without additives and with complex modifying additives were prepared with W/C = 0.4.

Heat and moisture treatment of prototypes is carried out according to the mode 2 + 4 + 1 h at a maximum temperature of 65 °C. In this case, the maximum processing temperature is reduced by 20 °C against the usual, and the duration of the isothermal exposure is reduced by 3 hours. Heat treatment was also carried out using solar energy at a maximum temperature of 65 °C during daylight hours in translucent chambers [24, 25].

3. Results and Discussion

The composition of the binder includes (in % by weight): cement CEM I 42.5 N SR – 70-80; silica fume – 5–10; enrichment waste – 10–20. The binder is prepared by joint dry grinding of the components to a specific surface of 320–350 m^2/kg.

Sulfate-resistant Portland cement CEM I 42.5N SR GOST 22266-2013 Standard-Cement LLP (Republic of Kazakhstan, Shymkent) was used as a binder without additives [26].

The enrichment waste of the Karagailinsky mining and processing plant (Kazakhstan) with a specific surface area of 160–205 m^2/kg consists mainly of quartz (76-85 %); there are minerals: montmorillonite (5–8 %), dolomite (5–10 %), repidomite (3–5 %), pyrite (1–6 %), albite (2–4 %), leuchtenbergite (3–10 %). Chemical composition of enrichment waste (% by weight): SiO_2 – 84.19; Fe_2O_3 1.18; Al_2O_3 – 1.58; CaO – 2.58; MgO – 0.60; C – 1.52; S_{total} – 0.54.

Silica fume, a nanomaterial, is a waste product of the production of silicon-containing alloys: ferrosilicon, crystalline silicon, etc. During melting of the charge and reduction of quartz at temperatures above 1800 °C, gel-like silicon is formed, when cooled and in contact with air, it oxidizes to SiO_2 and condenses in the form of ultrafine silica particles. The particle size of silica fume is 0.1–0.5 micrometers.

Table 1. Properties of modified low-linker binder.

Composition of the binder, mass %			Tensile strength at compression, MPa
cement	microsilica	enrichment waste	
100	-	-	44.5
84,5	5	10	51.5
74,2	7.5	15	57.0
64,0	10	20	54.0

The compositions and strength properties of the developed modified low-clinker binder are given in Table. 1. The test results show that the compressive strength of the modified small clinker binder at the age of 28 days hardening under normal conditions is 51.5–57.0 MPa. The introduction of a complex modifying additive to the cement composition CEM I 42.5 N SR increases the compressive strength at the age of 28 days by 15.7–28 %.

On roentgenograms of the modified low-clinker binder, there are also lines with d = 0.422; 0.390; 0.180; 0.260; 0.241 nm, indicating the presence of a C_2SH (A) type hydro silicate (Fig. 1), as well as the formation of two types of CSH (II) hydro silicates and gyrolite. They correspond to diffraction maxima with d = 0.304; 0.280; 0.182; 0.167 nm – CSH (II) and d = 0.424; 0.336; 0.384; 0.285; 0.265; 0.225 nm – gyrolite (Fig. 1). The formation in the stone of a modified low-clinker binder mineral gyrolite is explained by the high reactivity of silica fume and is associated with the presence in the latter of the predominant amount of amorphous finely divided silica. The results of X-ray phase analysis are confirmed by differential thermal analysis (DTA) (Fig. 2).

Analysis of thermograms showed that all thermograms in the low-temperature region have endo-effects associated with the primary dehydration of calcium hydro silicates. Moreover, as is known from the literature, the endo-effect at T = 120–150 ºC corresponds to a gyrolite, and the exo-effect at T = 200–250 ºC corresponds to CSH (II).

For C_2SH (A), dehydration is characteristic at a temperature of 420–480 ºC. Such endo effects were found only in steamed samples. This corresponds to a change in the stoichiometric ratio of CaO and SiO_2 oxides in raw mixtures.

Differential thermal studies (DTG curves and the results of moisture loss during heating) of a cement stone indicate a close correlation between the heating temperature and the ability of the hydrated phases to retain water when heated (Table 2).

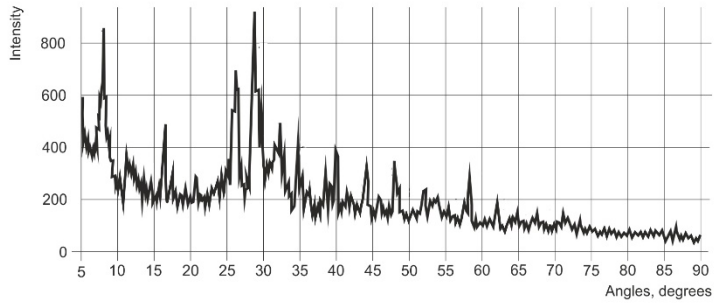

Figure 1. Radiograph of a modified low-clinker binder at 28 days of hardening.

Analysis of the mass loss during the heating of cement stone (Table 2) shows that complex additives contribute to an increase in the amount of chemically bound water.

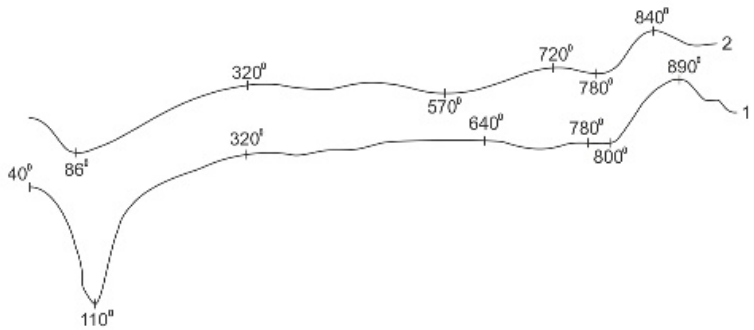

Figure 2. Thermogram of binders at the 28-day age of hardening:
1 – modified low-clinker binder; 2 – cement without additives.

Differential thermal studies confirm the data of x-ray analyzes. DTG curves and the results of cement stone moisture loss (Table 2) upon heating indicates a close correlation between the heating temperature and the ability of the hydrated phases to retain water when heated. Complex additives contribute to the increase in the amount of chemically bound water.

Table 2. Mass Loss during heating of cement stone from modified low-linker binder (MMV) according to DTA data.

Type of binder	Mass loss in % in the temperature interval, ºC			Relative mass loss, %
	20–200	20–600	20–1000	
CEM I 42.5 H SR	4.9	13.5	23	36
IIM	5.2	12.3	22	41

It can be assumed that these additives are enrichment waste, increasing the centers of crystallization and favor the growth of inter-crystalline cavities inside, which arise during the formation of a supramolecular layered structure. Such cavities are able to keep water molecules in a particularly oriented state, in which the rotational degrees of freedom of the molecule are inhibited and the translational ones are partially limited [27]. Within the monolayer, such water molecules have significant mobility and create conditions for easy sliding of the cement gel, which in turn facilitates the appearance of irreversible plastic deformations.

In the IR spectrum of cement stone, after 1 day in the wave number range of 700–1200 cm^{-1}, a wide band is distinguished, split into parts characteristic of calcium silicates. Absorption maxima at 930, 885, 840 cm^{-1} indicate the presence of dehydrated C3S (Fig. 3).

The infrared spectrum of the cement stone of modified low-clinker cement (Fig. 3) after 3 days shows absorption bands at 730, 780, 820, 860 and 880 cm^{-1}, which indicates the presence of a large degree of distortion in the structure of the mineral $[AlO_4]$.

In the cement stone of modified low-clinker cement, $[AlO_4]$ tetrahedra are severely deformed, which explains the high hydration activity in the initial stages of hardening. The absorption bands at 890, 860, 820, 780 cm^{-1} are due to the stretching vibrations of the bound $[AlO_4]$ groups, and the band at 730 cm^{-1} are due to the stretching vibrations of the isolated $[AlO_4]$ tetrahedra.

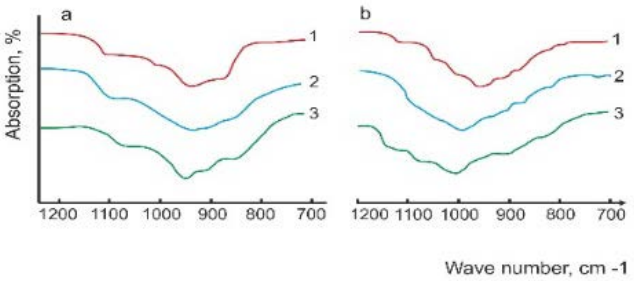

Figure 3. The infrared spectrum of cement stone
a – cement CEM I 42.5 N SR, b – modified low-clinker cement stone.
1, 2 and 3 after 1,3 and 28 days of normal hardening.

At the 28-day hardening age, the absorption band at 940 cm^{-1} observed in cement CEM I 42.5 N SR with the introduction of complex additives in it shifts toward large wavenumbers and is absorbed at 970 cm^{-1}. Such a shift of the bands shows the process of polycondensation of $[SiO_4]$ – tetrahedra; due to the modified binder, the basicity of hydro silicates decreases [28].

Using electron microscopes, the shapes, sizes, arrangement, and appearance of crystals were studied, volumetric images were obtained, and the compositions of individual sections of cement stone were determined. The processes of germination of the phases CH and C-S-H, as well as changes in the morphology of hydrates, were studied.

With an increase of 2500 times, micropores with a size of 2–3 microns are observed. Recrystallization and growth of hexagonal portlandite crystals obey the laws of collective growth and proceed metasomatically [29]. With an increase in the hardening time, crystallization of portlandite occurs by topochemical hydration processes inside anhydrous silicate crystals [30, 31]. The resulting calcium hydroxide can be almost amorphous due to the lack of space for diffusion, as well as due to disturbances created by inclusions of silicon-containing groups.

a) **b)**

Figure 4. Microstructure of a modified low clinker binder, x2500
a – micropores of cement stone are compacted with thin sheets with CSH foil (1)
(at 180 days of hardening age); b – Intergrowth of portlandite blocks with gel-like CSH.

Amorphous portlandite is very difficult to distinguish from poorly crystallized gel phases of CSH during X-ray phase and electron microscopy studies. However, the authors of [5] proved the existence of amorphous portlandite in the hydration products of C_3S and β-C_2S.

During hardening, Portlandite binds to active silica complex additives. If portlandite is in an amorphous form, the pozzolanic reaction (the binding process) is faster. In this case, the most typical form of CSH (1) is formed, which is large, but very thin sheets or foil with a thickness equal to the thickness of the main layer (Fig. 4, a). These sheets or foil stick together easily, forming loose folded aggregates up to 2 micrometers in size. The leaves of CSH (1) foil are so thin and transparent that only folds are observed, giving the impression of a fine-fiber structure.

Unlike the control one, in a cement stone with complex additives in portlandite blocks they are tightly fused with the cement gel, forming a monolith of gel and CH or areas of their mutual germination (Fig. 4, b). The structure of the external rhythm consists of embryos and growing crystals, obeying the laws of collective growth.

With an increase in the hardening time, crystals grow in the structures of the external rhythm and crystals arise in the structures of the internal rhythm, which leads to the recrystallization of crystals and their nuclei. Complex additives, affecting the nature of crystallization, can change the composition of the crystal, forming solid solutions.

In the process of cement stone hardening, portlandite layers are the matrix for the incorporation of various elements and ions into it with the subsequent formation of hydrated compounds. This explains the presence of structural elements of calcium hydroxide in many hydrated compounds of cement stone.

4. Conclusion

1. It was established that the introduction of a complex modifying additive to the composition of cement CEM I 42.5 N SR consisting of silica fume and enrichment waste from the Karagailinsky mining and processing plant increases compressive strength at the age of 28 days by 15.7–28 %.

2. DTG curves and the results of cement stone moisture loss upon heating indicates a close correlation between the heating temperature and the ability of the hydrated phases to retain water when heated. Complex additives contribute to the increase in the amount of chemically bound water.

3. To ensure the formation of the structure of a cement stone with minimal porosity and increased strength, it is necessary to stabilize the composition of hydrated neoplasms, prevent their phase transitions, regulate the hydration process, the optimal ratio of crystalline gel-like masses in hydration products by selecting the composition of mineral additives and micro-fillers.

4. An additional source of the formation of stable calcium hydro silicates is the pozzolanic reaction, which takes place with the absorption of portlandite released by hydration of clinker minerals with amorphous silica of a complex modifying additive.

References

1. Neville, A.M., Brooks, J.J. Concrete technology. Prentice Hall, 2010. 392 s.
2. Yusuf, M.O. Synergistic-effect of iron-filing and silica-fume on the absorption and shrinkage of cement paste. Magazine of Civil Engineering. 2019. 91(7). Pp. 16–26. DOI: 10.18720/MCE.91.2
3. Yusuf, M.O. Microstructure and strength of iron-filing Portland cement paste and mortar. Magazine of Civil Engineering. 2019. 90(6). Pp. 28–36. DOI: 10.18720/MCE.90.3
4. Hyun-Oh Shin, Doo-Yeol Yoo, Joo-Ha Lee, Seung-Hoon Lee, Young-Soo Yoon. Optimized mix design for 180MPa ultra-high-strength concrete. The Journal of Materials Research and Technology. Vol. 8. Issue 5. Pp. 4182-4196 (September – October 2019. DOI: 10.1016/j.jmrt.2019.07.027. http://www.jmrt.com.br/en-optimized-mix-design-for-180mpa-articulo-S223878541930153X
5. Timashev, V.V. Sintez i gidratatsiya vyazhuschih materialov [Synthesis and hydration of binders]. Izbrannyie trudyi. Moscow: Nauka, 1986. 424 p. (rus)
6. Kolbasov, V.M. Tehnologicheskie faktoryi upravleniya strukturoy tsementnogo kamnya. [Technological factors of controlling the structure of cement stone]. TSement, 1983. No. 5. Pp. 12–13. (rus)
7. Ayapov, U.A., Butt, Yu.M. Tverdenie vyazhuschih s dobavkami – intensifikatorami [Curing of binders with additives-amplifiers]. Alma-Ata: Nauka. 1978. 256 p. (rus)
8. Vlasov, V.K. Zakonomernosti optimizatsii sostava betona s dispersnyimi mineralnyimi dobavkami [Regularities of optimization of the composition of concrete with dispersed mineral additives]. Beton i zhelezobeton. 1993. 4. Pp. 10–12. (rus)
9. Tarakanov, O.V., Tarakanova, E.O. The formation of microstructure of the compounded cement materials. Magazine of Civil Engineering. 2009. 10(8). Pp. 13–16. (rus). DOI: 10.18720/MCE.10.1
10. Tokmyrza, B., Aruova, L., Dauzhanov, N., Ospanova, Zh., Utkelbaeva, A. Comprehensive heat treatment using solar energy to produce high quality foam concrete. E3S Web Conf. 2019. Vol. 116. International Conference on Advances in Energy Systems and Environmental Engineering (ASEE19). https://doi.org/10.1051/e3sconf/201911600092.
11. Sharonova, O.M., Yumashev, V.V., Solovyov, L.A., Anshits, A.G. The fine high-calcium fly ash as the basis of composite cementing material. Magazine of Civil Engineering. 2019. 91(7). Pp. 60–72. DOI: 10.18720/MCE.91.6
12. Wang, H., He, Y., Pan, Y., Yu, G. Mechanical properties of magnesium potassium phosphate cement. Magazine of Civil Engineering. 2019. 87(3). Pp. 59–65. DOI: 10.18720/MCE.87.5
13. Osuská, L., Ťažký, M., Hela, R. High-Performance Cement Composite for Architectural Elements with Elimination of Micro Cracks. International Journal of Engineering and Technology. 2019. Vol. 11. No. 2. P. 60.
14. Byoungsun, P., Choi, Y. Investigating a new method to assess the self-healing performance of hardened cement pastes containing supplementary cementitious materials and crystalline admixtures. Journal of Materials Research and Technology. 2019. 8. 10.1016/j.jmrt.2019.09.080.
15. Kumar, S., Rai, B. A review on wider application of supplementary cementitious materials on the development of high-performance concrete. International Journal of Civil Engineering and Technology. 2018. 9. Pp. 187–204.
16. Mukhametrakhimov, R., Galautdinov, A., Lukmanova, L. Influence of active mineral additives on the basic properties of the gypsum cement pozzolan binder for the manufacture of building products. MATEC Web of Conferences. 2017. 106. 03012 DOI: 10.1051/matecconf/20171060 SPbWOSCE-2016 3012.

17. Zulu, B.A., Miyazawa, Sh., Nito, N. Properties of blast-furnace slag cement concrete subjected to accelerated curing. Infrastructures. 2019. 4(4). 69. https://doi.org/10.3390/infrastructures4040069
18. Netinger Grubeša, I., Barisic I., Fucic, A., Bansode, S. Characteristics and Uses of Steel Slag in Building Construction. Woodhead Publishing, 2016. 194 p. https://www.elsevier.com/books/T/A/9780081003688
19. Zhakipbekov, Sh.K., Zhakipbekov, D.Sh. Tverdenie maloklinkernyh vyazhushchih s ispol'zovaniem kompleksnyh modificiruyushchih dobavok [Hardening of low-clinker binders using complex modifying additives]. Suhie stroitel'nye smesi. 2014. No. 5. Pp. 21–22. (rus)
20. Belyaeva, I.D. Elektronno-mikroskopicheskie issledovaniya metamiktnyih mineralov, [Electron microscopic studies of metamict minerals]. Moscow: Nauka, 1981. 80 p. (rus)
21. Plyusnina, I.I. Infrakrasnyie spektryi mineralov [Infrared spectra of minerals]. Moscow: izd. MGU, 1977. 175 p. (rus)
22. Russian State Standard GOST 310.4 -81 “Tsementyi. Metodyi opredeleniya predela prochnosti pri izgibe i szhatii” [SS 310.4 -81 “Cements. Methods for determining the ultimate strength in bending and compression”] [Online]. URL: https://online.zakon.kz/document/?doc_id=30-039052#pos=0;0 (reference date: 03.05.2020). (rus)
23. Aruova, L., Dauzhanov, N., Ospanova, Zh., Toleubayeva, Sh., Utkelbaeva, A. Technology of production of polystyrene concrete using solar energy. MATEC Web Conf. 2018. Vol. 251. 01003. VI International Scientific Conference “Integration, Partnership and Innovation in Construction Science and Education” (IPICSE-2018). https://doi.org/10.1051/matecconf/201825101003
24. Russian State Standard GOST 22266-2013 sulfatostoykiy portlandtsement [SS 22266-2013 Sulfate-resistant Portland cement] [Online]. URL: http://docs.cntd.ru/document/1200111313 (reference date: 03.05.2020). (rus)
25. Lee, Y., Kim, M., Chen, Zh., Lee, H., Lim, S. Chloride-Binding Capacity of Portland Cement Paste Blended with Synthesized CA2 ($CaO{\cdot}2Al_2O_3$). Advances in Materials Science and Engineering. Volume 2018. Article ID 5418930. https://doi.org/10.1155/2018/5418930.
26. Zhakipbekov, SH.K., Zhakipbekov, D.SH. Osobennosti tverdeniya modificirovannyh betonov na osnove mestnyh vyazhushchih veshchestv [Features of hardening of modified concrete based on local binders]. Tekhnologii betonov. 2014. No. 10. Pp. 10–11. (rus)
27. Chaunsali, P., Mondal, P. Hydration and early-age expansion of calcium sulfur aluminate cement-based binders: experiments and thermodynamic modeling. Journal of Sustainable Cement-Based Materials. 2016. Vol. 5. No. 4. Pp. 259–267. https://www.tandfonline.com/author/Chaunsali%2C+Piyush
28. Rao, M., Wei, J., Gao, Zh., Zhou, W., Li, Q., Liu, Sh. Study on strength and microstructure of cement-based materials containing combination mineral admixtures. Advances in Materials Science and Engineering. 2016. Vol. 2016. Article ID 7243670. http://dx.doi.org/10.1155/2016/7243670.

Contacts:

Shariphan Zhakipbekov, science_2019@mail.ru
Lyazat Aruova, ecoeducation@mail.ru
Shamshygaiyn Toleubayeva, shamshygaiyn@mail.ru
Talgat Ahmetganov, ecology_2018@mail.ru
Aizhan Utkelbaeva, ecoeducation@mail.ru

© Zhakipbekov, Sh.K., Aruova, L.B., Toleubayeva, Sh.T., Ahmetganov, T.B., Utkelbaeva, A.O., 2021

Magazine of Civil Engineering

ISSN 2712-8172

journal homepage: http://engstroy.spbstu.ru/

DOI: 10.34910/MCE.103.3

Reinforced concrete beams strength under power and environmental influences

N.V. Frolov*, G.A. Smolyago
Belgorod State Technological University named after V.G. Shukhov, Belgorod, Russia
**E-mail: frolov_pgs@mail.ru*

Keywords: durability, reinforced concrete beams, experimental investigations, bending strength, corrosion damages, mechanical properties, load

Abstract. The article is devoted to the problem of assessing and predicting the strength of normal sections of bended reinforced concrete elements, which are exposed during operation to long-term force and environmental influences. It is noted that together with the accumulation of concrete and steel reinforcement corrosion damages, the load bearing capacity of reinforced concrete structures can be significantly reduced. At the same time, the existing methods for strength calculating are still applied and do not allow from a single point of view to reflect sufficiently strictly and in detail the stress-strain state of normal sections of bended reinforced concrete elements, taking into account the influence of all operational factors on it. Thereby, based on the nonlinear deformation model of reinforced concrete, a universal calculation procedure was developed. To approve it, the experimental studies of reinforced concrete beams samples that were under static load in sulfate- and chloride-containing aggressive environments for a long time were carried out. New features of corrosion damages accumulation in concrete and steel reinforcement in these aggressive environments were determined. After comparing the experimental and calculated data of normal sections strength, it was concluded that the proposed method has sufficient accuracy and can be used for practical calculations of operated bended reinforced concrete elements with defects and damages.

1. Introduction

In many cases, during long-term operation, bended reinforced concrete elements, in addition to power loading, also perceive various aggressive environmental influences, which lead to corrosion initiation and, as a result, to concrete and reinforcement damages. Over time, together with corrosion damages accumulation, a significant decrease in bearing capacity of reinforced concrete structures can occur. In this regard, to ensure bended reinforced concrete elements durability and reliability during operation under load in aggressive environments, in our opinion, the valuation and prediction researches of their normal sections strength are relevant.

Despite the broad theoretical and experimental researches of bended reinforced concrete elements under various operating conditions, presented in publications [1–8], far from all the features of the stress-strain state of their normal sections are studied with the long-term joint force and environmental influences.

Based on scientific literature general analysis of corrosion damages development in reinforced concrete structures [9–17], it can be noted that among a wide range of environmental influences, the effects of sulfates are most aggressive with respect to concrete with a cement binder, and chloride effects with respect to steel reinforcement. As a result of corrosion damages, the sections geometric dimensions decrease and the deformation-strength characteristics of concrete and steel reinforcement decrease. In addition, breaking adhesion between concrete and reinforcement is possible [18, 19].

It was determined that corrosion damages accumulation of concrete and reinforcement in reinforced concrete structures often proceeds jointly and depends on the sign and level of stresses acting in the materials [20, 21]. But taking into account such temporary factors as strength set and concrete creep in bended concrete elements researches, these processes are considered superficially.

Frolov, N.V., Smolyago, G.A. Reinforced concrete beams strength under power and environmental influences. Magazine of Civil Engineering. 2021. 103(3). Article No. 10303. DOI: 10.34910/MCE.103.3

This work is licensed under a CC BY-NC 4.0

The most methods and approaches to solving problems of determining the normal sections strength of bended reinforced concrete elements with damages were developed before the computer technology existed. The lack of powerful computing tools forced scientists to go through the development of the so-called engineering methods of calculation [22–25]. However, such a path led to fragmented decisions, dividing the definition domain into a number of sections with different models and solutions, loading with empirical coefficients, and the need to correct them when expanding the types of materials and accumulating information about their work.

It was determined in [26] that structural materials degradation properties as a result of long-term force impacts can be calculated in reinforced concrete model deformation by adjusting the corresponding deformation diagrams and section sizes. At the same time, the existing calculation methods based on the deformation model make it possible to determine the normal sections strength of bended reinforced concrete elements with only corrosion damages of longitudinal reinforcement and concrete of the compressed zone [27–29, 33]. Concrete damages in the stretched zone and at the section side faces are outside of consideration. In addition, a linear, and even uniform damage plot is allowed for all sections, which cannot be linked in any way with a different level of stress distribution in different sections of the element, or with cases of uneven concentration of an aggressive medium over the span. Thus, these techniques do not allow, from a single point of view, to reflect in sufficient detail and objectively the stress-strain state of normal sections of bended reinforced concrete elements under prolonged force and environmental influences.

The purpose of this article is the development and experimental approval of a universal method for calculating the strength of normal sections of bended concrete elements subjected to prolonged force and environmental influences.

To achieve this goal, a number of tasks are solved:

- calculating method development for normal sections strength of bended reinforced concrete elements under long-term force and environmental influences, taking into account non-linear diagrams of concrete deformation and various schemes of corrosion damages development at the section boundaries, as well as various sections damage degrees within the span;
- conducting experimental researches of normal sections strength of bended reinforced concrete elements which were under load in aggressive environments for a long time;
- developed methodology verification by comparing theoretical and experimental data on normal sections strength of bended reinforced concrete elements with corrosion damage.

2. Method

2.1. Calculation method

The calculation method is based on a deformation model of reinforced concrete taking into account the following premises, working hypotheses and assumptions:

- The normal section is taken for calculation, the stress-strain state of which corresponds to the average state of the block between cracks;
- At all levels of element loading, the compatibility conditions of structural materials deformations and the hypothesis of flat sections remain valid for the section under consideration;
- The magnitude of the external load on the element and aggressive medium concentration near the section are considered constant throughout the entire observation period; environmental influences begin to appear with a relatively stable stress-strain state of the cross section;
- The kinetic stability of nonequilibrium processes of corrosion damage promoting and creep deformations development is accepted;
- Only concrete decaying corrosion damages with a kinetics parameter $m = 1$ [30, 31] is considered, the measure of which in the calculation is the damage depth, determined according to the expression V.M. Bondarenko:

$$\delta\left(t,t_0\right)=\left(1-\Delta\delta\left(t,t_0\right)\cdot e^{-\alpha(t-t_0)}\right)\delta_{cr}(t_0), \tag{1}$$

and nonlinear function of the damage coefficient $K^*(z)$, determined from the boundary conditions according to Fig. 1. For the concrete surface layer ($z = 0$), the damage coefficient $K^*_{=\min}$ is found in accordance with Russian State Standard GOST 25881. Hereinafter, designations with the symbol "*" refer to materials damaged by corrosion.

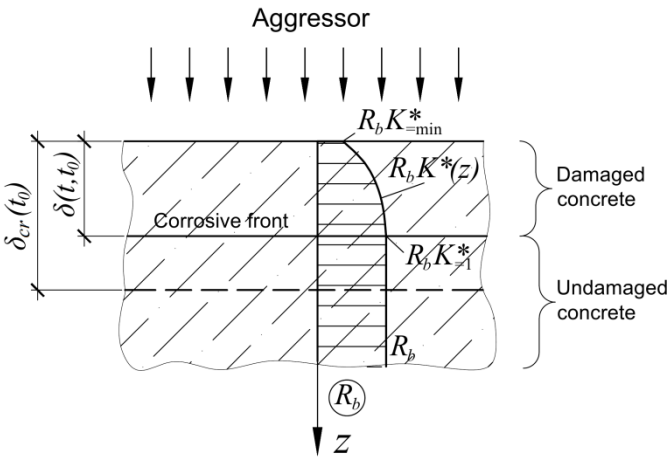

Figure 1. Concrete corrosion damages.

The following notation is introduced in formula (1) and in Fig. 1: $\delta_{кр}(t_0)$ and α are the kinetics parameters of concrete corrosion damages, determined from experimental data; $\Delta\delta(t,t_0)$ is the relative deficit of the current value of corrosion damage depth $\delta(t,t_0)$; t and t_0 are current and initial observation period, respectively; R_b is a characteristic of concrete mechanical properties, in this case is prism strength;

- Steel reinforcement corrosion damages is taken into account by a decrease in the calculated cross-sectional area according to the formula

$$A_s^* = A_s - A_s^{cor}, \tag{2}$$

where A_s^{cor} is lost area, determined by the Table 1 depending on the reinforcing bars wear model; reinforcement damage depth is determined by the formula

$$\delta_s(t) = \begin{cases} 0, & t \le t_{inc} \\ \dfrac{\delta_{s,0} \cdot (t - t_{inc})}{T + (t - t_{inc})}, & t > t_{inc} \end{cases}, \tag{3}$$

where: t_{inc} is reinforcement corrosion initiation time, found from the expression (1) with concrete damage depth equal to the thickness of the protective layer; $\delta_{s,0}$ and T are the parameters of the kinetics of corrosion damages of steel reinforcement, determined from experimental data.

Table 1 shows the main models of corrosion damage development along the cross section of a steel reinforcing bar. The model "continuous uniform corrosion" assumes that the aggressive conditions on the entire surface of the cross section of the rod are the same and its damages along the perimeter will be uniform with the depth δ_s. The models of "uneven corrosion" suggest that on one of the surfaces of the rod cross-section (in this case, on the bottom) the conditions are much more aggressive than on others, while its damage will be uneven with a maximum depth of δ_s. So, in the "pitting corrosion" model, the damage boundary is described by a circle curve with a radius δ_s and a with a center located in the corrosion area. In the "flat front" model, the damage boundary is described by a straight line outlying to distance δ_s from the corrosion area. In the "sickle-shaped front" model, the damage boundary is described by an arc with three parametric points, which are determined using the sector angle α and ordinate δ_s from the corrosion area;

- Diagrams of concrete deformation under short-term and long-term loading (Fig. 2) are described by a power polynomial of the form

$$\sigma_b = \sum_{k=1}^{n} a_k \varepsilon_b^k, \tag{4}$$

where: a_k is polynomial coefficients determined experimentally or by calculation, depending on the loading mode; k is an exponent equal to positive integers 1, 2 ... n. In this case, the value of n is taken based on the type of design diagram of concrete deformation, for example, for a nonlinear diagram with a descending branch n = 5.

The parameters of concrete deformation graphs under tension are determined experimentally or based on the corresponding parameters in compression using empirical dependence between them.

Table 1. Models of reinforcement bar corrosion wear.

Bar corrosion wear model		Reinforcement bar cross section	
		Design model	Calculated area of corrosion damage A_s^{cor}
	Continuous uniform corrosion	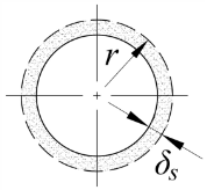	$\pi\delta_s(2r-\delta_s)$
Uneven corrosion	Pitting corrosion [Shmelev, G.D]	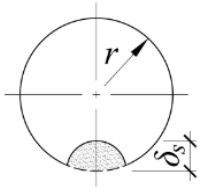	$\delta_s^2\sqrt{m-m^2}+\delta_s^2\arcsin\sqrt{m}-2r\delta_s\sqrt{m}+$ $+\delta_s\sqrt{mr^2-\delta_s^2m^2}+r^2\arcsin\frac{\delta_s\sqrt{m}}{r}$, where $m=1-\delta_s^2/4r^2$
	Flat front	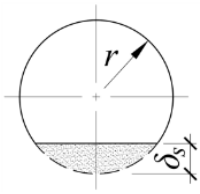	$(\delta_s-r)\sqrt{2r\delta_s-\delta_s^2}+r^2\arcsin\frac{\sqrt{2r\delta_s-\delta_s^2}}{r}$
	Sickle-shaped front [Ovchinnikov, I.G.]	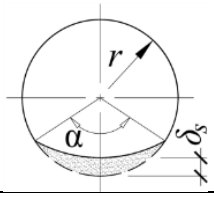	$\frac{r^2}{2}(\alpha-\sin\alpha)+\frac{(2r-\delta_s)^2}{2}\left(\frac{\alpha}{2}-\sin\frac{a}{2}\right)$, where $\alpha=4\arccos\left(1-\frac{\delta_s}{2r}\right)$

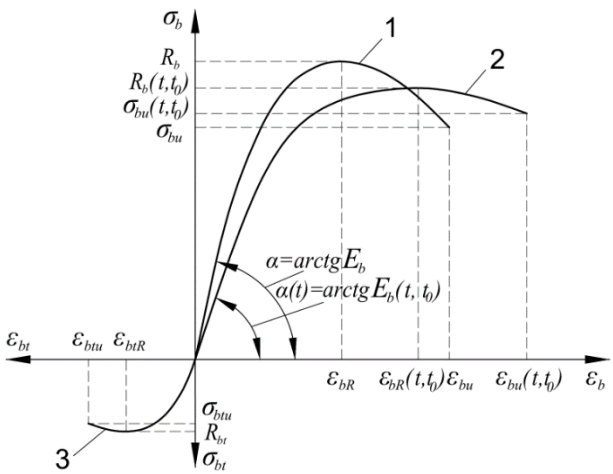

Figure 2. Concrete deformation diagrams under short-term (1, 3) and long-term (2) loadings.

Changes in concrete deformation diagrams parameters due to corrosion are taken into account using the damage coefficient K^*.

- After the concrete stretching deformations reach their limit values ε_{btu}, the stress diagram obtains a rectangular shape with the ordinate $\psi_{bt}R_{bt}$, where the coefficient ψ_{bt} takes into account the gradual decrease in the strength resistance of concrete of the stretched zone after crack formation and is determined based on studies [32] depending on the magnitude of the stresses acting in the tensile reinforcement according to the formula

$$\psi_{bt} = \begin{cases} \psi_{bt,1} = e^{\frac{1}{k_1 k_2} \times \frac{\varepsilon_{btu} - \varepsilon_{bt}}{\varepsilon_{btu}} \sum_{j=1}^{m} \frac{n_j d_j}{h_{0j}}}, & \text{at } \sigma_s < \sigma_{sy} \\ \psi_{bt,2} = \psi_{bt,1}^{(\sigma_{sy})} = \text{const}, & \text{at } \sigma_s = \sigma_{sy} \\ \psi_{bt,3} = \psi_{bt,2} \dfrac{\varepsilon_{bt,\sigma_{sy}}}{\varepsilon_{bt}}, & \text{at } \sigma_s = \sigma_{sy} \end{cases}, \tag{5}$$

where: k_1 is the number of armature rows; k_2 is the coefficient taking into account the armature profile; ε_{btu} is concrete stretching ultimate strains; ε_{bt}, ε_{bt}, σ_{sy} is the most stretched concrete fiber deformations, respectively, at the current value of stresses in the armature and at the moment of its transition to strengthening; n_j is the number of bars of the same diameter; d_j, h_{0j} is respectively the diameter of the j-th bar and the distance from its center of gravity to the most compressed concrete fiber.

- Steel reinforcement deformation diagrams under tension and compression, both for short-term and for long-term loading are piecewise linear.

Stress-strain determination state and normal section strength of flexural element is carried out according to Fig. 3.

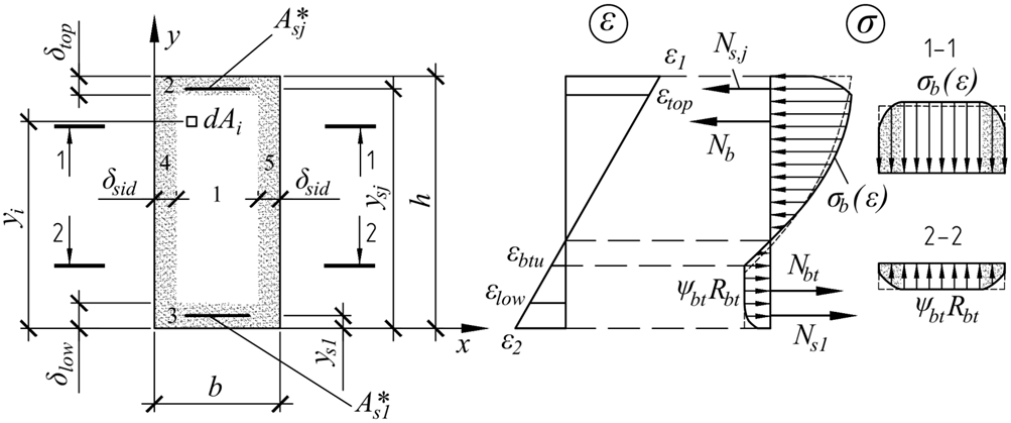

Figure 3. The stress-strain state of the normal section: 1 is the number of the characteristic undamaged area; 2, 3, 4, 5 are the numbers of characteristic damaged areas; δ_{top}, δ_{low}, δ_{sid} is the depth of concrete damage at the upper, lower and side faces, respectively; y_i, y_{sj} is the distance from the lower face of the section, respectively, to the elementary concrete ground dA_i and to the center of gravity of the section of steel reinforcement A^*_{sj}.

The calculated cross section is represented as the sum of elementary layers with a thickness of dy. For each characteristic section, the area of this layer, which has an even distribution of stresses along the width b_n, is $dA_b = b_n\, dy$, where n is parcel number. The designation of the relative section height to the elementary layer is introduced $\xi_i = y_i / h$. With this in mind, for a section without cracks, the equations of equilibrium of longitudinal forces and moments have the form

$$\begin{aligned} &(b - 2\delta_{sid})h \int_{\delta_{low}/h}^{(h-\delta_{top})/h} \sigma_{b1}(\varepsilon)d\xi + bh \int_{(h-\delta_{top})/h}^{1} \sigma_{b2}(\varepsilon)d\xi + \\ &+bh \int_{0}^{\delta_{low}/h} \sigma_{b3}(\varepsilon)d\xi + 2h \int_{\delta_{low}/h}^{(h-\delta_{top})/h} \int_{0}^{\delta_{sid}} \sigma_{b4}(\varepsilon)dxd\xi + \sum_{j=1}^{m} \sigma_{sj} A^*_{sj} = 0; \end{aligned} \tag{6}$$

$$\begin{aligned} &(b - 2\delta_{sid})h^2 \int_{\delta_{low}/h}^{(h-\delta_{top})/h} \sigma_{b1}(\varepsilon)\xi d\xi + bh^2 \int_{(h-\delta_{top})/h}^{1} \sigma_{b2}(\varepsilon)\xi d\xi + \\ &+bh^2 \int_{0}^{\delta_{low}/h} \sigma_{b3}(\varepsilon)\xi d\xi + 2h^2 \int_{\delta_{low}/h}^{(h-\delta_{top})/h} \int_{0}^{\delta_{sid}} \sigma_{b4}(\varepsilon)\xi dxd\xi + \sum_{j=1}^{m} \sigma_{sj} A^*_{sj} h\xi_{sj} - M = 0. \end{aligned} \tag{7}$$

The integrands $\sigma_{b,n}(\varepsilon)$, are functions of stress diagrams at characteristic parts of the section, equal to

$$\begin{aligned}
&\sigma_{b1}(\varepsilon)=\sigma_b(\varepsilon), && \varepsilon_{low}\le\varepsilon\le\varepsilon_{top};\\
&\sigma_{b2}(\varepsilon)=\left(\frac{\varepsilon-\varepsilon_{top}}{\varepsilon_1-\varepsilon_{top}}\right)^2\left(\sigma^*_{b,top}(\varepsilon_1)-\sigma_b(\varepsilon_{top})\right)+\sigma_b(\varepsilon_{top}), && \varepsilon_{top}\le\varepsilon\le\varepsilon_1;\\
&\sigma_{b3}(\varepsilon)=\left(\frac{\varepsilon-\varepsilon_{low}}{\varepsilon_2-\varepsilon_{low}}\right)^2\left(\sigma^*_{b,low}(\varepsilon_2)-\sigma_b(\varepsilon_{low})\right)+\sigma_b(\varepsilon_{low}), && \varepsilon_2\le\varepsilon\le\varepsilon_{low};\\
&\sigma_{b4}(\varepsilon)=-\frac{\sigma_b(\varepsilon)-\sigma^*_{b,sid}(\varepsilon)}{\delta^2_{sid}}x^2+2\frac{\sigma_b(\varepsilon)-\sigma^*_{b,sid}(\varepsilon)}{\delta_{sid}}x+\sigma^*_{b,sid}(\varepsilon), && \varepsilon_{low}\le\varepsilon\le\varepsilon_{top}.
\end{aligned} \tag{8}$$

After substituting (8) into (6-7) and transformations, equations are obtained which describe the stress-strain state of the cross section of a bended reinforced concrete element without cracks. Further, similar equations are obtained for the cases when cracks are formed and developed in height in damaged and healthy concrete of the stretched section zone. In general view, these equations are as follows

$$\frac{h}{\varepsilon_1-\varepsilon_2}\left(N'_{b1}+N'_{b2}+N'_{b3}+2N'_{b4}\right)+\sum_{j=1}^{m}\sigma_{sj}A^*_{sj}=0; \tag{9}$$

$$\frac{h^2}{\left(\varepsilon_1-\varepsilon_2\right)^2}\left(M'_{b1}+M'_{b2}+M'_{b3}+2M'_{b4}\right)+\sum_{j=1}^{m}\sigma_{sj}A^*_{sj}h\xi_{sj}-M=0, \tag{10}$$

here with the stresses in the reinforcement are determined according to the expression

$$\sigma_{sj}=f\left(\varepsilon_{sj}\right)=f\left[\varepsilon_2+\left(\varepsilon_1-\varepsilon_2\right)\xi_{sj}\right]. \tag{11}$$

Members of equation (9–10) are found for each characteristic part of section from the expressions

$$N'_{b1}=\left(b-2\delta_{sid}\right)\left(\psi_{bt}R_{bt}\left(\chi_1-\varepsilon_{low}\right)+\sum_{k=1}^{n}\frac{a_k}{k+1}\left(\varepsilon_{top}^{k+1}-\chi_1^{k+1}\right)\right); \tag{12}$$

$$N'_{b2}=b\cdot\frac{\left(\varepsilon_1-\varepsilon_{top}\right)\left(\sigma^*_{b,top}(\varepsilon_1)+2\sigma_b(\varepsilon_{top})\right)}{3}; \tag{13}$$

$$N'_{b3}=b\left(\frac{\psi_{bt}R_{bt}\left(K^*_{low}+2K^*_{low}(\chi_2)\right)\left(\chi_2-\varepsilon_2\right)}{3}+\frac{\left(\varepsilon_{low}-\chi_2\right)\left(\sigma^*_{b,low}(\chi_2)+2\sigma_b(\varepsilon_{low})\right)}{3}\right); \tag{14}$$

$$N'_{b4}=\delta_{sid}\frac{1}{3}\left(\begin{aligned}&\psi_{bt}R_{bt}\left(K^*_{sid}+2\right)\left(\chi_1-\varepsilon_{low}\right)+\\&+\sum_{k=1}^{n}\frac{a^*_{k,sid}}{k+1}\left(\varepsilon_{top}^{k+1}-\chi_1^{k+1}\right)+2\sum_{k=1}^{n}\frac{a_k}{k+1}\left(\varepsilon_{top}^{k+1}-\chi_1^{k+1}\right)\end{aligned}\right); \tag{15}$$

$$M'_{b1}=\left(b-2\delta_{sid}\right)\left(\begin{aligned}&\frac{\psi_{bt}R_{bt}\left(\chi_1-\varepsilon_{low}\right)\left(\varepsilon_{btu}-2\varepsilon_2+\varepsilon_{low}\right)}{2}+\\&+\sum_{k=1}^{n}\frac{a_k}{k+2}\left(\varepsilon_{top}^{k+2}-\chi_1^{k+2}\right)-\varepsilon_2\sum_{k=1}^{n}\frac{a_k}{k+1}\left(\varepsilon_{top}^{k+1}-\chi_1^{k+1}\right)\end{aligned}\right); \tag{16}$$

$$M'_{b2}=b\left(\varepsilon_1-\varepsilon_{top}\right)\left(\begin{aligned}&\frac{\varepsilon_1\left(3\sigma^*_{b,top}(\varepsilon_1)+3\sigma_b(\varepsilon_{top})\right)+\varepsilon_{top}\left(\sigma^*_{b,top}(\varepsilon_1)+5\sigma_b(\varepsilon_{top})\right)}{12}-\\&-\varepsilon_2\frac{\left(\sigma^*_{b,top}(\varepsilon_1)+2\sigma_b(\varepsilon_{top})\right)}{3}\end{aligned}\right); \tag{17}$$

$$M'_{b3} = b \cdot \left(\begin{array}{l} \dfrac{\psi_{bt} R_{bt} \left(K^*_{low} + 5K^*_{low}(\chi_2) \right) \left(\varepsilon_2 - \chi_2 \right)^2}{12} + \\ + \left(\varepsilon_{low} - \chi_2 \right) \left(\begin{array}{l} \dfrac{\varepsilon_{btu} \left(3\sigma^*_{b,low}(\chi_2) + 3\sigma_b(\varepsilon_{low}) \right)}{12} + \\ + \dfrac{\varepsilon_{low} \left(\sigma^*_{b,low}(\chi_2) + 5\sigma_b(\varepsilon_{low}) \right)}{12} - \\ -\varepsilon_2 \dfrac{\left(\sigma^*_{b,low}(\chi_2) + 2\sigma_b(\varepsilon_{low}) \right)}{3} \end{array} \right) \end{array} \right); \quad (18)$$

$$M'_{b4} = \delta_{sid} \frac{1}{3} \left(\begin{array}{l} \dfrac{\psi_{bt} R_{bt} \left(K^*_{sid} + 2 \right) \left(\chi_1 - \varepsilon_{low} \right) \left(\varepsilon_{btu} - 2\varepsilon_2 + \varepsilon_{low} \right)}{2} + \\ + \sum_{k=1}^{n} \dfrac{a^*_{k,sid}}{k+2} \left(\varepsilon_{top}^{k+2} - \chi_1^{k+2} \right) - \varepsilon_2 \sum_{k=1}^{n} \dfrac{a^*_{k,sid}}{k+1} \left(\varepsilon_{top}^{k+1} - \chi_1^{k+1} \right) + \\ +2 \sum_{k=1}^{n} \dfrac{a_k}{k+2} \left(\varepsilon_{top}^{k+2} - \chi_1^{k+2} \right) - 2\varepsilon_2 \sum_{k=1}^{n} \dfrac{a_k}{k+1} \left(\varepsilon_{top}^{k+1} - \chi_1^{k+1} \right) \end{array} \right). \quad (19)$$

The parameters values χ_1 and χ_2 in (12-19) are determined based on the conditions:

- if $\varepsilon_2 < \varepsilon_{btu}$, there are no cracks in the concrete and $\chi_1 = \varepsilon_{low}$, $\chi_2 = \varepsilon_2$;
- if $\varepsilon_2 \geq \varepsilon_{btu}$, but $\varepsilon_{low} < \varepsilon_{btu}$, cracks are formed and developed only in corrosion-damaged concrete at the lower boundary of the cross section, and $\chi_1 = \varepsilon_{low}$, $\chi_2 = \varepsilon_{btu}$. In this case $\sigma^*_{b,low}(\chi_2) = \psi_{bt} R_{bt} K^*_{low}(\varepsilon_{btu})$;
- if $\varepsilon_{low} \geq \varepsilon_{btu}$, the cracks form and exit into the healthy concrete zone, and $\chi_1 = \varepsilon_{btu}$, $\chi_2 = \varepsilon_{low}$.

After the deformations representing of the concrete of the upper face through the curvature in the section $\varepsilon_1 = \aleph\, h + \varepsilon_2$ in equation (9), $\aleph$ and ε_2 remain unknown. Determining the parameters of the cross section stress-strain state according to the given curvature values, the half-value method is used to find the value ε_2 and, accordingly, ε_1. Further, from the equation (10), the bending moment M acting in the section is determined, the limiting value of which is equal to the normal section strength M_{ult}.

It should be noted that changing in Fig. 3 damaged areas to healthy ones, and changing the corresponding terms of equations (12–19), one can describe particular schemes of the approach of an aggressive environment with respect to a rectangular section.

2.2. Experimental research methods

The purpose of the experimental researches was to obtain the necessary data on the accumulation of concrete and steel reinforcement damage over time and their effect on the normal sections strength of bended reinforced concrete elements under prolonged power and environmental influences, allowing us to evaluate the proposed calculation method reliability.

Experimental researches were carried out in accordance with the developed program, which provides for testing reinforced concrete beams samples in an amount of 27 pcs. The samples were made of a rectangular cross-section of 60×100 (h) mm with a calculated span of l_0 = 1400 mm.

After manufacturing, all samples were stored for 28 days in one laboratory with normal temperature and humidity conditions, after which they were divided into one control (11 pcs.) and two main (8 pcs.) groups of twin beams. Then, the first series of tests of reinforced concrete beams with a short-term load on static bending before failure was carried out, which included three samples from control group, the results of which determined the actual value of the design breaking load $P_u^{\text{BK-0}}$. The remaining 24 samples were loaded and placed for a certain period of time in various environmental conditions.

The samples of the control group were in the same laboratory as during strength gain. Samples of the first and second main groups were respectively in sulfate and chloride containing aggressive media, artificially created in the room to accumulate corrosion damages of concrete and steel reinforcement.

The subsequent series of tests of reinforced concrete beams with a static bending load before failure included two samples from each group. Thus, four more test series of six samples of reinforced concrete beams were formed. In these experimental studies, the main variable parameter was the duration of power and environmental impacts on the samples, equal to 180, 360, 720 and 1080 days from the moment they gained design strength. The accepted samples marking of reinforced concrete beams and series numbers of their tests with load before failure are given in Table 2.

Table 2. Beams samples marking and the series numbers of tests with load before failure.

Sample group	Type of environment	Reinforced concrete beams samples marking, taking into account the impact duration and the number of the test series of the load before failure				
		0 days, series no. 1	180 days, series no. 2	360 days, series no. 3	720 days, series no. 4	1080 days, series no. 5
Control (BK)	Non-aggressive environment	BK-0-1 BK-0-2 BK-0-3	BK-180-1 BK-180-2	BK-360-1 BK-360-2	BK-720-1 BK-720-2	BK-1080-1 BK-1080-2
Main no. 1 (BOS)	Sulphate aggressive environment	–	BOS-180-1 BOS-180-2	BOS-360-1 BOS-360-2	BOS-720-1 BOS-720-2	BOS-1080-1 БOS-1080-2
Main no. 2 (BOH)	Chloride aggressive environment	–	BOH-180-1 BOH-180-2	BOH-360-1 BOH-360-2	BOH-720-1 BOH-720-2	BOH-1080-1 BOH-1080-2
The number of samples in a test series		3	6	6	6	6

Reinforced concrete beams reinforcement was performed by flat single frames with working stretched reinforcement in the form of rods Ø8 mm of A240 class. To ensure anchorage, the ends of the rods are brought out beyond the supporting section of the beams by 90 mm with a bend length of 70 mm. As compressed reinforcement, Ø4 mm rods made of class B500 wire are structurally installed. The concrete protective layer for stretched and compressed reinforcement was adopted 10 mm. The transverse reinforcement is made in the form of clamps from rods Ø3 mm of class A240, installed with a constant pitch of 40 mm. The reinforcement scheme of laboratory beams samples is shown in Fig. 4.

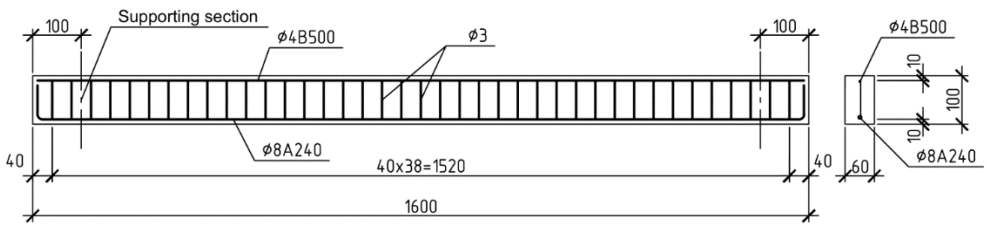

Figure 4. Reinforcement scheme for samples of reinforced concrete beams.

For all samples manufacture, concrete of class compressive strength B20 is used. At the same time, fine grinding sodium chloride (NaCl) in a ratio up to 5 % from cement weight was introduced into the concrete mixture intended for beams samples of the main group no. 2 (BOH). This did not lead to a significant decrease in the strength of concrete, but under wet conditions it contributed to steel reinforcement corrosion initiation.

After the first series of tests, based on the condition of the same rigidity, the remaining beams with the help of a hydraulic jack and a steel frame were pulled together in pairs by a force equal to $0.6P_u^{\text{BK-0}}$ (Fig. 5, a), which was further supported by ties. Force control was carried out using an exemplary compression dynamometer. The force transfer from the jack to the ties and, therefore, to the beams was carried out by uniformly nuts tightening at the ends of the ties with a torque spanner until the readings on the dynamometer decreased by 1 % or the total deflection of the beams increased by 0.01 mm, fixed by the dial indicator. The decrease in the ties force due to the corrosion damage development and the creep deformations growth was periodically replenished to the initial value. For this, two beams were again installed in a steel frame and reloaded with a jack with control of the force by a dynamometer. In this case, the force at which there was an increase in the total beams deflection by 0.01 mm was considered the total force acting at the moment in the ties. The real decrease in the load level of the beams during the tests did not exceed 5 %.

The design models for reinforced concrete beams during long-term tests and short-term load tests before failure are assumed to be the same: a single-span hinged-supported beam, loaded with two concentrated forces with the formation in clean bending zone of 0.164l_0 a span (Fig. 5, b).

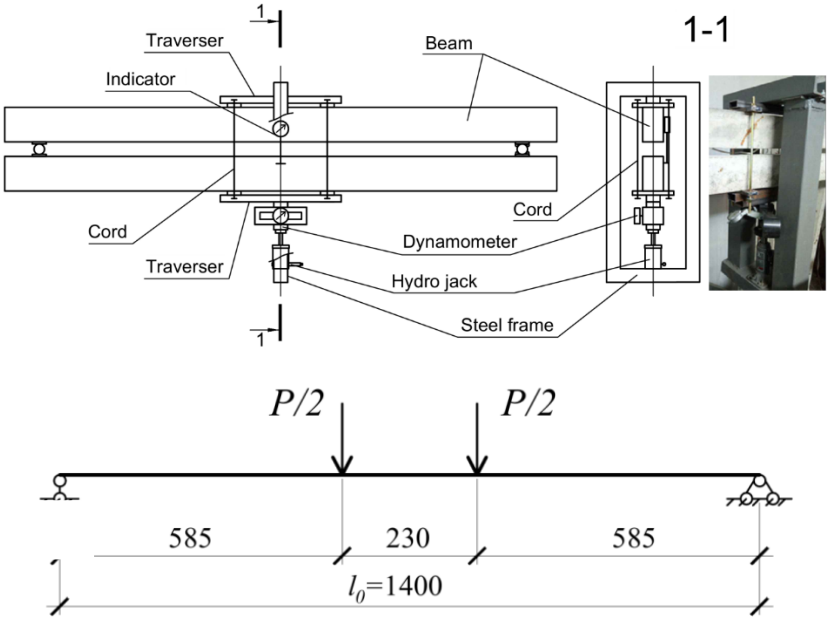

Figure 5. The principal (a) and calculated (b) loading scheme for reinforced concrete beams for long-time tests.

In order to initiate the development of corrosion processes in concrete and steel reinforcement, a special stand for long-term testing was made (Fig. 6). Its basic element was corrosion-resistant polymer baths with liquid electrolyte. A 2 % aqueous solution of sulphuric acid (H_2SO_4) was in one bath. It was intended to simulate a sulfate aggressive medium effect on the samples of BOS group, the other bath with distilled water was intended to simulate the effect of a chloride aggressive environment on the samples of BOH group containing an additive of sodium chloride (NaCl) in concrete. Using an electric telpher and rigging equipment, the samples were sink every day and at the same time for 15-20 minutes into the electrolyte baths for moistening, after which they were lifted and allowed to dry using conditions under which the control group samples were stored. The densities of electrolytes during the experiment were constant and were monitored by a hydrometer. All metal elements on reinforced concrete beams, ensuring the constancy of the design model and the power load magnitude, were coated with anticorrosive compounds. The number of damping-drying cycles was determined by the number of days from the long-time tests beginning to the reinforced concrete beams removal for destruction by a short-time load.

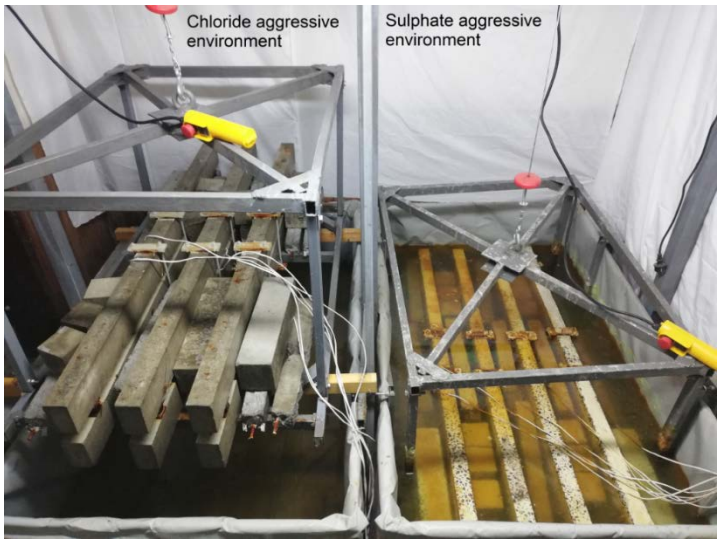

Figure 6. Stand for long-time samples tests.

At the end of long-time tests and samples unloading, the residual values of the deformation characteristics, mass, section sizes were measured, concrete strength was determined by non-destructive methods on all faces.

For reinforced concrete beams tests with a short-time bending load before failure, a test bench was made, the spatial rigidity and stability of which is many times higher than the prototypes rigidity. From the possible types of loading, gravitational piece loads using was adopted. The general tests view is shown in Fig. 7.

Figure 7. General view of reinforced concrete beams test before failure.

The tests were carried out in accordance with Russian State Standard regulations GOST 8829 step loading. At the loading stages preceding the cracks formation and samples fracture, the step size was up to 5 % of the expected breaking load, and at all the other stages was about 10 %. The retention interval at each stage of loading, taking into account the readout from the instruments, was 10-20 minutes. The readings from the measuring instruments were taken twice at each stage – at the end of loading and after loading.

After bringing the beams to failure, various parameters of structural materials corrosion damages were determined. Using the indicator method, by cross section color saturation with a 1 % phenolphthalein solution, the depth at which the concrete properties changes was determined at all its faces. Further, reinforcing bars were removed from the beams, which determined the corrosion depth, weight loss, and the change in the deformation-strength characteristics of steel reinforcement used in the experiment.

3. Results and Discussion

Long-time state of steel reinforcement in concrete. During long-time tests, under influence of aggressive sulfate environment, steel reinforcement in concrete reinforced beams was in a passive state. The absence of corrosion damages of reinforcement can be explained by the limited oxygen access to surface rods due to fracture plugging with concrete corrosion products [11, 31].

During prolonged exposure of a corrosive chloride environment, steel reinforcement corrosion in reinforced concrete beams was initiated. It was determined that with the complete concrete protective properties neutralization, corrosion damages (pittings) in the reinforcement of the greatest depth can be formed on the rod surface that is inverse with respect to the nearest face of the cross section element (Fig. 8).

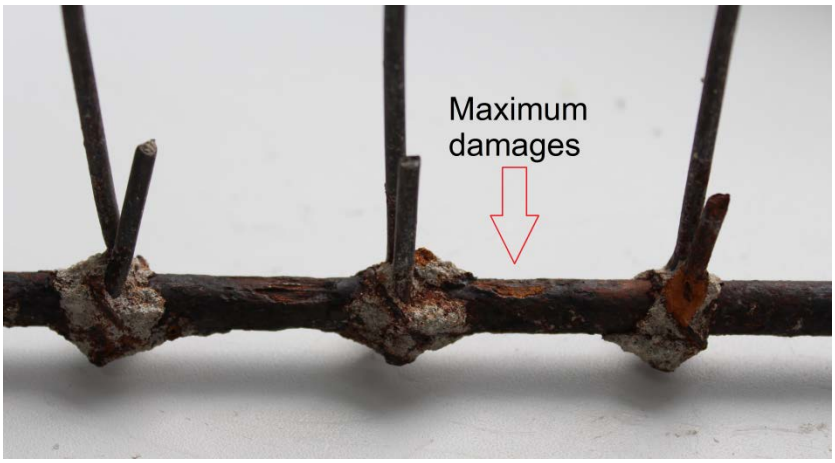

Figure 8. Steel reinforcement corrosion type damages of reinforced concrete beams.

The biggest steel reinforcement damages during chloride aggression were found in sections with operational cracks in concrete. These damages are the closest to the calculated model of uneven corrosion development by the type of "flat front" according to Table. 1.

A graph-based mapping of development rate of corrosion damages to the accepted steel reinforcement during chloride aggression, taking into account the existing stresses, is presented in Fig. 9.

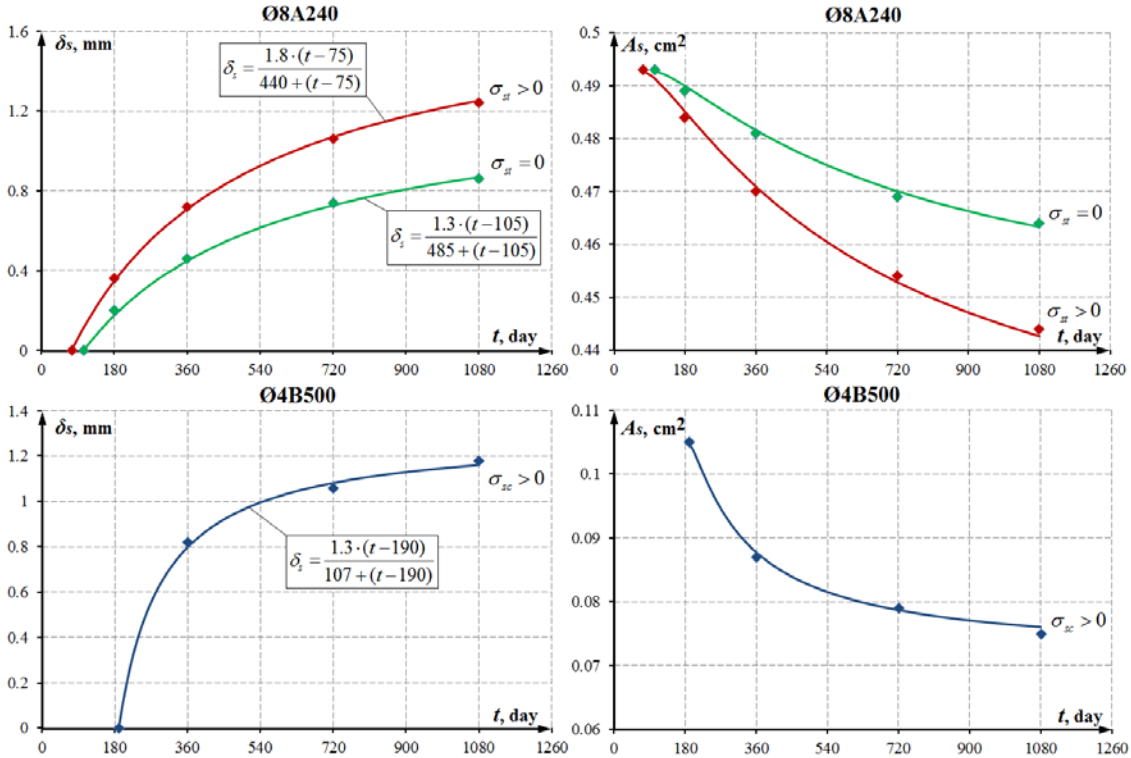

Figure 9. The development rate of steel reinforcement corrosion damages during chloride aggression in depth (left) and in area (right) of the rods cross-section.

Note: in Fig. 9 markers indicate the points, obtained during experimental studies, and the solid lines – calculated curves obtained by the formula (3).

The change nature in deformation diagrams of steel reinforcement obtained by tests of rod samples on axial tension is shown in Fig. 10. After a long-time influence to reinforced concrete beams of an external loading and a chloride aggressive environment, the deformation-strength characteristics of steel reinforcement remained within the limits of variations of the corresponding characteristics of control samples. In this case, like in works [13, 14] a decrease in the length of the yield area is observed.

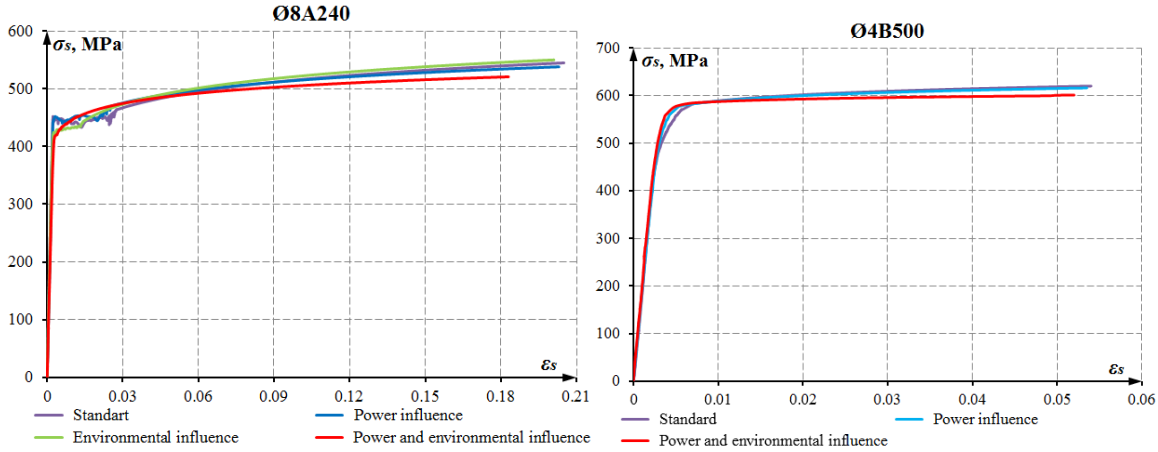

Figure 10. The change nature in the deformation diagrams of steel reinforcement during prolonged power and environmental influences.

Concrete prolonged condition. The concrete corrosion, related with the aggressive effect modeling of chloride on steel reinforcement, proceeded according to the first type, in which salt spots of dissolved cement stone components appeared on the samples surface [7]. Damages accumulation according to the scheme without complete concrete destruction and during the long-time tests was insignificant.

Under the influence of a sulfate-containing aggressive environment, concrete corrosion took place in according to the third form, in which the resulting chemical reaction products settled in the concrete structure, which eventually led to its complete destruction [11]. The corrosion damage accumulation corresponded to the design scheme, which has three zones with different destruction degree. At the same time, in the course of experimental studies it was found that for this scheme the function of the concrete damage coefficient $K^*(z)$ in the transition zone, where the composite resistance is partially preserved, does not take values equal to zero.

The experimental studies results of the concrete state in reinforced concrete beams and unloaded auxiliary samples during various operating environments are presented in Table 3 and Table 4.

Table 3. The concrete strength and deformation characteristics in various operating environments.

Concrete characteristics	Operating environment	Duration of power and environmental influences t, days				
		0	180	360	720	1080
Cube compressive strength R, MPa	Non-aggressive	31.0	39.2	39.6	39.9	40.1
	Sulfate		29.6	28.4	26.9	25.8
	Chloride		38.4	38.9	39.1	38.9
Prism compressive strength R_b, MPa	Non-aggressive	23.8	30.4	30.7	30.9	31.0
	Sulfate		23.7	22.7	21.5	20.6
	Chloride		29.6	29.9	30.0	29.7
Tensile strength R_{bt}, MPa	Non-aggressive	2.3	2.9	2.9	3.0	3.0
	Sulfate		2.4	2.3	2.2	2.2
	Chloride		2.9	2.9	3.0	2.9
Initial modulus of elasticity E_b, MPa	Non-aggressive	30000	35500	35500	36000	36000
	Sulfate		30500	30000	29500	29000
	Chloride		34000	34000	34500	34100
Deformations ε_{bR}	Non-aggressive	0.00180	0.00190	0.00193	0.00195	0.00195
	Sulfate		0.00190	0.00195	0.00200	0.00205
	Chloride		0.00195	0.00200	0.00205	0.00210

Table 4. Kinetics characteristics of concrete corrosion damages in various operating environments.

Concrete damages characteristics	Aggressive environment	Concrete stress	Duration of power and environmental influences t, days				
			0	180	360	720	1080
Corrosion damage depth δ, mm (including completely destroyed concrete layer thickness)	Sulfate	$\sigma_{bt} \approx R_{bt}$	0	6.5 (1.8)	10.5 (2.4)	12.5 (2.8)	13 (3.1)
		$\sigma_b = 0$		5 (1.6)	7.5 (2.1)	9 (2.4)	9.5 (2.6)
		$\sigma_b = 0.55R_b$		3.5 (1.4)	5 (1.9)	5.5 (2.2)	5.5 (2.4)
	Chloride	$\sigma_{bt} \approx R_{bt}$	0	17	21	22	22.5
		$\sigma_b = 0$		14	17.5	19	19
		$\sigma_b = 0.55R_b$		10	13	14	14
Damage coefficient $K^*_{\min}$	Sulfate	-	1	0.78	0.74	0.70	0.67
	Chloride	-		0.97	0.97	0.97	0.96

According to the data obtained, the change in the strength and deformation characteristics of concrete and corrosion damage development in it with time depends on the operating environment type, the sign and level of acting stresses. The concrete properties greatest degradation is observed under the sulfate aggressive environment influence. The maximum and minimum depth of concrete corrosion damage is determined respectively in the stretched and compressed zones of the sections of reinforced concrete beams. The concrete damages in unloaded auxiliary samples and in beams at the neutral axis level was approximately equal (Fig. 11, a, b). The corrosion frontal advance to the deep into the concrete was uniform at all faces, with the exception of cross sections side faces of the bent elements, where the sign and level of stress changes in height.

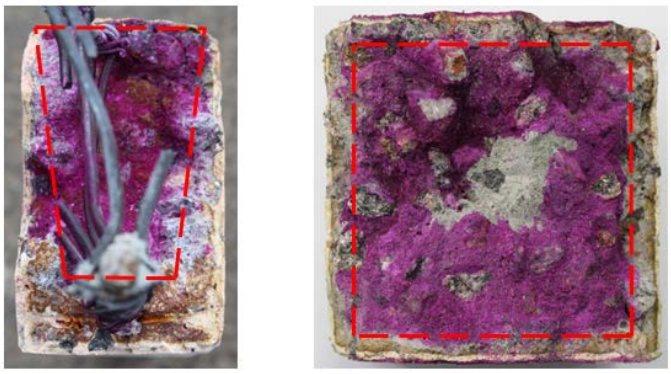

Figure 11. The nature of corrosion damages development in concrete of reinforced concrete beams (a) and unloaded auxiliary samples (b).

A graphic representation of the corrosion damages development rate in concrete under various operating environments is shown in Fig. 12. It should be noted that concrete damages accumulated under sulfate-containing environment influence at a lower development depth have a higher destruction degree than damages received in a chloride-containing environment. Herewith, both types of concrete damages have a damping in time character.

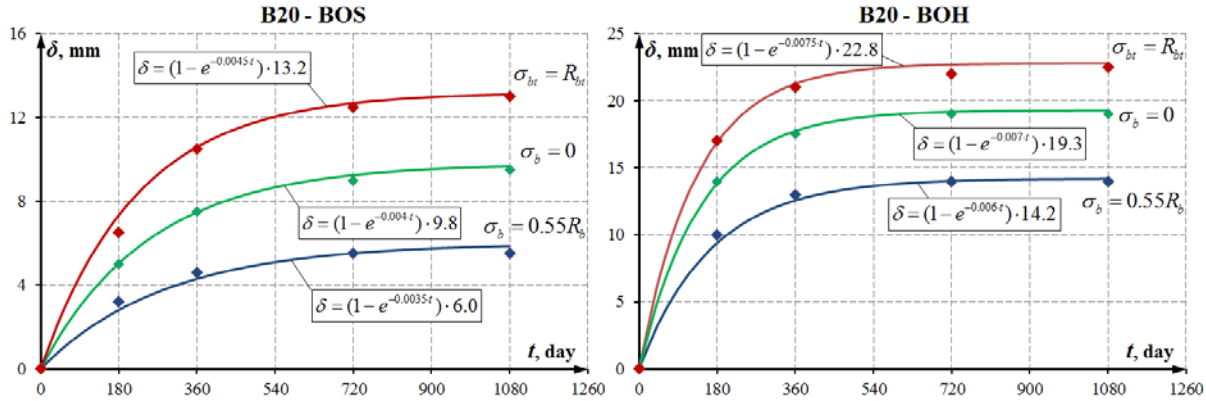

Figure 12. The corrosion damages development rate in concrete of class B20 with liquid sulfate (left) and chloride (right) aggression.

Note: in Fig. 12, the markers indicate the points obtained during the experimental studies, and the solid lines – calculated curves obtained by the formula (1).

Adhesion condition of reinforcement with concrete. The deformations development in concrete and tensile reinforcement in the area between cracks at different levels of beam loading is shown as an example in Fig. 13, from which it can be seen that until the ratio $P/P_u \approx 0.85$, it proceeded at approximately the same rate (deviations do not exceed 25 %). At the stage preceding the samples destruction, a partial breaking in the concrete and reinforcement deformation can be neglected due to many factors affecting the readings of tensiometers, and structural materials deformation as a whole can be considered the same with an acceptable error.

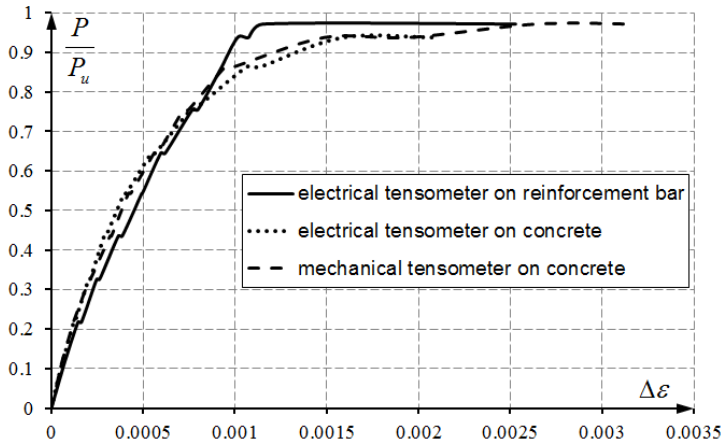

Figure 13. Deformations in tensile concrete and reinforcement.

Bendable reinforced concrete elements. The destruction of all reinforced concrete beams samples during load tests in the form of two concentrated forces occurred in the zone of pure bending along normal sections. The values of breaking loads are given in Table 5.

Table 5. The breaking loads values during reinforced concrete beams testing.

Duration of power and environmental influences before failure testing *t*, days	Control group (Non-aggressive environment)		Main group no. 1 (Sulphate-aggressive environment))		Main group no. 2 (Chloride-aggressive environment)	
	Sample marking	Breaking load, kN	Sample marking	Breaking load, kN	Sample marking	Breaking load, kN
0	BK-0-1	6.273	-	-	-	-
	BK-0-2	6.292	-	-	-	-
	BK-0-3	6.281	-	-	-	-
180	BK-180-1	6.383	BOS-180-1	6.222	BOH-180-1	6.229
	BK-180-2	6.360	BOS-180-2	6.191	BOH-180-2	6.203
360	BK-360-1	6.371	BOS-360-1	6.099	BOH-360-1	6.046
	BK-360-2	6.391	BOS-360-2	6.140	BOH-360-2	6.012
720	BK-720-1	6.381	BOS-720-1	6.024	BOH-720-1	5.846
	BK-720-2	6.402	BOS-720-2	6.068	BOH-720-2	5.868
1080	BK-1080-1	6.390	BOS-1080-1	6.038	BOH-1080-1	5.701
	BK-1080-2	6.414	BOS-1080-2	5.968	BOH-1080-2	5.609

For control group samples, an increase in the breaking load with time up approximately 2 % was observed, which is associated with concrete strength increasing by 30 %.

All samples of the main groups are characterized by a decrease in bearing capacity with an increase in the period of environmental impacts and corrosion damages accumulation in structural materials. After 1080 days, for beams that were in sulfate and chloride-containing aggressive environment, when compared with control beams of the same time, the breaking load decreased on average by 6.6 % and 13.2 %, respectively. Thus, with the same structural features, the beams strength with steel reinforcement corrosion damage decreases more than with concrete damage. This effect is coordinated with research results [5, 8, 12, 16, 17].

The general diagram of reinforced concrete beams destructive loads changes with the time is shown in Fig. 14.

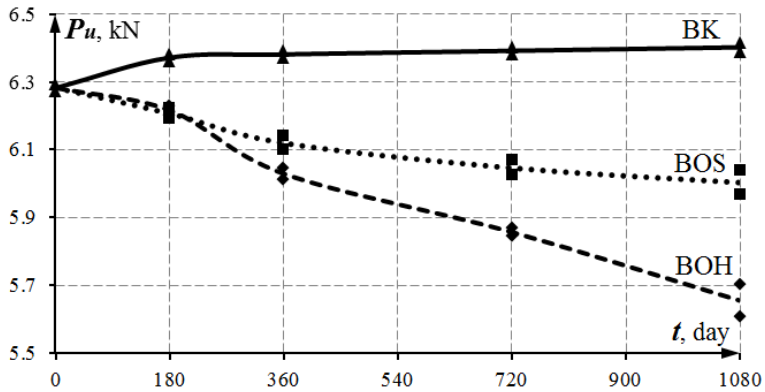

Figure 14. The change in the beams breaking load with the time.

In order to numerical realization of the developed design procedure, a calculation algorithm was formulated and computer program was written. Using them, the theoretical values of normal sections strength adopted for samples experimental studies of reinforced concrete beams are determined.

To compare with the theoretical values of the normal sections strength determined by the developed design procedure, the actual ultimate breaking loads values for each series of reinforced concrete beams samples tests were averaged and, in accordance with the design scheme, are presented as experimental values of the normal sections strength (Table 6). The average deviation between the corresponding experimental and calculated values of strength is about 1.5 %, the maximum deviation does not exceed

3 %. The root-mean-square deviation range does not exceed 1 %. Herewith, all calculated values do not exceed the experimental ones.

Table 6. Experimental and calculated values comparison of normal sections strength of reinforced concrete beams samples.

Samples series	Normal section strength M_u, кN·m		
	Observation value M_u^{obs}	Calculated value M_u^{cal}	$\frac{M_u^{cal}}{M_u^{obs}}$
Non-aggressive operating environment (the control group samples)			
BK-0	1.837	1.800	0.980
BK-180	1.864	1.844	0.989
BK-360	1.866	1.845	0.989
BK-720	1.870	1.848	0.988
BK-1080	1.873	1.849	0.987
Samples group average			0.987
Samples group root-mean-square deviation			0.0038
Sulphate-containing aggressive environment (samples of main group no. 1)			
BOS-180	1.816	1.772	0.976
BOS-360	1.790	1.754	0.980
BOS-720	1.769	1.745	0.986
BOS-1080	1.756	1.739	0.990
Samples group average			0.983
Samples group root-mean-square deviation			0.0062
Chloride-containing aggressive environment (samples of main group no. 2)			
BOH-180	1.818	1.796	0.988
BOH-360	1.764	1.730	0.981
BOH-720	1.713	1.679	0.980
BOH-1080	1.655	1.632	0.986
Samples group average			0.984
Samples group root-mean-square deviation			0.0039
Average of all samples			0.985
Root-mean-square deviation of all samples			0.0046

4. Conclusions

Based on the study results, taking into account the tasks, the following conclusions can be made:

1. Based on reinforced concrete deformation model, a universal method has been developed for strength calculating of normal sections of flexible reinforced concrete elements subject to prolonged force and environmental influences. It allows to take into account the concrete nonlinear deformation, various schemes of corrosion damage forming within the rectangular cross section, as well as various degrees of sections damage within the span.

2. New experimental data of normal sections strength of reinforced concrete beams samples that have been under stress in sulfate- and chloride-containing aggressive environments for a long time were obtained. For samples with corrosion damage of concrete and reinforcement compared to control samples, a decrease in the bearing capacity with an increase in the exposure time of an aggressive environment is characteristic. For samples with concrete and reinforcement corrosion damages as compared to control samples, a decrease in the bearing capacity with an increase in the exposure time of aggressive environment is characteristic. It was found that during sulfate aggression, the concrete damage coefficient function in the transition zone does not take values equal to zero. With chloride aggression and complete neutralization of concrete protective properties, pittings of the maximum depth can be formed on the reinforcement bar surface that is inverse to the nearest face of the element section.

3. A comparison of the experimental and calculated data on the strength of normal sections was carried out, which showed that the calculation method proposed in the work has sufficient accuracy and can be used for practical calculations of operated and newly designed flexible concrete elements taking into account manufacturing defects and corrosion damages accumulation to structural materials over time.

References

1. Ma, Y., Xiang, Y., Wang, L., Zhang, J., Liu, Y. Fatigue life prediction for aging RC beams considering corrosive environments. Engineering Structures. 2014. No. 79. Pp. 211–221. DOI: 10.1016/j.engstruct.2014.07.039
2. Adhikary, S.D., Li, B., Fujikake, K. Dynamic behavior of reinforced concrete beams under varying rates of concentrated loading. International Journal of Impact Engineering. 2012. No. 47. Pp. 24–38. DOI: 10.1016/j.ijimpeng.2012.02.001
3. Ye, H., Fu, C., Jin, N., Jin, X. Performance of reinforced concrete beams corroded under sustained service loads: A comparative study of two accelerated corrosion techniques. Construction and Building Materials. 2018. No. 162. Pp. 286–297. DOI: 10.1016/j.conbuildmat.2017.10.108
4. Zhang, W., Zhang, H., Gu, X., Liu, W. Structural behavior of corroded reinforced concrete beams under sustained loading. Construction and Building Materials. 2018. No. 174. Pp. 675–683. DOI: 10.1016/j.conbuildmat.2018.04.145
5. Bossio, A., Imperatore, S., Kioumarsi, M. Ultimate flexural capacity of reinforced concrete elements damaged by corrosion. Buildings. 2019. 9(7). P. 160. DOI: 10.3390/buildings9070160
6. Du, Y., Cullen, M., Li, C. Structural effects of simultaneous loading and reinforcement corrosion on performance of concrete beams. Construction and Building Materials. 2013. No. 39. Pp. 148–152. DOI: 10.1016/j.conbuildmat.2012.05.006
7. Yu, L., Francois, R., Dang, V.H., L'Hostis, V., Gagne, R. Structural performance of RC beams damaged by natural corrosion under sustained loading in a chloride environment. Engineering Structures. 2015. No. 96. Pp. 30–40. DOI: 10.1016/j.engstruct.2015.04.001
8. Hanjari, K.Z., Kettil, P., Lundgren, K. Analysis of mechanical behavior of corroded reinforced concrete structures. Aci Structural Journal. 2011. 108(5) Pp. 532–541.
9. Zhao, Y., Yu, J., Jin, W. Damage analysis and cracking model of reinforced concrete structures with rebar corrosion. Corrosion Science. 2011. 53(10). Pp. 3388–3397. DOI: 10.1016/j.corsci.2011.06.018
10. Otieno, M.B., Alexander, M.G., Beushausen, H.-D. Corrosion in cracked and uncracked concrete – influence of crack width, concrete quality and crack reopening. Magazine of Concrete Research. 2010. 62(6). Pp. 393–404. DOI: 10.1680/macr.2010.62.6.393
11. Okeniyi, J.O., Omotosho, O.A., Ajayi, O.O., Loto, C.A. Effect of potassium-chromate and sodium-nitrite on concrete steel-rebar degradation in sulphate and saline media. Construction and Building Materials. 2014. No. 50. Pp. 448–456. DOI: 10.1016/j.conbuildmat.2013.09.063
12. Zhu, W., Fransois, R., Coronelli, D., Cleland, D. Effect of corrosion of reinforcement on the mechanical behaviour of highly corroded RC beams. Engineering Structures. 2013. No. 56. Pp. 544–554. DOI: 10.1016/j.engstruct.2013.04.017
13. Boubitsas, D., Tang, L. The influence of reinforcement steel surface condition on initiation of chloride induced corrosion. Materials and Structures. 2015. 48(8). Pp. 2641–2658. DOI: 10.1617/s11527-014-0343-2
14. Pradhan, B. Corrosion behavior of steel reinforcement in concrete exposed to composite chloride-sulfate environment. Construction and Building Materials. 2014. No. 72. Pp. 398–410. DOI: 10.1016/j.conbuildmat.2014.09.026
15. Stewart, M.G., Suo, Q. Extent of spatially variable corrosion damage as an indicator of strength and time-dependent reliability of RC beams. Engineering Structures. 2009. 31(1). Pp. 198–207. DOI: 10.1016/j.engstruct.2008.08.011
16. Xia, J., Jin, W.-L., Li, L.-Y. Effect of chloride-induced reinforcing steel corrosion on the flexural strength of reinforced concrete beams. Magazine of Concrete Research. 2012. 64(6). Pp. 471–485. DOI: 10.1680/macr.10.00169
17. Zhu, W., Francois, R. Corrosion of the reinforcement and its influence on the residual structural performance of a 26-year-old corroded RC beam. Construction and Building Materials. 2014. No. 51. Pp. 461–472. DOI: 10.1016/j.conbuildmat.2013.11.015
18. Shamshina, K.V., Migunov, V.N., Ovchinnikov, I.G. Influence of corrosion longitudinal cracks on rigidity and strength of reinforced concrete structures. IOP Conference Series: Materials Science and Engineering. 2018. 451(1). P. 012058. DOI: 10.1088/1757-899X/451/1/012058
19. Kivell, A., Palermo, A., Scott, A. Complete model of corrosion-degraded cyclic bond performance in reinforced concrete. Journal of Structural Engineering (United States). 2014. 141(9). P. 04014222. DOI: 10.1061/(ASCE)ST.1943-541X.0001195
20. Bondarenko, V.M., Kolchunov, V.I. Kontseptsiya i napravleniya razvitiya teorii konstruktivnoy bezopasnosti zdaniy i sooruzheniy pri silovykh i sredovykh vozdeystviyakh [The concept and directions of development of the theory of structural safety of buildings and structures under the influence of force and environmental factors]. Industrial and Civil Engineering. 2013. No. 2. Pp. 28–31. (rus)
21. Ababneh, A., Sheban, M. Impact of mechanical loading on the corrosion of steel reinforcement in concrete structures. Materials and Structures/Materiaux et Constructions. 2011. 44(6). Pp. 1123–1137. DOI: 10.1617/s11527-010-9688-3
22. Wang, X.-H., Liu, X.-L. Simplified methodology for the evaluation of the residual strength of corroded reinforced concrete beams. Journal of Performance of Constructed Facilities. 2010. 24(2). Pp. 108–119. DOI: 10.1061/(ASCE)CF.1943-5509.0000083
23. Selyayev, V.P., Bondarenko, V.M., Selyayev, P.V. Prognozirovaniye resursa zhelezobetonnykh izgibayemykh elementov, rabotayushchikh v agressivnoy srede, po pervoy stadii predelnykh sostoyaniy [Forecasting the service life (resource) of reinforced concrete bending elements working in aggressive environment at the first stage of limit states]. Regional Architecture and Engineering. 2017. 2(31). Pp. 14–24. (rus)
24. Coronelli, D., Gambarova, P. Structural assessment of corroded reinforced concrete beams: Modeling guidelines. Journal of Structural Engineering. 2004. 130(8). Pp. 1214–1224. DOI: 10.1061/(ASCE)0733-9445(2004)130:8(1214)
25. Torres-Acosta, A.A., Navarro-Gutierrez, S., Teran-Guillen, J. Residual flexure capacity of corroded reinforced concrete beams. Engineering Structures. 2007. 29(6). Pp. 1145–1152. DOI: 10.1016/j.engstruct.2006.07.018
26. Karpenko, N.I., Karpenko, S.N., Yarmakovskiy, V.N., Yerofeyev, V.T. O sovremennykh metodakh obespecheniya dolgovechnosti zhelezobetonnykh konstruktsiy [The modern methods for ensuring of the reinforced concrete structures durability]. Academia. Architecture and Construction. 2015. No. 1. Pp. 93–102. (rus)
27. Murashkin, G.V., Pischulev, A.A. Using deformation models to determine the bearing capacity of reinforced concrete flexural members with corrosion damages of concrete compressed zone. Building and reconstruction. 2009. No. 6. P. 36. (rus)
28. Alfarah, B., Lopez-Almansa, F., Oller, S. New methodology for calculating damage variables evolution in Plastic Damage Model for RC structures. Engineering Structures. 2017. No. 32. Pp. 70–86. DOI: 10.1016/j.engstruct.2016.11.022
29. Chen, H., Nepal, J. Modeling residual flexural strength of corroded reinforced concrete beams. Aci Structural Journal. 2018. 115(6). Pp. 1625–1635. DOI: 10.14359/51702232

30. Kolchunov, V.I., Kolchunov, Vl.I., Fedorova, N.V. Deformatsionnyye modeli zhelezobetona pri osobykh vozdeystviyakh [Deformation models of reinforced concrete under special impacts]. Industrial and Civil Engineering. 2018. No. 8. Pp. 54–60. (rus)
31. Fedosov, S.V., Rumyantseva, V.E., Krasilnikov, I.V., Konovalova, V.S., Evsyakov, A.S. Mathematical modeling of the colmatation of concrete pores during corrosion. Magazine of Civil Engineering. 2018. 83(7). Pp. 198–207. DOI: 10.18720/MCE.83.18
32. Kryuchkov, A.A., Smolyago, G.A., Zhdanov, A.Ye. Issledovaniye napryazhenno-deformirovannogo sostoyaniya zhelezobetonnykh sterzhnevykh elementov s uchetom vliyaniya poperechnoy sily [Investigation of the stress-strain state of reinforced concrete core elements taking into account the influence of shear force]. Bulletin of BSTU named after. V.G. Shukhov. 2005. No. 10. Pp. 449–451. (rus)
33. Sazonov, E.V., Shmelev, G.D., Ishkov, A.N. Prakticheskie aspekty ispolzovaniya parametricheskikh metodov otsenki ostatochnogo resursa dlya plit pokrytiya [Practical aspects of using parametric methods of residual life assessment for roof slabs]. News of higher educational institutions. Construction. 2007. 557(1). Pp. 15–20. (rus)

Contacts:

Nikolay Frolov, frolov_pgs@mail.ru
Gennady Smolyago, tpk-psv@yandex.ru

© Frolov, N.V., Smolyago, G.A., 2021

Magazine of Civil Engineering

ISSN 2712-8172

journal homepage: http://engstroy.spbstu.ru/

DOI: 10.34910/MCE.103.4

Cement and animal bone powder on rheological characteristics of bitumen

G. Garedew
Mizan-Tepi University, Tepi, Ethiopia
** E-mail: girmegare@gmail.com*

Keywords: asphalt binder, animal bone, cements, rheological characteristics, mechanical properties, stiffness

Abstract. The developed countries have adopted the use of modifiers for assessment of asphalt binder long term performance. Asphalt contributes 90 to 95 % in cost estimation of Flexible pavement while compared to all other major material components. Since Ethiopia is one of the landlocked country without any fossils fuel source for the production of Asphalt, moreover Ethiopian importer depends on neighbour country Djibouti. This research analyzes the effect of modifiers on the rheological characteristics and also considers fatigue resistance with the main aim of preventing rutting in asphalt pavement due to different temperatures. Hence a seminal effort is assessed in evaluation of Portland cement and Waste Animal Bone as cost effective modifying agents. The conventional bitumen penetration grade (80/100) is used in this research. The control specimen four binders were obtained by mixing the asphalt binder with four different percentages (0 %, 1 %, 3 % and 5 %) of PCWAB by weight of asphalt binder. Rheological characteristics were evaluated with Dynamic Shear Rheometer test (DSR) such as Amplitude sweep test (AST), Frequency sweep Test (FST) and Multiple-stress creep and recovery test (MSCR). AST and FST were adopted for determining linear visco-elastic range, Master curve were developed for same temperature (21.1 °C, 37.8 °C, and 54.4 °C) respectively while MSCR and Performance Grade (PG) were determined for four different temperatures (52 °C, 58 °C, 64 °C, and 70 °C). Finally, the master curve shows that 3% and more addition of PCWAB on asphalt binder increases the stiffening property of asphalt binder at high temperatures and low loading frequencies (susceptible for rutting). On the other hand, from the test result obtained from MSCR test the smallest total strain value was 5 % for PCWAB followed by the 3 % and 1 %. Thus, up to 3 % addition of PCWAB significantly improves the resistance of asphalt binder to rutting. In addition, using PCWAB as asphalt binder modifier has a positive impact on environmental preservation. The performance grade determination also depicted the improvement in PG as content of modifier increases. Therefore, the evaluation showed that the 3 % modified binder is better in its rutting performance with improved performance grade.

1. Introduction

Road infrastructures have a huge contribution for rapidly economic growth of a country and a world as a whole. Thus rapidly economic growth increases number traffic volume per citizen and heavy axle load [1]. Bitumen binder are organic materials whose binding and hardening properties are caused by the temperature related change of adhesion and cohesion of their molecule [2]. Bitumen is often characterized by composition and the colloidal structure determine its physical and rheological properties [3, 4]. These binders are commonly used in the pavement construction to meet the raising requirements for durability of the road surface. In the road construction industry, asphalt binder used as an intermediate and surface layers of flexible pavement to provide tensile strength which resisting distortion, protect the asphalt binder pavement structure [5, 6]. Rutting in asphalt binder pavements leads to a serious problem that reduction in both structural and also reduce service life of the asphalt pavement [7–10]. Therefore the asphalt pavement roads are used to increases its ability to carry the traffic load under different condition without causing distress [11, 12]. From this perspective significant amount of work has been done using different additives and modifiers. Such as: crumb rubber, Styrene-butadiene-styrene, synthetic resins, metal-organic

Garedew, G. Cement and animal bone powder on rheological characteristics of bitumen. Magazine of Civil Engineering. 2021. 103(3). Article No. 10304. DOI: 10.34910/MCE.103.4

This work is licensed under a CC BY-NC 4.0

compounds, polyvinyl chloride, ethyl-vinyl-acetate, bone glue, lime, Portland cement, fly ash and paraffin Which improves the physical and rheological properties of asphalt binder [13–15]. Among them, Portland cement and waste animal bone a wide range of viscoelasticity to achieve long-lasting road surface, as it ensures consistency of bitumen rheological state in extreme service temperatures.

Several polymers have been tested as modifier for improving bitumen's performance involving filler, fiber, elastomers and plastomers [16, 17]. The most used modifiers for bitumen performance improvement are polymers. The physical and chemical properties of the polymers modified bitumen are dominated by the properties of the base bitumen [18, 19]. Moreover elastomers (Crumb rubber, styrene-butadiene-styrene and styrene-butadiene rubber) Increase stiffness at higher temperatures, decrease stiffness at lower temperatures to resist thermal cracking and Increase elasticity at medium range temperatures to resist any cracking [16, 20]. And plastomers (polyvinyl chloride, ethyl-vinyl-acetate and ethylene propylene) which increase high temperature performance, structural strength and increase resistance to rutting [19, 21]. As well as filler (lime, Portland cement and fly ash) improves fill voids, increase stability, improve bond between aggregate and binder [22–24] and also researchers investigated on different additives such as nano silica, nano clay as well as fibers and nano charcoal coconut-shell ash as a bitumen modifiers. The study improved the physical and rheological properties of asphalt binder for rutting and fatigue resistance [25, 26]. Additionally; crumb rubber also improve the performance grade of bitumen from PG64 to PG76 for permanent deformation of asphalt at high temperature [27]. 0.75 % soybean- derived biomaterial by weight of bitumen on neat bitumen binder and also polymer modified bitumen showed a significant effect on fatigue properties [28, 29].

Currently the most several researchers have been conducted on bone and cement modification, waste animal bone (WAB) mineral is composed of calcium, phosphate as well as hydroxyl ions, especially cattle bone has ultimate compressive strength and shear strength of more than 140 MPa and 85 MPa respectively. It is viscoelastic materials, with a density of 1810 kg/m^3 and melting point of 1670 °C [30, 31]. Moreover, former researchers conducted on bone glue for modification for enhancing pavement performance without significantly changing the asphalt binder's compaction and mixing temperatures of HMA and viscosity. The results showed that bone glue modification improved complex shear modulus. A modified binders with bone glue showed great improvements on shear fatigue, creep compliance, and complex shear modulus than control asphalt [31]. Furthermore, studies which have been conducted on partial replacement of cement with animal bone in concrete. For instance, a maximum of 10 % bone powder ash was incorporated into cement [32]. The results showed that the replacement of cement with 10 % bone powder ash showed an increase in the compressive strength of concrete. Up to 5 % bone powder replacement of cement increases both compressive and tensile strengths of concrete [33].This is because bone powder is acting as nucleation agent which increases the hydration ability of cement.

Portland cement and waste animal bone the major benefit of this particular combination is synergetic effect. It has been observed for binder elasticity and resistance to permanent deformation [23]. Moreover, Portland cement and waste animal bone improves bitumen stiffness, viscoelastic, to prevent stripping of binder from dried aggregate, increases dry resilient modulus of mixes and Reduce environmental problem. In addition, the stability of binder during long-time storage at elevated temperatures is increased [23, 24] and increases dry resilient modulus of mixes.

Therefore, this study aims to evaluate rheological characteristics and the performance of bitumen modified with Portland cement and Waste Animal Bone at high temperature for rutting resistance. The following binder properties were carried with conventional and Dynamic Shear Rheometer test (DSR) such as penetration, softening point, ductility, Amplitude Sweep Test (AST), Frequency Sweep Test (FST), Performance grade Determination (PG) test and Multiple-Stress Creep and Recovery test (MSCR) for both unaged and aged Rolling thin Film oven (RTFO) Test, as well as for both modified and unmodified bitumen. In developed countries performance-based asphalt binder specifications, super pave binder grading system is in use. Recently the more advanced asphalt binder specification method using MSCR has been conducted. This MSCR test method is becoming popular since it best predicts rutting and convenient to consider different levels of traffic were examined.

2. Material and Methods

This methodology and experimental work focus on identifying the linear viscoelastic (LVE) limit of different unmodified and modified bitumen as a function of different loading times and temperatures. Additionally, upon establishing the LVE limit, the viscoelastic behavior of bitumen in their linear region are evaluated. Understanding the properties of bitumen material is important to quantify its engineering performance. Materials such as bitumen which exhibit aspects of both elastic and viscous behavior, must be characterized with test methods and analytical techniques that account for the time (or rate) of loading and temperature.

The effect of rheological behavior of bitumen improved by modification of bitumen with Portland cement and waste animal bone. As well as every test approaches, equipment and conditioning machines used to investigate asphalt's both conventional and fundamental test Conventional test method such as penetration, ductility and softening test also RTFO (Rolling Thin Film Oven) test has conducted. Fundamental properties are assessed using MARVEL BOHILN Dynamic Shear Rheometer test. The test conducted under dynamic shear rheometer such as AST, FST, MSCR and PG determination. Generally, in this research a comprehensive literature review made to understand the previous efforts, which include the, academic journals, research papers and review of textbooks are conducted in this research.

2.1. Materials

Bitumen binder grade 80/100 penetration was used for the preparation of modified binders blend in this study this bitumen obtaining from chain road construction company and its physical properties penetration softening point, ductility and conditioning test [34–37] Were studied to qualify the bitumen before modification see Table 1. Two different filler additives namely waste animal bone and Portland cement was used for the binder modification. The waste Animal Bone and Portland cement both obtained from local source. According to express on Ethiopian pavement design Manual [10] three different penetration grades of bitumen 40/50, 60/70 and 80/100. For this study selected penetration grade 80/100 which is less stiff and the softer when compared to the others listed in above, the objective of the study, the softer bitumen is selected to evaluate stiffness and resistance against rutting when modified with PC (Portland cement) and WAB (waste Animal bone).

2.2. Sample Preparation in laboratory for modifiers

The first step to clean the Bone samples, can, sun-dried and oven dried to reduce its oil content before Powder bone and screening into the desired sizes. As well as Portland cement is used in this study, the required size of both modifiers to prepare bituminous mastic is (< 75 µm) and their chemical properties also studied and tabulated in Table 2.

Figure 1. Sample preparation for Portland cement and Waste Animal Bone.

2.3. Dynamic shear rheometer DSR test

Dynamic shear Rheometer (DSR) test Used to characterize the rheological behavior of bitumen and rutting resistance at high, intermediate and low Temperature. This was done by measuring the viscous and elastic characteristics of asphalt cement with Standard test for determined the viscoelastic characteristics of asphalt cement using DSR test is described in AASHTO T315-10. First the asphalt binder is heated until sufficient fluid to pour and to prepare the test specimens. Then a small sample of asphalt binder is sandwich between two plates. But before placing the sample the DSR is set to a particular temperature. DSR test utilized to measure different properties of bitumen before modification and after using modification.

The test can be done when the bitumen's sample is sandwiched between two parallel metal plates. The bottom (surface) plate is fixed (constant) and the upper plate oscillate forth and back across the sample to create a shearing action. Depending upon the type of bitumen being tested the test temperature, specimen size and plate diameter varies. Test temperatures greater than 46 °C use a sample 0.04 inches (1 mm) thick and 1 inch (25 mm) in diameter), Test temperatures between 4 °C and 40 °C use a sample 0.08 inches (2 mm) thick and 0.315 (8 mm) in diameter. DSR tests are conducted on BRTFO (Before Rolling Thin Film Oven), ARTFO (After Rolling Thin Film Oven) aged and then the rheological parameter is recorded such as complex shear modulus (G^*), dynamic viscosity, frequency, phase angle (δ) and

accumulated strain, etc. The complex modulus is a determined the resistance of asphalt cement to rutting (deformation) when exposed to a sinusoidal shear stress load and consists both visco-elastics when elastic (recoverable) and viscous (non-recoverable) component of material.

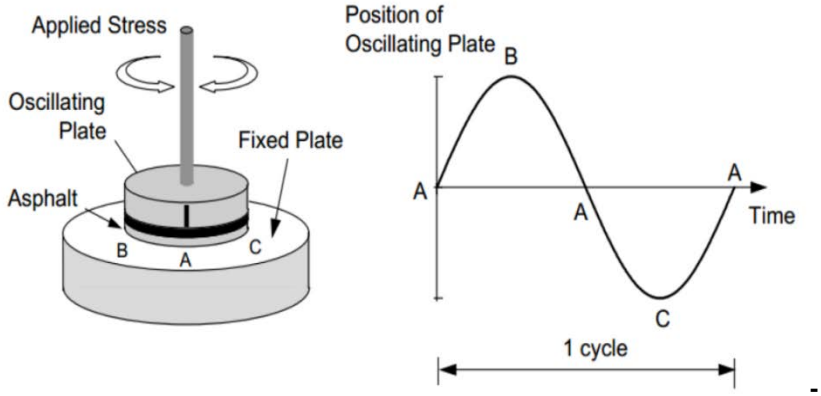

Figure 2**. Working principle of dynamic shear rheometer test [2].**

Phase angle (δ) is an indicator or represent of relative amounts of viscous and elastic components as well as the lag (difference) between the applied (load) shear stress and the resulting get shear strain. The values of complex modules G^* and the value of phase angle (δ) for asphalt binder are dependent on the frequency of loading and test temperature. The operation principle of the DSR is when generalized on the figure as follows. An asphalt sample is sandwiched between an oscillating spindle and the fixed base. As shown in Fig. 2 below the oscillating plate (often called a "spindle") starts at point A and moves to point B. From point B the oscillating plate moves back, passing point A on the way to point C. From point C the plate moves back to point A. This movement, from A to B to C and back to A comprises one cycle [38–40].

There are four main types of tests conducted under DSR test in this research to determine the rheological behavior of bitumen. These are: Amplitude Sweep test, Frequency Sweep Test, Performance grade test and Multiple Stress Creep and Recovery test (MSCR).

2.3.1. Amplitude Sweep Test

The Amplitude sweep test is used to determine the Linear Viscoelastic Range (LVR) of a visco-elastic material. The AST test shear stress is different while frequency kept constant at 1.59 Hz until the sample flow and breaks down and rheological material functions are not independent of the set parameter anymore LVE part is the region where the applied oscillation is nondestructive. In most cases log-log graph on the same scale is plotted as strain in the graph of x-axis and complex modulus G* in the graph of y-axis. The complex shear modulus (G^*) versus x-axis with strain plot used to determine the (LVE) region.

The amplitude sweep test was carried out following the test standard AASHTO T 315 at a constant frequency of 10 rad/sec at specific test temperatures (21.1 °C, 37.8 °C & 54.4 °C). The test was in shear stress control mode with minimum shear stress 100 pa and maximum shear stress 90000 pa.

Prior to mounting the asphalt binder specimen between the plates, the “zero gap” setting must be established at the test temperature because the frame and fixtures in the DSR change dimension with temperature. So, for every 12 °C temperature variation on the test, zero gap was maintained. in order to calculate the strain which is used as an input parameter for frequency sweep test using 8 mm plates and 2 mm gap for low and intermediate temperature (21.1 °C, 37.8 °C) as well as for high temperature 25 mm plate with 1 mm gap are conducted.

2.3.2. Frequency Sweep Test

Frequency sweep test is very important test to evaluate the rheological characteristics of asphalt binder oscillatory test with variable frequency and constant amplitude values. Using this test time dependent shear behavior can be examined. Short-term behavior is simulated by rapid movements (at high frequencies) and long-term behaviors by slow movements (at low frequencies). Parallel plates with diameters of 8 mm and 25 mm were used in the temperature ranges of 21.1 °C, 37.8 °C and 54.4 °C respectively with a frequency range of 0.1 Hz to 25 Hz. The final gap was adjusted to 1 mm for a 25 mm plate and 2 mm gap for the 8 mm spindle. Frequency sweep test helps to evaluate the rheological property of visco-elastic material in the form of complex modulus (G^*) and also phase angle (δ) parameters have been presented as isothermal plots and master curves for each type of bitumen. Because of the large amount of data (result) generated in these tests, these plots were very useful in presenting and interpreting the results. Master curves allow the rheological data to be presented over a wide (high) range of frequencies

and temperatures in one plot. Therefore, to avoid presenting a large (huge) number of graphs, the results are mainly presented and analyzed as master curves.

2.3.3. Performance grade determination (PG) test

Performance grade (PG) is a binder specification and mix design procedure developed by Strategic Highway Research Program (SHRP). This asphalt binder specification system works based on climate at which the pavement life is expected to serve by evaluating the contribution or role of the asphalt binder in resistance to permanent deformation (Rutting) at low temperature cracking and also fatigue cracking in asphalt pavements. According to the explanation of super pave, to carry out performance grade determination new set of tests of physical properties at a range of temperatures must be carried out. The performance grade (PG) of the asphalt binder is designated as PGxx-yy, where xx represents the average seven days maximum temperature and yy represents the minimum temperature. Super pave Asphalt Binder Specification the grading system is based on Climate [10]. Performance grade test (PG-test). This test was conducted at high temperature to categorize the tested bitumen binder sample in different temperatures, ± 6 °C increments [21, 41]. For the purpose of this study from the above indicated high temperatures 52 °C, 58 °C, 64 °C, 70 °C and 76 °C are used for performance grade determination and for MSCR test (e.g. PG70 No rutting until 70 °C).

2.3.4. Multiple stress creep and recovery (MSCR) test

MSCR is the latest indicate improvement on Superpave Performance Graded bitumen Binder specifications and addresses or measure at high temperature rutting (permanent deformation) both for unmodified and modified binders. This new test and specification provide that more accurately indicates the rutting performance of the binder and recovery measurement can Identify and quantify how the polymer is working in the binder MSCR is conducted after PG determination test because it relate rutting depth with both the environmental temperature and traffic loading [3, 42]. Sample preparation and the plate are the same as PG test but it require a little software adjustment. A major benefit of the new MSCR test is that it eradicate the need to run tests like as elastic recovery and also phase angle procedures designing in specific to indicate or measure polymers modification of bitumen binder.

Several studies have shown that the $G^*/\sin(\delta)$ based specification does not correlate well with field performance. The test protocol (AASHTO T350) requires that a 25 mm diameter and 1 mm thick asphalt specimen is subjected to 10 cycles of one second creep loading followed by 9 seconds rest period at stress levels of 100 Pa and 3200 Pa at the high PG temperature using a DSR. In this way 20 cycles at the 0.1 kPa stress level followed by 10 cycles at the 3.2 kPa stress level for a total of 30 cycles will be done. The first sample 10 cycle at 0.1 kPa was used for conditioning the specimen. There are no rest periods between creep and recovery cycles or changes in stress level. The total time required for completing the two-step creep and recovery test is 300 s. The sample has to be residue from T 240 (Rolling Thin-Film Oven Test). Generally, in MSCR test a constant stress is assigned and the time-related strain is measured and it is called shear compliance $J(t)$. It defines how complian the specimen is the higher the compliance the easier the sample can be deformed [38, 43]. From the MSCR test we can determine the following main parameters:

i. Non-recoverable creep compliance;
ii. Percent difference between non-recoverable creep compliance;
iii. Average percent recovery;
iv. Percent difference in recovery.

3. Result and Discussion

The test results and analysis have been organized under result and discussion. The result and discussion divide into two main parts: (I) Analysis of conventional characteristic of asphalt binder and (II) Analysis of rheological characteristic of asphalt binder. It starts with test parameter setup and trial tests. This part helped to acquire adequate experience on how to conduct the tests in a better way. The test procedure, specifications and methodology were described before. Generally, this result and discussion covers every test approaches, equipment and conditioning machines used to investigate binder containing different proportion of Portland cement and waste animal bone powder for both conventional and rheological properties. Rheological properties are assessed using MARVEL BOHILN Dynamic Shear Rheometer test. A summary of the test results is presented in Fig. 1–11 and Tables 1–4 have been organized to evaluate the binder characteristics in the following sections.

3.1. Elementary Analysis of Portland cement and waste Animal bone

As a result of the other researchers conducted original bitumen is mostly affected by chemical, physical and rheological characteristics of bitumen [39]. Rheological properties of asphalts with different

contents of nano-silica and rock asphalt were analyzed by univariate analysis and variance analysis [26]. The results of DSR test revealed that Qingcheng (QC) rock asphalt had a remarkable impact on the complex shear modulus (G) and phase angle, while the effects of nano-silica were relatively small, which mainly improved complex modules (G) [25]. As well as filler (lime, Portland cement and fly ash) improves fill voids, increase stability, improve bond between aggregate and binder [23–25], the result obtained from chemical component of Portland cement and waste animal bone test are displayed in Table 1. The result was conducted in Ethiopian central geological survey laboratory. Chemical component of Portland cement and waste animal bone varies depend on type of cement and bone. The raw materials found in the manufacture of Portland cement and waste animal bone consist mainly of lime, silicon, alumina and iron oxide (CaO, SiO_2, Al_2O_3, and Fe_2O_3) [24]. Table 1 below shows the chemical analysis of Portland cement and waste animal bone.

Table 1. Chemical analysis of Portland cement and waste animal bone.

Chemical	Animal bone (%)	Cement (%)
Sio_2	5.28	43.62
Al_2O_3	0.01	3.92
Fe_2O_3	0.40	2.92
Cao	42.92	43.80
MgO	0.94	1.00
Na_2o	1.34	0.32
K_2O	0.30	0.20
MnO	0.02	0.12
P_2O_5	26.94	0.14
TiO_2	0.01	0.25
H_2O	2.24	0.80
LOI	18.80	3.212

From the Table 1 above it is observed high percent of chemical component found in the manufacture of Portland cement and waste animal bone consist of calcium oxide (Cao). High percent of calcium oxide (Cao) implies high resilience modules, high softening point, High resist of moisture damage and hardest material [24] as well as silicon dioxide (Sio_2) and alumina oxide Al_2O_3 high role to improved pavement performance in Road construction [12].

3.2. Conventional test method results

The bitumen has a limited range of rheological properties and durability that are not sufficient to resist pavement distress [15]. Penetration grade 80/100 neat bitumen selected for modification since it is softer, low stiffness and not used for high temperature and became more viscous at high temperature [34–37]. Therefore, depend on above reason the quality of original bitumen was checked for its conformity by conducting conventional tests. And summary of convention test results with specification requirement are presented in Table 2 below.

Table 2. Summary of Convention Test Results with specification requirement.

Test type	Unaged	aged	Spec.(unaged)	Spec.(aged)
Penetration	97	77	80-100	50 (Min)
Ductility	100+	100+	100 (Min)	75 (Min)
Softening point	46		42-51	75 (Min)
RTFO		0.05%		0.8 (Max)

The conventional test result of the original bitumen was checked for its conformity with its specification requirement. As shown in Table 2 above the binder qualifies to be modified and to be evaluated with further fundamental tests as a control material.

3.3. Amplitude sweep test Result

Stiffness of asphalt binder and testing temperature had a significant effect on linear viscoelastic range [44]. The result obtained from amplitude sweep test, linear viscoelastic range, used for as an input for frequency sweep test. Thus, asphalt binder is viscoelastic material which expressed as a function of time and temperature. The linear viscoelastic range (LVR) illustrated in Fig. 3 and 4 by the relationship

between the complex shear modulus G* versus with shear strain. In SHRP study it is reported the linear viscoelastic range (LVR) was defined as the point where complex modulus decrease to 95 % of its initial value [17]. As a result of the other researchers conducted a modified binder with bone glue showed great improvements on shear fatigue, creep compliance, and complex shear modulus than control asphalt [31]. Based on this amplitude sweep test result from Fig. 3 and 4 indicated Portland cement and waste animal bone improves complex modules and linear viscoelastic behavior at high, intermediate and low temperature. limits, fundamental tests used the DSR test was performed at stress level well inside the linear region and the linear fundamental characters for modified and original bitumen. AST provide LVE-range by limiting strain value [7]. So that asphalt binder for which the stress-strain behavior is linear and independent of rate of loading and temperature Table 3 below illustrate linear viscoelastic range limiting strain value. Fig. 3 and 4 show (G^*) and (δ) versus temperature, obtained from DSR test of base and PCWAB modified asphalt binder before and after RTFO aging respectively. As shown in the Fig. 3 modification of Portland cement and waste animal bone improves linear viscoelastic also has shown in the Fig. 4 that the stiffness of asphalt binder decrease as the test temperature increases and the LVE-range becoming wider than lower test temperature at 3 % PCWAB addition. Fig. 3 expresses linear visco-elastic range for 3 % modified binder after aged.

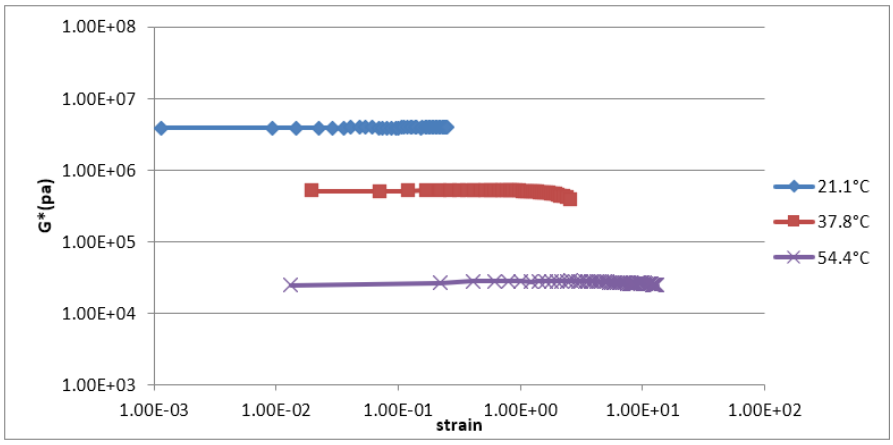

Figure 3. Linear visco-elastic range for 3% modified binder after aged.

Generally, in this study the required output from amplitude sweep test is determining the linear viscoelastic range of all binder containing different proportion of PCWAB at each temperature and in both unaged and RTFO aged conditions. Moreover, Portland cement and waste animal bone improves bitumen stiffness, viscoelastic, to prevent stripping of binder from dried aggregate, increases dry resilient modulus of mixes and reduce environmental problem.

Based on the results shown below in Table 3 and Fig. 4, the temperature, percent proportion of PCWAB and aging have a significant effect on the LVE-region. So, highest content of PCWAB lower linear visco-elastic range and higher stiffness. Fig. 4. below shows linear visco-elastic range for 3 % modified binder before aged.

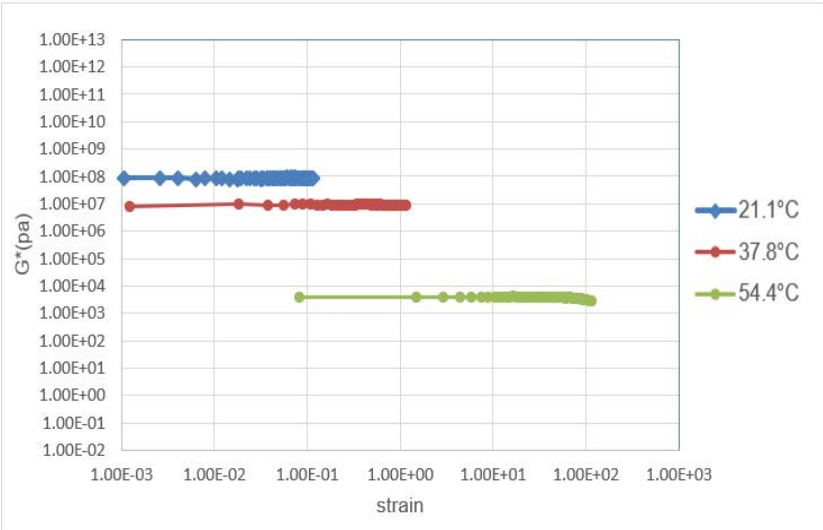

Figure 1. Linear visco-elastic Range for 3% modified binder before aged.

Based on the test result represented graphically the limiting strain values were analyzed considering the plateau strain values of each sample. The plateau modulus values are almost a constant value of G^* is observed for different values of shear stress and shear strain before the graph declines [19]. In this study the LVE strain limit can be calculated as the point beyond which the measured value of G^* decreased to 95 % of its zero-strain as shown on above Fig. 3 and 4. Finally for each and every curves of amplitude sweep results, a horizontal line along 0.95G^* will be constructed to intersect the curve at a point. Then the corresponding strain value of that intersection point will be considered to be the limiting stain value (γL). Table 3. Shows below Summary of linear viscoelastic limiting strain range value.

Table 3. Summary of linear viscoelastic range value.

Temperature	Modified (%)	0.95G^*	Limiting strain	ARTFO
21.1°C	0	8.43E+05	3.10	2.44
	1	2.42E+06	2.58	1.10
	3	3.75E+06	2.05	1.06
	5	7.38E+05	1.02	1.01
54.4°C	0	3.04E+03	74.08	53.01
	1	3.83E+03	58.94	48.19
	3	3.54E+03	49.90	36
	5	3.81E+03	31.00	32.85

The results obtained by other authors the response of LVE affected due to temperature, content of modifier and aging [27]. Depend on the summary Table 3 above the stiffness of asphalt binder increases with addition of PC and WAB. Binder with 5 % PCWAB have highest stiffness and lowest LVE-range at constant temperature. Conversely the lower stiffness shows a larger LVE-range; indicating it is more flexible and has better performance for the lower temperature regions. At 21.1 °C temperature the linear visco-elastic value for each sample is minimum and the effect of the modifier is not significant. At 54.4 °C temperature higher linear visco-elastic values are observed as the material gets softer or less stiff.

3.4. Frequency Sweep Test Result

Frequency sweep test (FST) data results are manipulated mainly used for constructing Master curve. Isothermal plots with log-log scale for complex shear modulus. The frequency varies from 25 Hz to 0.1 Hz to represent the damaging effect of the traffic load. The major rheological parameters determined from the FST plots to make some rheological discussions, but it is essential to make the observation and discussion after developing of master curves [45].

Isothermal plots -this plots the complex shear modulus as a function of frequency for all binders were represented Fig. 5 below shows Isothermal plots for 3 % binder Modified before aged isothermal graphs considering temperature, complex shear modulus, frequency, ageing and content of modifiers [21]. Isothermal Plots as shows on above Fig. 5 and 6 that by simply looking as the temperature increases the shear stiffness decreases for all the binders. The increase in content of modifier increases with complex modulus and also aging improves shear stiffness of the binder (complex modulus).

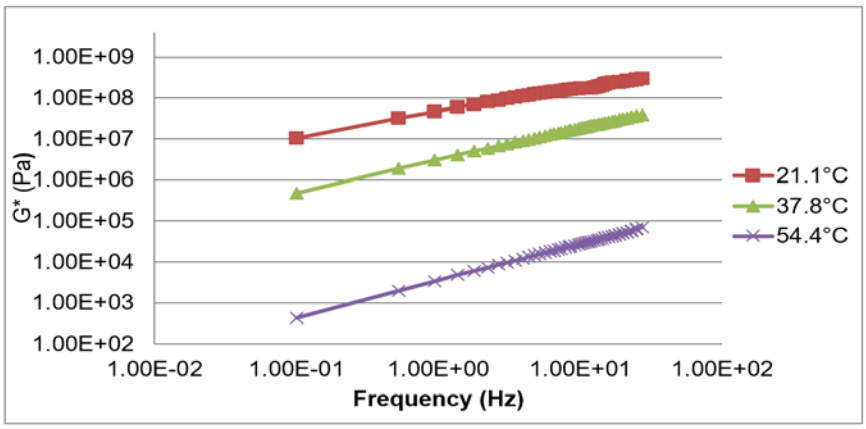

Figure 2. Isothermal plots 3% Modified binder before aged.

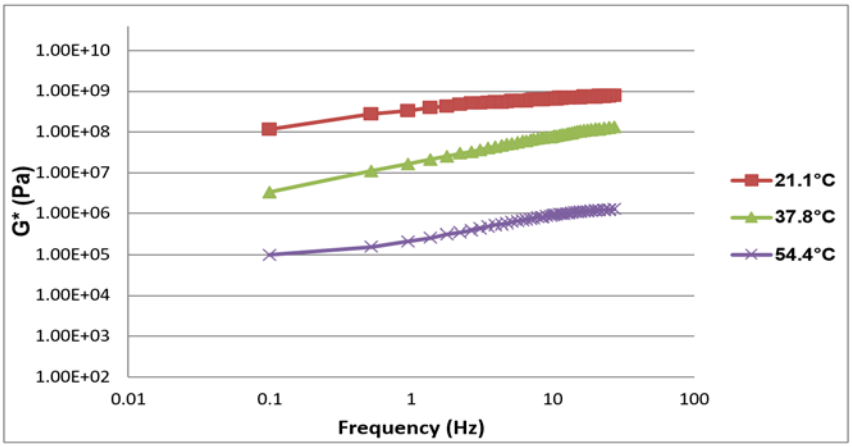

Figure 3. Isothermal plots (3 % binder Modified After aged.

3.5. Master Curves of Complex Shear Modulus

The construction of master curves is a powerful tool to understand the rheological properties of asphalt binder. The data at any other temperatures were shifted with respect to time until various curves overlap almost perfectly to form a single master curve using time-temperature superposition principles. Binder master curve graph extrapolate the test result up to very high frequency and very low frequency [46]. Also at high temperatures the modified bitumen binder has high complex shear modulus which is taken as indicate stiffness that helps for resisting rutting [16, 41]. It can be possible to seen that the addition of modifiers leads to a bitumen binder which performs good or better under high temperatures and also low frequencies (lower values of phase angle in pascal) which compared with neat bitumen shows Fig. 8 and 9.

At higher frequency values or low temperatures the ratio of increment of phase angle values due to modification becomes small, modulus master curves were developed using microsoft excel solver to best fit the sigmoid function for all asphalt binders [44]. The sigmoid function to best fit the obtained G^* data from the DSR is carried out with trial and error by changing the sigmoid constants and the shift factor. The sigmoid function to calculate the complex shear modulus is represented as. Different scholars use different models for shifting to single reference temperatures. But a research developed at the University of Maryland showed that the master curve for binders which represented by a sigmoidal function defined by equation.

$$log\,|G| = a + \frac{b}{1 + r^{d\,log_{fr} + \gamma}} \tag{1}$$

where a, b, c and d are sigmoid function constants.

fr is reduced frequency.

$|G^*|$ is complex shear modulus

In this research the master curves is constructed fitting a sigmoidal function to the measured the complex modulus test data which can be done by solver function in the excel spreadsheet and minimizing the error between the predicted value and the obtained value of the complex modulus at reference temperature 21.1 °C. William-Landel-Ferry (WLF) empirical relationship shown below was proposed by Williams to link the shift factor for each flow curve to the master curve, based on the time-temperature superposition to obtain the shift factor (aT) [47].

$$log\,aT = \frac{-c_1(T - T_{ref})}{c_2 + (T - T_{ref})} \tag{2}$$

where T is temperature, T_{ref} is the reference temperature c_1 and c_2 are taken as constants. From DSR data result three test temperatures (21.1 °C, 37.8 °C, and 54.4 °C) were used to construct the master curves for complex modules and the shift factors have been developed to construct the master curves for aged and unaged binder. All of these values vary for each aged and unaged binder. As for the temperature shift factors, a21.1 is zero for all the binder types because all the parameters are shifted to 21.1 °C. Whereas for a37.8 and a54.4 the values are all negative because the stiffness parameters are shifted to reduced temperature which is 21.1 °C.

Before developed final master curve, complex modules as a function of reduced frequency is plotted to illustrate how the temperature shift factors were used see in Fig. 7 below.

Reduced frequency is determined as;

$$log\ fr = log_f\ p + aT \tag{3}$$

where fr is reduced frequency, f is frequency and aT is temperature shift factor.

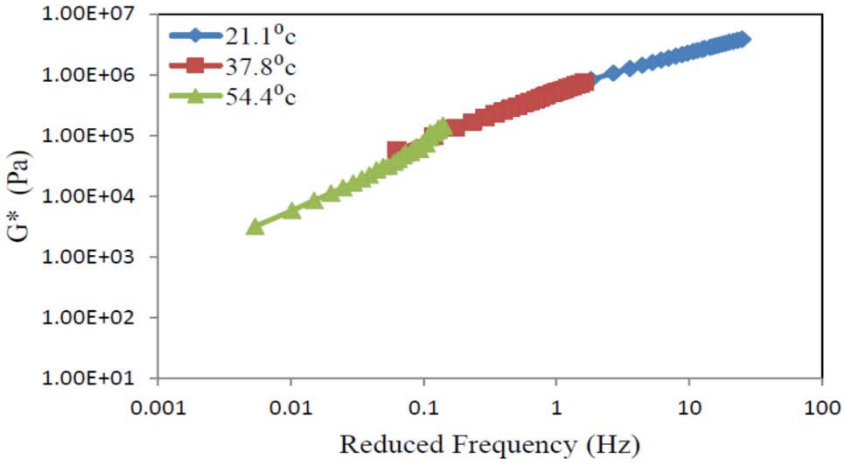

Figure 7. Temperature Shift @21.1°C Ref. Temperature for 0 % modified after RTFO.

Finally, modulus master curves were developed for both after modified and before modified binder Fig. 8 and 9 below shows Complex modulus master curve before aged and after aged respectively.

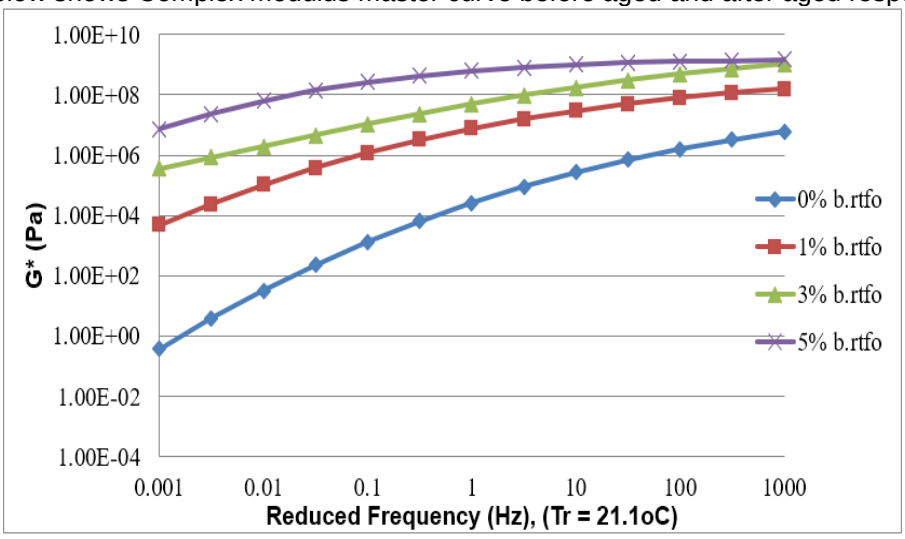

Figure 8. Complex modulus master curve before aged.

Furthermore, studies which have been conducted on partial replacement of cement with animal bone in concrete. For instance, a maximum of 10 % bone powder ash was incorporated into cement [32]. The results showed that the replacement of cement with 10 % bone powder ash showed an increase in the compressive strength of concrete. Up to 5 % bone powder replacement of cement increases both compressive and tensile strengths of concrete [33].This is because bone powder is acting as nucleation agent which increases the hydration ability of cement. As shown on the above Fig. 8 and below Fig. 9, it can be seen that stiffness of PCWAB increases from 1 % to 5% for unaged and aged bitumen at high temperature and low loading frequency this indicate modifier has great role for resist permanent deformation (rutting) at high Temperature. Addition of Portland cement and waste animal bone (PCWAB) has a positive effect on asphalt binder thereby increasing its stiffness and when temperature increasing also shear stiffness decreases. This implies that at high temperature and low frequency the smaller value of shear modulus is pronounced. Fig. 9 shows Complex modulus master curve after aged.

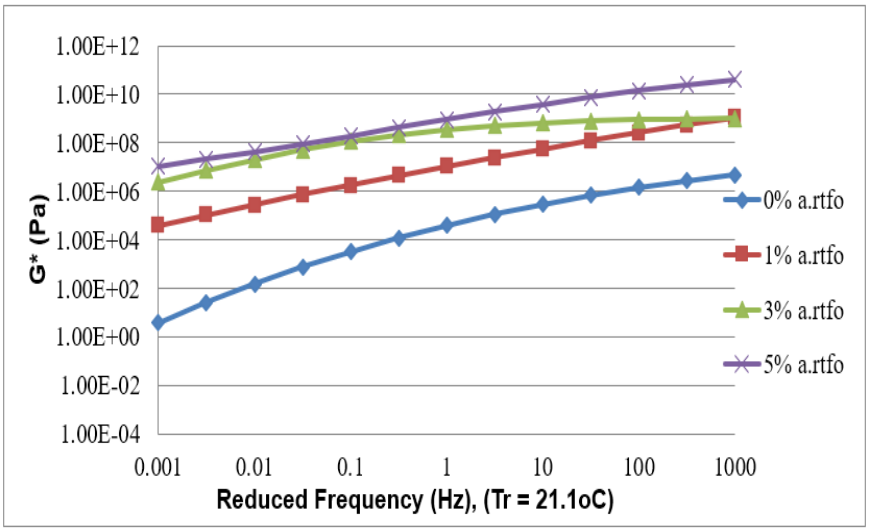

Figure 4. Complex modulus master curve after aged.

Permanent deformation (rutting) is a serious problem at high temperature due to slow moving traffic and as observed the as addition of modifier improves the pavement performance and decreasing the problem of distress by increasing the stiffness of the binder [41]. According to show on the above Fig. 9 addition of PCWAB has an advantage thereby improving the stiffness of asphalt binder for all loading frequencies and temperature conditions. But addition of 3 percent (%) proportion of PCWAB has no effect at low, intermediate and high temperature. At low frequency and high temperature, the modulus increases appreciably as modifier increases finally when we can summarize that the modifier appreciably improves the complex shear modulus of the original bitumen at low, intermediate and higher temperatures.

3.6. Performance Grade (PG) Determination

PG determination test is conducted at high temperature. As result shows crumb rubber also improve the performance grade of bitumen from PG64 to PG76 for permanent deformation of asphalt at high temperature [48]. As well as PG-temperature grade of base asphalt was shifted from PG58-xx to PG76-xx for PMN binders with concentrations of 7 % by weight. The PG76-xx binder can be successfully implemented into pavement construction in hot climates, owing to its good high-temperature performance [49]. The final rheological parameter $G^*/\sin\delta$, was believed to indicate the rutting resistance at high temperature of asphalt binder before MSCR test was discovered [27]. Performance grade of Portland cement and waste animal bone improve PG 58 to PG 70. The increment in PG clearly shows that modifying bitumen with this PCWAB material increases the stiffness of the asphalt binder. This study uses the parameter $G^*/\sin\delta$ to identify the maximum temperature that the asphalt binder could meet the minimum criteria of AASHTO M-320. The high temperature test result (output from the software) were organized in Tables 4 below illustrated for both before aged and after RTFO (Rolling Thin Film Oven) respectively.

Table 4. Determined High Temperature Performance Grade (AASHTO M 320).

Description	PG (brtfo)	PG (artfo)	PG(HT)
0% modified	58	58	58
1% modified	58	58	58
3% modified	64	70	64
5% modified	64	70	64

From the Table 4 above it is observed that there is a PG grade improvement from PG 58 to PG 64 when the neat bitumen is modified with 3 % PCWAB. When the content of the modifier is increased to 5 % then again, the PG will be further improved to PG70. Finally; from above we can summarize that the modifier appreciably improves the complex shear modulus of the virgin binder at higher temperatures and PG asphalt binder rutting resistance parameter $G^*/\sin\delta$ is based on complex modulus and phase angle. As mentioned above it has its own shortcomings to properly simulate field rutting performance. Based on this it is possible to guess that the improvement in rutting performance was pronounced due to the modifier. But recently it is proven that the current performance grade stiffness parameter ($G^*/\sin\delta$) is weak in predicting rutting potential [8]. Therefore; it is better to further evaluate the modified binder by MSCR tests since the parameter from this test termed as non-recoverable creep compliance best relates with rutting than any other parameter from binder test.

3.7. Multiple Stress Creep and Recovery (MCSR) Test Results

Fig. 10 displays the accumulated strain of PCWAB modified asphalt. This test is performed using the Dynamic Shear Rheometer test (DSR) by applying a controlled shear stress (100 and 3200 Pa) using a load for 1 second followed with 9-second rest period. During each cycle time the bitumen binder reaches a maximum or peak strain and also recovers before the next cycle stress is also applied again. The permanent strain is then accumulated for 10 cycle's totals of 100 seconds. This implies it is good information regarding the rheological characteristic of asphalt binder [3, 6]. Comparing Fig. 10 and 11 below it can be realized that a higher creep stress level was associated with a higher accumulated creep strain levels; it means that the stress level has a serious effect on the accumulated strain and the growth rate of strain direct proportion with stress level.

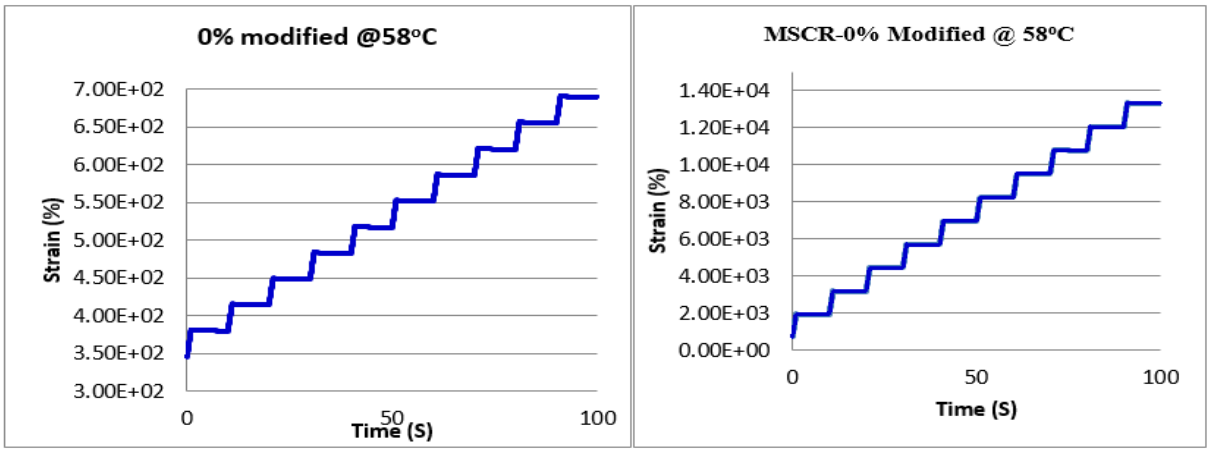

Figure 10. MSCR result of 0 % modified bitumen at 0.1 kPa and 3.2 kPa respectively.

Furthermore, Multiple Stress Creep Recovery (MSCR) tests conducted at a pre-determined temperature increasing the bitumen viscosity by blending in a micro-sized calcium carbonate filler or a nano-sized organo-clay filler were shown to affect the stress sensitivity but not the actual magnitude of failure stress which remained in line with the base bitumen. On the other hand, the SBS-modified bitumen had completely altered shear stress failure criterion. When considering non-polymer-modified bitumen's, simple high temperature strain sweeps have also been shown to be a potentially rapid and very useful creep performance ranking tool [9].

The MSCR test result (software output) contains huge data to represent in tables here. The Multiple stress creep and recovery test demonstrate that the PCWAB dramatically increases the resistance of binder to permanent deformation. In order to evaluate the strain response by asphalt binder to stress, the non-recoverable compliance (Jnr) is presented in Fig. 11 and Table 5 below. The Jnr is generally used as indicating to resistance against deformation of the binder at high temperature and repeated loading [50]. From above Fig. 10 Jnr values at both stress level (0.1 kPa and 3.2 kPa) of unmodified asphalt are greater than that of PCWAB modified asphalt at all temperature range. The Jnr decreased from 3.88 to 2.28 kPa-1 for as the dosage of PCWAB increased from 0 % to 5 %. This implies, the addition of PCWAB decreased the non-recoverable deformation of binder and can contribute to the rutting resistance of associated asphalt mixtures.

Table 5. MSCR test Summaries of Analyzed Jnr and % Recovery for Modified Binder.

Modified, %	0%	1%	3%	5%
Temperature °C	58	58	70	70
% Recovery @0.1kpa	5.32	26.33	16.82	10.03
% Recovery @3.2kpa	0.84	4.38	2.67	1.69
% Recovery difference	84.28	83.34	84.14	83.13
Jnr@0.1kpa	3.38	2.35	2.56	2.72
Jnr@3.2kpa	3.88	3.76	2.67	2.28
Jnr difference, %	14.76	60.15	31.01	20.66

Based on above result it is possible to evaluate all the binders by contrasting the calculated basic MSCR parameters with respect to the limits of those parameters described under standard specification for PG asphalt binder using MSCR test, AASHTO M 322. Percent difference in non-recoverable creep

compliance between 0.1 kPa and 3.2 kPa is also a requirement with maximum value 75 and Jnr indicated the Rutting resistance at high temperature and repeated load [3, 42, 51]. Therefore, MSCR test Result concluded as follows.

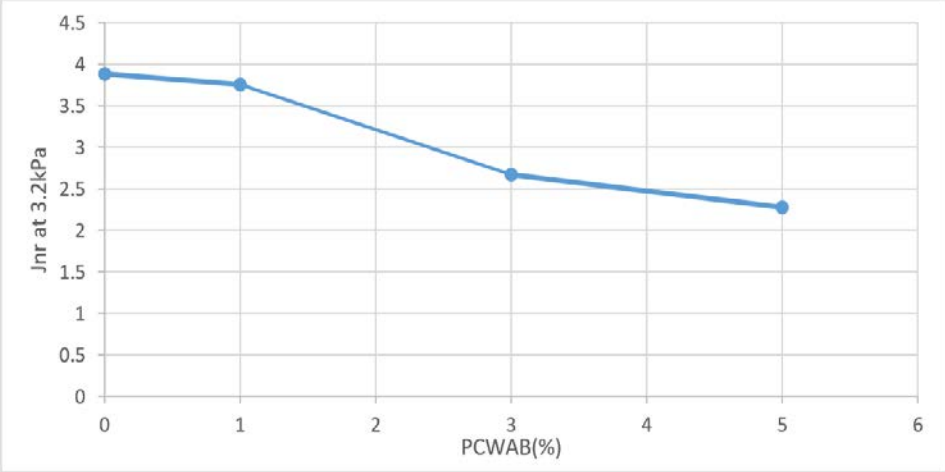

Figure 11. Effect of Portland cement and waste animal bone content on MSCR.

- The Jnr at 3.2 kPa is the fundamental parameter to evaluate rutting potential. The neat bitumen (0% modified) and the 1 % PCWAB modified binder have similar test temperature but different Jnr results. These two binders with test temperature 52, 58 & 64 °C will not be used for heavy and extremely heavy traffic in all cases of their test temperatures.
- The 3 % modified binder with test temperatures 58, 64 & 70 °C can be used for simply heavy traffic at 64 and for standard traffic at 70 °C. This binder shows a significant improvement than the previous two binders in rutting resistance by enhancing up the neat bitumen by one PG grade as per MSCR test also.
- A very good Jnr result is observed for 5 % modified binder this implies as content of modifier increasing Jnr give best result.
- To prove the improvement in rut performance, it is possible to make a clear comparison of Jnr values at the same test temperature (58 and 70). At this temperature the Jnr values are 3.88 and 2.28 for 0 % and 5 % modified binders respectively, which is a difference in rut resistance as per AASHTO M 332.

4. Conclusion

The main objectives of this research were to assessing the rheological characterize of locally available material with asphalt binders and the performance of bitumen modified with PC and WAB at high temperature in rutting resistance and at intermediate temperature in fatigue cracking resistance Using DSR test, this modifier is a new material mixed with a content of 1 %, 3 %, and 5 % percent by weight of binder was mixed with 80/100 penetration grade bitumen. Also, several laboratory tests are conducted in this research. After conducting laboratory tests on asphalt binder and analyzing the data, the results shows that the addition of modifier to the pure bitumen change the rheological characteristic of bitumen and its improved rheological behavior of the bitumen.

Depend on the laboratory results obtained from this study following conclusions have been drawn

1. Dynamic shear rheometer test rheological analysis shows that addition of PCWAB improves the viscoelastic rheological properties of the modified binders at high, intermediate and low intermediate.

2. Estimations of aging and rutting deformation indicates that, the modified binders will have significantly higher resistance to rutting (permanent deformation and aging has less effect on the modified binders as compared to control unmodified binder.

3. From test result obtained from FST, the master curve shows an improving behavior for asphalt binder up on addition 3 % and more percent addition of PCWAB on asphalt binder increases the stiffness property of asphalt binder at low loading frequencies and high temperature (rutting is susceptible). For all binders in almost similar pattern shear stiffness decreases as temperature increases.

4. At low frequency (such as from 0.01 up to 0.0001 Hz or below) and high temperature the effect of content of modifier is observed with difference in larger values of modulus. From this we can summarize that the modifier appreciably improves the modulus of the original bitumen at higher temperature and low frequency.

5. PG grade improvement from PG 58 °C to PG 64 °C. Was observed when the original bitumen is modified with 3 % PCWAB and when modified conducted with 5 % it was increased to PG 70 °C. This indicated as percent content of PCWAB increases also complex shear modulus (G^*) is increasing.

6. From the test result obtained from MSCR, the smallest total strain value was obtained for PCWAB of 5 %, followed by the 3 %, and 1 % PCWAB therefore addition of PCWAB improves the resistance of asphalt pavements to rutting.

5. Acknowledgements

I thank Mizan-Tepi and Addis Ababa Science and Technology University for their unlimited technical and unreserved financial suport .

References

1. Zemacheal, B.M. Effect of Different Types of Filler Materials on Characteristics of Hot-Mix-Asphalt Concrete. February 2007. 34 p.
2. McGennis, R.B., Anderson, R.M., Kennedy, T.W., Solaimanian, M. Background of superpave asphalt mixture design and analysis. Fhwa-Sa-95-003. 1995. (February). Pp. 160.
3. Zhang, J., Walubita, L.F., Faruk, A.N.M., Karki, P., Simate, G.S. Use of the MSCR test to characterize the asphalt binder properties relative to HMA rutting performance – A laboratory study. Construction & Building Materials. 2015. 94. Pp. 218–227. DOI: 10.1016/j.conbuildmat.2015.06.044
4. Merusi, F., Giuliani, F., Polacco, G. SIIV – 5th International Congress - Sustainability of Road Infrastructures Linear viscoelastic behaviour of asphalt binders modified with polymer / clay nanocomposites. Procedia – Social and Behavioral Sciences. 2012. 53. Pp. 335–345. DOI: 10.1016/j.sbspro.2012.09.885
5. Chin, C. Performance graded bitumen specifications. 2005. 70(2004). Pp. 1–10.
6. Science, M.O.F. Modification of Multiple Stress Creep and Recovery Test Procedure and Usage in Specification. 2011.
7. Rahimzadeh, B. Linear and non-linear viscoelastic. 2002. (March).
8. Street, D.S., Adamson, P., Yo, Y., Hoy, S. Final report Final report. (May) 2005.
9. Cosme, R.L., Teixeira, J.E.S.L., Calmon, J.L. Use of frequency sweep and MSCR tests to characterize asphalt mastics containing ornamental stone residues and LD steel slag. Construction and Building Materials. 2016. 122. Pp. 556–566. DOI: 10.1016/j.conbuildmat.2016.06.126
10. ERA. Pavement Design Manual. Roads Authority Ethiopian. 2013. I(March). Pp. 281.
11. Xie, J., Chen, J., Wu, S., Lin, J., Wei, W. Performance characteristics of asphalt mixture with basic oxygen furnace slag. Construction and Building Materials. 2013. 38. Pp. 796–803. DOI: 10.1016/j.conbuildmat.2012.09.056
12. Mubaraki, M., Ismael, S., Ali, A., Ismail, A., Yusoff, N.I. Rheological evaluation of asphalt cements modified with ASA polymer and Al_2O_3 nanoparticles. Procedia Engineering. 2016. 143(Ictg). Pp. 1276–1284. DOI: 10.1016/j.proeng.2016.06.135
13. Siddig, E., Cheng, P., Li, Y. Effects of polymer modified nanoclay on the performance of asphalt mixture. Magazine of Civil Engineering. 2019. 91(7). Pp. 98–111. DOI: 10.18720/MCE.91.9
14. Oliviero, C., Spadafora, A., Teltayev, B., Izmailova, G., Amerbayev, Y., Bortolotti, V. Polymer modified bitumen: Rheological properties and structural characterization. Colloids and Surfaces A: Physicochemical and Engineering Aspects. 2015. 480. Pp. 390–397. DOI: 10.1016/j.colsurfa.2015.02.048
15. Imaninasab, R., Bala, N., Kamaruddin, I., Napiah, M., Danlami, N. Effect of granular polymers on rutting performance of SMA with respect to modification process. Construction and Building Materials. 2017. 201(1). Pp. 64–72. DOI: 10.1088/1757-899X/201/1/012012
16. Alavi, M. Z., He, Y., Harvey, J., Jones, D. Evaluation of the Combined Effect s of Reclaimed Asphalt Pavement (RAP), Reclaimed Asphalt Shingles (RAS), and Different Virgin Binder Sources on the Performance of Blended Binders for Mixes with Higher Percentages of RAP and RAS. 2015.
17. Krishna, A., Devi, U., Kumar, P. Effect of HDPEH polymer on viscoelastic properties of SBS modified asphalt. Construction and Building Materials. 2017. 136. Pp. 230–236. DOI: 10.1016/j.conbuildmat.2017.01.049
18. Magadi, K.L., Anirudh, N. Evaluation of bituminous concrete mixture properties with steel slag. Transportation Research Procedia. 2016. 17. Pp. 174–183. DOI: 10.1016/j.trpro.2016.11.073
19. Golestani, B., Moghadas, F., Sadeghpour, S. Performance evaluation of linear and nonlinear nanocomposite modified asphalts. Construction and Building Materials. 2012. 35. Pp. 197–203. DOI: 10.1016/j.conbuildmat.2012.03.010
20. Sienkiewicz, M., Borz, K., Wojtkiewicz, A., Janik, H. Development of methods improving storage stability of bitumen modified with ground tire rubber : A review. 2017. 159. Pp. 272–279. DOI: 10.1016/j.fuproc.2017.01.049
21. Mohammed, M., Parry, T., Grenfell, J.J.R.A. Influence of fibres on rheological properties and toughness of bituminous binder. Construction and Building Materials. 2018. 163. Pp. 901–911. DOI: 10.1016/j.conbuildmat.2017.12.146
22. Yildirim, Y. Polymer modified asphalt binders. Construction and Building Materials. 2007. 21(1). Pp. 66–72. DOI: 10.1016/j.conbuildmat.2005.07.007
23. Al-khateeb, G.G., Al-akhras, N.M. Properties of Portland cement-modified asphalt binder using Superpave tests. Construction and Building Materials. 2011. 25(2). Pp. 926–932. DOI: 10.1016/j.conbuildmat.2010.06.091
24. Muslich, S., Nura, B., Fahmi, A.C., Sri, S. Effect of Hydrated Lime and Portland Cement on Asphalt Binders using DSR. 2018. 05006. Pp. 1–8.
25. Yao, H., Ph, D., You, Z., Ph, D., Asce, M., Li, L., Ph, D., Lee, C.H., Ph, D., Wingard, D., Ph, D., Asce, M., Yap, Y.K., Shi, X., Ph, D., Asce, M., Goh, S.W., Ph, D. Rheological Properties and Chemical Bonding of Asphalt Modified with Nanosilica. 2013. 25(November). Pp. 1619–1630. DOI: 10.1061/(ASCE)MT.1943-5533.0000690
26. Shi, X., Cai, L., Xu, W., Fan, J., Wang, X. Effects of nano-silica and rock asphalt on rheological properties of modified bitumen. Construction and Building Materials. 2018. 161. Pp. 705–714. DOI: 10.1016/j.conbuildmat.2017.11.162

27. Sousa, J.B., Mafra, M., Vorobiev, E.A., Svechinsky, E.G. Elastomeric Asphalt Extender – A New Frontier on Asphalt Rubber Mixes.
28. Elkashef, M., Podolsky, J., Williams, R.C., Cochran, E. Preliminary examination of soybean oil derived material as a potential rejuvenator through Superpave criteria and asphalt bitumen rheology. Construction and Building Materials. 2017. 149. Pp. 826–836. DOI: 10.1016/j.conbuildmat.2017.05.195
29. Jeffry, S.N.A., Jaya, R.P., Hassan, N.A., Yaacob, H., Mirza, J., Drahman, S.H. Effects of nanocharcoal coconut-shell ash on the physical and rheological properties of bitumen. Construction and Building Materials. 2018. 158. Pp. 1–10. DOI: 10.1016/j.conbuildmat.2017.10.019
30. Witzany, G. Pref ace. Biocommunication of Animals. 2014. 9789400774. Pp. vii. DOI: 10.1007/978-94-007-7414-8
31. Rizvi, H.R., Khattak, M.J., Gallo, A.A. Bone Glue Modified Asphalt : A Step towards Energy Conservation and Environment Friendly Modified Asphalts. 2014.
32. Akinyele, J.O., Adekunle, A.A., Ogundaini, O. The effect of partial replacement of cement. ANNALS of Faculty Engineering Hunedoara – International Journal of Engineering. 2016. 2(2007). Pp. 199–204.
33. Kotb, M., Assas, M., Abd-Elrahman, H. Effect of grounded bone powder addition on the mechanical properties of cement mortar. WIT Transactions on Ecology and the Environment. 2010. 138. Pp. 201–212. DOI: 10.2495/DN100181
34. Drews, A. Standard Test Method for Penetration of Bituminous Materials. Manual on Hydrocarbon Analysis, 6th Edition. 2008. i. Pp. 47-47–3. DOI: 10.1520/mnl10829m
35. ASTM. ASTM D 2872-12e1. Standard Test Method for Effect of Heat and Air on a Moving Film of Asphalt (Rolling Thin-Film Oven Test). 2004. (C). Pp. 1–6. DOI: 10.1520/D2872
36. Standards, R. Ductility of Bituminous Materials. 2007. i. Pp. 42–45. DOI: 10.1520/D0113-07.2
37. Drews, A. Standard Test Method for Softening Point of Bitumen (Ring-and-Ball Apparatus). Manual on Hydrocarbon Analysis, 6th Edition. 2008. 1(c). Pp. 50-50–4. DOI: 10.1520/mnl10830m
38. Modelling the Linear Viscoelastic Rheological Properties of Bituminous Binders. 2012. (April).
39. Nottingham, T., User, N.E. Airey, Gordon (1997) Rheological characteristics of polymer modified and aged bitumens. PhD thesis, University of Nottingham. 1997.
40. Tušar, M., Zupanc, A. Rheological and mechanical characterization of waste PMMA / ATH modified bitumen. 2013. 38. Pp. 119–125. DOI: 10.1016/j.conbuildmat.2012.07.101
41. Viet, C., Di, H., Sauzéat, C., Lesueur, D., Pouget, S., Olard, F. Complex modulus and fatigue resistance of bituminous mixtures containing hydrated lime. Construction and Building Materials. 2017. 139. Pp. 24–33. DOI: 10.1016/j.conbuildmat.2017.02.042
42. Instruments, M.A. Multiple Stress Creep Recovery (MSCR) testing.
43. Zoorob, S.E., Castro-gomes, J.P., Oliveira, L.A.P., Connell, J.O. Investigating the Multiple Stress Creep Recovery bitumen characterisation test. Construction and Building Materials. 2012. 30. Pp. 734–745. DOI: 10.1016/j.conbuildmat.2011.12.060
44. Engineering, C. The 2S2P1D : An Excellent Linear Viscoelastic Model. 2010. 1(2).
45. Liang, M., Xin, X., Fan, W., Luo, H., Wang, X., Xing, B. Investigation of the rheological properties and storage stability of CR / SBS modified asphalt. Construction and Building Materials. 2015. 74. Pp. 235–240. DOI: 10.1016/j.conbuildmat.2014.10.022
46. Kumar, A., Panda, M. Investigation on rheological performance of sulphur modified bitumen (SMB) binders. Construction and Building Materials. 2017. 149. Pp. 724–732. DOI: 10.1016/j.conbuildmat.2017.05.198
47. Ortuzar & Willumsen (2001) Modelling Transport (3rd Ed).pdf.
48. Xu, O., Xiao, F., Han, S., Amirkhanian, S.N., Wang, Z. High temperature rheological properties of crumb rubber modified asphalt binders with various modifiers. Construction and Building Materials. 2016. 112. Pp. 49–58. DOI: 10.1016/j.con-buildmat.2016.02.069
49. Kang, Y., Song, M., Pu, L., Liu, T. Rheological behaviors of epoxy asphalt binder in comparison of base asphalt binder and SBS modified asphalt binder. Construction and Building Materials. 2015. 76. Pp. 343–350. DOI: 10.1016/j.conbuildmat.20-14.12.020
50. Zoorob, S.E., Castro-Gomes, J.P., Pereira Oliveira, L.A., O'Connell, J. Investigating the Multiple Stress Creep Recovery bitumen characterisation test. Construction and Building Materials. 2012. 30. Pp. 734–745. DOI: 10.1016/j.conbuildmat.20-11.12.060
51. Anderson, M., Bukoski, J. Using the Multiple-Stress Creep Recovery (MSCR). 2012. (February).

Contacts:

Girmaye Garedew, girmegare@gmail.com

© Garedew, G., 2021

Magazine of Civil Engineering

ISSN 2712-8172

journal homepage: http://engstroy.spbstu.ru/

DOI: 10.34910/MCE.103.5

Pump-hose systems with universal fire barrels for extinguishing buildings

A. Marozau[a]*, H. Tran Duc[b], A. Kamluk[a], V. Parmon[a], M. Striganova[a]

[a] University of Civil Protection of the Ministry of Emergency Situations of the Republic of Belarus, Minsk, Respublika Belarus'

[b] University of Fire Safety of the Ministry of Public Security of the Socialist Republic of Vietnam, Than' Sjuan', Hanoj, Vietnam

** E-mail: morozow974@gmail.com*

Keywords: mechanical properties, pressure, buildings, experimental investigations, hydraulic calculation, hydraulic resistance, numerical methods

Abstract. The hydraulic calculation of pump-hose system was carried out, taking into account the influence of its elements on the performance of fire barrels. Corresponding dependences for mixed pump-hose systems consisting of one and three fire barrels are presented. Based on the hydraulic calculation of the pump-hose system, it was found that an increase in the number of hoses to 12 in the main and up to 3 in the working line leads to a decrease in barrel consumption by 1.5 %, which does not affect fire fighting process. As a result of the analysis of the pump-hose system with three fire barrels when changing the main parameters in one of them, we can conclude that a significant effect on the flow rate is exerted by a change in the position of the dispenser, the height of the barrel and the number of hoses in the working line (total line resistance). It was also established that the flow rate of the other two system trunks varies slightly (1.5 %), which in practice can be ignored. Based on the data obtained, recommendations are given to the operator working on the pump of a fire truck when feeding fire extinguishing substances to a height. The presented research results are obtained in the field of fire extinguishing agents and methods of their application and can be used in fire fighting and emergency response.

1. Introduction

According to the State Statistical Reporting, in the period from 2014 to 2019, more than 30000 fires occurred in the Republic of Belarus, in which 2856 people died (including 47 children) and 1668 were injured. At the same time, 91 % of the total number of fires falls on the housing stock [1–2]. A similar problem is encountered in many countries of the world, which is confirmed by studies by scientists from Russia [3], Japan [4], Spain [5], Sweden [6], USA [7], Netherlands [8], United Kingdom [9].

When extinguishing fires in residential buildings, a number of technical means are used: a car for water delivery, fire hoses, fire barrels. In this work, we studied the mutual influence of the elements of the pump-hose system (fire hoses in conjunction with one or more fire barrels) on its tactical and technical characteristics.

Currently, to extinguish such fires fire barrels with variable flow rate are used around the world. Unlike previously used, all of these barrels allow supplying water and aqueous solutions of extinguishing agents in a wide range of flow rates and head (form a spectrum of different types of jets and their combinations, while ensuring high quality spray with different torch angles), and if there is a nozzle, they generate air-mechanical foam of low multiplicity. TFT (USA) [10], POK (France) [11], Akron Brass Company (USA) [12], Yone Corporation (Japan) [13], R.PONS (France) [14], Delta Fire Ltd (England) [15], Rosenbauer (Austria) [16], Protek (Taiwan) [17]. In 2013, the Ministry of Emergency Situations of the Republic of Belarus began an import substitution of these foreign trunks with domestic counterparts SPRU-50/0.7 and SPRUK-50/0.7 “Viking” (Fig. 1) [18–19], manufactured by the Optron instrument-making plant.

This work is licensed under a CC BY-NC 4.0

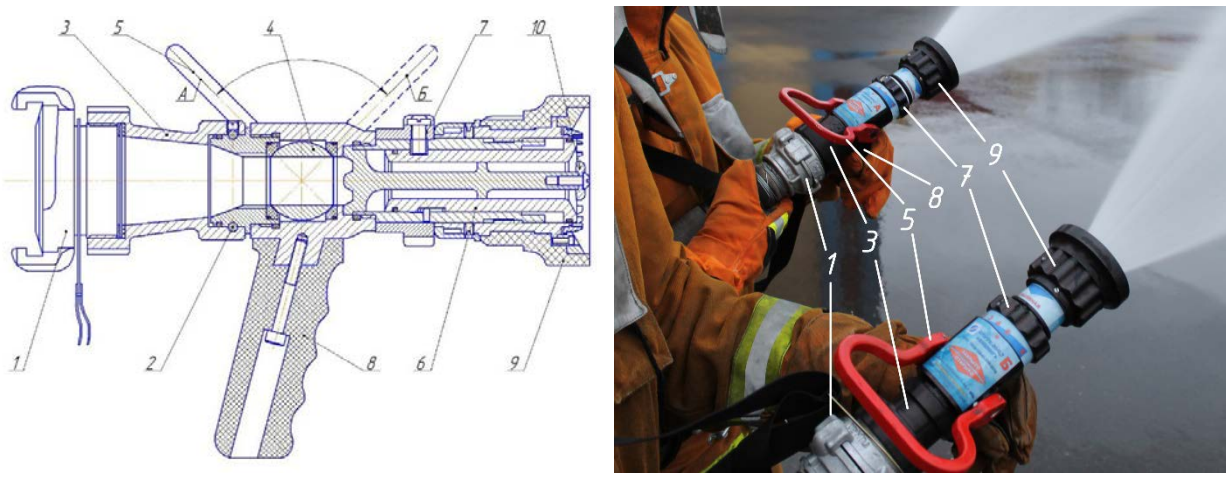

a b

Figure 1. The appearance of the barrel:
a is the diagram; b is the photo of the barrel while water supplying
1 is the connecting head HZ 50; 2 is the fixing element; 3 is the rotating adapter;
4 is the overlapping device; 5 is the control handle; 6 is the mechanism for controlling the flow of extinguishing agent; 7 is the dispenser (5 positions); 8 is the holding handle;
9 is the nozzles; 10 is the deflector.

The main purpose of fire barrels is the remote effective supply of extinguishing agent to the fire, which allows for fire extinguishing at a distance from the fire front within the radius of the jet. Obviously, they have certain tactical and technical characteristics: operating head, flow rate and range of extinguishing agent. In this regard, the problems arising from the supply of extinguishing agent for extinguishing buildings can be divided into two categories. The first concerns issues related to the localization of fires in high-rise buildings and buildings with increased number of storeys, and the second concerns the localization of fires in several places at the same time when apartments on different floors or in neighboring entrances are burning in parallel. While questions of the first category are considered enough, for example, in [20–25], the questions of the second category need to be studied additionally. This is due to the fact that the performance characteristics directly depend on the head on the pump of the fire truck, therefore, it is important for the operator working on it to know what optimal head value must be maintained during firefighting. Since the fire departments are currently using domestic barrels with variable flow rates for emergency situations, for which the dependence of the performance characteristics on required head, taking into account the composition of the pump-hose system in unknown, is necessary to conduct experimental studies.

Thus, the calculation of the pump-hose system is reduced to determining the required head at the pump at a given flow rate, as well as the actual head and flow rates at barrels at a given head on the pump. To achieve this goal in the work it is necessary to solve the following tasks:

1. To get the formula for calculating the head at the fire truck pump, taking into account the influence of the characteristics of all elements of the pump-hose system when using fire barrels with a variable flow rate.

2. To carry out a hydraulic calculation of the pump-hose system with one fire barrel with a variable flow rate.

3. To study the effect of a fire barrel with a variable flow rate on a pump-hose system with several barrels.

All calculations in this research were carried out for the fire barrel SPRUK 50/0.7 Viking at the University of Civil Protection of the Ministry of Emergencies of Belarus. Moreover, all the obtained dependencies will be valid for other modern barrels with variable flow rate. The difference will only be in the resistance of the barrels, due to various geometric parameters and material of manufacture.

2. Methods

In general terms, the pump and hose system (Fig. 2) is a combined fire pump, hose line and fire barrel (extinguishing agent supply device).

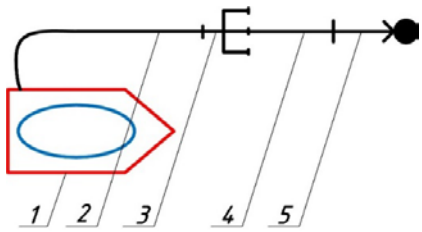

Figure 2. Scheme (general) of the pump-hose system
1 is the fire truck; 2 is the main hose line; 3 is the hose branching (dictating point);
4 is the working hose line; 5 is the fire barrel.

Depending on the method of connecting these elements, parallel, serial and mixed pump-hose systems are distinguished (Fig. 3).

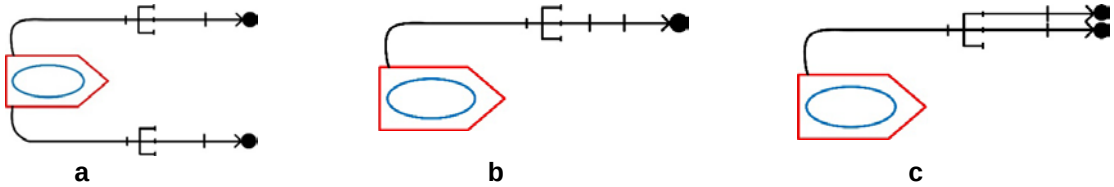

Figure 3. Types of pump-hoses systems: a is the parallel; b is the sequential; c is the mixed.

The basis for any hydraulic calculation of pump-hoses systems is the determination of flow head losses at a given flow rate. It is known that the total flow rate of the system in parallel connection of elements is equal to the sum of the flow rate in each of them, while in series – all flow rates are equal to each other. Moreover, the head losses in the parallel system are the same in all its elements, while in the serial system the losses on the elements are added up. Based on these rules, for a mixed pump-hose system, it can be written:

$$H_{p.} = H_{m.} + H_{w.}, \tag{1}$$

where $H_{p.}$ is head at the pump of the fire truck, m; $H_{m.}$ is head loss in the main hose line, m; $H_{w.}$ is head losses in the working hose lines or head in the dictating point, m.

In this case, the working hose lines are parallel, therefore the head losses in them are equal to each other.

Head loss are due to the presence of hydraulic resistance: linear and local. Linear resistances are caused by the friction of the fluid layers against each other, on the inner surface of the pipe (hose) and in practice causes head losses in the hose lines. Since the hose lines are cylindrical pipelines, and the fluid flow is turbulent [19], for calculating the head loss in them, one can use the Darcy-Weisbach formula:

$$h_{l.} = \lambda \frac{l}{d} \cdot \frac{\upsilon^2}{2g}, \tag{2}$$

where λ is the coefficient of hydraulic friction; l is the length of the plot, m; d is the diameter of the pipeline (hose), m; υ is the average flow velocity, m/s; g is acceleration of gravity, m/s^2.

Expressing from the condition of continuity

$$Q = \upsilon\omega, \tag{3}$$

where Q is the fluid flow rate, m^3/s; ω is area of water section, m^2,

the average flow velocity υ and, substituting in (2), we obtain:

$$h_{l.} = \lambda \frac{l}{d} \cdot \frac{Q^2}{2g\omega^2} = \lambda \frac{l}{d} \cdot \frac{16Q^2}{2g\pi^2 d^2} = \lambda \frac{8l}{g\pi^2 d^4} \cdot Q^2 = S_p Q^2,$$

$$S_p = \lambda \frac{8l}{g\pi^2 d^4} \cdot 10^{-6}. \tag{4}$$

where S_p is the hose resistance, m s^2/l^2.

Hose resistance was established experimentally as part of research work at the University of Civil Protection of the Ministry of Emergencies of Belarus and the Scientific Research Institute of Fire Safety and Emergencies (Table 1).

Table 1. Resistance of fire hoses.

Hose type	Resistance of fire hoses, m·s²/l², for a hose with a diameter, mm						
	38	51	66	77	89	110	150
Latexed	0.53	0.12	0.023	0.0117	–	–	–
Rubberized	–	0.15	0.035	0.0150	0.0046	0.002	0.0005

Local resistances are caused by a local change in flow velocity in magnitude and direction and cause head loss in the branches and fire barrels. The magnitude of such losses can be calculated by the empirical formula of Weisbach:

$$h_{loc.} = \xi_{loc.} \cdot \frac{\upsilon^2}{2g} = \xi_{loc.} \cdot \frac{Q^2}{2g\omega^2} = \frac{8\xi_{loc.}}{g\pi^2 d^4} \cdot Q^2 = S_{loc.} Q^2 ,$$

$$S_{loc.} = \frac{8\xi_{loc.}}{g\pi^2 d^4} \cdot 10^{-6} , \tag{5}$$

where $\xi_{loc.}$ is the coefficient of hydraulic resistance; d is the input diameter of local resistance, m; $S_{loc.}$ is local resistance, m s²/l².

We calculate the value of local resistance for branching and fire barrel.

According to [26], the coefficient of local resistance for hose branches of sizes RT-70 and RT-80 is 2 and 1.5, respectively. Knowing the input diameter of the branches (conditional passage of the inlet pipe), we can determine the local resistance value by the formula (5). The calculation results are presented in Table 2.

Table 2. Hose branch resistance.

Branch sizes	Conditional pass of an entrance branch pipe, m	Local resistance, m·s²/l²
RT-70	0.07	0.0052
RT-80	0.08	0.0030

The local resistance coefficient for the fire barrel SPRUK 50/0.7 Viking is not known. However, in [27], the flow rates for various positions of the dispenser are given for working heads at the entrance to the barrel. Since the resistance of the barrel does not depend on the head at the inlet and for each position of the flow controller remains constant regardless of the flow, then, knowing the head and flow, we can determine the resistance value for each position of the flow controller by the formula:

$$S_{loc.} = \frac{H_{barr.}}{Q^2}, \tag{6}$$

where $H_{barr.}$ is head on the barrel, m.

The calculation results are presented in Table 3.

Table 3. Resistance of a fire barrel SPRUK 50/0.7 "Viking".

Dispenser position	Parameter	Head, m				Average value of local resistance, m·s²/l²
		40	50	60	70	
1	The value of flow, l/s	0.53	0.58	0.67	0.69	142.93
	Resistance, m·s²/l²	142.40	148.63	133.66	147.03	
2	The value of flow, l/s	0.97	1.06	1.17	1.28	43.39
	Resistance, m·s²/l²	42.51	44.50	43.83	42.72	
3	The value of flow, l/s	1.83	2.06	2.28	2.42	11.81
	Resistance, m·s²/l²	11.94	11.78	11.54	11.95	
4	The value of flow, l/s	2.61	2.97	3.25	3.61	5.65
	Resistance, m·s²/l²	5.87	5.67	5.68	5.37	
5	The value of flow, l/s	3.15	3.45	3.73	4.17	4.14
	Resistance, m·s²/l²	4.03	4.20	4.31	4.03	
6	The value of flow, l/s	3.67	4.03	4.36	5	3.00
	Resistance, m·s²/l²	0.53	0.58	0.67	0.69	

Thus, the head loss in the main hose line add up to the head loss in the main fire hoses and hose branching, and the head loss in the working hose lines – from the loss of head in the working fire hoses, the fire barrel and the difference in elevation of the location of the pump and the fire barrel. With this in mind, we write formula (1) in the form:

$$H_{p.} = n \cdot S_{m.h.} \cdot Q^2 + S_{br.} \cdot Q^2 + n \cdot S_{w.h.} \cdot Q^2 + S_{barr.} \cdot Q^2 + Z \ , \quad (7)$$

where n is the number of sleeves; $S_{m.h.}$ is resistance of one main hose, m s²/l²; $S_{br.}$ is resistance of hose branching, m s²/l²; $S_{w.h.}$ is resistance of one working hose, m s²/l²; Z is the difference between the elevation marks of the pump and the fire barrel, m.

3. Results and Discussion

The research results presented in this section were obtained for the first time and were not covered in the works of other authors.

The pump-hose system with one barrel is sequential (Fig. 2, a) and formula (7) is applicable for its calculation. It is important for the operator working on the pump to know what head is needed on the pump to ensure the required flow rate on the fire barrel. From the formula (7) it is seen that the head is influenced by the resistance (diameter) and the number of hoses, as well as the difference between the elevation marks of the pump and the fire barrel.

Let us consider the case when the height difference is constant and equal to zero. At the same time, we change the number of hoses in the main line from 1 to 12 and in the working line from 1 to 3, as well as the head on the pump from 10 to 100 meters. Calculations are carried out for the 3rd position of the dispenser (Fig. 1, position 7) of one fire barrel SPRUK 50/0.7 "Viking", since in practice when extinguishing a fire this position allows creating the most optimal flow rate of extinguishing agent. As a result, we obtain the dependence of the flow rate of the extinguishing agent on the head at the pump for a different number of hoses (Fig. 4).

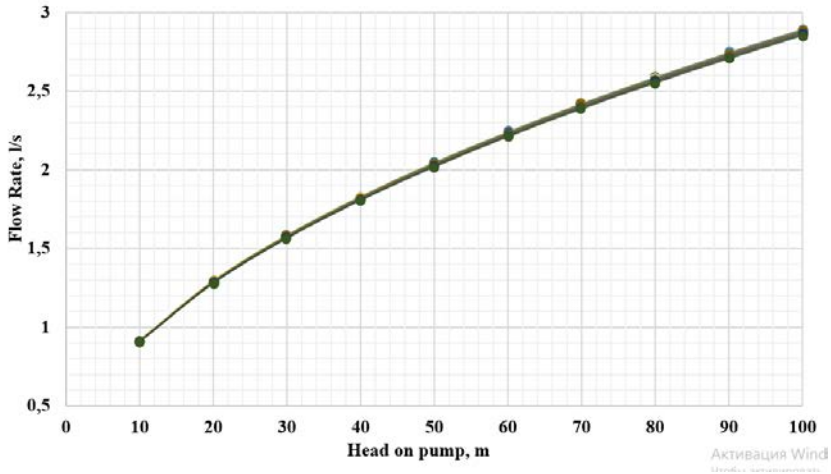

Figure 4. Dependence of the flow rate of extinguishing agent on the head at the pump when changing the number of hoses.

From the obtained dependencies it is seen that the flow rate of a fire barrel operating in a system consisting of a 1st trunk and 1st working hose is on average by 1.5 % higher than the flow rate of a barrel operating in a system of 12 trunks and 3 workers hoses. Such a difference is not noticeable during practical work, therefore it can be concluded that a change in the number of hoses has a slight effect on the flow rate of the extinguishing agent and may not be taken into account in further calculations.

Let us consider the effect of the difference in elevation of the pump and the fire barrel on the flow rate of the extinguishing agent. To do this, the dependence for various head on the pump is constructed (Fig. 5). The method “from pump to pump” is used to supply extinguishing agent to a considerable height: one tank truck is installed on a water source, a main line is laid to the pump of the second truck, installed at the entrance to the building, then a fire extinguishing substance is supplied to extinguish the fire. With this method, the total head is the sum of the head on the pumps of tank trucks, therefore, in the nomogram shown on Fig. 4, the head range varies from 10 to 200 meters. Calculations are also carried out for the 3rd position of the dispenser of the fire barrel SPRUK 50/0.7 "Viking" according to the formula (7).

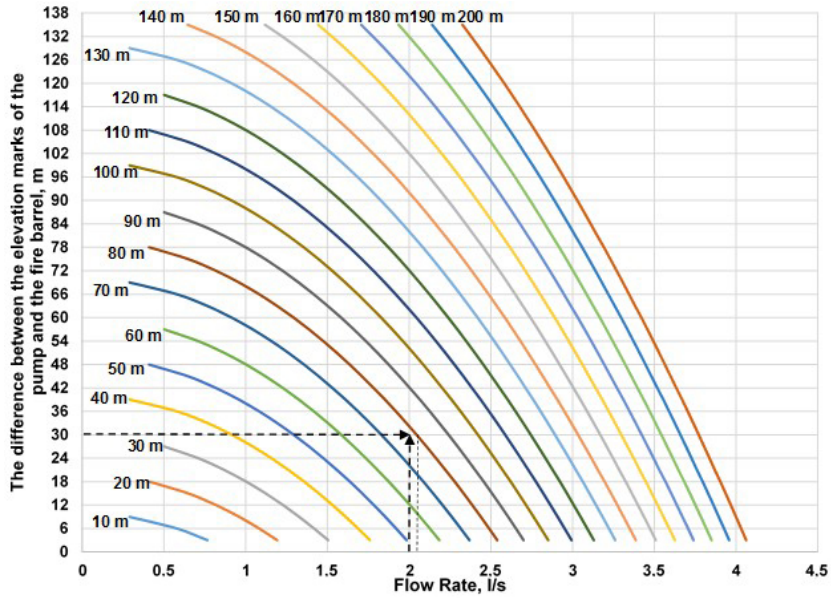

Figure 5. Dependence of the flow of extinguishing agent on the difference in elevation of the pump and the fire barrel for various heads on the pump.

Let us analyze the procedure for using the nomogram shown in Fig. 5. Suppose that we need to determine what head is required to be created at the pump of fire truck for the uninterrupted supply of extinguishing agent with a flow rate of 2 l/s to the 10th floor of an apartment building. Since the standard height of the floor is 3 m, the barrel must be fed to a height of 30 m. On the abscissa axis, we fix the required flow rate, and on the ordinate axis, the required height difference between the pump and the fire barrel. Then, from the point with these coordinates, we put the segment on the right to the intersection with the nearest chart. The head described by this graph is 80 m and it must be created on the pump. At the same time, we note that the actual consumption will be slightly higher than required, which is correct in the calculations of fire extinguishing tactics.

Let us consider the most common case is a mixed pump-hose system (Fig. 3c), consisting of one main and three working lines, branching and three barrels SPRUK 50/0.7 "Viking". The head losses in such a pump-hose system consist of the sum of the head losses in the main and one of the working hose lines. Moreover, the head losses in parallel working hose lines are equal to each other. Based on the expression (7) and taking into account that the head at the entrance to all working lines are equal, we can write the system of equations:

$$\begin{cases} H_{w.} = H_{p.} - \left(n \cdot S_{m.h.} + S_{br.}\right)\left(Q_1 + Q_2 + Q_3\right)^2, \\ H_{w.} = \left(n \cdot S_{w.h.1} + S_{barr.1}\right) \cdot Q_1^2 + Z_1, \\ H_{w.} = \left(n \cdot S_{w.h.2} + S_{barr.2}\right) \cdot Q_2^2 + Z_2, \\ H_{w.} = \left(n \cdot S_{w.h.3} + S_{barr.3}\right) \cdot Q_3^2 + Z_3, \end{cases} \tag{8}$$

where $S_{w.h.1}$, $S_{w.h.2}$, $S_{w.h.3}$ is resistance of one working hose of the first, second and third hose line, respectively, m·s²/l²; Z_1, Z_2, Z_3 is the difference between the elevation marks of the pump and the first, second and third fire barrel, respectively, m. In this system of equations, the unknowns are $H_{w.}$, Q_1, Q_2, Q_3.

Obviously, a change in the parameters of one of the working hose lines entails a change in the flow rate of fire barrels in the other two. The parameters considered in this case include: resistance of the working hose line, position of the dispenser of the fire barrel, and also the difference in the heights of the location of the pump and the fire barrel. Thus, the problem is reduced to solving the system of equations (8) to determine the relationship between the flow rates of fire barrels. As a result of calculations by expressing unknowns Q_1, Q_2, Q_3 in terms of $H_{w.}$ from the system (8), we obtain the equation

$$C_1 H_{w.}^4 + C_2 H_{w.}^3 + C_3 H_{w.}^2 + C_4 H_{w.} + C_1 = 0\,, \tag{9}$$

where

$$C_1 = B_1^2 + 64 A A_1 A_2 A_3\,,$$

$$C_2 = 2B_1 B_2 - 64AA_1A_2A_3(H_{н.} + Z_1 + Z_2 + Z_3),$$

$$C_3 = B_2^2 + 2B_1 B_3 + 64AA_1A_2A_3(Z_1H_{н.} + Z_2H_{н.} + Z_3H_{н.} + Z_1Z_2 + Z_2Z_3 + Z_1Z_3),$$

$$C_4 = 2B_2B_3 - 64AA_1A_2A_3(Z_1Z_2H_{н.} + Z_2Z_3H_{н.} + Z_3Z_4H_{н.} + Z_1Z_2Z_3),$$

$$C_5 = B_3^2 + 64AA_1A_2A_3Z_1Z_2Z_3H_{н.}$$

$$B_1 = (A_1 - A - A_2 - A_3)^2 - 4(A_2A_3 - AA_1),$$

$$B_2 = 2(A_1 - A - A_2 - A_3)(AH_{н.} - A_1Z_1 - A_2Z_2 - A_3Z_3) + 4(A_2A_3(Z_2 + Z_3) - AA_1(H_{н.} + Z_1)),$$

$$B_3 = (AH_{н.} - A_1Z_1 - A_2Z_2 - A_3Z_3)^2 - 4(A_2A_3Z_2Z_3 - AA_1H_{н.}Z_1)$$

$$A = \frac{1}{nS_{m.h.} + S_{br.}},\ A_1 = \frac{1}{nS_{w.h.1} + S_{barr.1}},\ A_2 = \frac{1}{nS_{w.h.2} + S_{barr.2}},\ A_3 = \frac{1}{nS_{w.h.3} + S_{barr.3}}.$$

Let us determine the dependence of the flow rate on the resistance of the working hose line, the position of the dispenser of the fire barrel, as well as the difference in the heights of the location of the pump and the fire barrel when changing them on one of the three working barrels in the system. Equation (9) was solved numerically in Microsoft Excel. The results obtained for the head at the pump of 100 m are presented in Fig. 6.

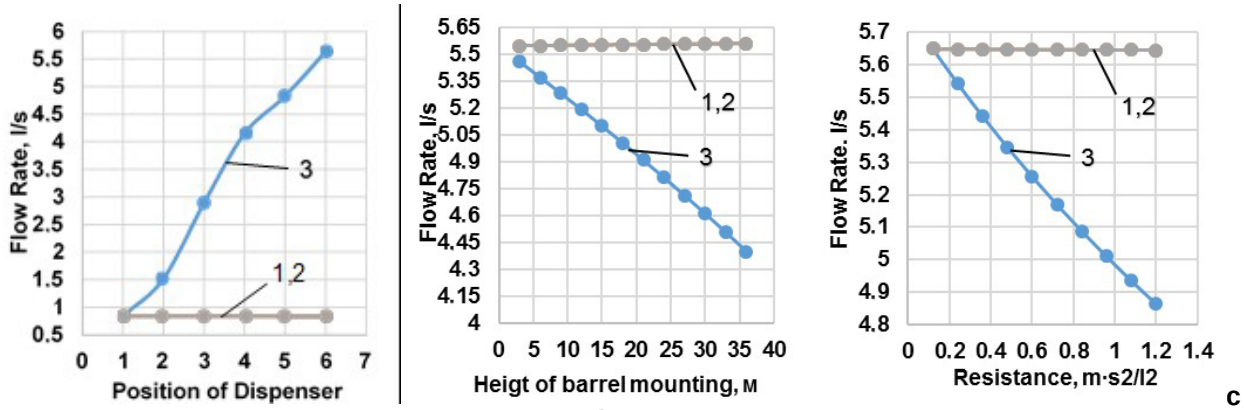

a b c

Figure 6. Dependence of the flow of three barrels when changing in one of them: a is the position of the dispenser; b is the location of height relative to the fire tank pump; c is the resistance of the working line 1 is the dependence for the first barrel; 2 is the dependence for the second barrel; 3 is the dependence for the third barrel.

From the graphs presented, it can be seen that the flow rates of two trunks are the same and change by no more than 1.5 % when changing these parameters on the third barrel. At the same time, analyzing Fig. 6a, we can conclude that when the position of the dispenser of the fire barrel changes, the flow rate increases by more than 5 times, which is due to an increase in the barrel cross live section of the barrel and, as a result, a significant decrease in local resistance. From Graph 3 in Fig. 6b, it follows that when the height difference between the barrel and the fire tank pump increases by more than 10 times, the barrel flow rate decreases by 20 %, which can affect firefighting, especially if the water is delivered to a considerable height. At the same time, the flow rate on the first and second trunks are almost the same. Fig. 6c shows that with a 10-fold increase in the total resistance of the working line of one of the trunks, the flow rate decreases by more than 15 %. Therefore, when fighting fires, the number of hoses in the working line is minimal and, as a rule, no more than three.

4. Conclusions

1. A formula has been obtained for calculating the head at the fire truck pump, taking into account the influence of the characteristics of all elements of the pump-hose system when using fire barrels with a variable flow rate.

2. The hydraulic calculation of the pump-hose system with one fire barrel with a variable flow rate has been done. It has been established that an increase in the number of hoses to 12 in the main and up to 3 in the working line leads to a decrease in barrel consumption by 1.5 %, which does not affect the firefighting process. Also the graphs have been compiled of the dependencies of the flow rate of the barrel

on the height of its location for various heads on the fire truck pump. The nomogram compiled from these graphs is applicable in practice to determine the actual flow rate on the barrel when feeding it to a considerable height.

3. The influence of a fire barrel with a variable flow rate on a pump-hose system with several barrels was studied. Based on the calculations, it can be concluded that a significant effect on the flow rate is exerted by a change in the position of the dispenser, the height of the barrel and the number of hoses in the working line (total line resistance). It was also established that the flow rate of the other two system barrels varies slightly (up to 1.5 %), which in practice can be ignored.

The listed results of the work are aimed at increasing the efficiency of the use of pump-hose systems by fire departments for extinguishing in multi-storey buildings.

References

1. Informatsiya o chrezvychaynykh situatsiyakh v Respublike Belarus po dannym ucheta MChS [Information on emergency situations in the Republic of Belarus according to the data of the Ministry of Emergencies] [Online]. URL: https://mchs.gov.by/ministerstvo/statistika/svedeniya-o-chs (date of application: 25.03.2020)
2. Informatsiya o boyevoy rabote podrazdeleniy po chrezvychaynym situatsiyam po likvidatsii avariy i drugikh chrezvychaynykh situatsiy [Information on the combat work of emergency units for the liquidation of accidents and other emergency situations] [Online]. URL: https://mchs.gov.by/ministerstvo/statistika/boevaya-rabota (date of application: 25.03.2020)
3. Gravit, M.V., Nedryshkin, O.V., Ogidan, O.T. Transformable fire barriers in buildings and structures. Magazine of Civil Engineering. 2018. 77(1). Pp. 38–46. DOI: 10.18720/MCE.77.4
4. Himoto, K. Risk of fire spread in densely-built environments: a review emphasizing cities in Japan. Journal of Disaster Research. 2007. No. 4. Pp. 276–283. DOI: 10.20965/jdr.2007.p0276
5. Fernández-Vigil, M., Gil Rodríguez, B. & Echeverría Trueba, J.B. Fire Safety Strategies to Reduce Mortality in Dwellings Occupied by Elderly People: The Spanish Case. Fire Technology. 2020. DOI: 10.1007/s10694-020-00972-4
6. Runefors, M. Measuring the Capabilities of the Swedish Fire Service to Save Lives in Residential Fires. Fire Technology. 2020. No. 2. Pp. 583–603. DOI: 10.1007/s10694-019-00892-y
7. Kerber, S., Regan, J.W., Horn, G.P. et al. Effect of Firefighting Intervention on Occupant Tenability during a Residential Fire. Fire Technology. 2019. No. 3, Pp. 2289–2316. DOI: 10.1007/s10694-019-00864-2
8. Kobes, M., Helsloot. I, Vries, B. G.Post, J. Building safety and human behaviour in fire: A literature review. Fire Safety Journal. 2010. No. 1. Pp. 1–11. DOI: 10.1016/j.firesaf.2009.08.005
9. Grimwood, P., Sanderson, I. The County/Metro research into fire-fighting suppressive capacity and the impact on building fire damage at >5000 UK building fires, 2009–2012. Fire Safety Journal. 2015. No. 1. Pp. 238–247. DOI: 10.1016/j.firesaf.20-14.11.027
10. Task Force Tips: firefighter equipment. [Online]. URL: https://www.tft.com/Product-Series/Dual-Force (date of application: 25.03.2020)
11. POK: firefighter equipment. [Online]. URL: https://www.pok.fr/en/catalogues-2 (date of application: 25.03.2020)
12. Acron Brass Company. [Online]. URL: https://www.akronbrass.com (date of application: 25.03.2020)
13. Yone corporation. [Online]. URL: https://www.yone-co.co.jp/english (date of application: 25.03.2020)
14. R. Pons – The safety of the people and the goods. [Online]. URL: http://www.r-pons.com/en (date of application: 25.03.2020)
15. Delta Fire – World Class Fire-fighting. [Online]. URL: https://www.deltafire.co.uk (date of application: 25.03.2020)
16. Rosenbauer. [Online]. URL: https://www.rosenbauer.com/de/int/world (date of application: 25.03.2020)
17. Protek. [Online]. URL: https://www.protekfire.com.tw (date of application: 25.03.2020)
18. Karpenchuk, I.V., Shafranskiy, D.A., Yankevich, N.G. Razrabotka i optimizatsiya gidrodinamicheskikh parametrov otechestvennoy modifikatsii eksperimentalnogo obraztsa stvola ruchnogo pozharnogo universalnogo [Development and optimization of hydrodynamic parameters of the domestic modification of the experimental model of the universal manual fire barrel]. [Online]. Vestnik Komandno-inzhenernogo instituta. 2013. 18(2). Pp. 270–279. (rus). URL: https://journals.ucp.by/in-dex.php/vice/article/view/463 (date of application: 25.03.2020)
19. Kamlyuk, A.N., Parmon, V.V., Morozov, A.A. Raschet i optimizatsiya geometrii protochnogo kanala pozharnogo stvola s raskhodom do 5 l/s [Calculation and optimization of the geometry of the flow channel of the fire barrel with a flow rate of up to 5 l/s]. [Online]. Vestnik Komandno-inzhenernogo instituta. 2016. 23(1). Pp. 51–59. (rus). URL: https://journals.ucp.by/in-dex.php/vice/article/view/539 (date of application: 25.03.2020)
20. Podgrushnyy, A.V., Denisov, A.N., Khong, Ch.D. Sovremennyye problemy tusheniya pozharov v zdaniyakh povyshennoy etazhnosti i vysotnykh zdaniyakh [Modern problems of high-rise and high-rise buildings]. [Online]. Pozharovzryvobezopasnost. 2007. 16(6). Pp. 53–57. (rus). URL: https://www.elibrary.ru/item.asp?id=12513091 (date of application: 25.03.2020)
21. Kopylov, N.P., Pivovarov, V.V., Pronin, D.G. Ensuring the safety of people in residential high-rise buildings. Fire and Explosion Safety. 2017. 26(9). Pp. 5–14. DOI: 10.18322/PVB.2017.26.09.5-14
22. Zelenkov, S.A., Podgrushnyy, A.V., Denisov, A.N., Bordik, R.I. Combined method of extinguishing fires in high-rise buildings using hose-pump high pressure system. Fire and Explosion Safety. 2017. 26(8). Pp. 56–64. DOI: 10.18322/PVB.2017.2-6.08.56-64
23. Karama, Ye.A., Arkanov, P.V., Dyakov, M.V. Sposoby podachi ognetushashchikh veshchestv po nasosno-rukavnym sistemam v vysotnyye zdaniya [Methods of supplying fire extinguishing substances through pump-hose systems to high-rise buildings]. Tekhnosfernaya bezopasnost. 2016. 11(2). Pp. 61–66. (rus). URL: https://www.elibrary.ru/item.asp?id=26293012 (date of application: 25.03.2020)
24. Kamlyuk, A.N., Grachulin, A.V. Kompressionnaya pena dlya nuzhd pozharnykh podrazdeleniy [Compression foam for the needs of fire departments]. Minsk: UCP, 2019. 224 p. (rus). ISBN 978-985-590-050-5
25. Kamlyuk, A.N., Navrotskiy, O.D., Grachulin, A.V. Fire extinguishing by compressed air foam systems. Journal of Civil Protection. 2017. No. 1. Pp. 44–53. (rus). DOI: 10.33408/2519-237X.2017.1-1

26. Sistema standartov pozharnoy bezopasnosti. Razvetvleniya rukavnyye. Tekhnicheskiye usloviya [Fire safety standards system. Branching hoses. Specifications]. [Online] URL: https://files.stroyinf.ru/Data2/1/4293724/4293724932.pdf (date of application: 25.03.2020). (rus)
27. Parmon, V.V., Andrey, K.N., Volchek, Y.S., Asilbeyli, R.R., Morozov, A.A. Experimental investigations of the fire barell SPRUK 50/0,7 «Viking» when supplying water. Journal of Civil Protection. 2017. No. 2. Pp. 159–166. (rus). DOI: 10.33408/2519-237X.2017.1-2

Contacts:

Artsiom Marozau, morozow974@gmail.com

Hoan Tran Duc, websitet34@yahoo.com.vn

Andrei Kamluk, kan@ucp.by

Valerij Parmon, niipb@yahoo.ru

Marina Striganova, striganovam@tut.by

© Marozau, A., Tran Duc, H., Kamluk, A., Parmon, V., Striganova, M., 2021

Magazine of Civil Engineering

ISSN 2712-8172

journal homepage: http://engstroy.spbstu.ru/

DOI: 10.34910/MCE.103.6

Mechanical safety of reinforced concrete frames under complex emergency actions

A.V. Alekseytsev
National Research Moscow State Civil Engineering University, Moscow, Russia
E-mail: aalexw@mail.ru

Keywords: reinforced concrete, dynamic behaviour, impact loading, column removal, progressive collapse, risk, safety, frames, nonlinear analysis

Abstract. An approach to the calculation of the frame reinforced concrete structures taking into account the potential risk of financial losses in an emergency is proposed. The simplified conditions for the strength of structural components considering the potential relative risk of the financial losses for the structure during emergency failure of these components is formulated. The strain-stress state analysis using the finite element method based on bar models can be performed in dynamics. The reinforced concrete structural component in the form of a package of concrete and reinforcement layers that can be deformed according to actual diagrams approximated by piecewise linear functions. The calculations were considered by accounting geometric, structural and physical nonlinearity. As an example, illustrating the operability of the presented approach, were considered the frame of the building with several scenarios for emergency actions. This is a complete or partial exclusion of one column from the calculation model, accompanied by a horizontal impact. The exclusion of 0.75 and 0.5 parts of the cross section of the column as well as its complete exclusion, accompanied by a horizontal impact pulse were examined. A collision of a damaged structure with a rigid barrier and with a deformable base were simulated. The proposed approaches to modeling the stress-strain state and strength conditions of the bar reinforced concrete systems have prospects for using in algorithms of optimum parametric synthesis of structures based on metaheuristic approaches.

1. Introduction

The safety of frame reinforced concrete structures of civil buildings and structures under mechanical emergency actions is investigated. To assess the stress-strain state, structural dynamics analysis is used taking into account physical, geometric and structural nonlinearities. In addition, the risk of local damage is taken into account.

In relation to the safety issue, many studies are devoted to the design of structures taking into account resistance to progressive collapse [1–3]. Many researchers considered the objective of ensuring the mechanical safety of building structures, in this case they studied the stability of the load-bearing structure to damages, including as a result of the impacts [4–10]. They examined the processes of deformation of a damaged system as well as the preservation of its geometrical invariability. At the same time, the sustainability (survivability) of the system should be ensured for the time necessary for the evacuation of people or equipment, and the shape of the deformed system should allow performing the evacuation. The most frequent local damage was the rapid removal of one of the column supports or pillars of the structure [11–14, 45]. One of the important objectives to be solved when assessing both the safety and the economic efficiency of the structural system is to take into account the nature of local damage that occurs during man-made actions and natural-climatic effects on operating buildings [15–17]. In most studies, in case of structural damage support bracing or columns is completely removed [18–20]. The force effect that caused the damage is also practically not considered. In fact, during structure failures, a case of collision of a damaged structure with a barrier often occurs. However, some of these barriers may collapse, and some may not. A characteristic case is a partial putting out of operation of the supporting component. Some illustrations of such failures are shown in Fig. 1.

Alekseytsev, A.V. Mechanical safety of reinforced concrete frames under complex emergency actions. Magazine of Civil Engineering. 2021. 103(3). Article No. 10306. DOI: 10.34910/MCE.103.6

This work is licensed under a CC BY-NC 4.0

Figure 1. Emergency actions on structures: a) impact with preservation of static force after action; b) local damage with partial exclusion of the pillar from work; c) the complete exclusion of the column, followed by the interaction of the structure with the deformable barrier; d) local damage without removing of the element.

In a number of works, experimental and theoretical studies were carried out in which a single local damage was considered in different parts of the structure. However, depending on the required level of structural safety, it may be necessary to take into account two, and three or more local damages [21–23]. Moreover, their occurrence may be dependent or independent of each other. Consideration of all these factors can significantly adjust the design results. As a rule, local structural damage that causes localized or progressive destruction is associated with socio-economic losses. At the same time, when calculating and optimizing structures, it is necessary to take into account reasonable safety factors [24, 25]. As a result of excessive resource saving, a less reliable and safe design can be obtained, the failure of which will cause large losses, that, in our opinion, is unacceptable. Therefore, along with the assessment of the conditions of strength, stiffness and stability for structures with a higher level of safety, it is necessary to apply criteria related to the risk assessment of such systems [26–30] and optimization of their parameters [31, 32]. One of the common types of load-bearing structures affected by loads not provided for normal operation are reinforced concrete frames and floor and roof slabs [33–35]. These structures in case of mechanical, high temperature and corrosion damage were studied.

Modern methods for calculating the load-bearing structures of buildings involve checking the requirements for the ultimate limit states. These requirements comprise satisfying inequalities such as $F<F_{ult}$, $f<f_{ult}$, etc. [36–40], where F, f are the calculated values of the force, deflection, etc., and F_{ult}, f are the limit values these variables, corresponding to the normal operation of the facility. Such an approach is described in regulatory documents; however, current socio-economic conditions show that this approach to design does not always ensure mechanical safety of structures. Therefore, improving methods for analyzing the stress-strain state and methods for assessing risks in the design of reinforced concrete structures is now especially important. The issue of modeling deformations of reinforced concrete frame structures during emergency under complex design conditions is also relevant. The proposed calculation models can be used both for optimum [41] and for traditional design of load-bearing structures for civil buildings [42, 43].

The purpose of research is to ensure the mechanical safety of reinforced concrete frame structures in complex emergency actions. This involves solving the following main tasks:

- the development of an approach to modeling deformations of structural systems with incomplete removal from load scheme of a damaged element, as well as taking into account the presence of barriers and interaction with them;
- taking into account local damage in the presence of a horizontal shock load, as well as in the presence of a foundation on deformable soil;
- the proposal to take into account the risks of the socio-economic consequences of an emergency.

2. Methods

2.1. Operation conditions for the load-bearing structures of buildings with an increased level of social responsibility

2.1.1. Strength conditions

The constraints of strength to ensure the mechanical safety of buildings and structures is formulated, accidents in which can lead to serious social consequences as well as for facilities that are strategically important for the development of the state. Analysis of numerous accidents and disasters associated with the destruction of buildings and structures has showed that progressive collapse is unacceptable for the facilities under consideration. According to this, we introduce the assumption that destruction in such facilities can lead to financial loss equal to n-times cost of the destroyed structure. Then the condition for ensuring the strength of structural systems can be written as follows:

$$\left(\frac{|\Omega|}{\Omega_{ult}} - r\right) \le 1;\ r = \frac{pU}{C}. \tag{1}$$

Where Ω is the internal force factor characterizing the mechanical stresses of the structure material; Ω_{ult} is the calculated (limit) value of Ω, r is the relative risk associated with the emergency, provided that it has occurred with probability p; C is the cost of the damaged structure, U is the amount of financial loss (cost) associated with damage to the other structures within the localization area of destruction.

In the formula (1) in a particular case, for example, for calculating steel structures, the value of the equivalent stress according to Mises maximum-strain-energy of failure can be taken as Ω, and the value of the design steel resistance can be taken as Ω_{ult}. Similarly, to calculate reinforced concrete structures, for example, according to normal sections under bending or sloping sections under the action of a transverse force, we can write:

$$\left(\frac{|M|}{M_{ult}} - r\right) \le 1;\quad \left(\frac{|Q|}{Q_b + Q_{sw}} - r\right) \le 1; \tag{2}$$

where M, Q are the internal forces in cross section; M_{ult} is the ultimate moment perceived by reinforced concrete section; Q_b, Q_{sw} are transverse (shear) forces perceived by concrete and reinforcement.

2.1.2. Deflection conditions

When assessing the stiffness of structures, first of all it means their ability not to show unacceptably large changes in geometry, determined by deflection $[f]$. In this case, even with local affecting adversely the strength of individual components, the condition of resistance to structural failure must be fulfilled. These changes in geometry should provide the ability to evacuate people and equipment from the building. As an example, we write the deflection condition for a multistoried building having floor-to-floor heights of 3 m and 4.2 m as follows:

$$f \le [f] = \begin{cases} 0.3H,\ (2.5 \le \mathrm{H} \le 3.2) \\ 0.5H,\ (3.2 < \mathrm{H} \le 4.6) \\ l/30,\ l \ge 12 \end{cases}, \tag{3}$$

where f, H, l (m) is the deflection of the structure the height of the floor and the span of the damages structure, respectively.

2.1.3. Buckling condition

The stability condition is formulated, similar to the strength condition, as an inequation into which the relative risk value is introduced to increase the structural stability margin:

$$\left(\frac{n}{n_{ult}} - r\right) \le 1; \tag{4}$$

where n, n_{ult} are the actual and limiting factors of buckling margin, respectively.

The probability of failure p during action associated with the occurrence of an emergency for facilities of industrial and civil construction is recommended to be taken in the range of 0.01–0.05. If the object belongs to the strategic military infrastructure facilities, then this probability can be increased to 0.5. It should be noted that for buildings not related to objects of strategic and social importance, the risk r cannot be taken into account, since the probability of failure for the structure, considering only its normal operation in such buildings, is (10^{-5}–10^{-7}), then $r \to 0$.

2.2. Finite-element modeling of local damage for engineering calculations and optimization algorithms in accidental situation

2.2.1. Formulation of structural analysis problems

In course of many studies of structural resistance to the progressive collapse during accidental exposures we have considered the quick removal of support bracing for one of the columns from the calculation model. In this case, the reason for this removal and the further interaction of the damaged and undamaged structure are hardly considered. Local damage is often examined without regard to the presence of a deformable ground. Let us consider the following simplified techniques for modeling the interaction of a damaged structure within the finite-element method:

- the complete exclusion of the element from the calculation model with a horizontal impact;
- the partial exclusion of the element from the calculation model with a horizontal impact;
- contact interaction of a damaged structure with an indestructible barrier;
- contact interaction of a damaged structure with a destructible barrier.

The modeling is performed for indicated types of local damages with finite element models using the bar elements with the possibility of taking into account structural-nonlinear behavior. We will perform the stress-strain analysis of the structure in dynamics based on numerical integration of the differential equation system for displacements of the damaged system, taking into account the simplified Rayleigh damping calculation model:

$$[M]\left(\alpha\dot{y}(t)+\ddot{y}(t)\right)+[K]\left(\beta\dot{y}(t)+y(t)\right)=F(t)+G\chi(t);\ \chi(t)=\begin{cases}0, t<t_0\\ 1, t\geq t_0\end{cases}, \tag{5}$$

where $[M],[K]$ are the global matrices of mass and stiffness of the finite element model, respectively; $\ddot{y}(t)$, $\dot{y}(t)$, $y(t)$ are the vectors of accelerations, velocities and nodal displacements, respectively; $F(t)$ is the vector of the external load reduced to the nodes, G is the vector of impactor gravity forces, $\chi(t)$ is the Heaviside function, t_0 is the time moment after which the gravity should be taken into account, G; α, β are inertial and structural damping ratios. The case is considered when $\alpha=0$, the coefficient $\beta=0.04-0.07$. The Newmark recurrence scheme is used.

2.2.2. The model of deformations with the complete exclusion of an element with a horizontal impact

The support model is shown in Fig. 2.

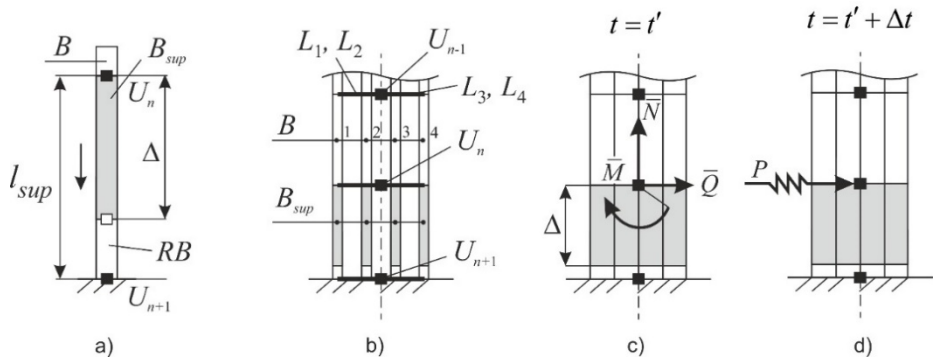

Figure 2. Modeling the support exclusion during emergency exposure: contact element (a); column support modelling (b); static equilibrium before emergency action (c); horizontal impact modelling (d).

Here, the elements $L_1 - L_4$ are rigid beams that define the eccentricities of the longitudinal axes of the bar elements B relative to the nodes U. Time moment t' is the point in time after which the the static equivalents of internal forces removing and applying the shock effect to the structure.

Let us introduce a spatial bar finite element $B_{\sup}$ having a length $l_{\sup}$, between nodes U_n, U_{n+1}, while one of the nodes must be fixed against displacements, and the other connected to the spatial rod B, modeling the structure (Fig. 2, a). It is provided for possibility to set the gap Δ, modeled by low stiffness. The value of this gap should be calculated based on the accepted height of the column section, which is removed from operation. When the formal task is started, deformation by the size of the gap occurs, and then deformation begins on the fragment of the bar RB, which may have stiffness, simulating a solid object or an elastic-plastic deformable soil base. Modeling the complete exclusion of the support is performed in the following sequence:

- the static equivalents attached of internal forces to the node U_n, in the general case $\bar{M}, \bar{Q}, \bar{N}$, of equal to the support reactions. When calculating in dynamics, these forces are considered suddenly applied;
- the dynamic calculation begins in the time interval $[0; t']$, where t' is the time moment of dynamic relaxation, that is, the time during which the oscillations of the system with applied static equivalents $\bar{M}, \bar{Q}, \bar{N}$ are completely damped (Fig. 2, c);
- at the next moment of time $t' + \Delta t$ the forces $\bar{M}, \bar{Q}, \bar{N}$ are assumed to be zero, and in the same node a horizontal impact force appears, which is defined as $P = mkG$, where m is the mass of the impactor, kG is the mass acceleration, m, k is the specified coefficient, G is the gravity acceleration. Formalization of the presence and absence of these forces is carried out by determining the functions shown in Fig. 3.

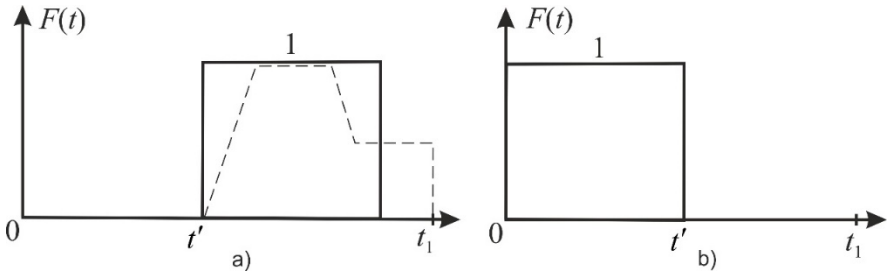

Figure 3. Functions for force P (a) and forces $\bar{M}, \bar{Q}, \bar{N}$ (b).

The dotted line in Fig. 3 shows a possible graph form for an impact pulse, a part of which is preserved after the maximum impact. Modeling of such a process corresponds to the action shown in Fig. 1, a.

2.2.3. Deformation model with partial exclusion of an element cross-section with a horizontal impact

To exclude support partially in case of local damage between nodes U_n, U_{n+1} it is introduced several elements on rigid consoles. In Fig. 2, four elements with consoles $L_1 - L_4$ are shown. For example, with the introduction of four elements of the same rigidity, it is possible to simulate the exclusion of 0.25 part of the section, if three elements B and one extreme element $B_{\sup}$ are introduced between the nodes under consideration. Accordingly, by increasing the number of elements $B_{\sup}$, it is possible to simulate the exclusion of 0.5 and 0.75 parts of the section.

2.2.4. Contact interaction of a damaged structure with an indestructible barrier

The deformation model is described by the diagram shown in Fig. 4, c. This diagram is set for the final element $B_{\sup}$, while the structural element "column" has a damaged section of length $l_{dam} = \varepsilon_0 l_{\sup}$, (Fig. 4 a, c).

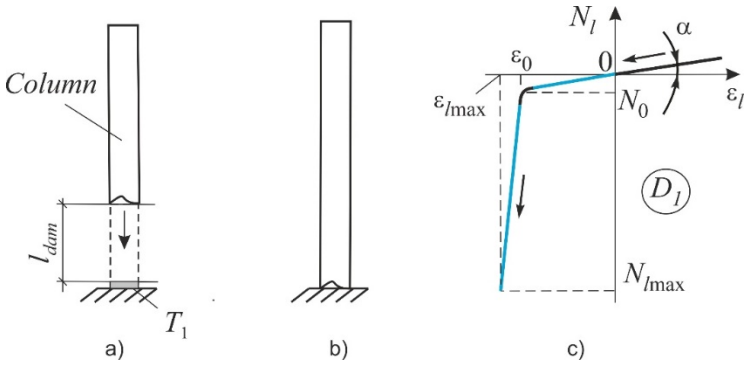

Figure 4. Modeling interaction with an indestructible barrier: the column exists before contact interaction with the barrier (a); the column is present after this interaction (b) the contact modeling diagram (c).

The segment of the diagram, limited by points $(\varepsilon_0; N_0)$ and $(\varepsilon_{l\max}; N_{l\max})$ determines the presence of a barrier T_1, which at large values $N_{l\max}$ can be approximately considered rigid. The deformations of the bar in this section correspond to the situation shown in Fig. 4, b. The parameter α in the diagram is a small number that ensures the stability of the numerical integration procedure; this parameter is the angle in radians varies between 0.01–0.1 depending on the type of chart.

At the point $(\varepsilon_0; N_0)$, the diagram has a rounding, which is also necessary to ensure the stability of the dynamic analysis procedure, where ε_0 is fictitious relative deformations of the contact element corresponding to the size of the damaged part of the rod that is loss. The Value N_0 is a fictitious small value of the longitudinal force, set equal to 10-100 N, which can be interpreted as the conditional resistance of the environment during deformation from the moment of local damage to contact interaction with the barrier.

Values $\varepsilon_{l\max}; N_{l\max}$ are relative deformation and longitudinal force arising from contact with an infinitely rigid barrier. In each computing process, these parameters are selected individually, but as the initial approximation for calculating frame structures, you can specify $\varepsilon_{l\max} \approx 1.02\varepsilon_0; N_{l\max} \approx 10^3 - 10^4 R_{\max}$, where $R_{\max}$ is the module of the maximum vertical support reaction for the calculated system.

2.2.5. Contact interaction of a damaged structure with a destructible barrier

The deformation process consists of the following stages:

- collision with a deformable barrier T_2. In this case, the final element has absolute shortening Δl_{01} (Fig. 5, a) at the value N_0 of the longitudinal force (segment 0;0 – $(\varepsilon_{01}; N_0)$ in the diagram of Fig. 5, d), which corresponds to the position of the structure in Fig. 5, b;
- deformation of the barrier T_2. The segment with the projection of its relative deformation determines the load-bearing capacity of this barrier ε_{br}. In this case, the ultimate longitudinal force that the barrier can withstand is equal N_{br}.
- destruction of the barrier and displacement before contact with the barrier T_1. In this case, the bar has relative shortening Δl_{02}, which corresponds to a length segment ε_{02}. Distances δ are fictitious small relative deformations that ensure the stability of the process of numerical integration. The last linear section of the diagram simulates the stiffness of the barrier T_1, considered rigid. The final position of the bar corresponds to Fig. 5, c.

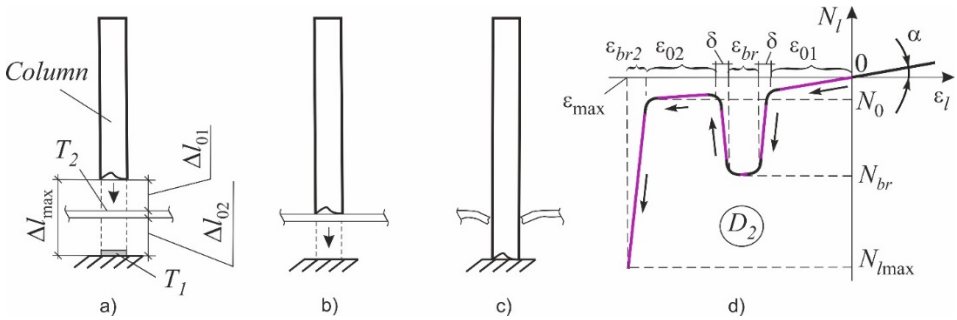

Figure 5. Modeling the interaction with destructible and indestructible barriers: structure after their part removing (a), T_1, T_2 – marks of the barriers; stages of interaction (b), (c); chart of modelling the barrier T_2 destruction; D_2 – diagram labeling.

The α parameter is the same as in Fig. 4. The maximum deformations $\varepsilon_{\max}$ of the contact element (Fig. 5) are the sum of: $\varepsilon_{\max} = 2\delta + \varepsilon_{01} + \varepsilon_{02} + \varepsilon_{br} + \varepsilon_{br2}$. The value ε_{br2} is the infinitesimal deformation of the barrier T_1. The value of the force N_0 is close to zero, it is approximately equal to the resistance of the environment on the segments Δl_{01} and Δl_{02}.

2.3. Finite-element modeling of reinforced concrete structures with local damage

2.3.1. Modeling damage that does not progress after local action

The deformation modeling the reinforced concrete beams is represented as a package of concrete layers C_b and reinforcing layers C_r (Fig. 6, a). In general, for the cross section, the Bernoulli hypothesis and the assumption that the layers do not exert pressure on each other are fulfilled. The implementation of such a model can be carried out by constructing a stiffness matrix for the element, taking into account the fact that each layer can have tension-compression strains. To modeling the deformations of reinforced concrete columns, parts of which can be excluded in the calculation process, another model is used (Fig. 6, b).

The cross-section is divided into parts 1-4, presented in the form of separate bars with common nodes. The position of these bars is determined by the length of the consoles defined by the projections y_b, z_b, y_r, z_r in the local axes of the element. For those elements that will be partially or fully susceptible to local damage, it may be possible to be operated according to the diagram D_1 (Fig. 4, c).

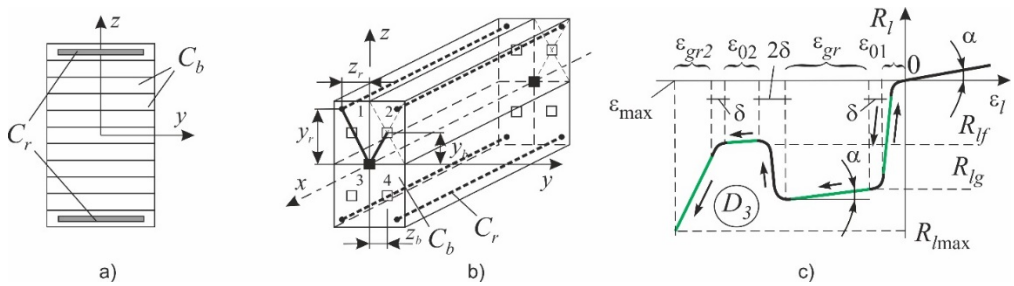

Figure 6. Modeling of deformation of reinforced concrete beams (a), columns (b) and soil foundation (c).

A simplified diagram of the deformation of the soil base (Fig. 6, c) can be described using the following sections. The first is determined by the point $(\varepsilon_{01}; R_{lg})$, ε_{01} where are the relative elastic deformations of the soil, R_{lg} is the calculated resistance to compression of the soil base. Further, the soil is deformed plastically and receives deformations ε_{gr}. The site corresponding to the level R_{lf} of stresses in the soil and deformations ε_{02} models the fail of the soil base associated with the loss of bearing capacity. This can happen if there are fluid lenses, karst cavities, etc. in the ground. Deformation $\varepsilon_{\max}$ here simulate the presence of incompressible soil, $\varepsilon_{\max} = 4\delta + \varepsilon_{01} + \varepsilon_{02} + \varepsilon_{gr} + \varepsilon_{gr2}$.

For the remaining elements, deformation diagrams are set that correspond to the operation of concrete and reinforcement under load. These diagrams for reinforcement and concrete, respectively, are presented in Fig. 7, a,b. The lines shown in black on these diagrams are introduced to ensure the stability of the process of numerical integration of equations (5). The magnitude of the forces and deformations $N_{s0}, \varepsilon_{s0}, \varepsilon_{s1}, N_{b1}, \varepsilon_{b1}, \varepsilon_{b2}, N_{bt}, \varepsilon_{bt}$ are determined depending on the class of concrete and reinforcement approved in the design of the structure. Fig. 7, c-f shows the model of the supporting part of the reinforced concrete column when considering the possibility of destruction 0.25, 0.5 and 0.75 parts of the concrete section. In each of these cases, an operation diagram D_1 is introduced for the one element or several elements to be excluded (Fig. 4).

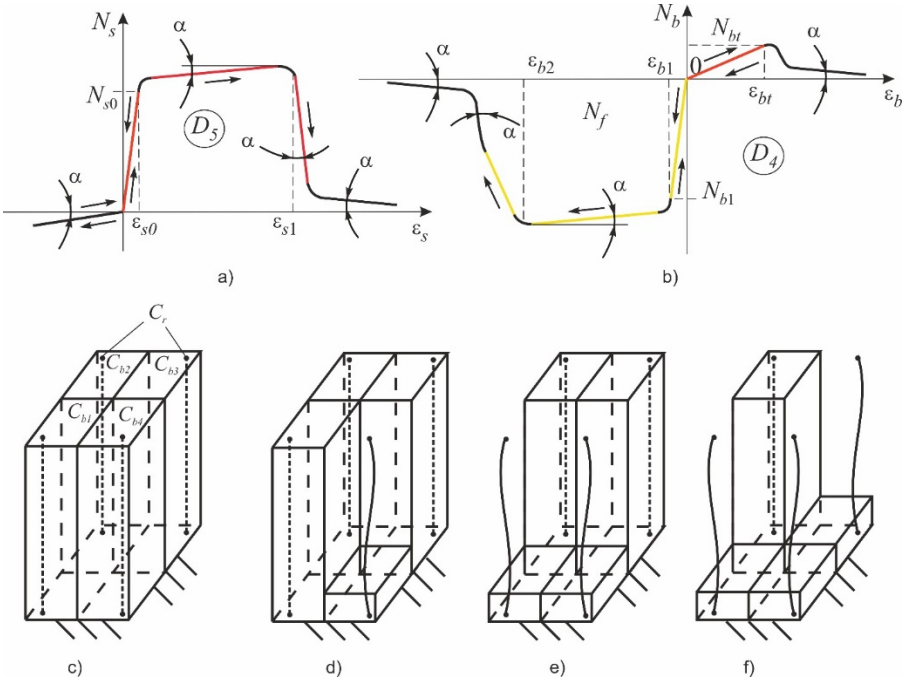

Figure 7. Diagrams of deformation of steel (a) and concrete (b) and a model of partial damage to the column: without damages (c), damage of a quarter (d), half (e) and three quarters (f) of column segment.

2.3.2. Progressive local damages

The structure of concrete makes it possible for propagating local damages to occur both during and after emergency action. These effects can be approximately modeled by dynamic calculations of damaged systems, taking into account structural nonlinearity in the operation of a part of the cross-section exposed to local effects. One of the common cases of such effects is mechanical damage to the column, for example, in a collision with a car or other moving deformable object. In the case of an angular collision (Fig. 8, a) or a frontal impact (Fig. 8, b), it is possible to approximately model the progressive collapse of the parts of the column that are shaded in gray. In a more general case, for example, with accumulated defects as a result of long-term operation, a local impact can initiate the exclusion of the outer layers of the column while maintaining the operability of the inner core (Fig. 8, c, Fig. 1, b). Modeling the exclusion of a cross section quarter from a concrete column in time will be shown using the example of Fig. 8, d, e. The cross section of the column is modeled by seven beam elements. Three of them, the cross sections of which are shown by squares without filling, are modeled by ordinary spatial bars, for which the operation diagram D_4 is provided. Bars with cross-sections 1-4 (Fig. 8, d) are contact elements that operate according to the diagram D_1. Initially, these elements are balanced by the static equivalents of the reactions $\bar{N}_1 - \bar{N}_4$, perceived by the quarter section. All these forces act during the relaxation time $[0;t']$. Then the force $\bar{N}_1$, acting over time $[t';t_1']$ is permanently equal to zero and does not act within the time interval $(t_1';t_1]$ (Fig. 8, e). The remaining forces $\bar{N}_2 - \bar{N}_4$ continue to operate. The time $[t_1';t_2']$ can be short, which approximately corresponds to the propagation time of local damage in the material. Further, the force $\bar{N}_2$ at time moment t_2' is removed similarly to the force $\bar{N}_1$. The process is repeated until the exclusion of

force $\overline{N}_4$. By the same scheme, it is possible to simulate the exclusion of any parts of the cross sections under various influences, for example, during impacts shown in Fig. 8, a, b.

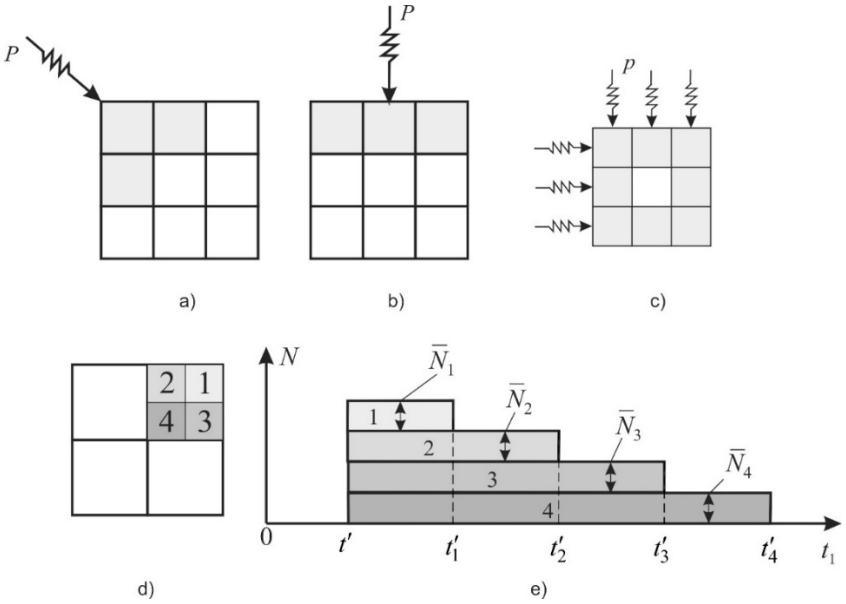

Figure 8. Modeling the exclusion of part of the cross sections of bar elements: (a)-(c) variants of emergency actions and damages volumes; sequence of emergency destruction the cross section material (d); time history of emergency action process (e).

The process of deformations propagation after local damage for reinforced concrete sections is a very difficult phenomenon for modeling, which depends on the type of emergency action, on the pre-emergency loading of the section, on the structure and percent of concrete reinforcement. According to many studies, the rate of deformations during impacts for concrete structures of columns varies within wide limits $\dot{\varepsilon} = 10^{-6} \div 10^{2}$ 1/sec, and the time of destruction of sections $\tilde{t}_d = 0.5 - 14$ ms. Initially, on the basis of experimental data or numerical simulation, the time t_d of complete exclusion of a part of the section from work is determined. With an equal area of the excluded elements, the intervals $t_1 - t_4$ are approximately equal:

$$t_1[t'_1;t'] = t_2[t'_2;t'_1] = t_3[t'_3;t'_2] = t_4[t'_4;t'_3] = t_d / 4 \tag{6}$$

With an unequal area, the size of the intervals is determined by the formula:

$$t_d = \frac{s_1}{s_d} t_1[t'_1;t'] + \frac{s_2}{s_d} t_2[t'_2;t'_1] + \frac{s_3}{s_d} t_3[t'_3;t'_2] + \frac{s_4}{s_d} t_4[t'_4;t'_3], \tag{7}$$

where $s_1 - s_4$ are the areas of elements 1-4 on Fig. 8., s_d is the area of the entire part of the excluded section.

3. Results and Discussion

3.1. Description of the object calculation model

The reinforced concrete frame of the building is considered, shown in Fig. 9. Three design cases are considered:

- *Case 1. "Calculation of a plane frame on a foundation slab (interaction with an indestructible barrier)"*. We performed the support exclusion modeling using the diagram B1 on Fig. 9. At the same time, the parameters of the GAP element provided a gap of 15 cm, after which the system interacted with the element having stiffness exceeding 1,000 times stiffness of the column. The gap is assigned on the condition that it should be less than the length of the contact element, that is, 0.5 m. Some results of dynamic analysis are presented in Fig. 11 a, c, d. The abscissa axis shows the calculation numbers corresponding to the integration step.

- *Case 2. "Calculation when excluding the support without contact interaction".* This calculation was performed according to the well-known scheme described in many papers, but taking into account the horizontal impact interaction. Some data on system displacements are shown in Fig. 11. b, d. Obviously, these oscillations of the system are abstract in nature. Fig. 11, d shows that the deflection of the crossbars during contact interaction (with the exception of a fragment of a structure measuring 15 cm) is less than during oscillations without contact constraints.
- *Case 3. "Calculation of the frame on an inelastic soil, taking into account the partial exclusion of the middle pillar".* The exclusion of 0.75 and 0.5 parts of the column section is modeled. We denote these scenarios as S1 and S2. Soil was taken in the form of clay with porosity ratio of 0.5 and index of liquidity as IL = 1. It was supposed that under each support there is a square foundation of 2.5 m wide with a depth of 2 m. Soil deformations are described by a diagram D_3 in Fig. 6, c at R_{lf} = R_{lg} = 430 kPa. In case of removal of 0.75 part of the cross section, the remaining part of the section quickly collapsed. The time for excluding parts of the cross sections was taken equal: $t_{d,075}$ = 7.5 ms, $t_{d,05}$ = 5 ms. Fig. 13 shows some calculation results. With the exclusion of part of the column, significant displacements from the plane of the frame are observed, which is a sign of the need to take into account the survivability of the structure as a whole, considering its spatial deformation.

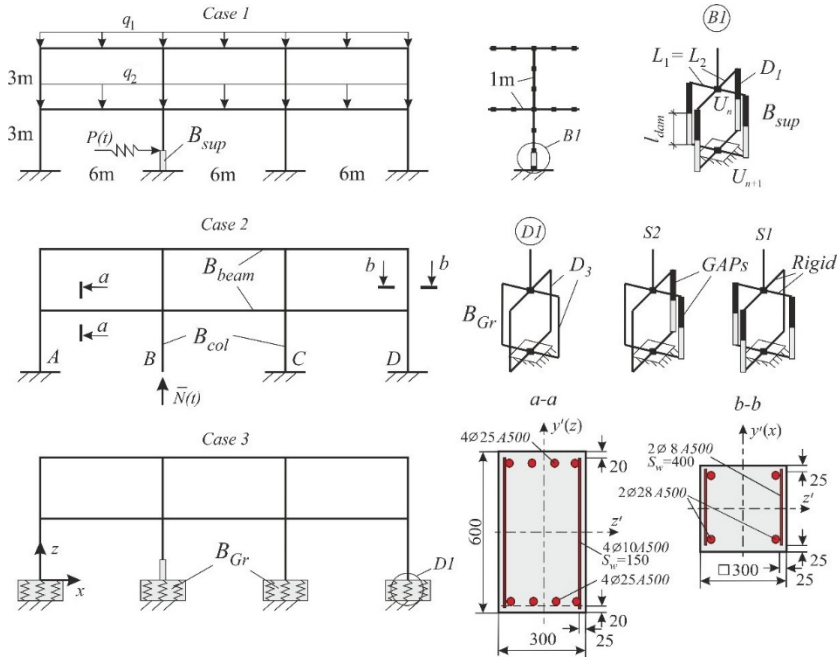

Figure 9. An example of the calculation of a reinforced concrete frame: load scheme (a) and stress-strain state modelling (b); B_{beam}, B_{col} – finite element packages for rigel and column modelling shown in Fig. 6, a, b; B_{sup}, B_{Gr} – same packages for support and soil modelling.

The calculation was performed using the Femap software package with the NX Nastran solver. Module «Nonlinear Transient Response» is used. The integration step was selected automatically. It was assumed q_1 = 18 kN/m, q_2 = 24 kN/m, $P(t) = Pf_1(t)$, see Fig. 9, 10, a. The constraint force in the removed element changes $R(t) = R_{st}f_2(t)$, see Fig. 10, b. P = 80 kN, R_{st} is the reaction (axial forces, bending moments, shear forces) selected taking into account the static calculation. Concrete has design compression resistance of 25 MPa, tensile strength of 1.45 MPa. The reinforcement has design resistance of 450 MPa. Physically nonlinear operation on D_4, D_5 diagrams was taken into account for these materials. The transient nonlinear dynamic process had duration of 5 sec, after 2 sec, in event of the structure with the barrier interaction, the oscillations completely damped. If there was no contact interaction, the oscillations were observed for 4 sec. Therefore, the abscissa axis in Fig. 10 are limited to 4.1. The dynamic relaxation time after application of the load was taken to be 1 s. Overall structural damping with a ratio equal 0.05 was taken into account.

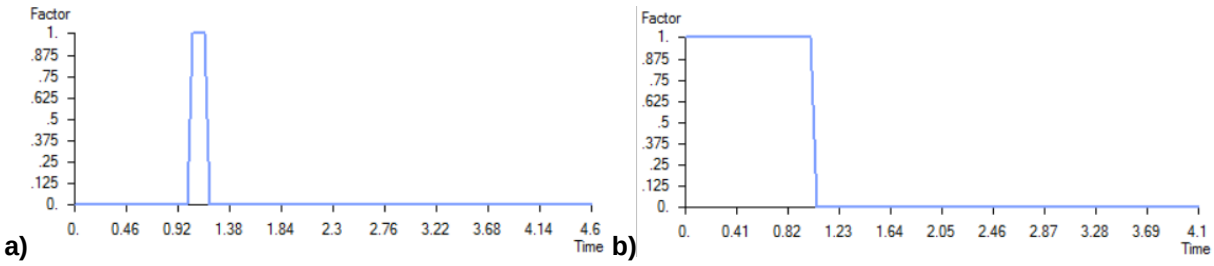

Figure 10. The form of the functions $f_1(t)$ (a) and $f_2(t)$ (b).

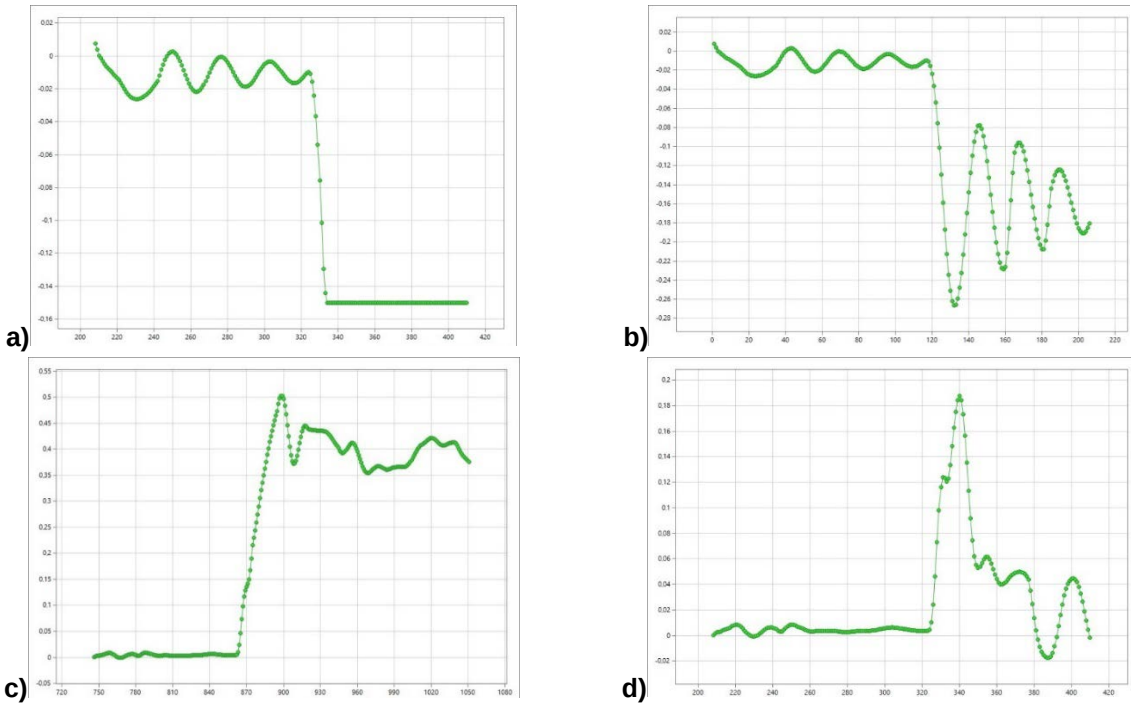

Figure 11. Dependence on the displacements in the time: a) vertical displacements of the damaged end part of the column upon impact with a barrier; b) the same without considering the contact interaction; c) horizontal movements when exposed to horizontal impact, taking into account contact interaction; d) the same, without contact interaction.

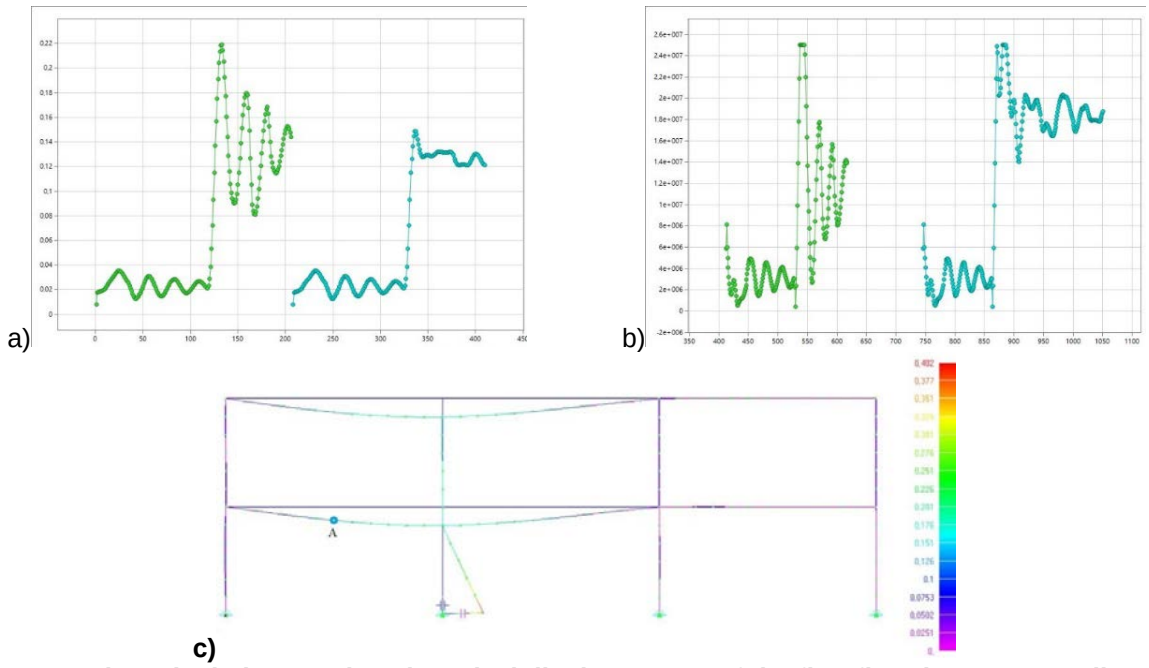

Figure 12. The calculation results: a) vertical displacements of the first floor beam at 3 m distance from the leftmost support (point A) without contact interaction (left) and with it (right); b) compression stress in concrete (in modulus) at point A; c) deformed frame layout after horizontal impact and taking into account contact interaction.

3.2. Example of calculating a structural component taking into account the risks of financial losses

As financial loss U in the formula (1), we take into account components in which deformations occur equal or close to ultimate fracture deformations. It is assumed that the probability of emergency action to be p = 0.8, which means that it will happen rather than not. Designing an intact middle column were performed. As a complete structure, only the frame in question were considered. During normal operation, the cross-sectional area is determined primarily by structural requirements, and the operational compression stresses in concrete are in modulus about 6 MPa, $\Omega = 6MPa$, $\Omega_{ult} = 25MPa$. In case of local destruction, including the Case 1 scenario, while ensuring survivability, beams of the 1st and 2nd floors in 2 spans and the middle column on each floor can fail. Then conditionally the damage can be calculated as the ratio of the lengths of the components $r = 0.8 \cdot 30 / 60 = 0.4$, $\Omega / \Omega_{ult} =$ 6/25=0.24. Then, according to the formula (1): 0.24+0.4=0.64≤1, the condition is satisfied. That is, the approved structural solution for the column contains the necessary margin of safety to ensure survivability with an emergency action the probability of occurrence of which is 0.8. It should be noted that if the actual margin of safety for the column is less than 36 %: $\Omega / \Omega_{ult} \geq 0.64$, the column would lose strength or stability if the emergency scenario under consideration occurs.

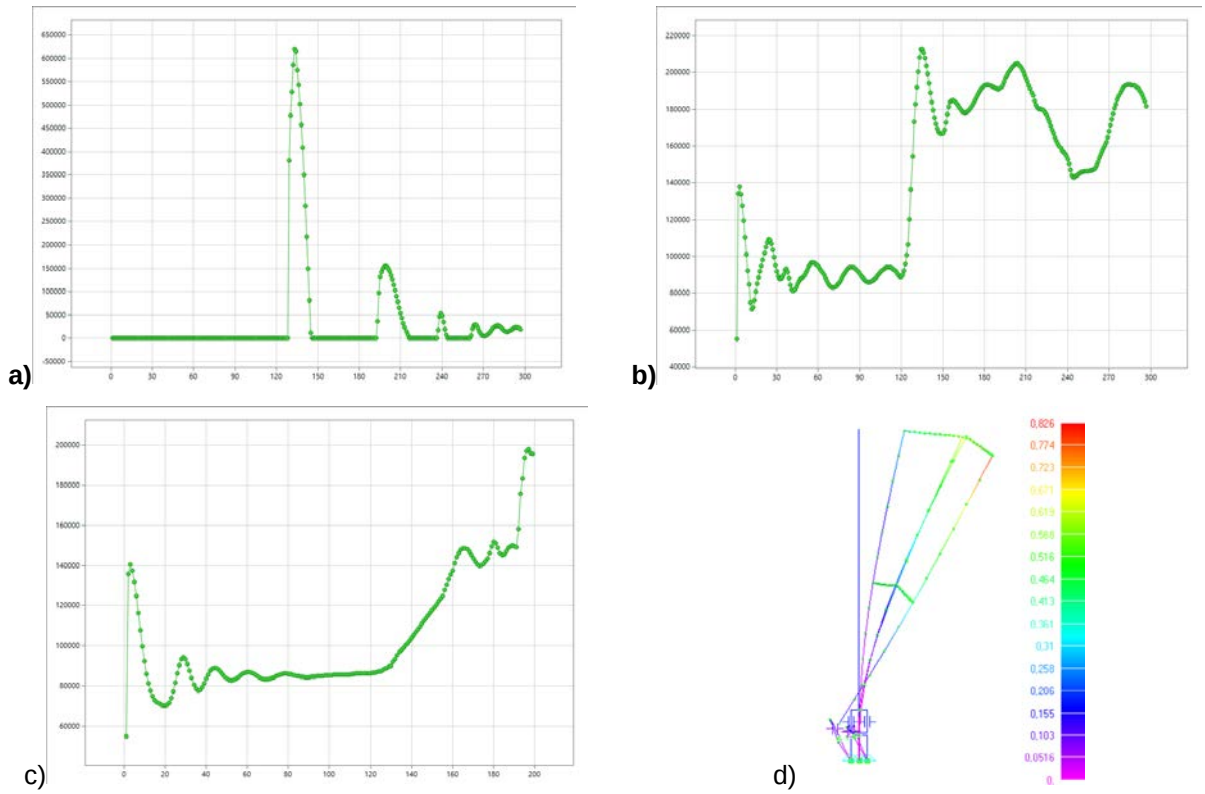

Figure 13. Results of the calculation with partial local damage: a) contact stresses during the interaction of the damaged column with the foundation; b) change in time of the compression stresses in the soil of the middle support (S1); c) the same, but under scenario (S2); d) total translations of the system (view from the plane of the frame)

3.3. Discussion

The proposed deformation modeling methods are simplified, but have an acceptable amount of computation for use in optimization algorithms, for example, [18, 26, 44]. It seems promising to use these models for an approximate assessment of the deformations of reinforced concrete structures under high-temperature effects [25] and a combination of mechanical damage and the action of temperature. Existing approaches to the rapid exclusion of column supports from the calculation model, which do not include consideration of the reasons for this exclusion (for example, horizontal impact, modeling a structure collision with barriers), can significantly distort the picture of the stress-strain state of these structures. In turn, this can affect the provision of mechanical safety in an emergency.

4. Conclusion

1. The methodology for the approximate calculation of the frame reinforced concrete load-bearing structures, which takes into account on equal terms the limiting conditions and risks of financial losses associated with the possible occurrence of an emergency were proposed. This approach can be used to optimize design solutions under constraints associated with the mechanical safety of facilities.

2. For calculation of the stress-strain state of reinforced concrete structures based on the finite element method the alternative simplified approaches were proposed which allow modeling a horizontal impact with the subsequent complete or partial exclusion of part of the concrete cross-section from operation, collision of the damaged structure with a destructible or non-destructible barrier, simplified interaction of the damaged structure with a soil foundation.

References

1. Kokot, S., Anthoine, A., Negro, P., Solomos, G. Static and dynamic analysis of a reinforced concrete flat slab frame building for progressive collapse. 2012. Engineering Structures. 40. Pp. 205–217. DOI: 10.1016/j.engstruct.2012.02.026
2. Serpik, I.N., Alekseytsev, A.V. Optimization of frame structures with possibility of emergency actions. 2013. Magazine of Civil Engineering. 44 (9). DOI: 10.5862/MCE.44.3
3. Qian, K., Zhang, X. De, Fu, F., Li, B. Progressive collapse-resisting mechanisms of planar prestressed concrete frame. 2019. ACI Structural Journal. 116 (4). Pp. 77–90. DOI: 10.14359/51715567
4. Baca, M., Rybak, J., Tamrazyan, A.G., Zyrek, T. in (2016) Int. Multidiscip. Sci. GeoConference Surv. Geol. Min. Ecol. Manag. SGEM. Pp. 945–950. DOI: 10.5593/SGEM2016/B11/S02.119
5. Chen, Y., May, I.M. Reinforced concrete members under drop-weight impacts. 2009. Proceedings of the Institution of Civil Engineers: Structures and Buildings. 162 (1). Pp. 45–56. DOI: 10.1680/stbu.2009.162.1.45
6. Chuzel-Marmot, Y., Ortiz, R., Combescure, A. Three dimensional SPH-FEM gluing for simulation of fast impacts on concrete slabs. 2011. Computers and Structures. 89 (23–24). Pp. 2484–2494. DOI: 10.1016/j.compstruc.2011.06.002
7. Del Linz, P., Fan, S.C., Lee, C.K. Modeling of combined impact and blast loading on reinforced concrete slabs. 2016. Latin American Journal of Solids and Structures. 13 (12). Pp. 2266–2282. DOI: 10.1590/1679-78252516
8. Gokkaya, B.U., Baker, J.W., Deierlein, G.G. Estimation and impacts of model parameter correlation for seismic performance assessment of reinforced concrete structures. 2017. Structural Safety. 69. Pp. 68–78. DOI: 10.1016/j.strusafe.2017.07.005
9. Leppänen, J. Dynamic behaviour of concrete structures subjected to blast and fragment impacts. 2002. … of Structural Engineering, Concrete Structures. Pp. 96. https://www.msb.se/Upload/Insats_och_beredskap/Olycka_kris/Skydds-rum/Litteratur/Akademiska avhandlingar/Dynamic Behaviour of Concrete Structures subjected to Blast and Fragment Impacts.pdf
10. Qasrawi, Y., Heffernan, P.J., Fam, A. Dynamic behaviour of concrete filled FRP tubes subjected to impact loading. 2015. Engineering Structures. 100. Pp. 212–225. DOI: 10.1016/j.engstruct.2015.06.012
11. Weng, J., Tan, K.H., Lee, C.K. Modeling progressive collapse of 2D reinforced concrete frames subject to column removal scenario. 2017. Engineering Structures. 141. Pp. 126–143. DOI: 10.1016/j.engstruct.2017.03.018
12. Yang, T., Han, Z., Deng, N., Chen, W. Collapse responses of concrete frames reinforced with BFRP bars in middle column removal scenario. 2019. Applied Sciences (Switzerland). 9 (20). DOI: 10.3390/app9204436
13. Tamrazyan, A., Alekseytsev, A. Evolutionary optimization of reinforced concrete beams, taking into account design reliability, safety and risks during the emergency loss of supports in (2019) E3S Web Conf. DOI: 10.1051/e3sconf/20199704005
14. Mistri, A., Sarkar, P., Davis, R. Column-beam moment capacity ratio and seismic risk of reinforced concrete frame building. 2019. Proceedings of the Institution of Civil Engineers: Structures and Buildings. 172 (3). Pp. 189–196. DOI: 10.1680/jst-bu.17.00100
15. Lazar Sinković, N., Dolšek, M. Fatality risk and its application to the seismic performance assessment of a building. 2020. Engineering Structures. 205. DOI: 10.1016/j.engstruct.2019.110108
16. Araya-Letelier, G., Parra, P.F., Lopez-Garcia, D., Garcia-Valdes, A., Candia, G., Lagos, R. Collapse risk assessment of a Chilean dual wall-frame reinforced concrete office building. 2019. Engineering Structures. 183. Pp. 770–779. DOI: 10.1016/j.engstruct.2019.01.006
17. Haselton, C.B., Liel, A.B., Deierlein, G.G., Dean, B.S., Chou, J.H. Seismic collapse safety of reinforced concrete buildings. I: Assessment of ductile moment frames. 2011. Journal of Structural Engineering. 137 (4). Pp. 481–491. DOI: 10.1061/(AS-CE)ST.1943-541X.0000318
18. Kabantsev, O.V., Tamrazian, A.G. Allowing for changes in the calculated scheme during the analysis of structural behaviour. 2014. Magazine of Civil Engineering. 49(5). Pp. 15–26; 123–124. DOI: 10.5862/MCE.49.2
19. Nguyen, W., Bandelt, M.J., Trono, W., Billington, S.L., Ostertag, C.P. Mechanics and failure characteristics of hybrid fiber-reinforced concrete (HyFRC) composites with longitudinal steel reinforcement. 2019. Engineering Structures. 183. Pp. 243–254. DOI: 10.1016/j.engstruct.2018.12.087
20. Tamrazyan, A., Avetisyan, L. in (2014) Appl. Mech. Mater. Pp. 62–65. DOI: 10.4028/www.scientific.net/AMM.638-640.62
21. Alekseytsev, A. V. in (2020) J. Phys. Conf. Ser. DOI: 10.1088/1742-6596/1425/1/012014
22. Prokurov, M., Indykin, A., Alekseytsev, A. in (2018) MATEC Web Conf. DOI: 10.1051/matecconf/201825104017
23. Terrenzi, M., Spacone, E., Camata, G. Collapse limit state definition for seismic assessment of code-conforming RC buildings. 2018. International Journal of Advanced Structural Engineering. 10 (3). Pp. 325–337. DOI: 10.1007/s40091-018-0200-6
24. Alekseytsev, A.V., Akhremenko, S.A. Evolutionary optimization of prestressed steel frames. 2018. Magazine of Civil Engineering. 81 (5). Pp. 32–42. DOI: 10.18720/MCE.81.4
25. Serpik, I.N., Alekseytsev, A.V., Balabin, P.Y., Kurchenko, N.S. Flat rod systems: Optimization with overall stability control. 2017. Magazine of Civil Engineering. 76 (8). Pp. 181–192. DOI: 10.18720/MCE.76.16
26. Shokrabadi, M., Burton, H.V. Risk-based assessment of aftershock and mainshock-aftershock seismic performance of reinforced concrete frames. 2018. Structural Safety. 73. Pp. 64–74. DOI: 10.1016/j.strusafe.2018.03.003

27. Sinković, N.L., Brozovič, M., Dolšek, M. Risk-based seismic design for collapse safety. 2016. Earthquake Engineering and Structural Dynamics. 45 (9). Pp. 1451–1471. DOI: 10.1002/eqe.2717
28. Xue, B., Le, J.L. in (2016) Am. Concr. Institute, ACI Spec. Publ. Pp. 105–121.
29. Yu, X., Lu, D., Li, B. Estimating uncertainty in limit state capacities for reinforced concrete frame structures through pushover analysis. 2016. Earthquake and Structures. 10 (1). Pp. 141–161. DOI: 10.12989/eas.2016.10.1.141
30. Nili, M., Ghorbankhani, A.H., Alavinia, A., Zolfaghari, M. Assessing the impact strength of steel fibre-reinforced concrete under quasi-static and high velocity dynamic impacts. 2016. Construction and Building Materials. 107. Pp. 264–271. DOI: 10.10-16/j.conbuildmat.2015.12.161
31. Alekseytsev, A.V. Evolutionary optimization of steel trusses with the nodal joints of rods. 2013. Magazine of Civil Engineering. 40 (5). Pp. 28–37. DOI: 10.5862/MCE.40.3
32. Ngo, T., Mendis, P. Modelling the dynamic response and failure modes of reinforced concrete structures subjected to blast and impact loading. 2009. Structural Engineering and Mechanics. 32 (2). Pp. 269–282. DOI: 10.12989/sem.2009.32.2.269
33. Kyriakides, N., Sohaib, A., Pilakoutas, K., Neocleous, K., Chrysostomou, C., Tantele, E., Votsis, R. Evaluation of Seismic Demand for Substandard Reinforced Concrete Structures. 2018. The Open Construction and Building Technology Journal. 12 (1). Pp. 9–33. DOI: 10.2174/1874836801812010009
34. Mastali, M., Ghasemi Naghibdehi, M., Naghipour, M., Rabiee, S.M. Experimental assessment of functionally graded reinforced concrete (FGRC) slabs under drop weight and projectile impacts. 2015. Construction and Building Materials. 95. Pp. 296–311. DOI: 10.1016/j.conbuildmat.2015.07.153
35. Magnusson, J., Hallgren, M., Ansell, A. Shear in concrete structures subjected to dynamic loads. 2014. Structural Concrete. 15 (1). Pp. 55–65. DOI: 10.1002/suco.201300040
36. Ismail, M., Mueller, C.T. Computational structural design and fabrication of hollow-core concrete beams. 2018. Proceedings of the IASS Symposium 2018.
37. Mansur, M.A., Tan, K.-H., Weng, W. Analysis of Reinforced Concrete Beams with Circular Openings Using Strut-and-Tie Model. 2001. Structural Engineering, Mechanics and Computation. Pp. 311–318. DOI: 10.1016/b978-008043948-8/50030-8
38. Niroomandi, A., Pampanin, S., Dhakal, R.P., Ashtiani, M.S., De La Torre, C. Rectangular RC walls under bi-directional loading: recent experimental and numerical findings. 2018. The Concrete NZ Conference 2018.
39. Abed, F., Alhafiz, A.R. in (2018) 2018 Adv. Sci. Eng. Technol. Int. Conf. ASET 2018. Pp. 1–5. DOI: 10.1109/ICASET.20-18.8376768
40. Zeng, X. Finite Element Analysis of Square RC Columns Confined by Different Configurations of Transverse Reinforcement. 2017. The Open Civil Engineering Journal. 11 (1). Pp. 292–302. DOI: 10.2174/1874149501711010292
41. Alekseytsev, A.V., Al Ali, M. Optimization of hybrid I-beams using modified particle swarm method. 2018. Magazine of Civil Engineering. 83 (7). Pp. 175–185. DOI: 10.18720/MCE.83.16
42. Ranade, R., Li, V.C., Heard, W.F., Williams, B.A. Impact resistance of high strength-high ductility concrete. 2017. Cement and Concrete Research. 98. Pp. 24–35.
43. Pontiroli, C., Arlery, M., Rouquand, A. in (2015) Response Struct. Under Extrem. Load. Pp. 523–529.
44. Alekseytsev, A.V., Gaile L., Drukis, P. Optimization of steel beam structures for frame buildings subject to their safety requirements. Magazine of Civil Engineering. 2019. 91(7). Pp. 3–15. DOI: 10.18720/MCE.91.1
45. Tusnin, A. Dynamic factors in case of damaging continuous beam supports. Magazine of Civil Engineering. 2018. 78(2). Pp. 47–64. DOI: 10.18720/MCE.78.4

Contacts:

Anatoly Alekseytsev, aalexw@mail.ru

© Alekseytsev, A.V., 2021

Magazine of Civil Engineering

ISSN 2712-8172

journal homepage: http://engstroy.spbstu.ru/

DOI: 10.34910/MCE.103.7

Composition and properties of cement system with glutaraldehyde

V.V. Strokova[a], G. Le Saout[b], V.V. Nelubova[a]*, Y.N. Ogurtsova[a]

[a] V.G. Shukhov Belgorod State Technological University, Belgorod, Russia

[b] IMT Mines Alès, Alès, France

** E-mail: nelubova@list.ru*

Keywords: concrete construction, biodegradation, biocide, cements, hydration, fungi, chemical attack, Aspergillus

Abstract. The experience of operating livestock farms shows that periodic reorganization does not prevent biological corrosion of building structures. In this work, the possibility of using glutaraldehyde as a fungicide for volumetric administration in the preparation of biostable concrete was investigated. The study aims to minimize the adverse effects of the components of commercial biocidal products on the physical and mechanical characteristics of products. For research, we used an aqueous solution of glutaraldehyde with an active substance concentration of 0.5 and 1 %, which was introduced into Portland cement CEM I 42.5 N as mixing water. The degree of influence of the active substance on the properties of cement paste and mortar was estimated according to data on heat release during hydration, strength, and phase composition. The fungicidal activity evaluation of glutaraldehyde in cement systems and the degree of their growth with the Aspergillus niger test culture were evaluated. It was established by isothermal calorimetry that, in mixtures with glutaraldehyde, a delay in the achievement of the main hydration peak is observed – by 30 minutes for 0.5 %, by 1 hour for 1 %. After 72 hours of hydration, a lower total amount of released heat of hydration is observed – for 0.5 and 1% solutions by 6.8 and 5.8 %, respectively. According to X-ray phase and differential thermal analyzes, the phase composition of the initial and aldehyde-modified cement stone on day 28 does not differ and consists of the following phases: ettringite, portlandite, calcite and clinker minerals. Varying the phase composition leads to a change in strength: when using a 0.5 % solution of aldehyde, the power of the cement-sand mortar increases by 6.5 %, and a 1 % solution decreases by 6.7 %. The use of a 0.5 % solution of glutaraldehyde provides a decrease in the intensity of fungal development and the formation of a fungistatic effect. Based on the results, a 0.5 % solution of glutaraldehyde can be recommended for the development of cement composites with prolonged bio-resistance.

1. Introduction

The construction of new agricultural construction objects is becoming more and more in demand, which is due to an increase in the consumption of livestock products and crop production. The ability to achieve a high level of environmental safety of food products and technologies for their production depends, among other things, on the conditions of keeping animals, birds, or plants [1–3]. Therefore, regular sanitary and preventive maintenance is essential, as well as costly, part of the general technological process of agricultural enterprises. The experience of the operation of farms shows that periodic cleaning and sanitation of premises does not allow preventing the "biological fatigue" of building materials and structures [4−8]. In particular, biological corrosion, which is the result of many interrelated chemicals, physical, and (micro-) biological processes, affects elements of building structures, which is a problem with social and economic consequences [3, 9–13].

The most used method of protecting building cement materials of already constructed structures against biological corrosion is the use of coatings based on polyurethane, acrylic and epoxy resins, silanes, siloxanes [14, 15]. The disadvantages of using surfaces include a decrease in the breathability of structures,

Strokova, V.V., Le Saout, G., Nelubova, V.V., Ogurtsova, Y.N. Composition and properties of cement system with glutaraldehyde. Magazine of Civil Engineering. 2021. 103(3). Article No. 10307. DOI: 10.34910/MCE.103.7

This work is licensed under a CC BY-NC 4.0

poor adhesion, and low durability, which leads to the need for periodic updating of the protective layer. As volumetric methods to increase the natural resistance of cement materials, structure compaction is used by reducing the water-cement ratio, using active mineral additives or polymer fillers [16]. The disadvantage of introducing polymer fillers is the slowdown of cement hydration and their low affinity for concrete components.

It is assumed that the most appropriate solution for the construction of agricultural facilities is the use of building materials with initial resistance to biological corrosion agents. The biological strength of the building material will impede the formation, growth, and development of microorganisms in the inter-recovery period, both on the surface and in volume [2, 17, 18].

Previous studies have justified the need to use biocides as components of building materials that ensure the resistance of finished products to corrosion agents. For example, the volumetric introduction of bactericidal and fungicidal additives, such as nickel powder, calcium tungstate, calcium formate, silver-containing zeolite is well known [16].

The main problem of using this approach is the negative effect on the processes of phase and structure formation, physicomechanical characteristics of the cement system [19−21].

In this regard, when choosing an additive to increase the biological resistance of concrete in the conditions of farms, it is necessary to evaluate both its biocidal activity and the effect on cement paste and mortar, as a factor of durability and safety of the designed composite [3, 20, 22–26].

This work is aimed at studying the possibilities of minimizing the adverse effects of the components of commercial sanitation products on the phase and structure formation of cement. Based on this goal, glutaraldehyde (HA) was selected as a biocide for volumetric administration as a part of a significant amount of commercial biocides as the primary substance active against micromycetes. Glutaraldehyde interacts with the amino group of the cell wall to form an amine bridging bond. It thereby stops cell division, which slows down or stops the growth and development of microorganisms. In an acidic environment, glutaraldehyde can penetrate the cell; in an alkaline environment, it quickly reacts with the outer layers of cells [27]. A study of its effect on cement systems has not been previously conducted, that was the purpose of this study.

2. Materials and Methods

In this work, glutaraldehyde as a biocidal additive; Portland cement CEM I 42.5 N according to Russian State Standard GOST 31108-2016 "Cement for general construction. Special conditions" produced by Belgorodsky Cement CJSC (Belgorod, Belgorod Oblast, RF); reference multifunctional sand according to Russian State Standard GOST 6139−2003 "Sand for cement testing Technical conditions" were used.

Glutaraldehyde $CH_2(CH_2CHO)_2$ is a water-soluble oily liquid containing two aldehyde groups, used as a disinfectant. The biocidal activity of glutaraldehyde is due to the alkylation of sulfhydryl, hydroxyl, carboxyl, and amino groups of the proteins of microorganisms, which violates their vital functions and leads to their death. Glutaraldehyde is actively used for disinfecting livestock and poultry facilities, subject to the recommended concentrations. In this case, the optimal dosage of the active substance in the preparation of its aqueous solution for prophylactic disinfection of premises is a concentration in the range 0.1–0.3 %. With this concentration, degradation of pathogenic microflora is ensured in the absence of toxic effects on animals in farms.

To assess the effect of glutaraldehyde on the properties of the cement system, we used an aqueous solution with an active substance concentration of 0.5 and 1 %, which was introduced into the cement as mixing water. In the volume of the composite, this concentration does not exceed the recommended dosages for the preventive disinfection of rooms.

The following physicochemical and physicomechanical characteristics of cement paste and mortar were studied: heat release during hydration, mineral composition, compressive strength, and also mushroom resistance.

For the manufacture of cement paste and mortar samples, the ratio of glutaraldehyde/cement solution was 0.4. In the manufacture of control samples, the cement was closed with water at a water-cement ratio of 0.4. Hardening of cement was carried out under standard conditions at a temperature of 20±2 °C and relative humidity of 90±5 % until the test age was reached.

For the study, the kinetics of the set of strength, cement-sand mortar samples prepared by EN 196-1 were used. The cement-sand ratio was 3:1. The water-cement ratio of cement-sand mortar and the ratio "glutaraldehyde solution / cement" ratio was 0.55. The increase of water-cement ratio is justified by the need to obtain materials with a higher predetermined porosity in order to create conditions for more

complete unhindered development of the fungus on their surface and / or in volume. The compressive strength of cement-sand mortars was determined per the requirements of Russian State Standard GOST 30744–2001 "Cement. Test Methods Using Polyfractional Sand". To determine the strength, beam samples with size 40×40×160 mm were prepared. For the compressive strength, the arithmetic mean value of the test results of six halves of the beam samples for each composition was taken.

To determine the heat release during portland cement hydration, we used a ToniCAL model 7338 differential heat flow calorimeter (Toni Technik Baust off prüf Systeme GmbH, Germany). Differential thermal analysis with thermogravimetry of cement stone samples at the age of 28 days was performed on an STA 449 F5 thermal analysis device (NETZSCH-Geräte Bau GmbH, Germany); X-ray phase analysis – on a D8 Advance X-ray diffractometer (BRUKER Corporation, USA) (Cu Kα, λ = 1.54 Å).

The fungus resistance of cement stone was assessed by the growth of samples (the ability to grow and propagate on them) by mold fungi. The test was conducted according to Russian State Standard GOST 9.049–91 "Unified system of corrosion and ageing protection. Polymer materials and their components. Methods of laboratory tests for mould resistance"(Method 3).

The evaluation of the fouling of the cement material by microscopic fungi was carried out using an AXIOSCOPEA1 biological microscope. The degree of development of fungi was evaluated on a 6-point scale, according to GOST 9.048–89. Material has fungicidal properties if no fungi are found on its surface or the intensity of their development is estimated with less than 1 point.

After 28 days of hardening, mortars placed under ultraviolet light in a laminar cabinet for 6 hours with a calculation of 3 hours on one side in order to remove possible organic contaminants from other microflora on the surface and in the volume of the sample.

For the glutaraldehyde fungicidal activity evaluation of in cement systems (pastes and mortars), the *Aspergillus niger* test culture was used. This fungus is one of the most aggressive types of molds. The development of this fungus on the surface of construction sites due to its high survival rate causes the maximum degree of degradation effect [19].

As a nutrient medium for the test culture, Chapek's prepared medium was used, having the composition: 1000 ml of distilled water (pH = 6.7): monosubstituted potassium phosphate – 0.7 g; potassium phosphate disubstituted 3-water – 0.3 g; magnesium sulfate 7-water – 0.5 g; sodium nitrate – 2.0 g; potassium chloride – 0.5 g; iron (II) sulfate 7-water – 0.01 g; sucrose – 9 g; distilled water – 1000 ml, agar – 20 g. The finished mixture was poured into 15 ml tubes and placed vertically in an MLS-2420U Sanyo autoclave for heat treatment for 15 minutes at 122 °C. At the end of the process, the tubes were placed in a laminar cabinet, and the nutrient medium was uniformly poured on the bottom of the Petri dishes, followed by sterilization of the latter.

The infection of the nutrient medium was carried out by spraying a solution containing the spores of the control fungus with a spray gun. After sowing, samples of mortars were placed in the center of the Petri dishes. Then, closed Petri dishes were placed in a RI 115 thermostat with natural ventilation red LINE by Binder for 14 days at t = 30 °C, W = 90 %.

3. Results and Discussion

3.1. Effect of the biocide at early age

A study of the heat release of a cement paste with glutaraldehyde (Fig. 1) showed that its introduction does not lead to significant changes in the hydration process in the first 72 hours. The similar nature of the heat release of all the compositions under consideration, which corresponds to a typical Portland cement test, is noted. The peak in the first five minutes of the study refers to the process of exothermic wetting and reactions of the early stage of hydration. The second (central) peak mainly corresponds to the reactions of the middle stage of hydration with the formation of phases C-S-H and CH. Then, the heat release rate gradually decreases, while slow reactions of the late stage of hydration also occur with the formation of C-S-H and CH. An unclear third peak (about 13 hours for the materials understudy) is associated with the formation of AFm phase from C_3A and ettringite [28–30].

In mixtures with glutaraldehyde, there is a slight delay in reaching the main hydration peak – by 30 minutes for 0.5 %, by 1 hour for 1 %. Its intensity (Fig. 1a) also decreases slightly. As a result, after 72 hours of hydration, a lower total amount of released heat of hydration is observed in comparison with the control composition.

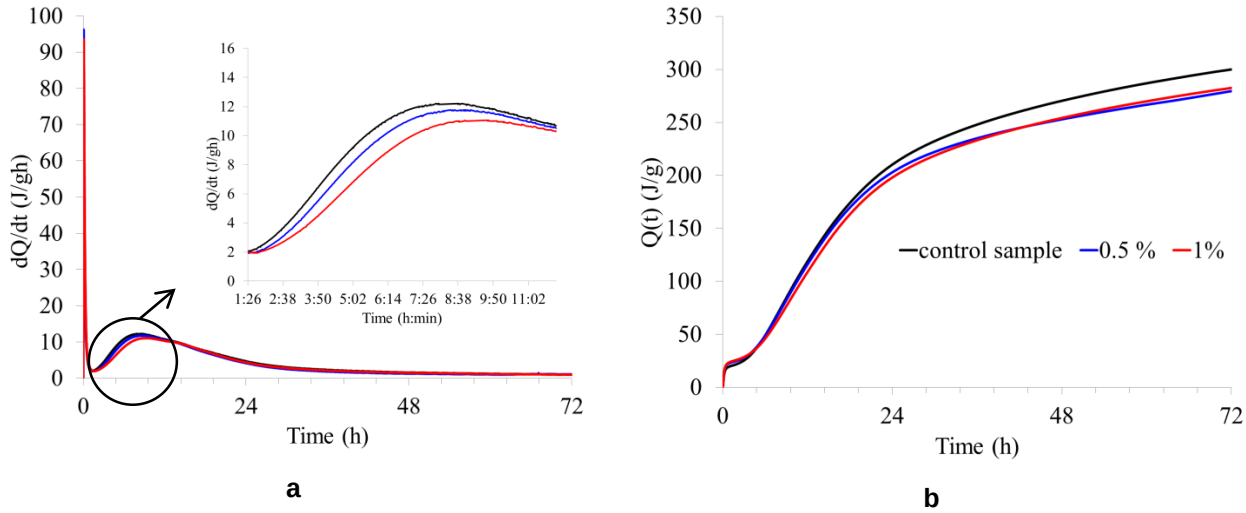

Figure 1. Rate of heat evolution (a) and total heat of hydration (b) for different glutardialdehyde content.

According to the data obtained, it can be said that glutaraldehyde in the early stages slightly slows down the hydration of Portland cement. Most likely, this process may occur due to adsorption. In this process, one or both of its functional groups are capable of reacting with hydroxyl groups on the surface of Portland cement particles.

3.2. Effect of the biocide at 28 days

The results of differential thermal analysis with thermogravimetry show the presence of an equal endo effect at 100–120 °C for all three samples, which is attributed to dehydration of C-S-H and ettringite (Fig. 2). Mass losses at temperatures of 430-470 °C correspond to the decomposition of portlandite. The end effect attributable to portlandite is most intense for the composition with 0.5 % glutaraldehyde. The subsequent end effect at higher temperatures corresponds to the decarbonization of calcite present in the anhydrous cement.

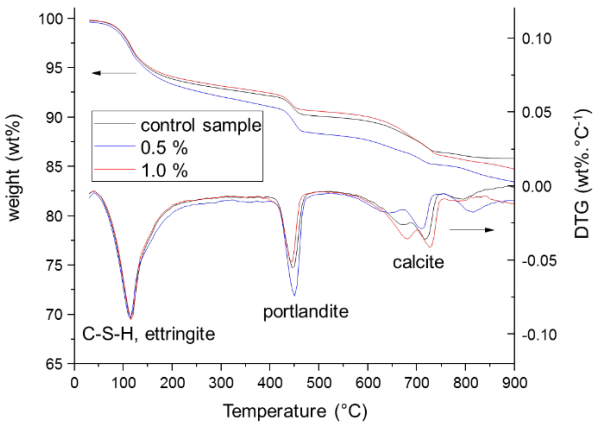

Figure 2. TGA/DTG of cement paste with different glutardialdehyde content after 28 days hydration.

As reported in [31, 32], A CO_2 weight loss peak is observed at around 720 °C because of the presence of relatively coarse calcite in the anhydrous cement and a second weight loss peak may be present at 600 to 650 °C because of the presence of mono- or hemicarbonates and due to the carbonation of portlandite and possibly C-S-H. The peak above 800°C may be due to the decomposition of C-S-H to wollastonite [31].

The absence of a significant effect of glutaraldehyde on the phase formation processes of Portland cement is also confirmed by the results of x-ray phase analysis of hardened cement at the age of 28 days (Fig. 3).

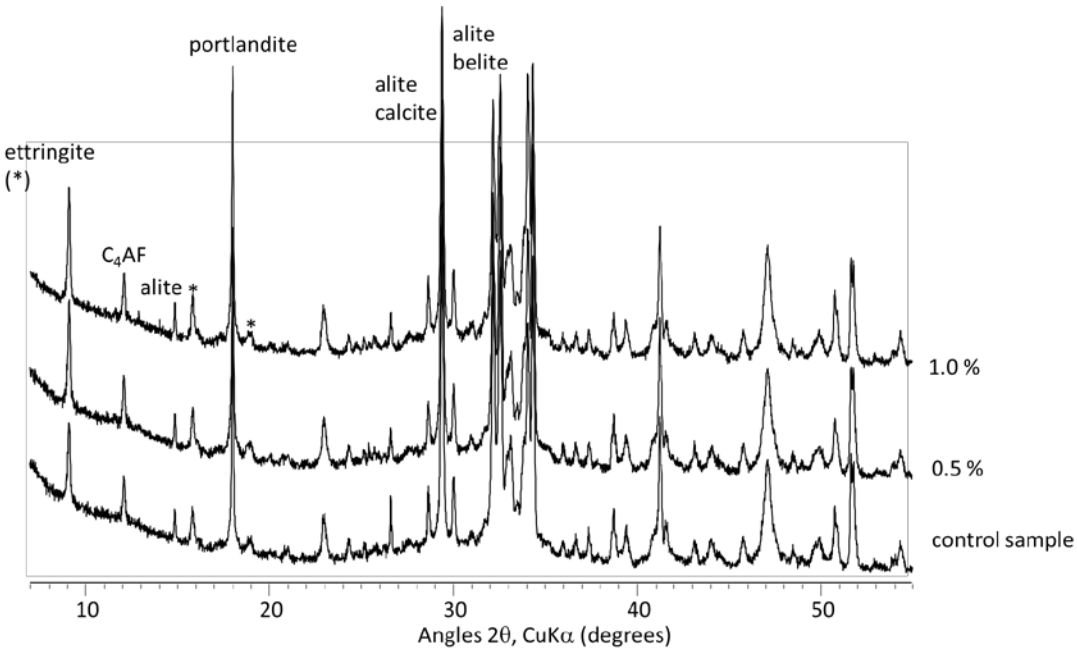

Figure 3. X-ray diffraction patterns of hardened cement paste with different glutardialdehyde content after 28 days hydration (Standard cement chemistry notation is used. As per this simplified notation: C = CaO, A = Al_2O_3, F = Fe_2O_3 and S = SiO_2).

In all the studied samples, both control and glutaraldehyde, the following were noted: the remains of unreacted clinker minerals (alite, belite, calcium aluminate C_3A and calcium aluminoferrite C_4AF phases) and crystalline hydration products (ettringite, portlandite).

When studying the kinetics of the set of compressive strength of a cement-sand mortar with glutaraldehyde, its significant influence is also not observed (Fig. 4).

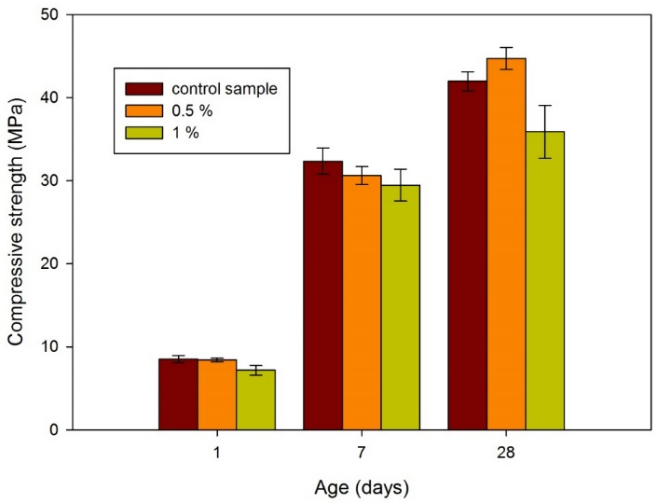

Figure 4. Compressive strength of hardened cement-sand mortar with different glutardialdehyde content.

The use of an aldehyde solution at a concentration of 0.5 % leads to a slight increase in the strength of the system on the 28th day of hydration hardening compared with the control sample, and in a concentration of 1 % to a decrease.

3.3. Effect of the biocide at antifungal effect

After 14 days from the start of the experiment, the active growth of Aspergillusniger fungus on the surface of the nutrient medium in all Petri dishes can be noted. Moreover, spores, conidia, and mycelium are absent on the surface of the studied samples of Portland cement stone (Fig. 5).

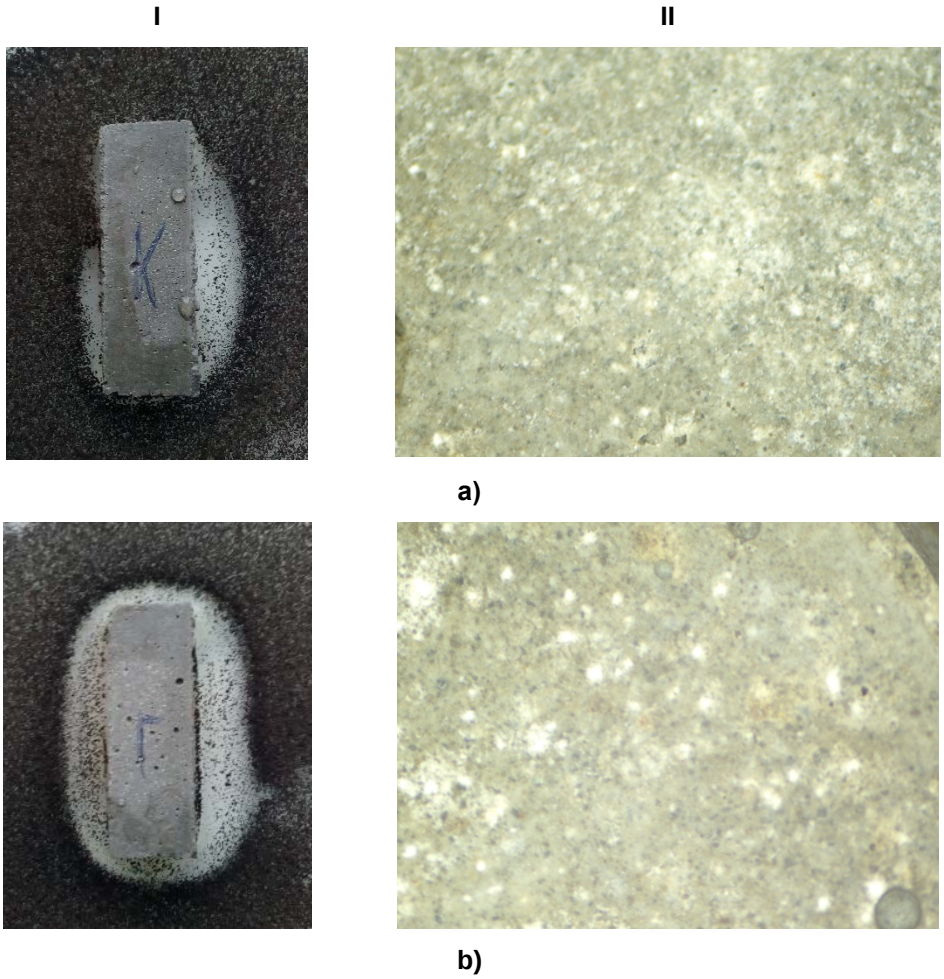

Figure 5. Development of the Aspergillus niger test culture on a growth medium in the presence of a Portland cement stone sample: a – control, b – with glutaraldehyde (0.5 %): I – general view; II – shooting with a biological microscope (× 60 times).

The cement system has a porous structure, which contributes to the growth of the microorganisms on the surface and in the volume of the material, and a high alkalinity in the early stages of hardening. Terms can reach several months before the onset of a high degree of carbonation during operation. However, despite these features of cement, the composition of cement impedes the growth of living organisms [26]. In this regard, a small zone of fungicidal activity is noted even around the control sample (Fig. 5 a). However, it can be noted that the use of glutaraldehyde increases the fungicidal zone around cement stone samples (Fig. 5, b). The data are confirmed by surveying the surface of the samples under a biological microscope (Fig. 5, II).

On the surface of the control sample of cement-sand mortar based on Portland cement (Fig. 6, a), the significant development of *Aspergillus niger* fungus is noted. On a sample with glutaraldehyde (Fig. 6, b), only individual elements of the mycelium are present. This is probably due to a decrease in the total alkalinity of the samples due to a decrease in the mass percentage of the active component – cement – when adding a filler. The result is a decrease in the resistance of the material to the action of filamentous fungi [33].

When assessing the fouling of samples in points (Table 1), we can quantitatively note an increase in the fungal resistance of a sample with glutaraldehyde. In the case of the original cement stone and with the addition of glutaraldehyde, a fungistatic effect to *Aspergillus niger* fungus is observed: the inhibition zone increases significantly. In the case of a cement-sand mortar without additives, there is no fungicidal effect. The aldehyde-modified mortar retains fungicidal properties with a slight decrease in the zone of inhibition.

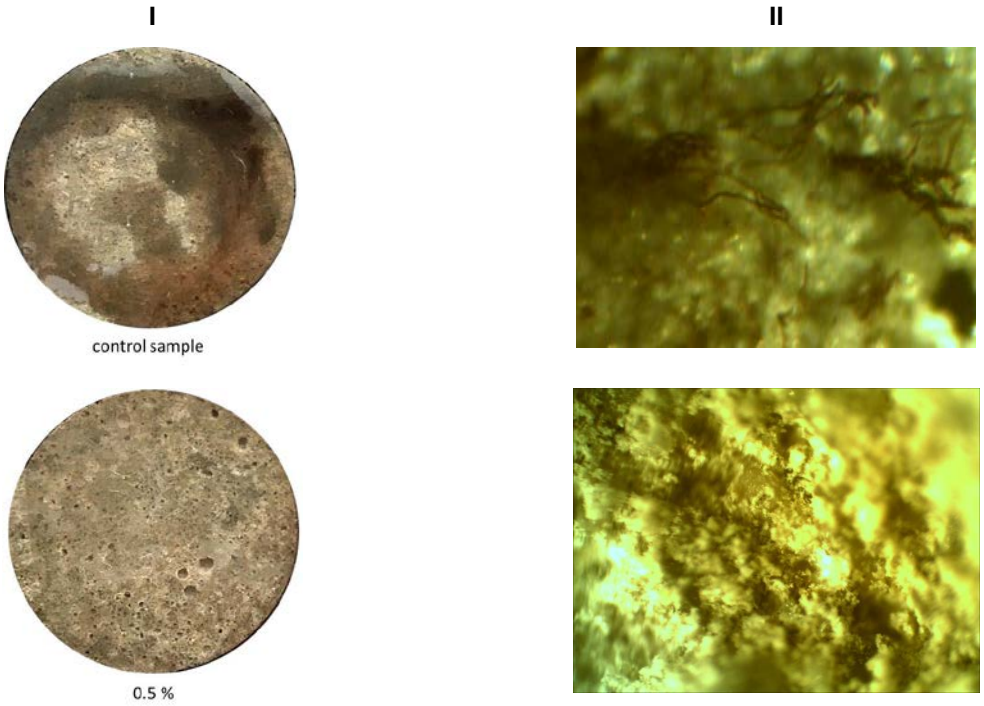

Figure 6. Antifungal effect of hardened cement-sand mortar (diameter 5 cm) with different glutardialdehyde content I – general view; II – shooting with a biological microscope (× 60 times).

Table1. Biostability of cement stone and cement-sand mortar samples to Aspergillus niger.

Sample	Evaluation of fungi growth, points	Inhibition zone, mm	Material evaluation
Cement stone			
Control sample	0	4	Fungicidal
0.5 %	0	10	Fungicidal
Cement-sand mortar			
Control sample	3	–	Fungus-proof (no fungicidal effect)
0.5 %	0	7	Fungicidal

4. Conclusions

A comprehensive analysis of the glutaraldehyde effect as a fungicidal additive on the composition and properties of the cement system was carried out.

1. The effect of fungicidal additives on the heat release of cement paste during hydration in the first 72 hours is established. In mixtures with glutaraldehyde, a delay in the achievement of main hydration peak is observed – by 30 minutes for 0.5 %, by 1 hour for 1 %. After 72 hours of hydration, a lower total amount of released heat of hydration is observed – for 0.5 and 1 % solutions by 6.8 and 5.8 %, respectively.

2. Composition change leads to varying in strength: when using a 0.5 % aldehyde solution, the strength of the cement-sand mortar increases by 6.6% and 1% decreases by 14.5 %.

3. An increase in the resistance of samples for *Aspergillus niger* fungus is shown. The use of a solution of glutaraldehyde (0.5 %) in the case of cement stone leads to an increase in the fungicidal zone. The introduction of the biocide into the composition of the cement-sand mortar provides a fungistatic effect: the development of the fungus on the surface of modified samples is not observed.

Thus, the main effect of glutaraldehyde is to slow down hydration of the hydrating system by possible adsorption on the surface of cement particles and hydrated formations without a subsequent critical negative effect on the compressive strength of cement at early age. At the same time, a significant change in the mineral composition of cement stone is not observed, and the fungal resistance increases. On this

basis, a recommendation is proposed for the use of a 0.5 % solution of glutaraldehyde for the development of cement composite materials with bio-resistance. If it is necessary to use a 1 % solution (in environments with increased bioaggression), it is recommended to take into account a negative effect on the rate of increase in compressive strength and its final value.

5. Acknowledgements

The reported study was funded by RFBR, according to research project No. 18-29-12011 using the equipment of the Center for High Technologies of BSTU named after V.G. Shukhov and of the Centre for Materials Engineering of IMT Mines Alès.

References

1. Kobeticova, K., Cerny, R. Ecotoxicology of building materials: A critical review of recent studies. Journal of Cleaner Production. 2017. No. 165. Pp. 500–508. DOI: 10.1016/j.jclepro.2017.07.161
2. De Muynck, W., De Belie, N., Verstraete, W. Antimicrobial mortar surfaces for the improvement of hygienic conditions. Journal of Applied Microbiology. 2010. No. 108. Pp. 62–72. DOI: 10.1111/j.1365-2672.2009.04395.x
3. Ryparova, P., Wasserbauer, R., Racova, Z. The cause of occurrence of microorganisms in civil engineering and the dangers associated with their growth. Procedia Engineering. 2016. No. 151. Pp. 300–305. DOI: 10.1016/j.proeng.2016.07.402
4. Jacob, J., Mascelani, A.G., Steinmetz, R.L.R., Dalla Costa, F.A., Dalla Costa, O.A. Use of silica fume and nano-silica in mortars attacked by acids present in pig manure. Procedia Structural Integrity. 2018. No. 11. Pp. 44–51. DOI: 10.1016/j.prostr.2018.11.007
5. Chromková, I., Čechmánek, R. Influence of biocorrosion on concrete properties. Key Engineering Materials. 2018. 760 KEM. Pp. 83–90. DOI: 10.4028/www.scientific.net/KEM.760.83
6. Estokova, A., Harbulakova, V.O., Luptakova, A., Kovalcikova, M. Analyzing the relationship between chemical and biological-based degradation of concrete with sulfate-resisting cement. Polish Journal of Environmental Studies. 2019. 28(4). Pp. 2121–2129. DOI: 10.15244/pjoes/91079
7. Strokova, V.V., Nelubova, V.V., Rykunova, M.D. Resistance of cement stone in sanitation solutions. Magazine of Civil Engineering. 2019.90(6). Pp. 72–84. DOI: 10.18720/MCE.90.7
8. Strokova, V.V., Zhernovsky, I.V., Nelubova, V.V., Rykunova, M.D. Structural transformations of cement stone in conditions of development of the biocenosis of a poultry enterprise. Materials Science Forum. 2018. No. 945. Pp. 269–275. DOI: 10.4028/www.scientific.net/MSF.945.269
9. Erofeev, V.T., Bogatov, A.D., Bogatova, S.N., Kaznacheev, S.V., Smirnov, V.F. Influence of the operational environment on biological firmness of building composites. Magazine of Civil Engineering. 2012.33(7). Pp. 23–31. DOI: 10.5862/MCE.33.3
10. Anikina, N.A., Smirnov, V.F., Smirnova, O.N., Zaharova, E.A. Protection of construction materials based on acrylates from biodeterioration. Magazine of Civil Engineering. 2018. 5(81). Pp. 116–124. DOI: 10.18720/MCE.81.12
11. Gaylarde, C., Otlewska, A., Celikkol-Aydin, S., Skora, J., Sulyok, M., Pielech-Przybylska, K., Gillatt, J., Beech, I., Gutarowska, B. Interactions between fungi of standard paint test method BS3900. International Biodeterioration& Biodegradation. 2015. No. 104. Pp. 411–418. DOI: 10.1016/j.ibiod.2015.07.010
12. Cwalina, B. 11 – Biodeterioration of concrete, brick and other mineral-based building materials. Understanding Biocorrosion. Fundamentals and Applications. 2014. Pp. 281–312. DOI: 10.1533/9781782421252.3.281
13. Manzhilevskaya, S.E. Environmental monitoring of ecological safety in areas of construction, reconstruction and operation of objects // Construction Materials and Products. 2019. 2 (3). Pp. 78–84. (rus)
14. Beech, I., Otlewska, A., Skóra, J., Gutarowska, B., Gaylarde, C. Interactions of fungi with titanium dioxide from paint coating. Indoor and Built Environment. 2018. 27(2). Pp. 263–269. DOI: 10.1177/1420326X16670716
15. De Muynck, W., Ramirez, A.M., De Belie, N., Verstraete, W. Evaluation of strategies to prevent algal fouling on white architectural and cellular concrete. International Biodeterioration & Biodegradation. 2009. No. 63. Pp. 679–689. DOI: 10.1016/j.ibiod.2009.04.007
16. Noeiaghaei, T., Dhami, N., Mukherjee, A. Nanoparticles surface treatment on cemented materials for inhibition of bacterial growth. Construction and Building Materials. 2017. No. 150. Pp. 880–891. DOI: 10.1016/j.conbuildmat.2017.06.046
17. Noeiaghaei, T., Mukherjee, A., Dhami, N., Chae, S.-R. Biogenic deterioration of concrete and its mitigation technologies. Construction and Building Materials. 2017. No. 149. Pp. 575–586. DOI: 10.1016/j.conbuildmat.2017.05.144
18. Strokova, V., Nelyubova, V., Rykunova, M. Investigation of fungicidal activity of biocides by method of direct contact with test cultures. MATEC Web of Conferences. 2018. No. 251. Article No. 01018. DOI: 10.1051/matecconf/201825101018
19. Travush, V.I., Karpenko, N.I., Erofeev, V.T., Rodin, A.I., Rodina, N.G., Smirnov, V.F. Development of biocidal cements for buildings and structures with biologically active environments. Power Technology and Engineering. 2017.51(4). Pp. 377–384. DOI: 10.1007/s10749-017-0842-8
20. Do, J., Song, H., So, H., Soh, Y. Antifungal effects of cement mortars with two types of organic antifungal agents. Cement and Concrete Research. 2005. No. 35. Pp. 371–376. DOI: 10.1016/j.cemconres.2004.06.021
21. Strigáč, J., Martauz, P., Eštoková, A., Števulová, N., Luptáková, A. Bio-corrosion resistance of concretes containing antimicrobial ground granulated blastfurnace slag BIOLANOVA and novel hybrid H-CEMENT. Solid State Phenomena. 2016. 244. Pp. 57–64. DOI: 10.4028/www.scientific.net/SSP.244.57
22. Nematzadeh, M., Dashti, J., Ganjavi, B. Optimizing compressive behavior of concrete containing fine recycled refractory brick aggregate together with calcium aluminate cement and polyvinyl alcohol fibers exposed to acidic environment. Construction and Building Materials. 2018. 164. Pp. 837–849. DOI: 10.1016/j.conbuildmat.2017.12.230
23. Nelyubova, V., Strokova, V., Vasilenko, M., Rykunova, M., Danakin, D. Comparative characteristics of binders resistance for building composites to mold fungi. MATEC Web of Conferences. 2018. No. 196. Article No. 04050. DOI: 10.1051/matecconf/201819604050

24. Elistratkin, M.Yu., Minakov, S.V., Shatalova, S.V. Composite binding mineral additive influence on the plasticizer efficiency. Construction Materials and Products. 2019. 2 (2). Pp. 10–16. (rus)
25. Fediuk, R.S., Lesovik, V.S., Mochalov, A.V., Otsokov, K.A., Lashina, I.V., Timokhin, R.A. Composite binders for concrete of protective structures. Magazine of Civil Engineering. 2018. 82(6). Pp. 208–218. DOI: 10.18720/MCE.85.3
26. Tolstoy, A.D. Fine-grained high-strength concrete. Construction Materials and Products. 2020. 3 (1). Pp. 39–43. (rus). DOI: 10.34031/2618-7183-2020-3-1-39-43
27. Ozerov, M.Yu., Karkishchenko, V.N., Popov, D.V., Pchelintsev, S.Yu., Popov, V.G., Grishin, D.A. Sredstva dlya obezzarazhivaniya obyektov, kontaminirovannykh sporami B. Anthracis [Disinfectants for B. Anthracis contaminated objects]. Biomeditsina. 2009. No. 1. Pp. 28–37. (rus)
28. Taylor, H.F.W. Cement Chemistry. London, 1990. 475 p.
29. Tran, T.H., Govin, A., Guyonnet, R., Grosseau, P., Lors, C., Garcia-Diaz, E., Damidot, D., Devès, O., Ruot, B. Influence of the intrinsic characteristics of mortars on biofouling by Klebsormidium flaccidum. International Biodeterioration & Biodegradation. 2012. No. 70. Pp. 31–39. DOI: 10.1016/j.ibiod.2011.10.017
30. Scrivener, K.L., Juilland, P., Monteiro, P.J.M. Advances in understanding hydration of Portland cement. Cement and Concrete Research. 2015. No. 78. Pp. 38–56. DOI: 10.1016/j.cemconres.2015.05.025
31. Lothenbach, B., Durdziński, P.T., De Weerdt, K. A Practical Guide to Microstructural Analysis of Cementitious Materials. Boca Raton, 2016. 560 p.
32. Gabrovšek, R., Vuk, T., Kaučič, V. Evaluation of the hydration of Portland cement containing various carbonates by means of thermal analysis. Acta Chimica Slovenica. 2006. 53(2). Pp. 159–165.
33. Erofeev, V.T., Rodin, A.I., Yakunin, V.V., Bogatov, A.D., Bochkin, V.S., Chegodajkin, A.M. Alkali-activated slag binders from rock-wool production wastes. Magazine of Civil Engineering. 2018. 82(6). Pp. 219–227. DOI: 10.18720/MCE.82.20

Contacts:

Valeria Strokova, vvstrokova@gmail.com
Gwenn Le Saout, gwenn.le-saout@mines-ales.fr
Victoria Nelubova, nelubova@list.ru
Yulia Ogurtsova, ogurtsova.y@yandex.ru

© Strokova, V.V., Le Saout, G., Nelubova, V.V., Ogurtsova, Y.N., 2021

Magazine of Civil Engineering

ISSN 2712-8172

journal homepage: http://engstroy.spbstu.ru/

DOI: 10.34910/MCE.103.8

Model for determining the elastic moduli of road pavement layers

A.N. Tiraturyan[a]*, E.V. Uglova[b], D.A. Nikolenko[a], M.A. Nikolenko[a]

[a] Don State Technical University, Rostov-on-Don, Russia

[b] Academy of Construction and Architecture Don State Technical University, Rostov-on-Don, Russia

** E-mail: tiraturjanartem@gmail.com*

Keywords: asphalt pavements, mechanical properties, durability, backcalculation, numerical model, deflection bowl

Abstract. A mathematical model of dynamic stress-strain state of a multilayer half-space, and a method for constructing and adjusting the design bowl of dynamic deflections under shock loading were developed to solve the problem of determining the elastic moduli of layers of non-rigid road pavement at the stage of its operation. Using this method, the actual dynamic elastic moduli of pavement layer materials were determined for a test section of road. In conclusion, the development prospects of the presented method are discussed as a result of analysis of amplitude-time characteristics of displacements recorded on road pavement surface under shock loading.

1. Introduction

Diagnostics of roads is one of the most technologically advanced and rapidly developing sectors of the road industry. An important task to be solved at the stage of road operation is adoption of rational repair measures to ensure the estimated service life of non-rigid road pavements. To solve this problem, one needs information on the actual state of both the pavement as a whole, and its individual layers.

In-depth experimental studies of stress-strain states of non-rigid road pavements and their temperature and moisture operation modes were carried out in the works of B.B. Teltayev [1, 2]. The results of these works made it possible to directly determine the actual values of stresses and strains at critical points of pavement structure.

In [3–6], the theoretical foundations of backcalculation method for elastic moduli of non-rigid road pavement layers are presented. It combines instrumental measurements for recording elastic deflection bowls on surfaces of road structures and mathematical modeling for construction of design deflection bowls on surfaces of non-rigid roads pavements.

The works [7–11] consider the advantages and disadvantages of mathematical models, which are basis of software systems for construction of deflection bowls. It is noted that for the most part, they all solve the problem of determining the stress-strain state (SSS) in a multilayer half-space under a load uniformly distributed over a circular plate. Solutions for determining the dynamic SSS of road pavements are rarely implemented despite their obvious advantages, in particular, the possibility of taking into account the different time of dynamic load impact and the nature of dynamic impact pulse from various shock loading installations.

In [12–20], the authors analyze software systems for backcalculation of elastic moduli of structural layers of non-rigid road pavements. They consider the Evercalc, Wesdef, Julea software which are universal systems (not associated with specific installations), and Elmod, Primax software, which are specialized systems, i.e. supplied with shock loading systems FWD (falling weight deflectometer) Dynatest and PRIMAX. However, all software systems are mainly based on static models of stress-strain state of the multilayer half-space, which does not correspond to the actual test conditions. Moreover, the shock loading installations are of great diversity, they vary significantly in the impulse time of impact on the pavement,

Tiraturyan, A.N., Uglova, E.V., Nikolenko, D.A., Nikolenko, M.A. Model for determining the elastic moduli of road pavement layers. Magazine of Civil Engineering. 2021. 103(3). Article No. 10308. DOI: 10.34910/MCE.103.8

This work is licensed under a CC BY-NC 4.0

and in the parameters of the fall height and the load mass. Another point is perspectivity of the approach, which takes into account the viscoelastic behavior of materials when determining the elastic moduli of the road structure layers. So, development of a method for determining the elastic moduli of layers of non-rigid road pavements, based on application of SSS dynamic model of a multilayer half-space, is of current interest.

To achieve this goal, it is necessary to solve the following tasks:

- To develop an algorithm for constructing and adjusting the design deflection bowls relative to the experimental ones recorded by shock loading installations in the field conditions;
- To test the proposed method for determining the elastic moduli of layers of non-rigid road pavements for the operated section of road;
- To recommend additional indicators characterizing the structural properties of layers of road pavements.

2. Methods

The methods considered in this work are solutions and algorithms obtained by the authors and embedded in the AEM software package. The process of determining the elastic moduli of structural layers of non-rigid road pavements can be represented in the form of a diagram (Fig. 1). The FWD shock loading unit used at the first stage is a semi-trailer with a shock loading mechanism mounted on it with 5–10 geophone sensors, as a rule. The geophones placement scheme has various configurations. The most common scheme is when geophone sensors are spaced at intervals of 30 cm at a distance from the shock loading point. Under the shock impact at the FWD unit, the impact of the calculated load from the vehicle wheel on the pavement surface is simulated. At the same time the deflection bowl on the pavement surface is recorded by geophone sensors.

Stage I – Experimental registration of dynamic deflection bowl of a road structure

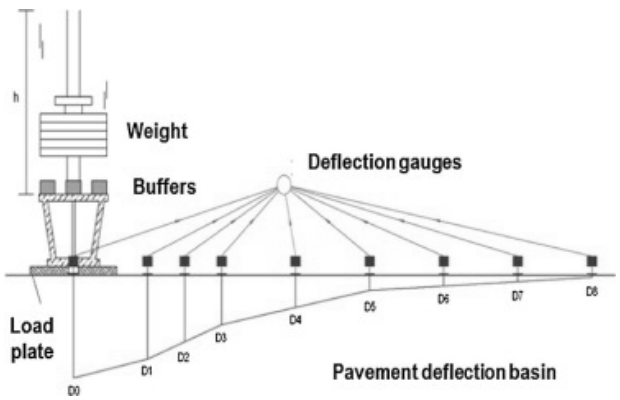

Stage II – Calculation of dynamic deflection bowl of a road structure

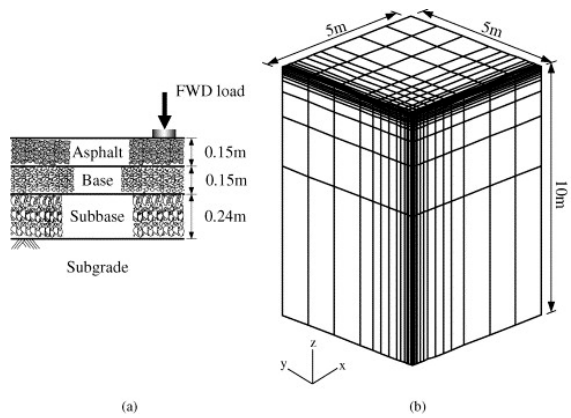

Stage III – Determination of elastic moduli of layers of road structure at the current operation stage

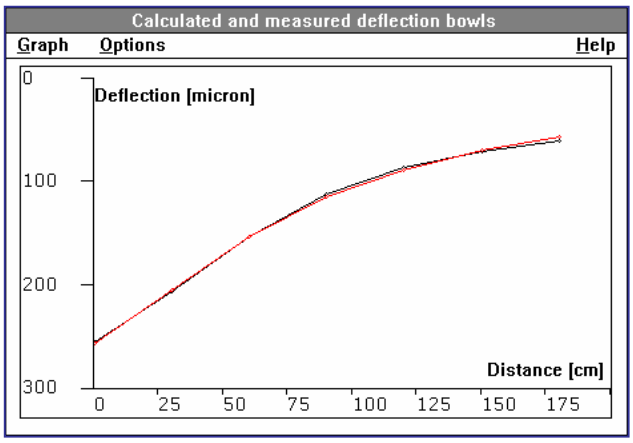

Figure 1. Method for calculation the elastic moduli of structural layers of non-rigid road pavements at the operational stage.

The mathematical model is based on the solution of problem of determining the dynamic SSS of a multilayer half-space under a shock load. The proposed algorithm for solving this problem is based on the

works of I.I. Vorovich, V.A. Babeshko, A.N. Belokon, E.V. Glushkov, M.G. Seleznev, S.K. Iliopolov, H. Grundmann, J. Prozzi, M. Schanz et al. [21–27]. The statement of the problem is written as follows.

Road pavements is a N-layer elastic half-space $D = D_1 \cup D_2 \cup ... \cup D_N$, described in cylindrical coordinate system (R, θ, z) as (Fig. 2):

$$D_1 = \{R \in (0, +\infty), \theta \in (0, 2\pi), z < 0\}$$

is a half-space; $D_j = \{R \in (0, +\infty), \theta \in (0, 2\pi), z \in (z_{j-1}, z_j)\}$, $z_j = \sum_{i=1}^{j} h_i$; $(h_1 = 0)$ is the j-th layer (j = 2,...,N).

The elastic properties of media in D_j, $j = 0, 1, ..., N$ are determined by density ρ_j elastic modulus E_j Poisson's ratio ν_j expressed in terms of Lame parameters λ_j, μ_j.

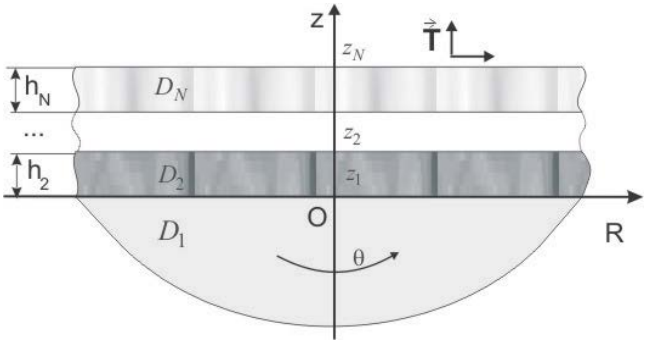

Figure 2. Multilayer half-space in a cylindrical coordinate system.

The displacement of medium under the action of an impact load is described by dynamic Lame equations. The viscous properties of layers are taken into account by introducing the tangents of loss angles of longitudinal and transverse waves, when determining the reduced vibration frequencies.

$$\nabla\nabla \cdot \mathbf{u}^{(j)}(\mathbf{r}) - \frac{\theta_{j1}^2}{\theta_{j2}^2} \nabla \times \nabla \times \mathbf{u}^{(j)}(\mathbf{r}) + \theta_{j1}^2 \mathbf{u}^{(j)}(\mathbf{r}) = 0, \tag{1}$$

$\theta_{j1}^2 = \omega^2 / V_{Pj}^2, \theta_{j2}^2 = \omega^2 / V_{Sj}^2$ are the reduced vibration frequencies, $V_{Pj} = \sqrt{(\lambda_j + 2\mu_j)/\rho_j}$, $V_{Sj} = \sqrt{\mu_j / \rho_j}$ are the velocities of longitudinal and transverse waves propagations in the j-th medium.

The solution to this system of equations is the Hankel integral transformation in the form:

$$\mathbf{U}^{(j,N)}(\mathbf{R}, \omega) = \int_{\Gamma_+} J_k(uR) \sum_{n=1}^{2} \mathbf{P}^{(j,n)}(u, z) \cdot \overline{\mathbf{X}}^{(j,n)}(u) u du \tag{2}$$

where J_k is Bessel function;

$\mathbf{P}^{(j,n)}$ is the core of the integral representation for a multilayer half-space;

$\overline{\mathbf{X}}^{(j,n)}$ are the Hankel transforms for voltage at the boundaries of layers (n = 1,2), determined from the boundary conditions.

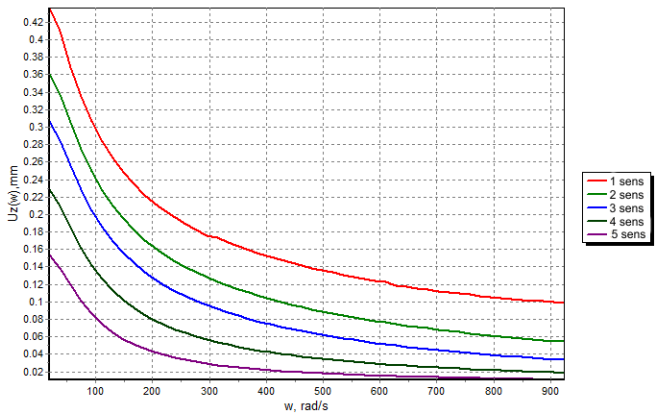

Figure 3. Frequency response of displacement of surface points of a road structure.

A solution is constructed for each characteristic frequency ω_k (Fig. 3) calculated as:

$$\omega_k = k\pi / (T + \tau) \tag{3}$$

where T is the time of observation over the deformation of the road structure surface under shock loading, selected from the damping conditions of the previous pulse, s.

τ is the duration of the loading pulse, s;

k is the amount of decomposition harmonics, determined from conditions of accuracy for shock loading pulse approximation $P(t)$.

The multiple layers of medium are taken into account via the superposition principle. It implies the replacement of variables for a homogeneous half-space by variables of the j-th layer in the equation, and the components of displacement vectors at the boundaries of the road pavement layers are set equal.

The amplitude-time characteristics (ATC) of displacements (Fig. 4) at given points on the pavement surface are calculated using the formula

$$\mathbf{U}^{(N)}(\mathbf{R},t) = \sum_{k=1}^{M} p_k \left\{ -\cos\eta_k \operatorname{Im}\left[\mathbf{U}^N(\mathbf{R},\omega_k)\exp(-i\omega_k t)\right] + \sin\eta_k \operatorname{Re}\left[\mathbf{U}^N(\mathbf{R},\omega_k)\exp(-i\omega_k t)\right]\right\} \tag{4}$$

for all observation points on the surface of a multilayer half-space. Here p_k are the coefficients of the shock loading pulse $P(t)$ expansion into the Fourier series, calculated by the formula:

$$p_k = \int_0^{\tau} \sin(\omega_k t + \eta_k) P(t) dt \tag{5}$$

$$\eta_k = 0.5 \cdot k \cdot \pi \cdot T / (T + \tau), \tag{6}$$

and $\operatorname{Re}(\mathbf{U}^{(N)}(\mathbf{R},\omega_k)$, $\operatorname{Im}(\mathbf{U}^{(N)}(\mathbf{R},\omega_k)$ are the real and imaginary parts of the vertical displacement vector at given frequencies ω_k.

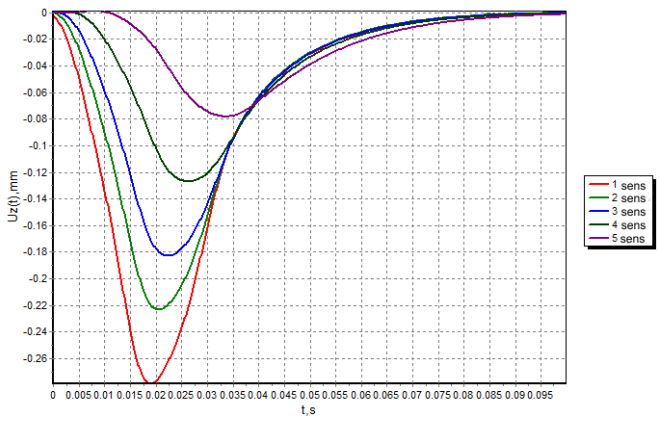

Figure 4. The amplitude-time characteristics of displacements.

The final stage of construction the calculated bowl of maximum dynamic deflections is to select the maximum amplitudes of vertical displacements of the medium surface points $\max_t \left| U_z^{(N)}(R,t) \right|$. It is selected within the studied time interval for each of the observation points set on the road structure surface. Further these values are put on the final plot of dynamic deflection bowl (Fig. 5).

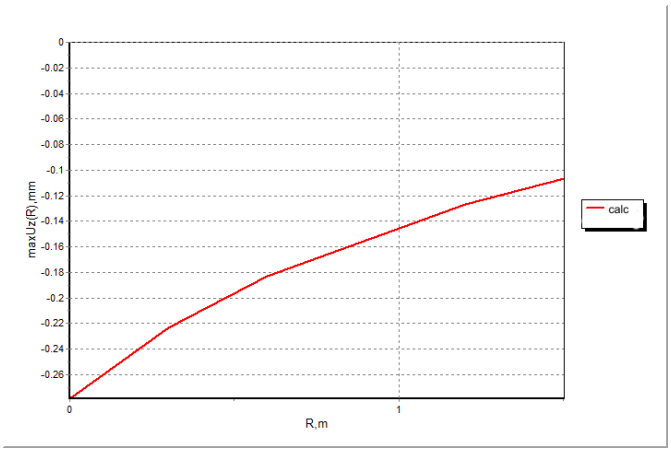

Figure 5. The calculated bowl of dynamic deflections of road pavement.

The resulting calculated bowl of maximum dynamic deflections is constructed for the design values of the elastic moduli of the structural layers of the road pavement. Further it is corrected taking into account the experimental bowl of dynamic deflections recorded in field conditions. The inflection points on the graph show the locations of geophone sensors, in accordance with the setup configuration selected for testing.

To integrate the software package with FWD impact loading installations, a batch mode was developed. It allows exporting data on the actual deflection bowls recorded during impact loading from the output file of the installation software in *.fwd format.

The method of adjusting the calculated deflection bowl relatively to the experimental one is implemented in the form of a first-order method for an iterative process that includes the following sequence of actions:

1. One numerically finds $\dfrac{\partial U_y\left(x_k^{(0)}, E_1^{(0)}, E_2^{(0)}, E_3^{(0)}\right)}{\partial E_j}$, $j = 1, 2, 3$, according to the calculated bowl of maximum dynamic deflections for the design values $E_j = E_j^{(0)}$.

2. These values are compared with those obtained from processing of experimental data. Based on this comparison, one identifies the points $x = x_k^{(0)}$ at which their maximum divergence takes place. The number of points should coincide with the number of defined parameters (in this case $k = 1, 2, 3$).

3. The main terms of expansion of the left side of equation (1) – the calculated bowl of maximum dynamic deflections – are determined in increments of unknown parameters.

$$U_y\left(x, E_1^{(0)} E_2^{(0)} E_3^{(0)}\right) + \sum_{j=1}^{3} \frac{\partial U_y\left(x, E_1^{(0)}, E_2^{(0)}, E_3^{(0)}\right)}{\partial E_j^{(0)}} \Delta E_j \tag{7}$$

This expression in nodes $x = x_k$ must be equal to the experimentally obtained maximum dynamic deflections in the corresponding points. As a result one gets the following system of linear algebraic equations for ΔE_j determination.

$$\sum_{j=1}^{3} \frac{\partial U_y\left(x_k^{(0)}, E_1^{(0)}, E_2^{(0)}, E_3^{(0)}\right)}{\partial E_j^{(0)}} \Delta E_j = \varphi(x) - U_y\left(x_k^{(0)}, E_1^{(0)}, E_2^{(0)}, E_3^{(0)}\right), \quad k = 1, 2, 3. \tag{8}$$

Using values ΔE_j obtained as a result of solving the system, one obtains the first approximation of the desired elasticity models

$$E_j^{(1)} = E_j^{(0)} + \Delta E_j, \tag{9}$$

4. The bowl of maximum dynamic deflections is calculated for the obtained values of $E_j^{(1)}$, and the procedures 1-3 are repeated until the required accuracy is achieved.

To compare the results obtained by the presented mathematical model using the software package that implements it, we used the engineering approach presented in the draft of the Belarusian normative document TKP 140 “Roads. Diagnostic procedure”. This document makes it possible to calculate the elastic moduli of layers of road pavements based on deflection bowls recorded in the field conditions. The elastic modulus of the asphalt-concrete (a-c) layer is defined as:

$$E_{a-c} = \frac{D(E_{total} - E_{base})}{0.3h}, \tag{9}$$

where h is the thickness of an assembly of asphalt-concrete layers, cm;

E_{total} is the total elastic modulus of the surface of road pavements, MPa;

E_{base} is the total elastic modulus of the base layer surface, MPa;

D is the diameter of the calculated wheel print, cm.

The elastic modulus of the base layer surface is:

$$E_{base} = K \cdot E_{total}, \tag{10}$$

K is the coefficient considering the thickness of asphalt-concrete layers and the ratio of deflections under geophones 2-4.

The elastic modulus of subgrade soil is calculated using deflections recorded by the sensors 4-9 of the shock loading installation

$$E_{s.s.(4-9)} = \frac{p \cdot D^2 \cdot (1-\mu^2)}{4 \cdot r \cdot l_{\mathrm{st(4\text{-}9)}}}, \tag{11}$$

$l_{st(4\text{-}9)}$ are the static deflections recorded by the sensors 4-9;

D-diameter of load circle;

r is the distance from the center of load application to geophones 4-9,

P is the pressure on the surface, kPa.

3. Results and Discussion

To assess the adequacy of results obtained by this method, the elastic moduli of road pavement layers calculated using the AEM software package were compared with that calculated by the Belarusian technique described in Belarusian normative document TKP 140 “Roads. Diagnostic procedure”. The comparison was carried out for a section of the 3rd category road in the Rostov region. This road section was completed by major repairs in 2017. The construction of road pavements on this site includes two layers of asphalt-concrete with a total thickness of 12 cm, and an incoherent base layer with a thickness of 35 cm. The surface temperature during testing was 8 °C. The FWD PRIMAX 1500 impact loading apparatus was used to register experimental elastic deflection bowls [20].

The determined actual elastic moduli using both methods are presented in Fig. 6.

The determined actual elastic moduli of road pavement layers

in forward direction **in backward direction**

Figure 6. The actual elastic moduli of road pavement layers calculated using the AEM software package and according to the TKP-140 technique.

The plots show that elastic moduli of road pavement layers calculated using the AEM software package and using the technique described in TKP 140, are generally described by a common pattern of changes along the length of the examined section of road. We believe it confirms the adequacy of the used bowl processing algorithms.

At the same time, differences in the absolute values of actual elastic moduli of individual layers of road pavements are obvious. The dynamic elastic moduli of the asphalt-concrete layer calculated in the software package significantly exceed that obtained using the TKP 140 method [28]. The latter is based on reduction of the calculated elastic moduli of pavement layers to static values at the design temperature of 10 °C. The character of this phenomenon is known and is associated with the fact that the modulus of elasticity of asphalt concrete depends on temperature and frequency, which was noted in many works [29, 30]. The elastic moduli of layers of the unreinforced base and subgrade soil, determined both by the TKP-140 methodology and calculated using the AEM software package, are quite close to each other. Nevertheless, it should be emphasized that layers of non-cohesive materials operate in conditions of all-side compression, and the layer elastic modulus is essentially non-linear along their depth. Currently, there exist methods for taking into account the nonlinearity of elastic modulus of a granular material. However, they all imply the division of one layer of a non-cohesive material into a number of sublayers, and the elastic modulus is calculated within each of them taking into account octahedral stresses. This problem is relatively easy to solve at the stage of designing road pavement, but it is quite complex in terms of configuration of these sublayers at the stage of pavement operation. Now the authors are working to improve the proposed algorithm.

The field results should be refined from the standpoint of assessing the structural properties of individual layers of road pavements. It can be made based on analysis of the amplitude-time characteristics (ATC) of displacements recorded under shock loading. To confirm this conclusion, we examined the ATC displacements on the surface of road pavements. As test systems we used a new section of road without defects, and a road section with critical defects on the asphalt-concrete pavement, which has been in operation for 6 years (Fig. 7, 8).

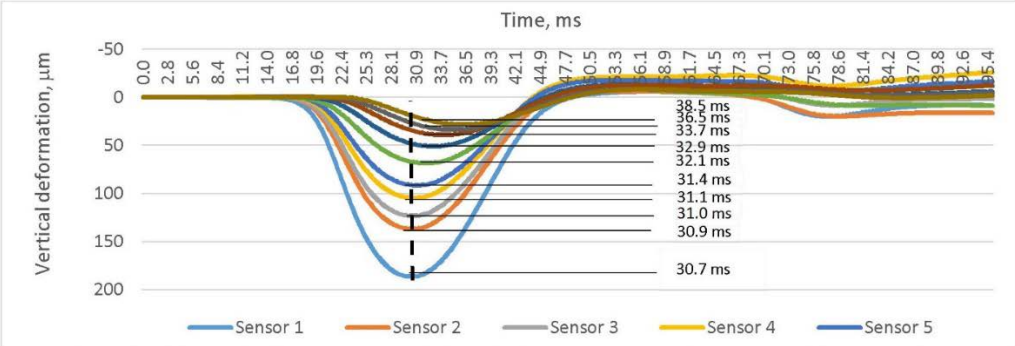

Figure 7. The amplitude-time characteristic of displacements recorded under a shock impact on the pavement surface without defects.

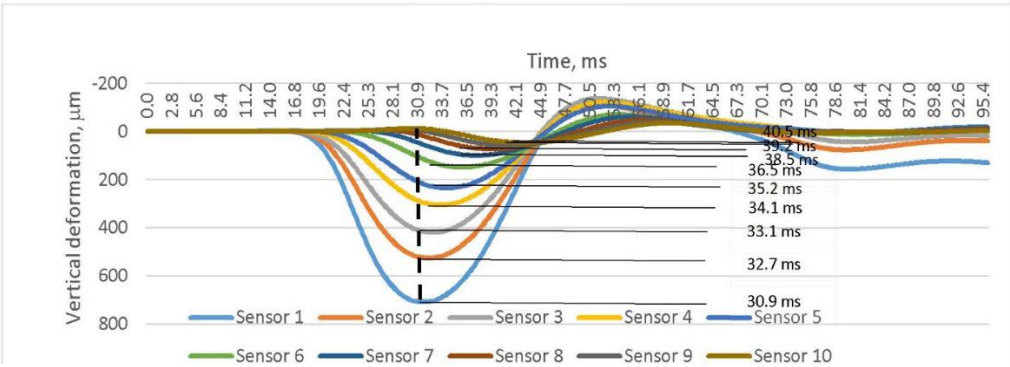

Figure 8. The amplitude-time characteristic of displacements recorded under a shock impact on the pavement surface with defects.

As it can be seen from the plots, the time delay between the extrema of amplitude-time characteristics of displacements on a road section with defects significantly exceeds the time delay between peaks of ATC displacements recorded on pavements without defects.

It is possible to quantitatively characterize the obtained results by calculating the damping coefficients of individual layers of road pavements using formulas:

$$\zeta = \frac{\delta}{\sqrt{(2\pi)^2 + \delta^2}},$$

$$\delta = \ln \frac{A_1}{A_2} \cdot \Delta t^{-1},$$

where δ is the damping logarithmic decrement;

A_1, A_2 are the extrema of amplitude-time characteristics of displacements recorded in field conditions;

Δt is the delay time between the extrema of amplitude-time characteristic recorded by individual sensors.

We presented the results of numerical modeling in [31]. It showed that the greatest influence on change in time delay in the zone closest to the impact point (0–0.25 m) is associated with a change in mechanical parameters of the asphalt-concrete layers. The changes in time delay in the middle and in the far zones relative to the impact point are mainly associated with mechanical characteristics of layers of base and subgrade soil, respectively. Thus, the data recording and determination of mechanical

characteristics, taking into account analysis of the amplitude-time characteristics of displacements recorded under shock loading, are an urgent task requiring further detailed study.

4. Conclusion

1. A mathematical model of dynamic stress-strain state of a multilayer half-space in an axisymmetric setting has been developed. It allows constructing design bowls of elastic deflections on the surface of non-rigid road pavements, for installations with various parameters of impact loading;

2. The developed method was tested in the field conditions on a section of the M-4 DON highway. The developed mathematical model was used as a base for AEM software package creating. The elastic moduli of road pavement layers were calculated using the AEM software package created by the authors and they were compared with that calculated by the Belarusian technique described in normative document TKP 140. It was established that the obtained results are generally described by a common pattern of changes along the length of the examined section of road. We believe it confirms the adequacy of the used bowl processing algorithms.

3. The damping coefficient is proposed to use as an additional indicator characterizing the structural state of road pavement layers. It is calculated based on the ratio of amplitudes between the extrema of the amplitude-time characteristics and the time delay between them. For the asphalt concrete layers it is calculated in the zone near to the impact point (0–0.25 m), for the base layers (0.25–1.25 m.) it is calculated in the middle zone, for the soil subgrade it is calculated in the far zone (1.25–2.25 m). These results were obtained using mechanical and mathematical modeling, the results of which are presented in [31]. Within the framework of the presented task, the obtained results can be used to further improve the presented approach with regard to determine the actual elastic moduli of the road pavement layers, as well as the actual damping coefficients.

References

1. Teltayev, B.B., Liu, J., Suppes, E.A. Distribution of temperature, moisture, stress and strain in the highway. Magazine of Civil Engineering. 2018. 83(7). Pp. 102–113. DOI: 10.18720/MCE.83.10
2. Teltayev, B.B., Aitbayev, K.A. Modeling of transient temperature distribution in multilayer asphalt pavement. Geomechanics and Engineering. 2015. Vol. 8(2). Pp. 133–52.
3. Lytton, R. Backcalculation of Pavement Layer Properties. Nondestructive Testing of Pavements and Backcalculation of Moduli. ASTM International, 2008. Pp. 7-7–32.
4. Ma, X., Dong, Z., Yu, X., Chen, F., Cao, C., Sun, J. Monitoring the structural capacity of airfield pavement with built-in sensors and modulus back-calculation algorithm. Construction and Building Materials. 2018. 175. Pp. 552–561. DOI: 10.1016/j.conbuildmat.2018.04.198
5. Zhang, Y., Roesler, J. Improved Backcalculation Procedure for Continuously Reinforced Concrete Pavement. Transportation Research Record. 2018. 2672(40). Pp. 336–347. DOI: 10.1177/0361198118758010
6. Kheradmandi, N., Modarres, A. Precision of back-calculation analysis and independent parameters-based models in estimating the pavement layers modulus-Field and experimental study. Construction and Building Materials. 2018. 171. Pp. 598–610. DOI: 10.1016/j.conbuildmat.2018.03.211
7. Solatifar, N., Kavussi, A., Abbasghorbani, M., Katicha, S.W. Development of dynamic modulus master curves of in-service asphalt layers using MEPDG models. Road Materials and Pavement Design. 2019. 20(1). Pp. 225–243. DOI: 10.1080/14680629.2017.1380688.
8. El-Raof, H.S.A., El-Hakim, R.T.A., El-Badawy, S.M., Afify, H.A. Simplified Closed-Form Procedure for Network-Level Determination of Pavement Layer Moduli from Falling Weight Deflectometer Data. Journal of Stomatology. 2018. 144(4). DOI: 10.1061/JPEODX.0000080
9. Dalla Valle, P., Thom, N. Improvement to method of equivalent thicknesses (MET) for calculation of critical strains for flexible pavements. International Journal of Pavement Engineering. 2018. 19(12). Pp. 1053–1060. DOI: 10.1080/10298436.2016.1238698
10. Ng, K., Hellrung, D., Ksaibati, K., Wulff, S.S. Systematic back-calculation protocol and prediction of resilient modulus for MEPDG. International Journal of Pavement Engineering. 2018. 19(1). Pp. 62–74. DOI: 10.1080/10298436.2016.1162303
11. Uddin W., Barros R., Jaafar Z.F.M. Sensitivity analysis of mechanistic-empirical pavement structural design methods considering climate impacts on layer modulus values //Bituminous Mixtures and Pavements VII: Proceedings of the 7th International Conference Bituminous Mixtures and Pavements (7ICONFBMP), June 12-14, 2019, Thessaloniki, Greece. – CRC Press, 2019. – 357 p.
12. Devulapalli, L., Kothandaraman, S., Sarang, G. Erratum to: A review on the mechanisms involved in reclaimed asphalt pavement. International Journal of Pavement Research and Technology. 2019. 8(5). DOI: 10.1007/s42947-019-1024-x
13. Miller, H., Daniel, J.S., Eftekhari, S., Kestler, M., Mallick, R.B. Research on Sustainable Pavements: Changes in In-Place Properties of Recycled Layers Due to Temperature and Moisture Variations. Airfield and Highway Pavements 2017: Pavement Innovation and Sustainability – Proceedings of the International Conference on Highway Pavements and Airfield Technology. 2017-August. Pp. 69–78. DOI: 10.1061/9780784480946.007
14. Huang, H., Luo, J., Moaveni, M., Qamhia, I.I., Tutumluer, E., Tingle, J.S. Advanced analytical tool for flexible pavement design and evaluation. Airfield and Highway Pavements 2019: Design, Construction, Condition Evaluation, and Management of Pavements - Selected Papers from the International Airfield and Highway Pavements Conference 2019. Pp. 61–71. DOI: 10.1061/9780784482452.007

15. Plati, C., Georgiou, P., Papavasiliou, V. Simulating pavement structural condition using artificial neural networks. Structure and Infrastructure Engineering. 2016. 12(9). Pp. 1127–1136. DOI: 10.1080/15732479.2015.1086384
16. Elbagalati, O., Elseifi, M., Gaspard, K., Zhang, Z. Development of the pavement structural health index based on falling weight deflectometer testing. International Journal of Pavement Engineering. 2018. 19(1). Pp. 1–8. DOI: 10.1080/10298436.2016.1149838
17. Enhanced Analysis of Falling Weight Deflectometer Data for Use With Mechanistic-Empirical Flexible Pavement Design and Analysis and Recommendations for Improvements to Falling Weight Deflectometers 2017.
18. Zhang, R., Ren, T., Ashrafuzzaman Khan, M., Teng, Y., Zheng, J. Back-Calculation of Soil Modulus from PFWD Based on a Viscoelastic Model. 2019. DOI: 10.1155/2019/1316341.
19. Fan, Q., Li, S., Xu, X. IOP Conference Series: Earth and Environmental Science Bearing capacity evaluation of asphalt pavement based on dynamic deflection equivalent Bearing capacity evaluation of asphalt pavement based on dynamic deflection equivalent. DOI: 10.1088/1755-1315/300/5/052041
20. Uglova, E. V., Tiraturyan, A.N., Shamraev, L.G. Modern approach to assessment of transport and operating condition of roads implemented in State Company “Russian Highways.” CAD&GIS for roads SAPR i GIS avtomobilnykh dorog. 2016. (1(6)). Pp. 38–51. DOI: 10.17273/cadgis.2016.1.7
21. Vorovich, I., Babeshko, V., Pryakhina, O. Dynamics of massive bodies and resonance phenomena in deformable media. 1999.
22. Babeshko, V.A. Dynamics of inhomogeneous linearly elastic media. The science. Ch. ed. Phys.-Math. lit., 1989.
23. Iliopolov S.K., Seleznev M.G., Uglova E.V. Dynamics of road structures: monograph. Rostov-on-Don: Publishing house of Rostov State University of Civil Engineering, 2002. 258 p.
24. Grundmann, H., Lieb, M., Trommer, E. The response of a layered half-space to traffic loads moving along its surface. Archive of Applied Mechanics. 1999. 69(1). Pp. 55–67. DOI: 10.1007/s004190050204
25. Xu, Q., Prozzi, J.A. A time-domain finite element method for dynamic viscoelastic solution of layered-half-space responses under loading pulses. Computers and Structures. 2015. 160. Pp. 20–39. DOI: 10.1016/j.compstruc.2015.07.005
26. Schanz, M. Poroelastodynamics: Linear models, analytical solutions, and numerical methods. 62(3)05-2009.
27. Uglova, E.V, Tiraturyan, A.N., Lyapin, A.A. Integrated approach to studying characteristics of dynamic deformation on flexible pavement surface using nondestructive testing. PNRPU Mechanics Bulletin. 2016. 0(2). Pp. 111–130.
28. Burtyl, U.V., Leonovich, I.I. Improving methods for assessing the transport and operational condition of roads. Highways and Bridges. 2010. No. 8. P. 95–105.
29. Kirillov, A.M., Zavialov, M.A. Modeling of change in asphalt concrete dynamic modulus. Magazine of Civil Engineering. 2015. 54(2). Pp. 70–76. (rus). DOI: 10.5862/MCE.54.8.
30. Yashnov A.N., Polyakov S.Yu. Analysis of computational models for determining the modulus of elasticity of asphalt concrete. Politransport systems. 2017. Pp. 73–79.
31. Uglova, E.V, Tiraturyan, A.N. Calculation of the Damping Factors of the Flexible Pavement Structure Courses According to the In-place Testing Data. Procedia Engineering. 2017. 187. Pp. 742–748. DOI: 10.1016/j.proeng.2017.04.431

Contacts:

Artem Tiraturyan, tiraturjanartem@gmail.com
Evgenia Uglova, uglova.ev@yandex.ru
Denis Nikolenko, d.a.nikolenko@mail.ru
Maxim Nikolenko, twinmax@mail.ru

© Tiraturyan, A.N., Uglova, E.V., Nikolenko, D.A., Nikolenko, M.A., 2021

Magazine of Civil Engineering

ISSN 2712-8172

journal homepage: http://engstroy.spbstu.ru/

DOI: 10.34910/MCE.103.9

The behavior of CFRP strengthened RC beams subjected to blast loading

A. Jahami[a]*, Y. Temsah[a], J. Khatib[a], O. Baalbaki[a], S. Kenai[b]
[a] Beirut Arab University, Beirut, Lebanon
[b] University of Blida, Blida, Algeria
** E-mail: ahjahamy@hotmail.com*

Keywords: blast loading, CFRP sheets, deflection, dynamic analysis, impact damage, strengthening

Abstract. Carbon Fiber Reinforced Polymer (CFRP) sheets have been widely used in strengthening different concrete elements such as beams, slabs, and columns. This sparked the interest of many researchers to conduct research on CFRP sheets; to have a better understanding for their behavior. This paper studied numerically the effect of using CFRP as a strengthening technique for Reinforced Concrete (RC) beams subjected to blast loading. A previous experimental investigation done by a Chinese researchers was considered in this study as a reference, and was modeled numerically (using ABAQUS) for this study. The model was then calibrated in order to conduct the numerical analysis on the effect of CFRP. Three different configurations of CFRP were considered: bottom CFRP strips for flexural strengthening, diagonal side strips for shear strengthening, and U-shaped strips for both shear and flexural strengthening. The variables considered in this study were; the mid-span deflection, strain in steel reinforcement and structural damage in both beams and CFRP sheets. Results showed that using CFRP in the bottom tensile face of RC beams helps in absorbing blast energy. In addition, using CFRP has shown a reduction in the tensile strain of the beam reinforcements.

1. Introduction

Temsah [1, 2] and Jahami [3] have studied numerically the effect of impact loads due to close explosions on the behavior of reinforced concrete beams. The effect of impact loading condition on both concrete and steel reinforcement material properties was considered. It was found that reinforced concrete beams failed locally due to plastic hinge formation. A spalling of concrete was realized at the tension zone in addition to the crushing of concrete at the compression zone. In addition, Iso – damage curves were derived for all beams considered in the study. Other researchers studied numerically the behavior of structural element when subjected to direct impact due to falling objects. These studies included impact of falling object on reinforced concrete beams [4, 5], and on post-tensioned slabs [6–8]. The behavior of these structural elements and its modes of failure were presented. It was shown that a local failure occurred in both studies: a plastic hinge occurred in the reinforced concrete beam, and a punching shear failure occurred in the posttensioned slab at the position of the falling object.

Many researchers [9–13] studied the usage of Carbon fiber Reinforced Polymers (CFRP) sheets in strengthening reinforced concrete beams. Kishore [14] investigated the effect of using CFRP sheets on the flexural and shear capacity of RC beams. The main variables considered in this study were the reinforcement ratio (flexural and shear) and the position of CFRP sheets. Results indicated that beams strengthened by CFRP laminates were structurally efficient. It was concluded that using CFRP sheets increases the flexural and shear capacity of RC beams by 40 % and 45 % respectively.

Other researchers investigated the behavior of RC beams strengthened with CFRP under impact loading conditions [15–19]. Fujikake [20] examined the impact responses of CFRP strengthened reinforced concrete (RC) beams experimentally. The studied parameters were; the height of the falling object, the number of blows, and the CFRP scheme. Four different types of CFRP strengthening schemes were applied to RC beams. This experimental study proved that RC beams strengthened with CFRP have better

Jahami, A., Temsah, Y., Khatib, J., Baalbaki, O., Kenai, S. The behavior of CFRP strengthened RC beams subjected to blast loading. Magazine of Civil Engineering. 2021. 103(3). Article No. 10309. DOI: 10.34910/MCE.103.9

This work is licensed under a CC BY-NC 4.0

resistance to impact loadings. In addition, by strengthening RC beams with CFRP in flexure, crack width was decreased compared to unstrengthen RC beams.

Some studies regarding strengthening techniques for posttensioned slabs subjected to punching shear failure due to direct impact load from a falling object were done. One of them studied the efficiency of using Carbon fiber reinforced polymers “CFRP” to reduce punching shear damage in posttensioned slabs due to impact loads [21]. It was found that using CFRP reduced the mid-span displacement of reinforced concrete slabs when subjected to impact loads. A drop between 15% to 30% was obtained when using this strengthening technique. In addition, more energy was dissipated using CFRP as internal energy. The CFRP sheets proved to be good in absorbing impacts and energy from different loads. It reduced the tensile damage occurred in concrete due to the increase in energy absorption. Similar studies were performed for the same strengthening technique and reached the same conclusions [22, 23].

This work demonstrates the efficiency of using different CFRP sheet configurations on the structural behavior of reinforced concrete beams subjected to blast loading. Both flexural and shear stresses and strains were checked due to different configurations. Also the damage at both top and bottom faces were checked too.

2. Methods

2.1. Experimental data

The input data used in this numerical study were obtained from the experimental work done by Zhang [24] at National University of Defense Technology. The beams studied in this work had dimensions of 85 cm×7.5 cm×7.5 cm, 110 cm×10 cm×10 cm, and 135 cm×12.5 cm×12.5 cm. However, in this numerical study, the beams with dimensions 110 cm×10 cm×10 cm were considered. All steel reinforcements have diameter of 6 mm as shown in Fig. 1. Four different explosive weights were considered, each was placed over the center of the reinforced concrete (RC) beam. A steel frame was used to support the reinforced concrete beam. The experimental setup and details are shown in Fig. 1, while the experimental program is summarized in Table 1. As for material strength, the concrete compressive strength was 40 MPa, while the steel yield and ultimate strength were 395 MPa and 501 MPa respectively.

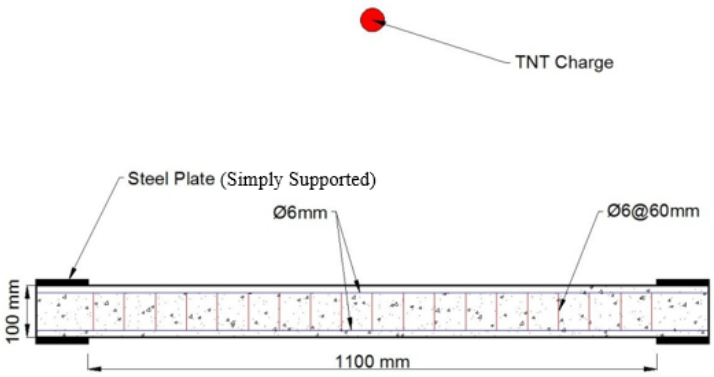

Figure 1. Experimental setup [24].

Table 1. Number and Dimensions of beams.

Beam	Dimensions (mm)	TNT (Kg)	Standoff distance (m)
B2-1	100×100×1100	0.36	0.4
B2-2		0.45	0.4
B2-3		0.51	0.4
B2-4		0.75	0.4

2.2. Numerical Modeling

As indicated earlier that the data used in the computer simulation were those of Zhang’s experiment [24]. The software used for this purpose was "ABAQUS”. The concrete body and steel supports were modelled as solid elements (C3D8R), whereas steel rebars were modelled as wire elements (T3D2) as shown in Fig. 2 and 3 [25]. As for blast loading, ABAQUS built-in model "CONWEP" was used to simulate the explosion, and that was achieved easily by assigning an equivalent TNT explosive to a reference point set at a distance from the target.

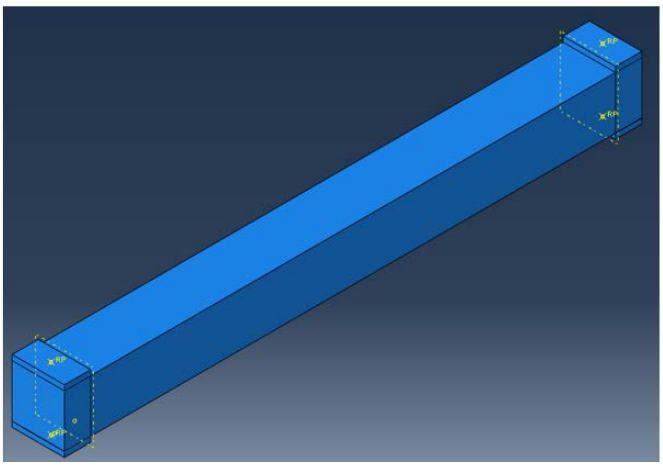

Figure 2. 3D view of beam modelled in ABAQUS.

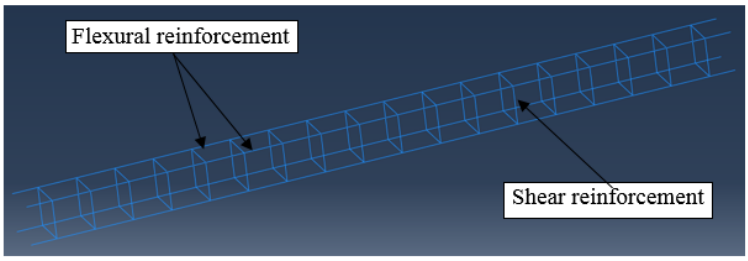

Figure 3. Flexural and Shear reinforcement modelling.

The Concrete Damage Plasticity (CDP) model was used to define the mechanical properties of concrete. This model was derived by Lubliner [26] and developed by Lee [27]. CDP model represents the nonlinear behaviour of concrete using different input parameters like inelastic strain, cracking strain, stiffness degradation and recovery, and other parameters. In addition, the effect of dynamic load conditions on concrete properties was included as per the study done by Jahami [3]. Equations 1 to 5 show the formulas used to determine the dynamic properties of concrete:

$$\frac{f_{cd}}{f_{cm}} = \left(\frac{\varepsilon'_c}{30\times10^{-6}}\right)^{\left(\frac{1.016}{5+0.9\,f_{cm}}\right)} \tag{1}$$

$$\frac{f_{ctd}}{f_{ctm}} = \left(\frac{\varepsilon'_{ct}}{10^{-6}}\right)^{\left(\frac{1}{1+0.8\,f_{cm}}\right)} \tag{2}$$

$$\frac{E_{cd}}{E_{cm}} = \left(\frac{\varepsilon'_c}{30\times10^{-6}}\right)^{0.026} \tag{3}$$

$$\frac{E_{ctd}}{E_{ctm}} = \left(\frac{\varepsilon'_{ct}}{3\times10^{-6}}\right)^{0.026} \tag{4}$$

$$\frac{\varepsilon_{cd}}{\varepsilon_{cm}} = \left(\frac{\varepsilon'_c}{30\times10^{-6}}\right)^{0.02} \tag{5}$$

Where "ε'_c" is the compressive strain rate in concrete, "f_{cm}" is the static compressive strength of concrete, "f_{cd}" is the dynamic compressive strength of concrete, "ε'_{ct}" is the tensile strain rate in concrete, "f_{ctm}" is the static tensile strength of concrete, "f_{ctd}" is the dynamic tensile strength of concrete, "E_{cm}" is the static elastic modulus of concrete in compression, "E_{cd}" is the dynamic elastic modulus of concrete in compression, "E_{ctm}" is the static elastic modulus of concrete in tension, "E_{ctd}" is the dynamic elastic modulus of concrete in tension, "ε_{cm}" is the static compressive strain at maximum compressive stress, and "ε_{cd}" is the dynamic strain at maximum compressive stress. Concrete mechanical properties for both static and dynamic load conditions are shown below in Table 2:

Table 2. Mechanical Properties of Concrete.

Parameter	Notation	Static Condition	Dynamic condition
Elastic Modulus (MPa)	E	29725	46341
Poisson's ratio	υ	0.2	0.2
Density (Kg/m^3)	ρ	2400	2400
Compressive strength (MPa)	f'_c	40	56.8
Peak Compressive strain (mm/m)	$\acute{\varepsilon}_c$	2.3	3.2
Tensile Strength (MPa)	f_t	3.86	5.48
Dilation angle (^{0})	ψ	36	36
Eccentricity	ε	0.1	0.1
Bi-axial to Uni-axial strength ratio	f_{b0}/f_{t0}	1.16	1.16
Second stress invariant ratio	K	0.67	0.67
Viscosity parameter	μ	0	0

As for the reinforcing steel, the Elasto-Plastic behaviour was implemented in this study [3], and a perfect bond was considered between the rebars and the surrounding concrete. Regarding the contact between the steel supports and the concrete slab, a frictional coefficient of 0.7 was considered. Equations 6 and 7 were used to determine the dynamic yield and ultimate strength of steel rebars.

$$\frac{f_{yd}}{f_y} = \left(\frac{\varepsilon'_s}{10^{-4}}\right)^{\left(0.074-0.04\frac{f_y}{414}\right)} \tag{6}$$

$$\frac{f_{ud}}{f_u} = \left(\frac{\varepsilon'_s}{10^{-4}}\right)^{\left(0.019-0.009\frac{f_y}{414}\right)} \tag{7}$$

Where "ε'_s" is the strain rate in steel, "f_y" is the static yield strength of steel, and "f_{yd}" is the dynamic yield strength of steel. "f_u" is the static ultimate strength of steel, and "f_{ud}" is the dynamic ultimate strength of steel. The steel material property details used in this study are illustrated in Table 3.

Table 3. Mechanical Properties of Steel reinforcement.

Parameter	Notation	Static Condition	Dynamic condition
Elastic Modulus (MPa)	E	200000	200000
Poisson's ratio	υ	0.3	0.3
Density (Kg/m^3)	ρ	7850	7850
Yield strength (MPa)	f_y	395	590
Ultimate strength (MPa)	f_u	501	620

2.3. Model Calibration

The numerical model was successfully validated and matched with the experimental work. Table 4 represents the mid-span deflection results. All cases were validated with an average error of 6 %. Mid-span deflection curves due to numerical modeling for all beams are shown in Fig. 4. The peak deflection was increased as the blast intensity increased.

Table 4. Mid-Span Deflection for experimental, SDOF, and Finite element modeling analysis.

Beam	TNT (Kg)	Standoff distance (m)	Mid-Span Deflection (mm)		Error (%)
			Experimental	ABAQUS	
B2-1	0.36	0.4	9	8.8	2.22
B2-2	0.45	0.4	25	23.5	6
B2-3	0.51	0.4	35	32.1	8.29
B2-4	0.75	0.4	40	36.3	9.25

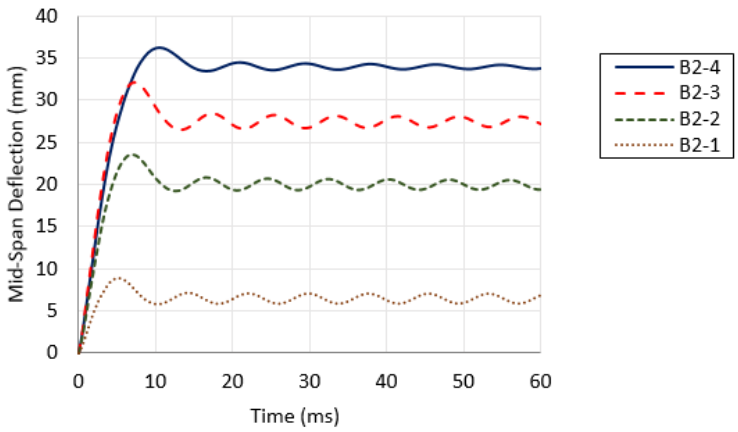

Figure 4. Mid-Span Deflection (ABAQUS Results).

The width of both tensile and compressive damage zones was also considered in the validation process. Table 5 shows the damage zone width for both experimental and numerical modeling. Fig. 5 to 8 show the damage extent for beams B2-2 and B2-4 due to blast loading, both at bottom (tension) and top (compression) face. For both beams, the damaged area in compression is larger than that in tension.

Table 5. Top and Bottom Damage.

Beam Sample	Compression Fracture Zone Width (cm)			Tensile Fracture Zone Width (cm)		
	Experiment	ABAQUS	Error %	Experiment	ABAQUS	Error %
B2-1	0	0	0	0	0	0
B2-2	8	6	25	7	5.9	15.8
B2-3	10	9	10	12	10.8	10.4
B2-4	12	10.3	14.6	15	13.8	8.3

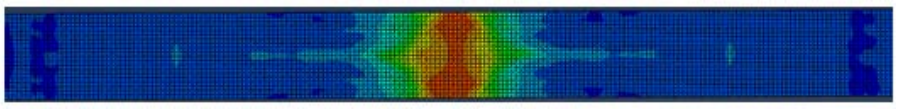

Figure 5. Compression Damage (B2-2).

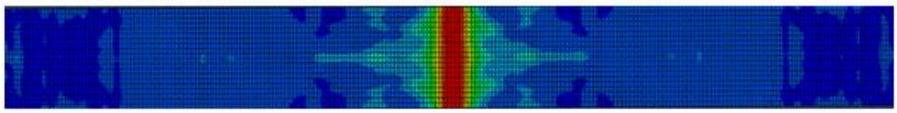

Figure 6. Tensile Damage (B2-2).

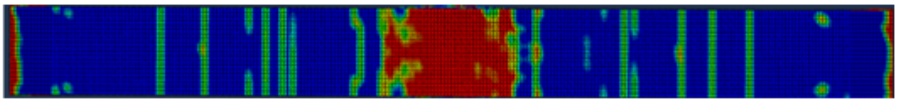

Figure 7. Compression Damage (B2-4).

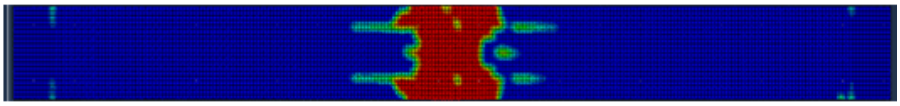

Figure 8. Tensile Damage (B2-4).

2.4. Strengthening Plan

After calibration, beam (B2-2) was studied numerically in order to check the efficiency of deferent applications of CFRP sheets on the mentioned beam. Four cases were considered. The first case was the beam (B0) which represent the beam (B2-2) without any strengthening. The second case was the beam (B1) which was strengthened by 2 bottom strips of CFRP each with 3.5 cm width and 90 cm length. Both strips were placed in a symmetric way as shown in Figure 9. The third case was the beam (B2) which was

strengthened with U-shape strips each with a width of 5 cm as shown in Fig. 10. Finally, the fourth case was the beam (B3) that was strengthened by diagonal strips each with 5 cm width as can be seen from Fig. 11. The properties of the used CFRP are illustrated in Table 6:

Table 6. Mechanical properties of CFRP sheets used strengthening.

Parameter	Notation	Value
Modulus of Elasticity	E	74.7 GPa
Tensile strength	F_t	933 MPa
Maximum strain	ϵ_t	1.25%

Figure 9. The bottom face of beam (B1) strengthened with bottom strips.

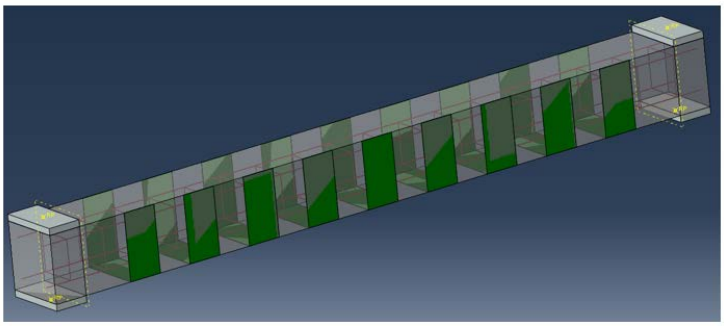

Figure 10. Beam (B2) strengthened with U-Strip.

Figure 11. Beam (B3) strengthened with diagonal strip.

3. Results and Discussion

3.1. Mid-Span deflection

It can be shown from Figure 12 that the beam strengthened with bottom strip “B1” had a less mid-span deflection than the unstrengthen beam “B0”, with a reduction percentage of 23 %. Similarly, the beam strengthened with U shape strip had a similar mid-span deflection value as beam B1, but with a less reduction percentage (around 21 %). These reductions are due to the high tensile strength of the CFRP sheets that helps in dissipating the energy from blast loading. These are similar to the findings reached by previous studies [17, 19]. On the other side, the beam strengthened with diagonal strips near supports (B3) experienced an increasing in the mid-span deflection as shown in Fig. 12. This is logical since diagonal strips will not affect the flexural behavior of RC beams; it is expected to affect the shear response of the beam. More details about mid-span deflection results are presented in Table 7.

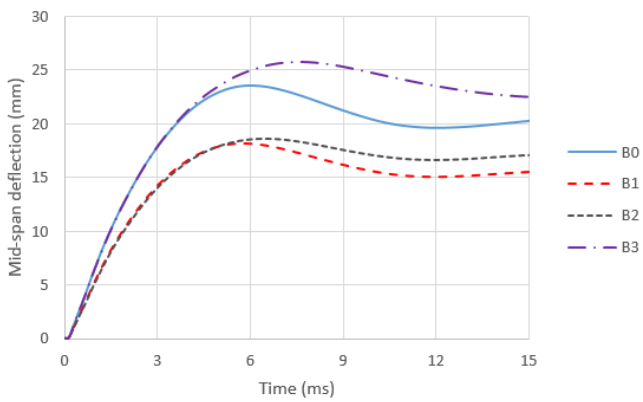

Figure 12. Mid-Span deflection for all beams.

3.2. Reinforcement strain

Using CFRP as strengthening techniques affects the strain in steel reinforcement depending on its position. For the beam strengthened with bottom strip “B1”, it can be clearly seen from Fig. 13 that the strain in steel reinforcement was reduced. The reduction was about 16.6 % as shown in Table 7. Also for the beams strengthened with U-shape strip and diagonal strip a similar behavior realized (around 16.1 % reduction for “B2” and 18.2 % for “B3”). This is similar to the bottom rebar strain findings by [16, 23]. This is from the high tensile strength of the CFRP sheets that resist a part of the tensile stresses resulted from the blast load.

As for strain at compression steel the behavior is different. According to Fig. 14, the strain at compression reinforcement for the beam strengthened with bottom strips “B1” was increased by 65.8 %. This is because the strengthened section is resisting the blast load without failing, and that requires from it more resistance, which mean on other words more stresses at tension and compression. A similar behavior was realized for the beam strengthened with diagonal strips “B3”, where the strain at compression reinforcement was increased by 30.5 %. The reason for this reduction is the same as for beam “B1” (the increasing in section strength). On the other side, beam “B2” that was strengthened with U-shape strips experienced a reduction in strain at compression reinforcement (around 60 %). This is due to the high confinement from the U-shape that makes the CFRP works at compression zone and drag some of the compression stresses from the compression reinforcement. More strain results are shown in Table 7.

Regarding strain at shear reinforcement, it can be concluded from Fig. 15 that both beams (B2) strengthened with U-shape strips and (B3) strengthened with diagonal strip experienced a reduction in strain at shear reinforcement stirrups near supports. This is due to the contribution of the U-shape and the diagonal CFRP sheets that have great contribution in resisting shear stress near supports. As for the beam strengthened with bottom strips (B1), the strain in shear reinforcement remains similar to that for the unstrengthen beam; since it works only in bottom tensile zone and had no contribution at shear zone near supports. Shear strain results for all beams are shown in Table 7.

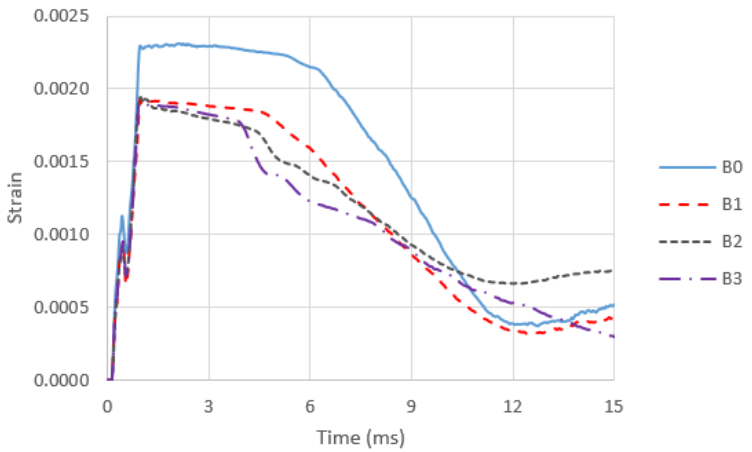

Figure 13. Tensile reinforcement strain.

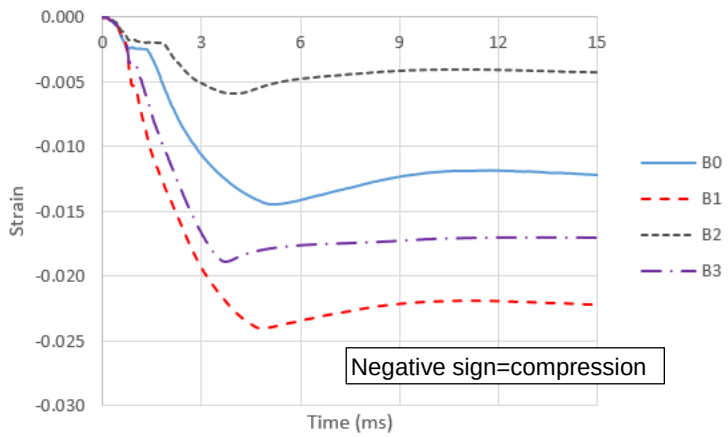

Figure 14. Compressive reinforcement strain.

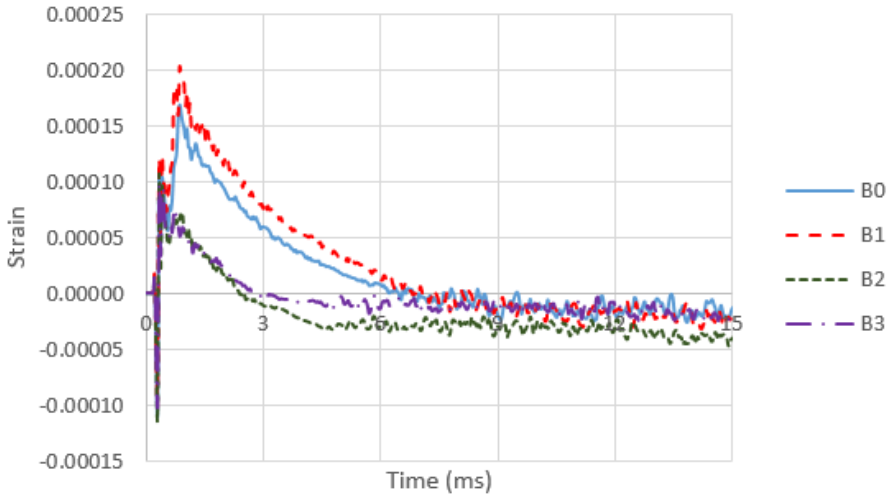

Figure 15. Shear reinforcement strain.

Table 7. Mid-span deflection, tensile strain, compressive strain, and shear strain results for all beams.

Beam	Mid-Span deflection "d" (mm)	Ratio ($d_{1,2,3}/d_0$)	Tensile reinforcement strain "ε_t"	Ratio ($\varepsilon_{t1,2,3}$ / ε_{t0})	Compressive reinforcement strain "ε_c"	Ratio ($\varepsilon_{c1,2,3}$ / ε_{c0})	Shear reinforcement strain "ε_s"	Ratio ($\varepsilon_{s1,2,3}$ / ε_{s0})
B0	23.5	-	0.00230	-	0.014	-	0.00017	-
B1	18.0	0.77	0.00192	0.83	0.023	1.66	0.00020	1.18
B2	18.5	0.79	0.00193	0.84	0.006	0.40	0.00011	0.65
B3	26.0	1.10	0.00188	0.82	0.019	1.35	0.00009	0.53

3.3. Structural damage

The tensile damage at bottom face for each beam is shown in Fig. 16 to 19. The un-strengthened beam experienced a tensile damaged zone with a width of 5.9 cm according to Fig. 6 and Table 5. This damage is due to plastic hinge formation at the middle of the beam and that may lead at some point to a total collapse of the beam due to un-stability. Although using CFRP in the beam with bottom strip "B1" has reduced the deflection and the strain at bottom steel reinforcement, it has increased the tensile damage at the bottom zone due to the shear failure between the CFRP sheet and the concrete bottom surface. As for the beams with U-shape strips "B2" and diagonal strips "B3", the tensile damage was not as concentrated as the beam "B1" since the CFRP surface was not fully attached to the concrete bottom surface. However, it still has less damage than the reference beam (two major cracks each has a width of nearly 1.5 cm).

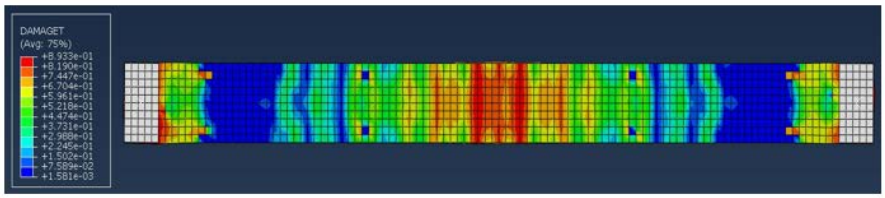

Figure 16. Bottom face damage for beam B0.

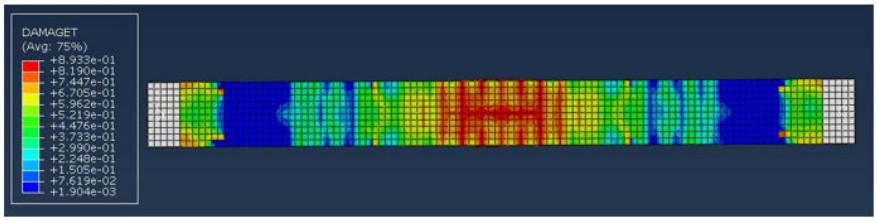

Figure 17. Bottom face damage for beam B1.

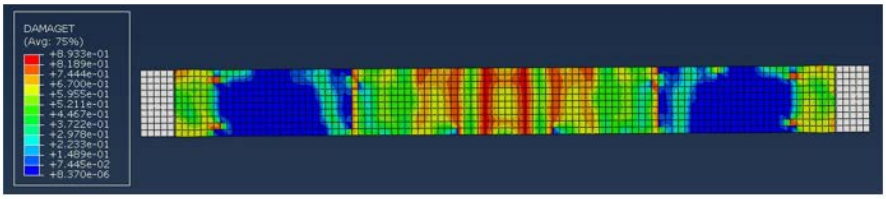

Figure 18. Bottom face damage for beam B2.

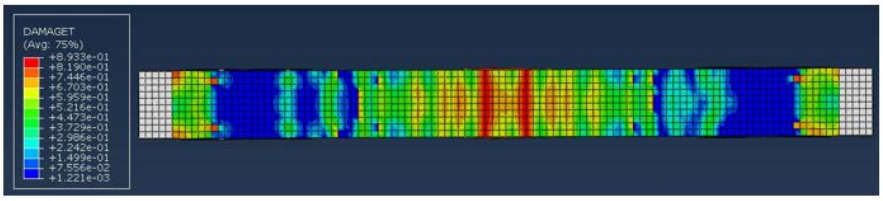

Figure 19. Bottom face damage for beam B3.

Fig. 20 to 23 show the compression damage in all beams. It can be seen that using CFRF sheets in deferent forms increased the compression damage at the beam top face. This is due to the bending resistance provided by the CFRP sheets that leads to a stress concentration in both tension and compression and as a results a more damage occurred at the top face. Both damage results (top and bottom) were similar to many previous researches [16, 17, 19, 23].

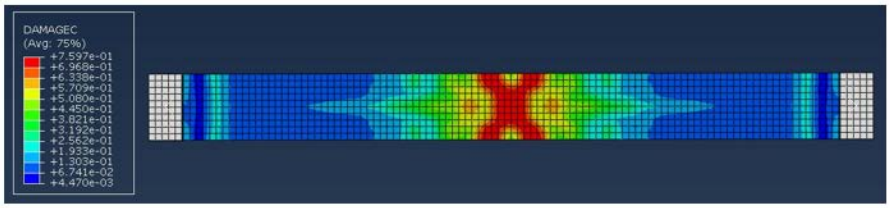

Figure 20. Top face damage for beam B0.

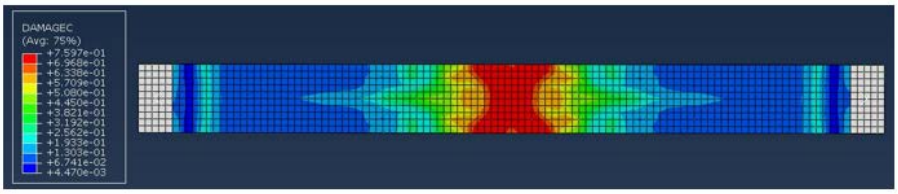

Figure 21. Top face damage for beam B1.

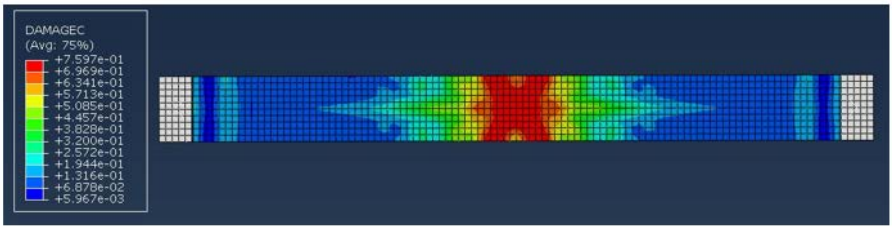

Figure 22. Top face damage for beam B2.

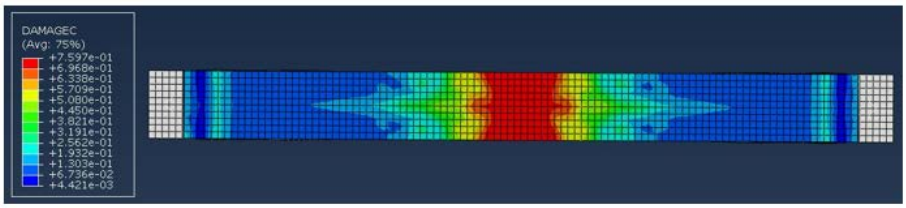

Figure 23. Top face damage for beam B3.

Tensile stresses in CFRP sheets are represented in Fig. 24 to 29. Fig. 24 shows the tensile stress in the CFRP used in the beam strengthened with bottom strip. The maximum stress was at the middle of the strip since the maximum moment was at the beam mid-span. It can be concluded that the CFRP did not

reach its tensile capacity. Fig. 25 shows the position of the maximum axial stress in the CFRP sheet. Similarly, the stresses in CFRP sheets in the strengthened beams with U-shape didn't reach the tensile capacity as shown in Figure 26 The critical strips lied at the mid-span of the strengthened beam as in Fig. 27. This also applies for the beam strengthened with diagonal strip where the critical strip lies near the support (Figure 28 and 29).

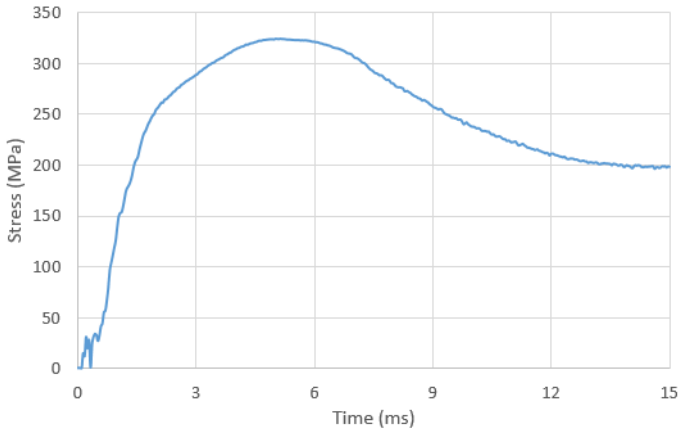

Figure 24. Tension stress in CFRP for beam B1.

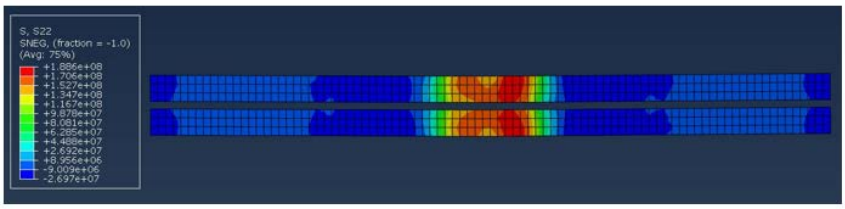

Figure 25. Position of maximum CFRP tension stress for beam B1.

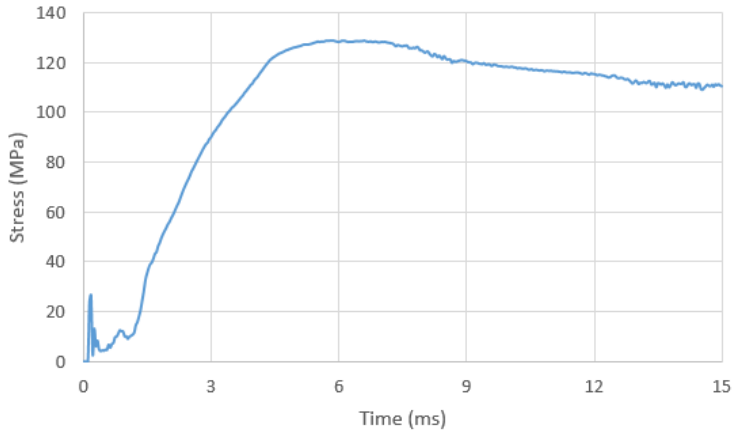

Figure 26. Tension stress in CFRP for beam B2.

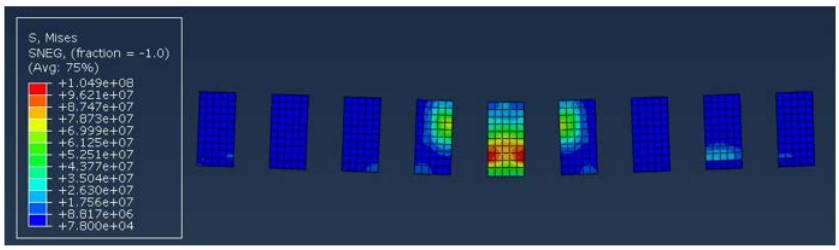

Figure 27. Position of maximum CFRP tension stress for beam B2.

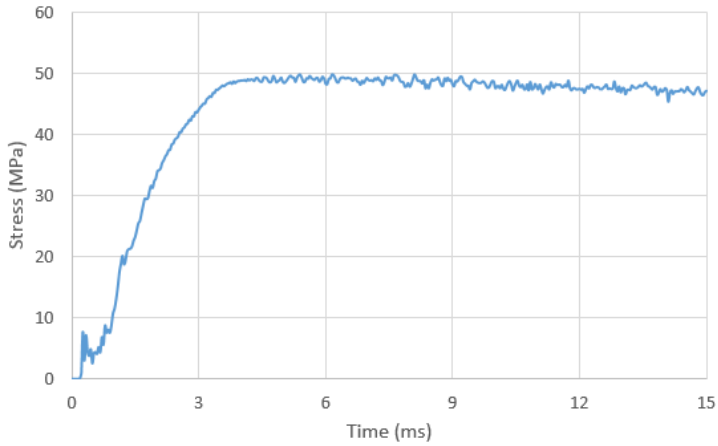

Figure 28. Tension stress in CFRP for beam B3.

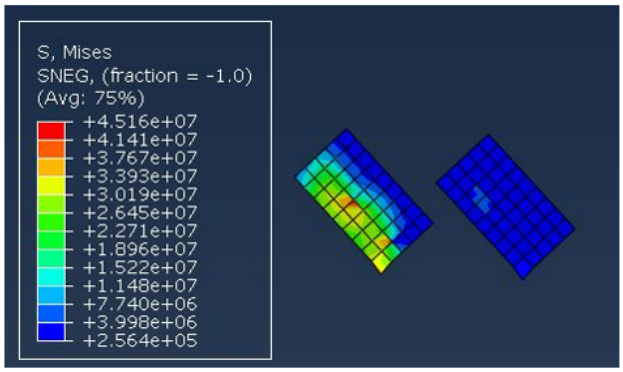

Figure 29. Position of maximum CFRP tensile stress for beam B3.

4. Conclusion

The following conclusions can be made:

- Using CFRP in the bottom tensile face of RC beams helped in absorbing blast energy. This led to the reduction of the mid-span deflection for beams strengthened with bottom strips and U-shaped strips, with a better performance for the bottom strips (23 % reduction for bottom strips compared to 21 % for the U-shaped strips). As for the beam strengthened with diagonal strips this was not efficient as expected since the diagonal strips will act against shear stresses.
- Regarding steel reinforcement in tensile zone, using CFRP led to a reduction in the tensile strain in flexural reinforcement in all cases. The reduction was similar in all cases. On the other side, using CFRP in U-shapes was proved to confine the beam, which leads into a reduction in the compression steel strain too. This was not the case for beams with other strengthening techniques. As for shear reinforcement the best system was both diagonal and the U-shaped strips; since they both have vertical layers that resist the shear stresses. In contrast, the beam strengthened with bottom strips had no effect nearly on the shear reinforcement, which is logic too.
- Although using CFRP helped in dissipating blast energy, the beam strengthened with bottom strips (B1) has experienced more extensive tensile damage than the unstrengthen beam (B0). On the other side, both beams (B2) and (B3) that were strengthened with U-shaped and diagonal strips respectively had less tensile extensive damage than beams (B0) and (B1) due to the less contact area at the bottom face of the beam. As for compression damage at the top face of the beams, all strengthened beams (B1, B2, and B3) were damaged more than the reference beam (B0); since the CFRP laminates provide more confinement for the beam and hence more compression resistance were performed which led to the increased damage.
- There is no damage in any of the CFRP sheets since the maximum stresses inside each sheet did not reach their tensile capacity.

References

1. Temsah, Y., Jahami, A., Khatib, J., Sonebi, M. Numerical analysis of a reinforced concrete beam under blast loading. MATEC Web of Conferences. 2018. 149. Pp. 02063. DOI: 10.1051/matecconf/201814902063
2. Temsah, Y., Jahami, A., Khatib, J., Sonebi, M. Numerical Derivation of Iso-Damaged Curve for a Reinforced Concrete Beam Subjected to Blast Loading. MATEC Web of Conferences. 2018. 149. Pp. 02016. DOI: 10.1051/matecconf/201814902016

3. Jahami, A., Temsah, Y., Khatib, J. The efficiency of using CFRP as a strengthening technique for reinforced concrete beams subjected to blast loading. International Journal of Advanced Structural Engineering. 2019. 11(4). Pp. 411–420. DOI: 10.1007/s40091-019-00242-w
4. Cotsovos, D.M., Pavlović, M.N. Modelling of RC beams under impact loading. Proceedings of the Institution of Civil Engineers: Structures and Buildings. 2012. 165(2). Pp. 77–94. DOI: 10.1680/stbu.2012.165.2.77
5. Damasceno, I.I.R., Ferreira, M. de P., de Oliveira, D.R.C. Vigas de concreto armado sob cargas de impacto. Acta Scientiarum – Technology. 2014. 36(1). Pp. 23–31. DOI: 10.4025/actascitechnol.v36i1.17561
6. Rajput, A., Iqbal, M.A. Ballistic performance of plain, reinforced and pre-stressed concrete slabs under normal impact by an ogival-nosed projectile. International Journal of Impact Engineering. 2017. 110. Pp. 57–71. DOI: 10.1016/j.ijimpeng.20-17.03.008.
7. Jahami, A., Temsah, Y., Khatib, J., Baalbaki, O., Darwiche, M., Chaaban, S. Impact behavior of rehabilitated post-tensioned slabs previously damaged by impact loading. Magazine of Civil Engineering. 2020. 93(1). Pp. 134–146. DOI: 10.18720/MCE.9-3.11.
8. Al Rawi, Y., Temsah, Y., Baalbaki, O., Jahami, A., Darwiche, M. Experimental investigation on the effect of impact loading on behavior of post- tensioned concrete slabs. Journal of Building Engineering. 2020. 31. Pp. 101207. DOI: 10.1016/j.jobe.2020.101207.
9. Mhanna, H.H., Hawileh, R.A., Abdalla, J.A. Shear strengthening of reinforced concrete beams using CFRP wraps. Procedia Structural Integrity. 2019. 17. Pp. 214–221. DOI: 10.1016/j.prostr.2019.08.029.
10. Michałowska-Maziejuk, D., Goszczyńska, B., Trąmpczyński, W. Effectiveness of strengthening pre-loaded RC beams with CFRP strips in conventional and accelerated strengthening procedures. MATEC Web of Conferences. 2019. 284. Pp. 06005. DOI: 10.1051/matecconf/201928406005
11. Naser, M.Z., Hawileh, R.A., Abdalla, J.A. Fiber-reinforced polymer composites in strengthening reinforced concrete structures: A critical review. Engineering Structures. 2019. 198(June). Pp. 109542. DOI: 10.1016/j.engstruct.2019.109542.
12. Yu, F., Zhou, H., Jiang, N., Fang, Y., Song, J., Feng, C., Guan, Y. Flexural experiment and capacity investigation of CFRP repaired RC beams under heavy pre-damaged level. Construction and Building Materials. 2020. 230. Pp. 117030. DOI: 10.1016/j.conbuildmat.2019.117030.
13. Yuan, X., Zhu, C., Zheng, W., Hu, J., Tang, B. Flexure Performance of Externally Bonded CFRP Plates-Strengthened Reinforced Concrete Members. Mathematical Problems in Engineering. 2020. 2020. DOI: 10.1155/2020/2604024
14. Kishore, R., Zia Nasiry, N., Muslim Rujhan, A. Strengthening of Reinforced Concrete Beams using CFRP laminates. ASIAN JOURNAL OF CIVIL ENGINEERING (BHRC). 2016. 17(2). Pp. 159–167.
15. Osman, B.H., Wu, E., Ji, B., Abdulhameed, S.S. Effect of reinforcement ratios on shear behavior of concrete beams strengthened with CFRP sheets. HBRC Journal. 2018. 14(1). Pp. 29–36. DOI: 10.1016/j.hbrcj.2016.04.002.
16. Bodzak, P. Flexural behaviour of concrete beams reinforced with different grade steel and strengthened by CFRP strips. Composites Part B: Engineering. 2019. 167(January). Pp. 411–421. DOI:10.1016/j.compositesb.2019.02.056.
17. Ali, M.I., Saleh, Y.A., Al Hasani, L.E., Khazaal, A.S., Abdulla, A.I. Behavior of RC Beams Strengthened by CFRP and Steel Rope under Frequent Impact Load. Journal of advanced Sciences and Engineering Technologies. 2018. 1(1). Pp. 30–42. DOI: 10.32441/jaset.v1i1.74
18. Pham, T.M., Chen, W., Elchalakani, M., Karrech, A., Hao, H. Experimental investigation on lightweight rubberized concrete beams strengthened with BFRP sheets subjected to impact loads. Engineering Structures. 2020. 205(December 2019). Pp. 110095. DOI: 10.1016/j.engstruct.2019.110095.
19. Wang, W., Chouw, N. Behaviour of CFRC beams strengthened by FFRP laminates under static and impact loadings. Construction and Building Materials. 2017. 155. Pp. 956–964. DOI: 10.1016/j.conbuildmat.2017.08.031.
20. Fujikake, K., Soeum, S., Matsui, T. CFRP strengthened RC beams subjected to impact loading. Procedia Engineering. 2017. 210. Pp. 173–181. DOI: 10.1016/j.proeng.2017.11.063.
21. Jahami, A., Temsah, Y., Khatib, J., Sonebi, M. NUMERICAL STUDY FOR THE EFFECT OF CARBON FIBER REINFORCED. Symposium on Concrete Modelling (CONMOD2018). (August)Delft, Netherlands, 2018. Pp. 259–267.
22. Almusallam, T., Al-Salloum, Y., Alsayed, S., Iqbal, R., Abbas, H. Effect of CFRP strengthening on the response of RC slabs to hard projectile impact. Nuclear Engineering and Design. 2015. 286. Pp. 211–226. DOI: 10.1016/j.nucengdes.2015.02.017
23. Radnić, J., Matešan, D., Grgić, N., Baloević, G. Impact testing of RC slabs strengthened with CFRP strips. Composite Structures. 2015. 121. Pp. 90–103. DOI: 10.1016/j.compstruct.2014.10.033
24. Zhang, D., Yao, S.J., Lu, F., Chen, X.G., Lin, G., Wang, W., Lin, Y. Experimental study on scaling of RC beams under close-in blast loading. Engineering Failure Analysis. 2013. 33. Pp. 497–504. DOI: 10.1016/j.engfailanal.2013.06.020
25. Hibbitt, Karlsson, Sorensen. ABAQUS User's Manual, Pawtucket. 6th Edition. 2011.
26. Lubliner, J., Oliver, J., Oller, S., Onate, E. a Plastic-Damage Model. International Journal of Solids and Structures. 1989. 25(3). Pp. 299–326.
27. Lee, J., Fenves, G. Plastic-damage model for cyclic loading of concrete structure. Engineering Mechanics. 1998. 124(8). Pp. 892–900.

Contacts:

Ali Jahami, ahjahamy@hotmail.com

Yehya Temsah, ytemsah@bau.edu.lb

Jamal Khatib, j.khatib@bau.edu.lb

Ossama Baalbaki, obaalbaki@bau.edu.lb

Said Kenai, sdkenai@yahoo.com

© Jahami, A., Temsah, Y., Khatib, J., Baalbaki, O., Kenai, S., 2021

Magazine of Civil Engineering

ISSN 2712-8172

journal homepage: http://engstroy.spbstu.ru/

DOI: 10.34910/MCE.103.10

Bending of stiffened plates considering different stiffeners orientations

V. Pinto, M. Cunha, K. Martins, L. Rocha, E. Dos Santos, L. Isoldi*
Federal University of Rio Grande – FURG, Rio Grande, Brazil
** E-mail: liercioisoldi@gmail.com*

Keywords: stiffeners, geometric optimization, deflection, numerical simulation, computational modeling

Abstract. In engineering, the search for geometric configurations that lead to superior performance is always a design goal. Regarding structural components, such as plates, it is necessary to guarantee limits for its deflections, according to design standards. In this sense, methodologies devoted to reducing the out-of-plane displacements by geometric analysis are a relevant to subject research. Therefore, the present work is addressed to study several arrangements of stiffened steel plates defined by the Constructal Design Method (CDM). These plates were analyzed and solved applying computational modeling based on the Finite Element Method (FEM), aiming through the Exhaustive Search (ES) technique to evaluate the influence of stiffeners orientation on to the maximum deflection. Taking a non-stiffened plate as reference and keeping the total material volume constant, portions of its volume were transformed into stiffeners through the volumetric fraction parameter, representing the ratio between the volumes of stiffeners and reference plate. Adopting volumetric fraction values of 0.1; 0.2; 0.3; 0.4 and 0.5, it were established for each one 25 geometric arrangements of stiffened plates, considering the stiffeners orientations in 0 ° and 45 °, varying for each new arrangement the ratio between the height and thickness of the stiffeners h_s/t_s. The results showed that transforming a portion of material from a non-stiffened plate into stiffeners can decrease the maximum deflections by more than 95 %. Besides that, it has been demonstrated that stiffeners oriented at 45 ° can reduce maximum deflection by more than 60 % compared to stiffeners traditionally oriented at 0 °.

1. Introduction

Plates are flat and two-dimensional structural elements, whose main feature is the thickness much smaller than the width and length. Generally, the plates are subjected to loads that cause out-of-plane displacements. Those loads are transmitted in two directions, generating resistant bending, shearing and torsion efforts, allowing the plates to blend lightness and good load support capacity [1, 2].

Plates are broadly used in civil, aerospace and naval engineering. However, due to slenderness, it is usual to introduce reinforcements (stiffeners), in order to increase the flexural rigidity. The stiffeners can take on different cross section shapes and are traditionally welded to the plane of the plates in the longitudinal and/or transverse directions [3, 4].

In the analysis of non-stiffened thin plates, stresses and displacements can be obtained in a relatively simple way, using the classic Kirchhoff differential equation, applying for instance, Navier or Lévy solutions [3]. In its turn, regarding non-stiffened thick plates it is possible applying the Reisner's theory [5]. In addition, Ref. [6] indicates that the method based on the fundamental principles of the minimum of additional energy and possible displacements can be applied to solve both thin and thick non-stiffened plates.

Concerning stiffened plates, analytical solutions are unusual. Among the existing studies it is possible to quote Powell and Ogden [7] that proposed to idealize the stiffened plate into an equivalent orthotropic plate in order to analyze bridge decks.

This work is licensed under a CC BY-NC 4.0

However, analytical approaches for stiffened plates have limitations related to geometry, boundary conditions and loading, which can lead to inaccurate results. Thus, numerical methods become a good alternative that has been developed and applied by several researches over the past few years.

Rossow and Ibrahimkhail [8] applying the Constraint Method, studied the behavior of stiffened plates under uniform transverse loading with stiffeners in eccentric and concentric conditions, verifying their results using the Finite Element Method (FEM) by the NASTRAN® and STRUDL® software. Mukhopadhyay and Satsangi [9] used the FEM and developed a numerical model using isoparametric elements to analyze stiffened plates under bending, which made possible to insert the transverse shear deformations and curvature limits. Based on the energy principle, Kukreti and Cheraghi [10] presented an approach for stiffened plates where the deflection was determined by the product of polynomial and trigonometric series. Bedair [11] used Sequential Quadratic Programming (SQP) to analyze stiffened plates subject to uniform transverse loading, where the proposed model considered the system plate-stiffener rigidly connected. The Boundary Element Method (BEM) was applied by Tanaka et al. [12] to study the behavior of stiffened plates under bending, so that the forces and moments that interact in the plate-stiffener connection were treated as unknown variables and implemented in the numerical solution, being approximated through interpolation functions. In turn, the study proposed by Sapountzakis and Katsikadelis [13] used continuity equations to determine the forces that cause deflection and deformation between the plate-stiffener interface. In its turn, some numerical studies have been carried out seeking a better structural performance of stiffened plates. Singh et al. [14] used the ANSYS® software to perform a parametric analysis on stiffened plates under bending, considering different loads and boundary conditions. Also using the ANSYS® software, Troina et al. [15] applied the Constructal Design Method (CDM) allied to the Exhaustive Search (ES) technique for the analysis of different plate arrangements with orthogonal stiffeners in order to minimize the central deflection of stiffened plates.

More specifically, in structural engineering when it comes to the design of flat components subject to transverse loads, whether in metallic (present study) or reinforced concrete (e.g., slabs) structures, besides to ensure the safety, it is necessary to evaluate conditions of usability, for instance, to avoid deflections that are not in accordance with design standards. In this context, the development of methodologies related to the geometric evaluation dedicated to improving the mechanical performance of this kind of structure by means the minimization of its maximum deflection are relevant.

Given the above, the present study consists in the application of the CDM in a structural engineering component (stiffened steel plate), since this geometric evaluation method is a consecrated approach largely applied for heat transfer and fluid mechanics problems, however its application in mechanic of materials area it has not yet been properly investigated by the scientific community.

Therefore, as in Troina et al. [15], the present study applies CDM to define the geometric configurations of analyzed stiffened plates (search space), being the mechanical behavior of these plates numerically simulated through ANSYS® software. Finally, employing the ES technique, the geometric optimization of the stiffened plates was performed, aiming the minimization of the maximum deflection. It is important to highlight that there are three important differences in relation to the work of Troina et al. [15] which justify the research carried out here: i) the validation of proposed computational model by means of an experimental test; ii) the evaluation of the influence of stiffeners oriented at 45 °; and iii) the consideration of the maximum deflection as performance indicator.

2. Methods

2.1. Computational Modeling

Nowadays, computational modeling is an indispensable tool for analysis of complex engineering problems, enabling to test and extrapolate hypotheses till extreme values with safety and accuracy. The numerical methods, that are the basis of CAD tools (Computer-Aided Design), such as Finite Difference Method (FDM) and Finite Element Method (FEM), are applied in a range of scientific and industrial solutions that deal with analysis, optimization and development of products and projects [16, 17].

In this study, the FEM was adopted by means of the ANSYS® software. The finite element used to discretize all analyzed computational domains was the SHELL281 in the triangular version. This is a two-dimensional shell-type element, suitable for modeling thin plates, which has 6 nodes with 6 degrees of freedom per node: 3 rotations and 3 translations in relation to the x, y and z axes [18].

2.1.1. Computational Model Verification

The case used for computational model verification, as shown in Fig. 1, it was previously solved by Troina et al. [19] through ANSYS®, using the three-dimensional finite element SOLID95 in the hexahedral version.

The stiffened plate with a boundary condition of simply supported edges was subjected to a uniform transverse loading of 68.95 kPa and has material with an elastic modulus of 206.8427 GPa and Poisson's ratio of 0.3.

Here, the case was solved using the finite element SHELL281 in the triangular version, with a mesh that totaled 30,400 elements, defined according to the mesh convergence test presented in Fig. 2, where the result obtained by Troina et al. [19] is also presented.

Observing Fig. 2, it is possible to infer that the difference between the central deflection results U_z obtained in the present study of 0.281 mm and by Troina et al. [19] of 0.278 mm is 1.08 %, verifying the proposed computational model.

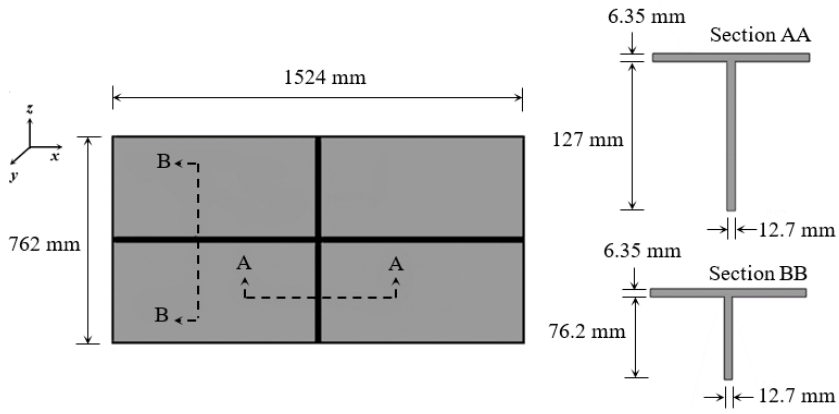

Figure 1. Rectangular plate with 2 orthogonal stiffeners.

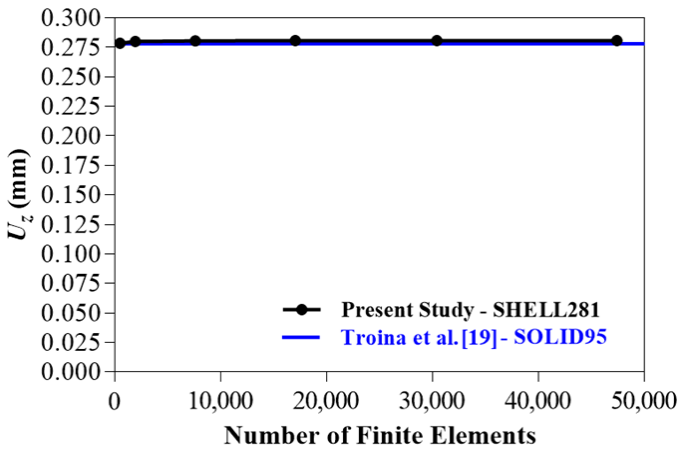

Figure 2. Computational model verification.

2.1.2. Computational Model Validation

The experimental test used for validation was presented by Carrijo et al. [20], as shown in Fig. 3. The square plate with eight stiffeners has an elastic modulus of 2.5 GPa and a Poisson's ratio of 0.36, being subjected to a uniform transverse load of 0.96 kPa. Concerning the boundary conditions, the plate is simply supported just on its four corners.

The experiment was numerically simulated using the finite element SHELL281 in its triangular version, with a mesh that totaled 5,070 elements, defined after the mesh convergence test presented in Fig. 4, which also shows the result found by Carrijo et al. [20].

Observing Fig. 4 it is possible to perceive that the difference for the central deflection U_z between the present study (6.505 mm) and the experimental results (6.220 mm) is 4.58 %, validating the computational model.

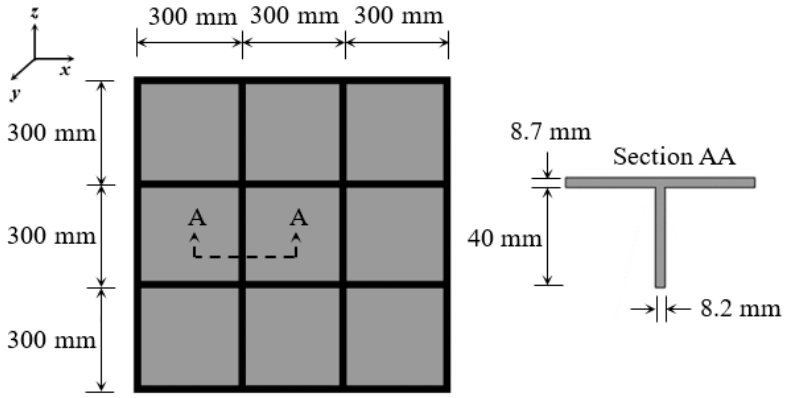

Figure 3. Square plate with eight stiffeners.

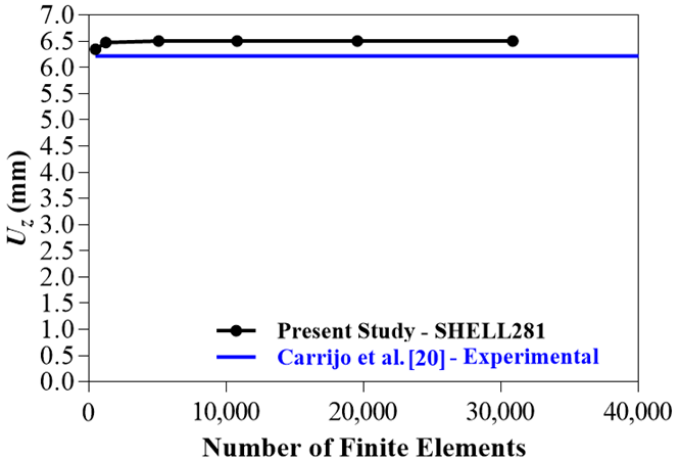

Figure 4. Computational model validation.

2.2. Constructal Design Method (CDM)

The physical phenomenon behind the vast geometric complexity of flow systems that occur in nature is called the Construct Law. These systems, whether animated or inanimate, tend to be imperfect, thus they evolve in time in order to distribute these imperfections in the best possible way, facilitating access to the currents that flow through them [21].

The performance of a flow system brings inherent restrictions, which can be, e.g., the space allocated for the development of the system, the material available and also limited rates of pressure, temperature or stress. The Constructal Design Method (CDM) is the practical application of the Constructal Law. Respecting the imposed restrictions, the degrees of freedom of the problem related to the geometric parameters are modified in order to assess its influence on a predefined performance indicator. Therefore, the CDM provides a guide for the designer to evaluate the flow system geometry, aiming to improve its performance, based on restrictions and objectives [22–24].

As earlier mentioned, the CDM is widely applied in problems of fluid mechanics and heat transfer, being possible to find several publications regarding these topics. However, in structural analysis, there are only a few studies employing the CDM, as in Bejan and Lorente [23], Lorente et al. [25] and Isoldi et al. [26], where the viability of its application in the analysis of structures was checked, analogously to applications in fluid mechanics and heat transfer.

Recently, some studies have proven the effectiveness of the CDM in structural applications: in the buckling analysis of perforated plates (Helbig et al. [27]; and Da Silva et al. [28]); in the buckling analysis of stiffened plates (Lima et al. [29] and Lima et al. [30]); in the bending analysis of stiffened plates (De Queiroz et al. [31]; Pinto et al. [32]); and Troina et al. [15]); and in the analysis of aircraft structures (Mardanpour et al. [33] and Izadpanahi et al. [34]).

To apply the CDM in this study, a non-stiffened steel plate with fixed dimensions was taken as reference: length a = 2000 mm, width b = 1000 mm and thickness t = 20 mm (thickness before transforming the volume portion into stiffeners). So, keeping the total material volume constant, as well as the dimensions a and b, different percentages of material deducted entirely from the thickness of this reference plate were converted into stiffeners through the volumetric fraction ϕ, which represents the ratio between the stiffeners

volume V_s and the reference plate volume V_r. So, five volumetric fractions values were adopted: ϕ = 0.1; 0.2; 0.3; 0.4; and 0.5; generated, respectively, by the t_p values of: 18 mm, 16 mm, 14 mm, 12 mm and 10 mm. Emphasizing that t_p is the thickness of the stiffened plates, i.e., after transforming the volume portion of the non-stiffened plate into stiffeners.

Regarding the stiffeners, two orientations were considered: 0° (not inclined, being positioned in the longitudinal and transverse directions), and 45° (inclined in relation to the plate edges). Because of that, the volumetric fraction ϕ for the 0 ° and 45 ° orientations are defined, respectively, by:

$$\phi = \frac{V_s}{V_r} = \frac{n_{sx}\left(ah_s t_s\right) + n_{sy}\left[\left(b - n_{sx}t_s\right)h_s t_s\right]}{abt} \tag{1}$$

$$\phi = \frac{V_s}{V_r} = \frac{\sum_{d=1}^{n}\left[\left(d_1+d_2+d_3+Ld_n\right)h_s t_s\right]-\left(n_{int}h_s t_s^2\right)}{abt} \tag{2}$$

where h_s and t_s are, respectively, the height and thickness of the stiffeners. Exclusively for plate arrangements formed with stiffeners oriented at 45 °, the parameters d_1, d_2, d_3, ...d_n represent the length of the stiffeners, being n the total number and n_{int} the number of intersections. Moreover, to identify the plates arrangements, it was adopted the following format: $\mathrm{P}(n_{sx},n_{sy})$ for plates with stiffeners oriented at 0° and $\mathrm{P}'(n_{sx'},n_{sy'})$ for plates with stiffeners oriented at 45 °, being n_{sx} and n_{sy} the number of stiffeners in the x and y directions, as well as, $n_{sx'}$ and $n_{sy'}$ representing the number of stiffeners in the x' and y' directions. All of these parameters are shown in Fig. 5.

For each ϕ value, it were varied the degrees of freedom (stiffeners orientation, number of stiffeners and h_s/t_s ratio) defining the different geometric configurations which composes the search space. So, the plates were classified into groups according to the number of stiffeners, which varied from 2 to 6 in each direction (x, y and x', y'). The values of h_s/t_s ratio was consequence of the stiffeners heights h_s, established by Eqs. (1) and (2) for the different ϕ values, respecting each orientation, when different stiffeners thicknesses t_s were assigned (according to commercial plates thickness, in inches): $\frac{1}{8}$; $\frac{3}{16}$; $\frac{1}{4}$; $\frac{5}{16}$; $\frac{3}{8}$; $\frac{1}{2}$; $\frac{5}{8}$; $\frac{3}{4}$; $\frac{7}{8}$; 1; $1\frac{1}{4}$; $1\frac{1}{2}$; $1\frac{5}{8}$; $1\frac{3}{4}$; 2; $2\frac{1}{4}$; $2\frac{1}{2}$; and 3. The ranges of h_s/t_s variation can be identified in the graphs presented in the Figs. 11 to 35 and are exactly presented in Tables 1 to 5.

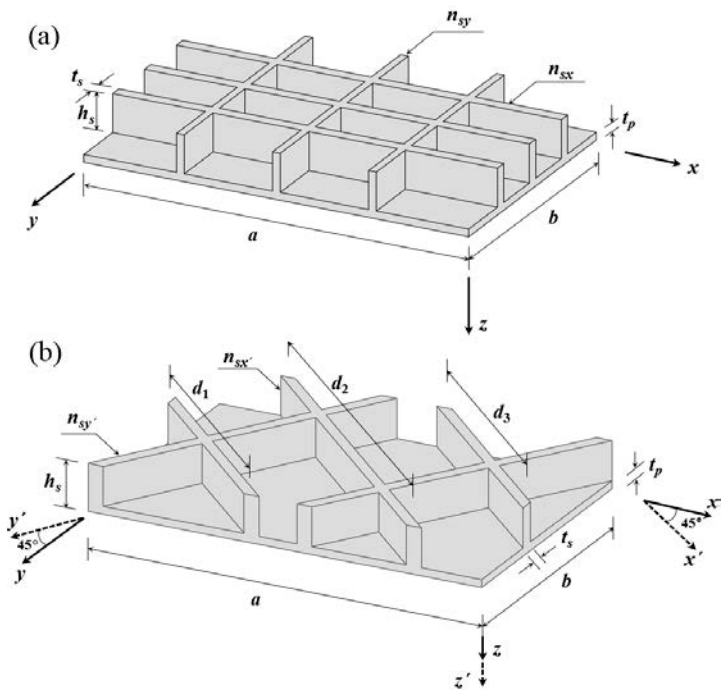

Figure 5. Geometric parameters of stiffened plates: (a) P(3,3); (b) P'(3,2).

Fig. 6 shows schematically the definition of the plate arrangements (search space) generated from the CDM application, which were numerically simulated in this study.

Table 1. Range of h_s/t_s for ϕ = 0.1.

Groups	P(n_{sx},n_{sy}) P'($n_{sx'}$,$n_{sy'}$)	h_s/t_s Range	
		Stiffeners Orientation	
		0°	45°
A	(2,2)	1.051 ≤ h_s/t_s≤ 66.065	1.106 ≤ h_s/t_s≤ 70.003
	(2,3)	1.182 ≤ h_s/t_s≤ 56.662	1.293 ≤ h_s/t_s≤ 62.280
	(2,4)	1.037 ≤ h_s/t_s≤ 49.602	1.117 ≤ h_s/t_s≤ 53.881
	(2,5)	1.230 ≤ h_s/t_s≤ 44.106	1.295 ≤ h_s/t_s≤ 46.721
	(2,6)	1.109 ≤ h_s/t_s≤ 39.706	1.181 ≤ h_s/t_s≤ 42.650
B	(3,2)	1.031 ≤ h_s/t_s ≤ 49.562	1.293 ≤ h_s/t_s ≤ 62.280
	(3,3)	1.228 ≤ h_s/t_s ≤ 44.091	1.558 ≤ h_s/t_s ≤ 56.091
	(3,4)	1.110 ≤ h_s/t_s ≤ 39.707	1.364 ≤ h_s/t_s ≤ 49.186
	(3,5)	1.012 ≤ h_s/t_s ≤ 36.116	1.199 ≤ h_s/t_s ≤ 43.150
	(3,6)	1.351 ≤ h_s/t_s ≤ 33.121	1.603 ≤ h_s/t_s ≤ 39.654
C	(4,2)	1.101 ≤ h_s/t_s ≤ 39.656	1.490 ≤ h_s/t_s ≤ 53.881
	(4,3)	1.006 ≤ h_s/t_s ≤ 36.085	1.364 ≤ h_s/t_s ≤ 49.186
	(4,4)	1.347 ≤ h_s/t_s ≤ 33.103	1.773 ≤ h_s/t_s ≤ 43.826
	(4,5)	1.248 ≤ h_s/t_s ≤ 30.577	1.584 ≤ h_s/t_s ≤ 38.993
	(4,6)	1.162 ≤ h_s/t_s ≤ 28.409	1.465 ≤ h_s/t_s ≤ 36.116
D	(5,2)	1.336 ≤ h_s/t_s ≤ 33.050	1.886 ≤ h_s/t_s ≤ 46.721
	(5,3)	1.240 ≤ h_s/t_s ≤ 30.539	1.745 ≤ h_s/t_s ≤ 43.150
	(5,4)	1.156 ≤ h_s/t_s ≤ 28.383	1.584 ≤ h_s/t_s ≤ 38.993
	(5,5)	1.084 ≤ h_s/t_s ≤ 26.511	1.418 ≤ h_s/t_s ≤ 35.061
	(5,6)	1.019 ≤ h_s/t_s ≤ 24.870	1.326 ≤ h_s/t_s ≤ 32.735
E	(6,2)	1.146 ≤ h_s/t_s ≤ 28.331	1.720 ≤ h_s/t_s ≤ 42.650
	(6,3)	1.075 ≤ h_s/t_s ≤ 26.471	1.603 ≤ h_s/t_s ≤ 39.654
	(6,4)	1.013 ≤ h_s/t_s ≤ 24.841	1.465 ≤ h_s/t_s ≤ 36.116
	(6,5)	1.492 ≤ h_s/t_s ≤ 23.399	2.072 ≤ h_s/t_s ≤ 32.735
	(6,6)	1.414 ≤ h_s/t_s ≤ 22.116	1.949 ≤ h_s/t_s ≤ 30.713

Table 2. Range of h_s/t_s for ϕ = 0.2.

Groups	P(n_{sx},n_{sy}) P'($n_{sx'}$,$n_{sy'}$))	h_s/t_s Range	
		Stiffeners Orientation	
		0°	45°
A	(2,2)	1.347 ≤ h_s/t_s ≤ 59.283	1.414 ≤ h_s/t_s ≤ 62.785
	(2,3)	1.162 ≤ h_s/t_s ≤ 50.860	1.268 ≤ h_s/t_s ≤ 55.882
	(2,4)	1.021 ≤ h_s/t_s ≤ 44.533	1.095 ≤ h_s/t_s ≤ 48.340
	(2,5)	1.418 ≤ h_s/t_s ≤ 88.213	1.488 ≤ h_s/t_s ≤ 93.443
	(2,6)	1.279 ≤ h_s/t_s ≤ 79.414	1.357 ≤ h_s/t_s ≤ 85.301
B	(3,2)	1.013 ≤ h_s/t_s ≤ 44.480	1.268 ≤ h_s/t_s ≤ 55.882
	(3,3)	1.414 ≤ h_s/t_s ≤ 39.585	1.792 ≤ h_s/t_s ≤ 50.347
	(3,4)	1.279 ≤ h_s/t_s ≤ 35.660	1.568 ≤ h_s/t_s ≤ 44.142
	(3,5)	1.168 ≤ h_s/t_s ≤ 72.232	1.379 ≤ h_s/t_s ≤ 86.300
	(3,6)	1.074 ≤ h_s/t_s ≤ 66.242	1.266 ≤ h_s/t_s ≤ 79.309
C	(4,2)	1.266 ≤ h_s/t_s ≤ 35.592	1.710 ≤ h_s/t_s ≤ 48.340
	(4,3)	1.159 ≤ h_s/t_s ≤ 32.402	1.568 ≤ h_s/t_s ≤ 44.142
	(4,4)	1.070 ≤ h_s/t_s ≤ 66.206	1.401 ≤ h_s/t_s ≤ 87.652
	(4,5)	1.293 ≤ h_s/t_s ≤ 61.154	1.637 ≤ h_s/t_s ≤ 77.986
	(4,6)	1.205 ≤ h_s/t_s ≤ 56.817	1.514 ≤ h_s/t_s ≤ 72.232

Groups	P(n_{sx},n_{sy}) P'($n_{sx'}$,$n_{sy'}$))	h_s/t_s Range Stiffeners Orientation 0°	45°
D	(5,2)	1.056 ≤ h_s/t_s ≤ 66.101	1.488 ≤ h_s/t_s ≤ 93.443
	(5,3)	1.281 ≤ h_s/t_s ≤ 61.079	1.801 ≤ h_s/t_s ≤ 86.300
	(5,4)	1.197 ≤ h_s/t_s ≤ 56.766	1.637 ≤ h_s/t_s ≤ 77.986
	(5,5)	1.124 ≤ h_s/t_s ≤ 53.022	1.463 ≤ h_s/t_s ≤ 70.122
	(5,6)	1.059 ≤ h_s/t_s ≤ 49.741	1.369 ≤ h_s/t_s ≤ 65.469
E	(6,2)	1.182 ≤ h_s/t_s ≤ 56.662	1.772 ≤ h_s/t_s ≤ 85.301
	(6,3)	1.112 ≤ h_s/t_s ≤ 52.943	1.653 ≤ h_s/t_s ≤ 79.309
	(6,4)	1.049 ≤ h_s/t_s ≤ 49.681	1.514 ≤ h_s/t_s ≤ 72.232
	(6,5)	1.320 ≤ h_s/t_s ≤ 46.798	1.823 ≤ h_s/t_s ≤ 65.469
	(6,6)	1.252 ≤ h_s/t_s ≤ 44.232	1.717 ≤ h_s/t_s ≤ 61.426

Table 3. Range of h_s/t_s for ϕ = 0.3.

Groups	P(n_{sx},n_{sy}) P'($n_{sx'}$,$n_{sy'}$)	h_s/t_s Range Stiffeners Orientation 0°	45°
A	(2,2)	1.041 ≤ h_s/t_s ≤ 31.418	1.088 ≤ h_s/t_s ≤ 33.240
	(2,3)	1.042 ≤ h_s/t_s ≤ 42.747	1.135 ≤ h_s/t_s ≤ 46.951
	(2,4)	1.074 ≤ h_s/t_s ≤ 37.438	1.160 ≤ h_s/t_s ≤ 40.679
	(2,5)	1.367 ≤ h_s/t_s ≤ 59.409	1.431 ≤ h_s/t_s ≤ 62.891
	(2,6)	1.234 ≤ h_s/t_s ≤ 53.490	1.313 ≤ h_s/t_s ≤ 57.464
B	(3,2)	1.064 ≤ h_s/t_s ≤ 37.378	1.331 ≤ h_s/t_s ≤ 46.951
	(3,3)	1.362 ≤ h_s/t_s ≤ 33.278	1.733 ≤ h_s/t_s ≤ 42.353
	(3,4)	1.234 ≤ h_s/t_s ≤ 29.989	1.520 ≤ h_s/t_s ≤ 37.153
	(3,5)	1.128 ≤ h_s/t_s ≤ 48.666	1.332 ≤ h_s/t_s ≤ 58.129
	(3,6)	1.038 ≤ h_s/t_s ≤ 44.639	1.234 ≤ h_s/t_s ≤ 53.488
C	(4,2)	1.218 ≤ h_s/t_s ≤ 29.912	1.657 ≤ h_s/t_s ≤ 40.679
	(4,3)	1.118 ≤ h_s/t_s ≤ 27.243	1.520 ≤ h_s/t_s ≤ 37.153
	(4,4)	1.033 ≤ h_s/t_s ≤ 44.604	1.359 ≤ h_s/t_s ≤ 59.072
	(4,5)	1.489 ≤ h_s/t_s ≤ 41.213	1.893 ≤ h_s/t_s ≤ 52.577
	(4,6)	1.389 ≤ h_s/t_s ≤ 38.302	1.757 ≤ h_s/t_s ≤ 48.729
D	(5,2)	1.016 ≤ h_s/t_s ≤ 44.497	1.431 ≤ h_s/t_s ≤ 62.891
	(5,3)	1.474 ≤ h_s/t_s ≤ 41.137	2.075 ≤ h_s/t_s ≤ 58.129
	(5,4)	1.379 ≤ h_s/t_s ≤ 38.249	1.893 ≤ h_s/t_s ≤ 52.577
	(5,5)	1.295 ≤ h_s/t_s ≤ 35.740	1.686 ≤ h_s/t_s ≤ 47.228
	(5,6)	1.221 ≤ h_s/t_s ≤ 33.540	1.588 ≤ h_s/t_s ≤ 44.153
E	(6,2)	1.358 ≤ h_s/t_s ≤ 38.145	2.046 ≤ h_s/t_s ≤ 57.464
	(6,3)	1.279 ≤ h_s/t_s ≤ 35.660	1.918 ≤ h_s/t_s ≤ 53.488
	(6,4)	1.209 ≤ h_s/t_s ≤ 33.480	1.757 ≤ h_s/t_s ≤ 48.729
	(6,5)	1.145 ≤ h_s/t_s ≤ 31.550	1.588 ≤ h_s/t_s ≤ 44.153
	(6,6)	1.089 ≤ h_s/t_s ≤ 66.348	1.504 ≤ h_s/t_s ≤ 92.275

Table 4. Range of h_s/t_s for ϕ = 0.4.

Groups	P(n_{sx},n_{sy}) P'($n_{sx'}$,$n_{sy'}$)	h_s/t_s Range Stiffeners Orientation 0°	45°
A	(2,2)	$1.070 \le h_s/t_s \le 29.550$	$1.116 \le h_s/t_s \le 31.248$
	(2,3)	$1.200 \le h_s/t_s \le 25.375$	$1.306 \le h_s/t_s \le 27.849$
	(2,4)	$1.057 \le h_s/t_s \le 31.502$	$1.126 \le h_s/t_s \le 34.144$
	(2,5)	$1.092 \le h_s/t_s \le 44.402$	$1.139 \le h_s/t_s \le 46.974$
	(2,6)	$1.155 \le h_s/t_s \le 39.985$	$1.216 \le h_s/t_s \le 42.873$
B	(3,2)	$1.045 \le h_s/t_s \le 22.180$	$1.306 \le h_s/t_s \le 27.849$
	(3,3)	$1.087 \le h_s/t_s \le 28.002$	$1.375 \le h_s/t_s \le 35.597$
	(3,4)	$1.155 \le h_s/t_s \le 25.242$	$1.407 \le h_s/t_s \le 31.199$
	(3,5)	$1.057 \le h_s/t_s \le 36.388$	$1.240 \le h_s/t_s \le 43.406$
	(3,6)	$1.385 \le h_s/t_s \le 33.385$	$1.623 \le h_s/t_s \le 39.881$
C	(4,2)	$1.137 \le h_s/t_s \le 25.161$	$1.531 \le h_s/t_s \le 34.144$
	(4,3)	$1.045 \le h_s/t_s \le 22.927$	$1.407 \le h_s/t_s \le 31.199$
	(4,4)	$1.377 \le h_s/t_s \le 33.349$	$1.799 \le h_s/t_s \le 44.088$
	(4,5)	$1.280 \le h_s/t_s \le 30.824$	$1.614 \le h_s/t_s \le 39.263$
	(4,6)	$1.195 \le h_s/t_s \le 28.655$	$1.491 \le h_s/t_s \le 36.356$
D	(5,2)	$1.354 \le h_s/t_s \le 33.243$	$1.908 \le h_s/t_s \le 46.974$
	(5,3)	$1.263 \le h_s/t_s \le 30.748$	$1.770 \le h_s/t_s \le 43.406$
	(5,4)	$1.184 \le h_s/t_s \le 28.602$	$1.614 \le h_s/t_s \le 39.263$
	(5,5)	$1.114 \le h_s/t_s \le 47.653$	$1.439 \le h_s/t_s \le 62.944$
	(5,6)	$1.052 \le h_s/t_s \le 44.720$	$1.348 \le h_s/t_s \le 58.778$
E	(6,2)	$1.162 \le h_s/t_s \le 28.498$	$1.738 \le h_s/t_s \le 42.873$
	(6,3)	$1.097 \le h_s/t_s \le 26.657$	$1.623 \le h_s/t_s \le 39.881$
	(6,4)	$1.038 \le h_s/t_s \le 25.039$	$1.491 \le h_s/t_s \le 36.356$
	(6,5)	$1.527 \le h_s/t_s \le 42.067$	$2.099 \le h_s/t_s \le 58.778$
	(6,6)	$1.452 \le h_s/t_s \le 39.775$	$1.980 \le h_s/t_s \le 55.169$

Table 5. Range of h_s/t_s for ϕ = 0.5.

Groups	P(n_{sx},n_{sy}) P'($n_{sx'}$,$n_{sy'}$)	h_s/t_s Range Stiffeners Orientation 0°	45°
A	(2,2)	$1.059 \le h_s/t_s \le 20.843$	$1.103 \le h_s/t_s \le 22.019$
	(2,3)	$1.158 \le h_s/t_s \le 17.909$	$1.258 \le h_s/t_s \le 19.642$
	(2,4)	$1.021 \le h_s/t_s \le 27.792$	$1.084 \le h_s/t_s \le 30.101$
	(2,5)	$1.181 \le h_s/t_s \le 35.034$	$1.229 \le h_s/t_s \le 37.038$
	(2,6)	$1.067 \le h_s/t_s \le 31.553$	$1.119 \le h_s/t_s \le 33.801$
B	(3,2)	$1.007 \le h_s/t_s \le 15.649$	$1.258 \le h_s/t_s \le 19.642$
	(3,3)	$1.174 \le h_s/t_s \le 24.704$	$1.484 \le h_s/t_s \le 31.397$
	(3,4)	$1.067 \le h_s/t_s \le 22.276$	$1.296 \le h_s/t_s \le 27.514$
	(3,5)	$1.130 \le h_s/t_s \le 28.722$	$1.323 \le h_s/t_s \le 34.234$
	(3,6)	$1.042 \le h_s/t_s \le 26.358$	$1.213 \le h_s/t_s \le 31.450$
C	(4,2)	$1.047 \le h_s/t_s \le 22.191$	$1.407 \le h_s/t_s \le 30.101$
	(4,3)	$1.116 \le h_s/t_s \le 20.230$	$1.501 \le h_s/t_s \le 27.514$
	(4,4)	$1.034 \le h_s/t_s \le 26.322$	$1.345 \le h_s/t_s \le 34.773$
	(4,5)	$1.126 \le h_s/t_s \le 24.338$	$1.417 \le h_s/t_s \le 30.983$
	(4,6)	$1.053 \le h_s/t_s \le 35.819$	$1.308 \le h_s/t_s \le 45.445$

Groups	P(n_{sx},n_{sy}) P'($n_{sx'}$,$n_{sy'}$)	h_s/t_s Range	
		Stiffeners Orientation	
		0°	45°
D	(5,2)	1.012 ≤ h_s/t_s ≤ 26.216	1.423 ≤ h_s/t_s ≤ 37.038
	(5,3)	1.109 ≤ h_s/t_s ≤ 24.262	1.550 ≤ h_s/t_s ≤ 34.234
	(5,4)	1.041 ≤ h_s/t_s ≤ 22.579	1.417 ≤ h_s/t_s ≤ 30.983
	(5,5)	1.392 ≤ h_s/t_s ≤ 33.420	1.799 ≤ h_s/t_s ≤ 44.088
	(5,6)	1.314 ≤ h_s/t_s ≤ 31.374	1.685 ≤ h_s/t_s ≤ 41.177
E	(6,2)	1.017 ≤ h_s/t_s ≤ 22.476	1.520 ≤ h_s/t_s ≤ 33.801
	(6,3)	1.371 ≤ h_s/t_s ≤ 21.035	2.029 ≤ h_s/t_s ≤ 31.450
	(6,4)	1.298 ≤ h_s/t_s ≤ 31.298	1.864 ≤ h_s/t_s ≤ 45.445
	(6,5)	1.233 ≤ h_s/t_s ≤ 29.507	1.685 ≤ h_s/t_s ≤ 41.177
	(6,6)	1.173 ≤ h_s/t_s ≤ 27.910	1.592 ≤ h_s/t_s ≤ 38.664

Following the constraints indicated in Troina et al. [15], the heights of the stiffeners h_s were limited to 300 mm, avoiding excessive disproportion in relation to the dimensions of the plate; as well as, h_s/t_s ratios less than one were disregarded, preventing stiffeners thicknesses greater than heights.

It is important to mention that all stiffened plates analyzed in this study were considered as simply supported and subjected to a uniformly distributed transverse load equal to 10 kPa, aiming to guarantee a linear-elastic material behavior and a geometric linear structural analysis. To apply this type of load in the ANSYS® software, a pressure in the positive z direction over the plate surface was imposed. The material was structural steel A-36 with an elastic modulus of 200 GPa and Poisson's ratio of 0.3. Taking as example the stiffened plate P'(3.3), Fig. 7 illustrates how the boundary conditions and loading were imposed, while Fig. 8 show the discretization of the computational domain. These aspects were considered in a similar way for all other studied geometric configurations.

In addition, the simplifying hypothesis of ideal structures, i.e., the non-consideration of initial geometric imperfections was assumed for all simulated plates. This assumption ensures that the only difference among the studied plates is really its geometric configuration.

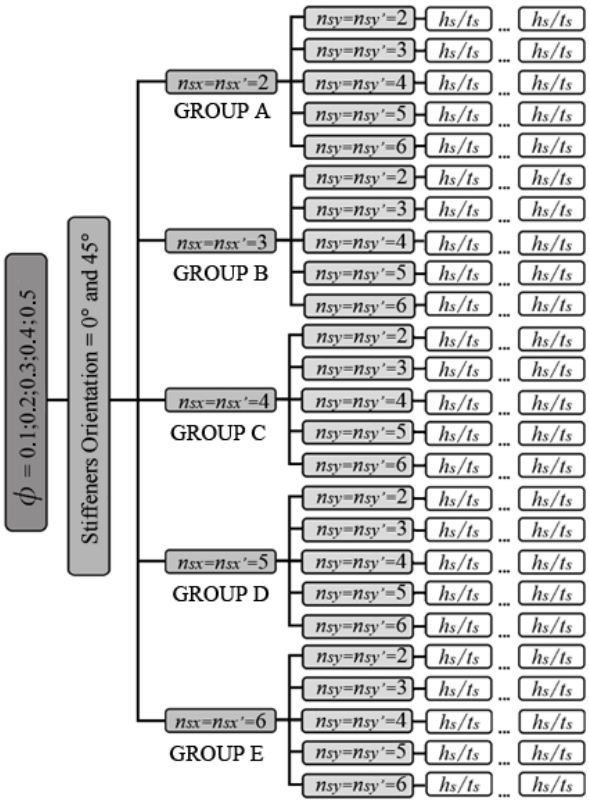

Figure 6. Application of the CDM in the definition of the search space.

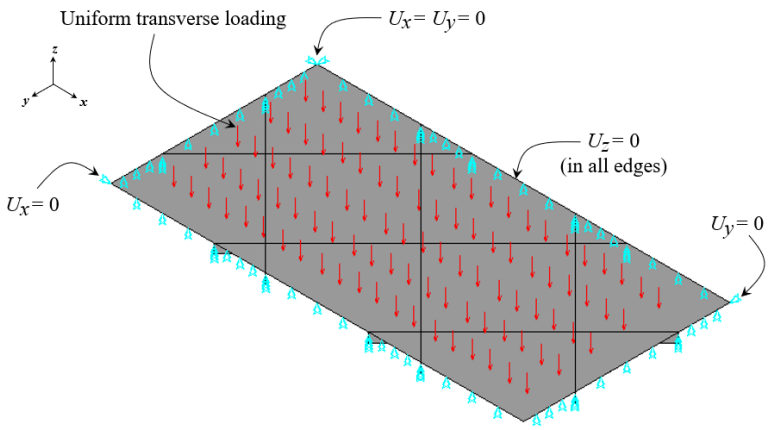

Figure 7. Plate P'(3,3): Boundary conditions and loading.

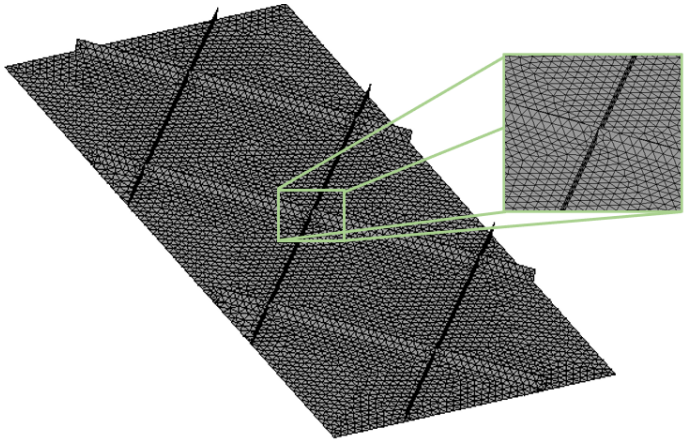

Figure 8. Plate P'(3,3): Discretized model.

2.3. Geometric Optimization

From the definition of the search space (see Fig. 6), the Exhaustive Search (ES) technique was used to compare the mechanical behavior of all proposed geometric configurations. The optimum geometry is one that minimizes the maximum deflection of the stiffened plates.

In summary, the methodology adopted in this work is showed in Fig. 9.

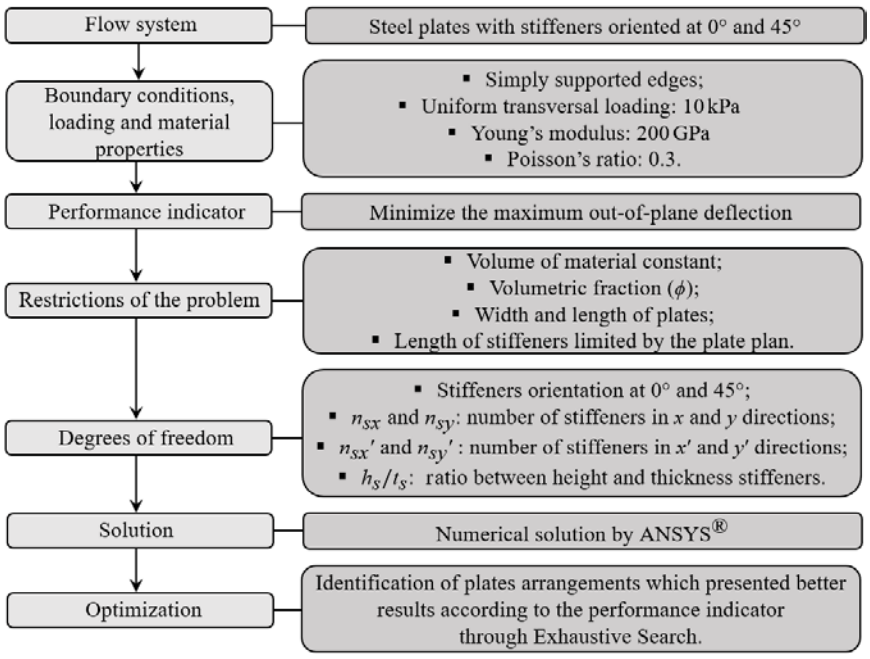

Figure 9. Geometrical optimization methodology.

3. Results and Discussion

Initially, a mesh convergence test was carried out in order to determine the appropriate size of finite elements that would compose the meshes of the cases to be numerically simulated. For this purpose, it was adopted the most complex geometry of the search space: the plate P'(6,6) with a volumetric fraction ϕ = 0.5 and higher ratio h_s/t_s = 38.664. The size of the finite elements has been reduced successively, taking as reference the width of the plate *b* = 1000 mm, following to the criterion established by Troina et al. [15]. The result can be observed in Fig. 10.

As can be seen in Fig. 10, from the mesh M_3 with finite element size of 16.67 mm, there was a convergence of values for the maximum deflection U_zMax, so that this is the finite element size stated to discretize the meshes of all computational domains.

The variation of the maximum deflection according to the variation of ratio h_s/t_s, for all proposed plates, is presented in Figs. 11 to 35. Observing these results, it was possible to attest that transforming a portion of material from the non-stiffened reference plate, maintaining the total material volume constant, as predetermined by the CDM, improvements of the mechanical behavior regarding the maximum deflection U_zMax can be reached, since all maximum deflections found for the stiffened plates are smaller than the U_zMax = 0.697 mm, obtained for the reference plate. This behavior is in agreement with Troina et al. [15] for plates with stiffeners oriented at 0°, being also observed for plates with stiffeners oriented at 45°. For instance, comparing the plate P'(6,5) with h_s/t_s = 58.778 and U_zMax = 0.0174 mm, referring to ϕ = 0.4, which presented the lowest maximum deflection among the places with stiffeners at 45°, with the reference plate, the reduction of maximum deflection was 97.50 %. In its turn, comparing the reference plate with the worst result for plates with stiffeners at 45 °, obtained by the plate P'(2,2) with h_s/t_s = 22.019 and U_zMax = 0.2134 mm for ϕ = 0.5, there was a reduction of 69.30 % in maximum deflection.

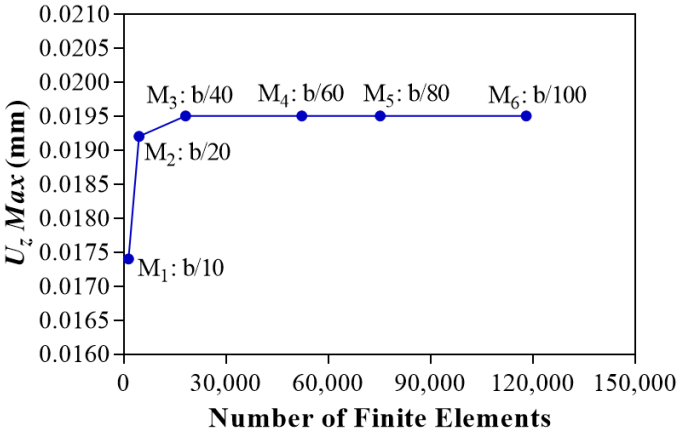

Figure 10. Mesh convergence test.

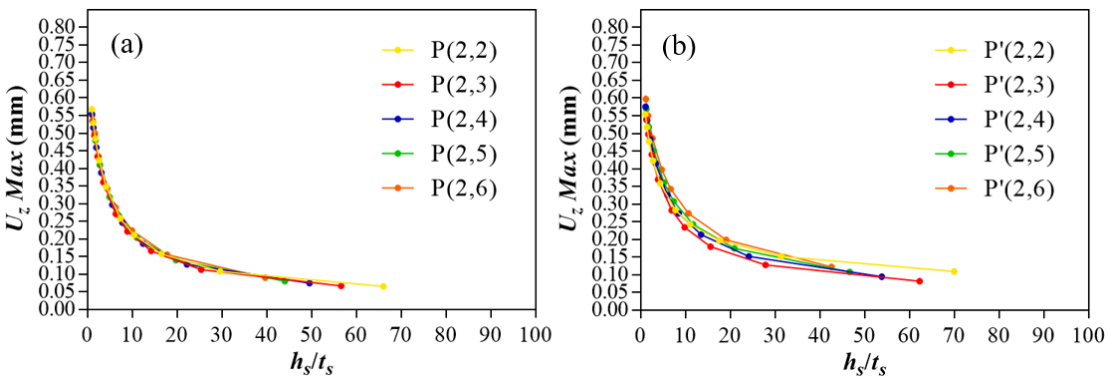

Figure 11. ϕ = 0.1 - Group A: (a) stiffeners at 0 °; (b) stiffeners at 45 °.

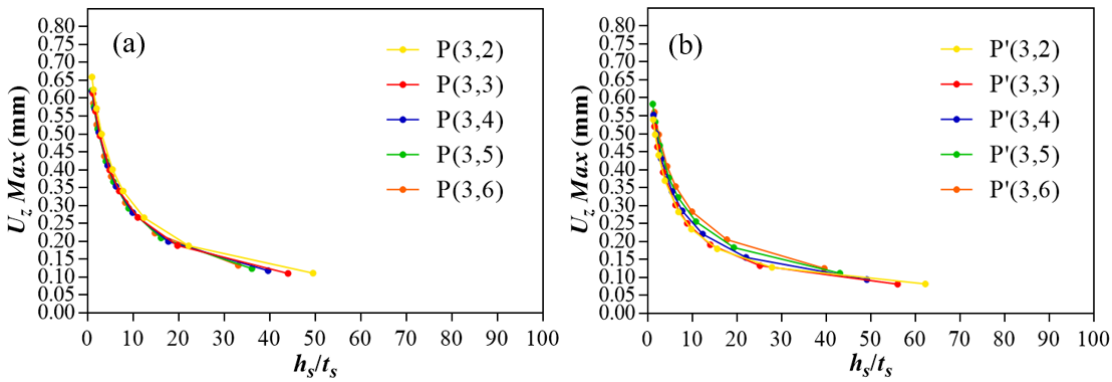

Figure 12. ϕ = 0.1 - Group B: (a) stiffeners at 0 °; (b) stiffeners at 45 °.

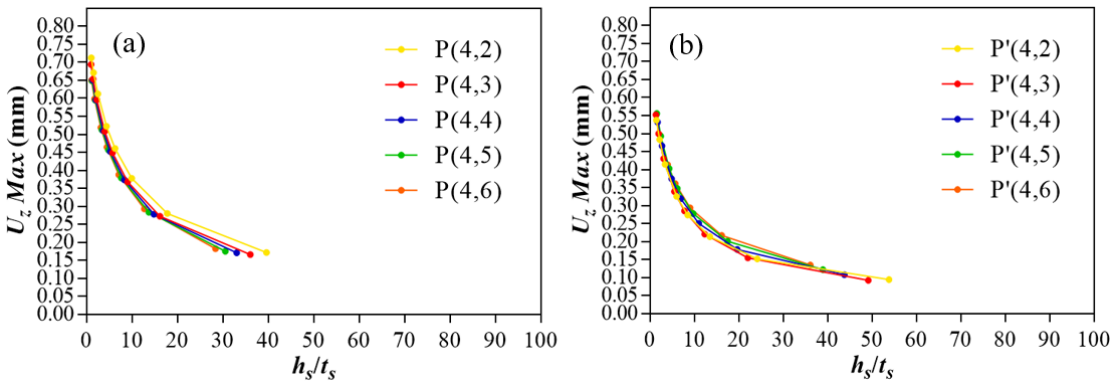

Figure 13. ϕ = 0.1 - Group C: (a) stiffeners at 0 °; (b) stiffeners at 45 °.

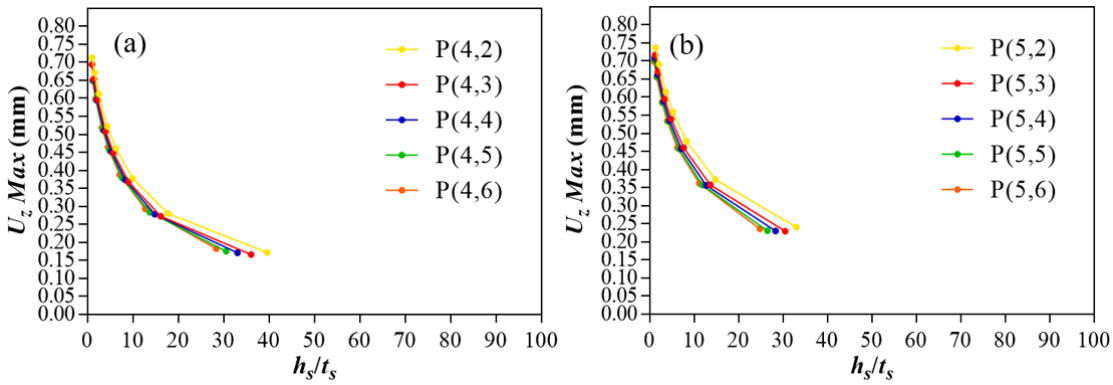

Figure 14. ϕ = 0.1 - Group D: (a) stiffeners at 0 °; (b) stiffeners at 45 °.

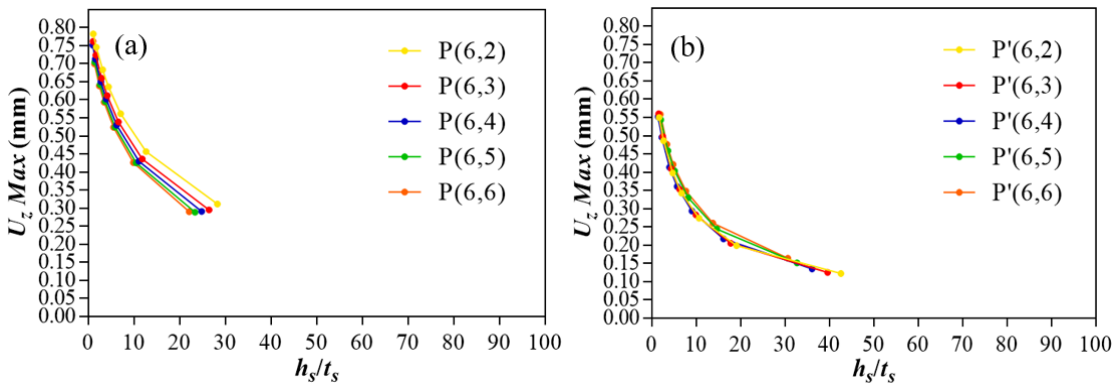

Figure 15. ϕ = 0.1 - Group E: (a) stiffeners at 0 °; (b) stiffeners at 45 °.

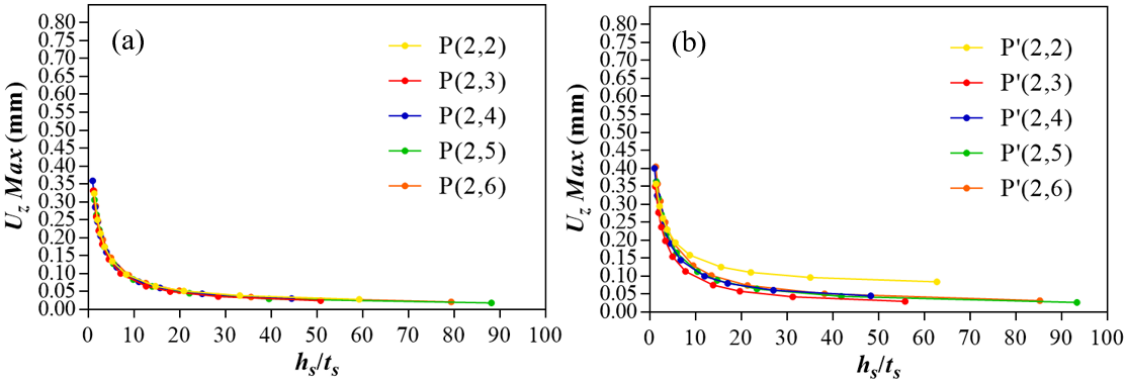

Figure 16. ϕ = 0.2 - Group A: (a) stiffeners at 0 °; (b) stiffeners at 45 °.

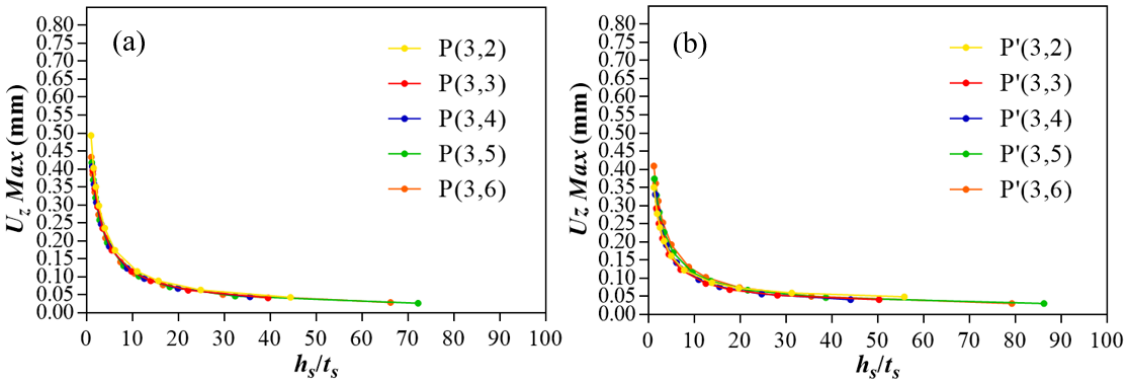

Figure 17. ϕ = 0.2 - Group B: (a) stiffeners at 0 °; (b) stiffeners at 45 °.

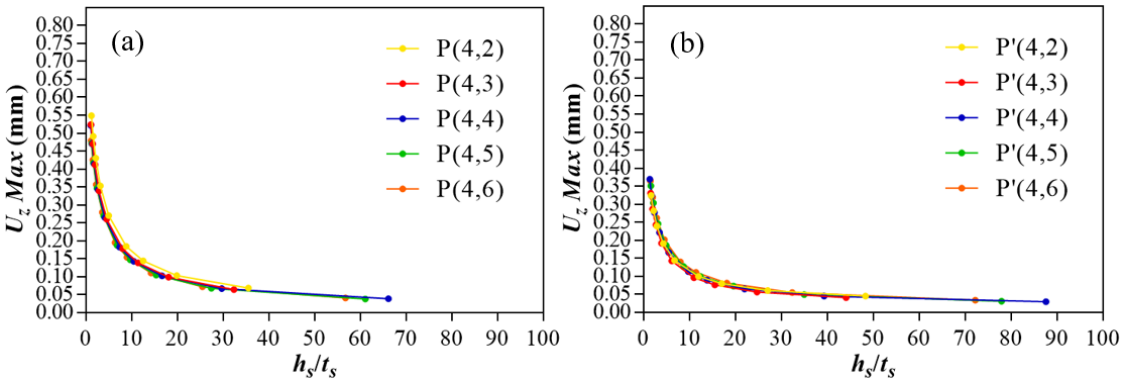

Figure 18. ϕ = 0.2 - Group C: (a) stiffeners at 0 °; (b) stiffeners at 45 °.

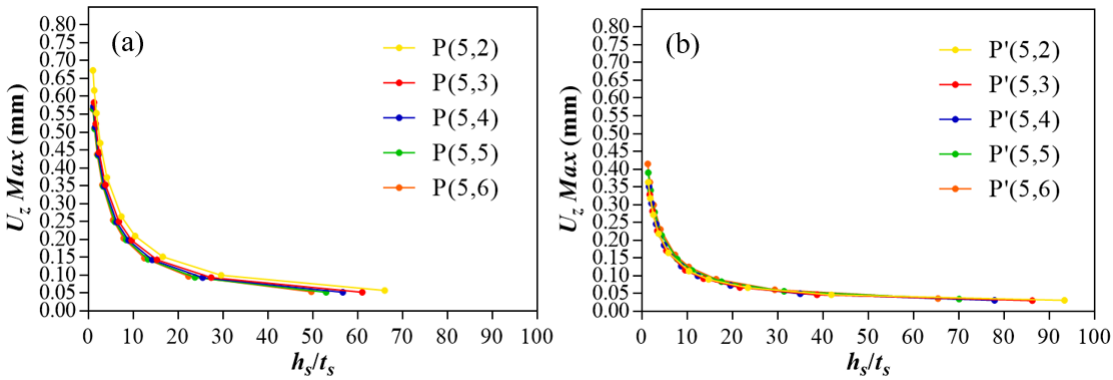

Figure 19. ϕ = 0.2 - Group D: (a) stiffeners at 0 °; (b) stiffeners at 45 °.

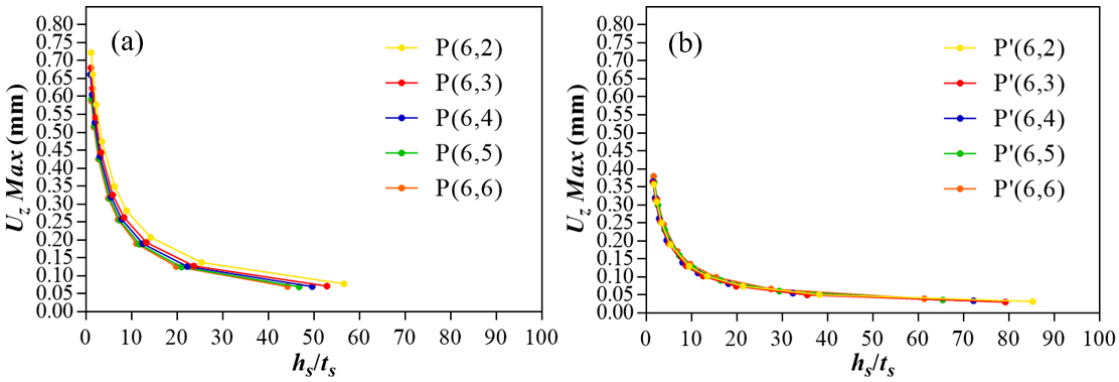

Figure 20. ϕ = 0.2 - Group E: (a) stiffeners at 0 °; (b) stiffeners at 45 °.

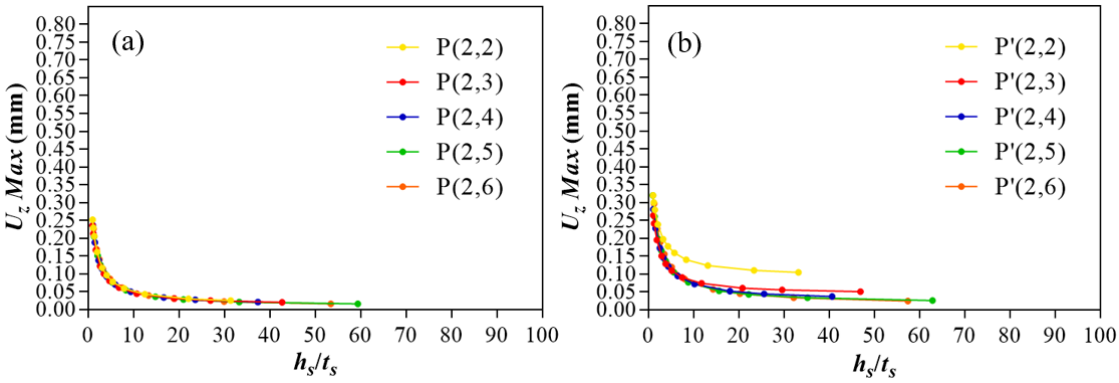

Figure 21. ϕ = 0.3 - Group A: (a) stiffeners at 0 °; (b) stiffeners at 45 °.

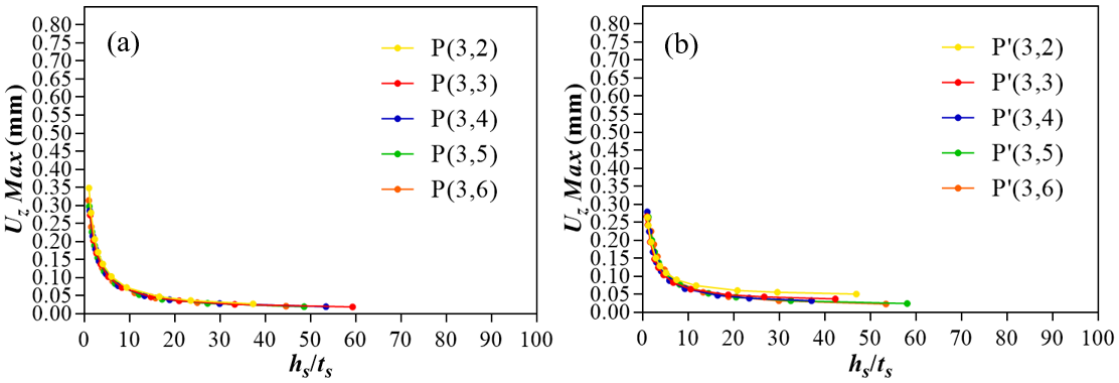

Figure 22. ϕ = 0.3 - Group B: (a) stiffeners at 0 °; (b) stiffeners at 45 °.

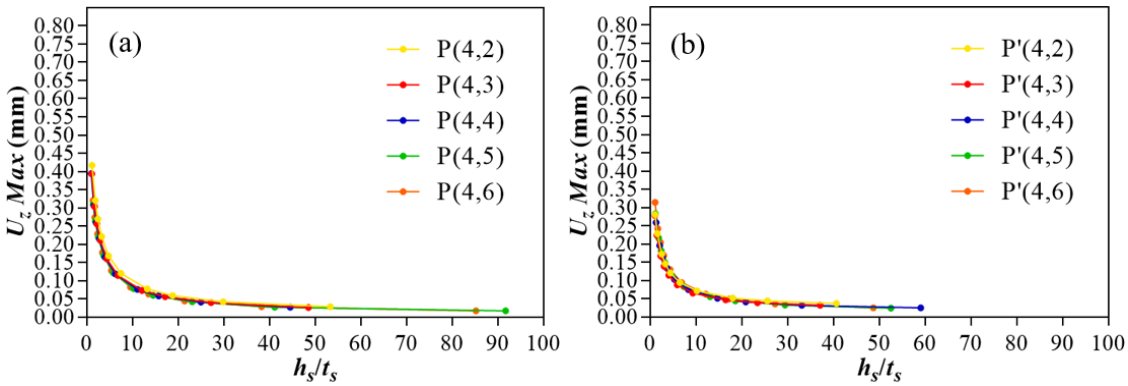

Figure 23. ϕ = 0.3 - Group C: (a) stiffeners at 0 °; (b) stiffeners at 45 °.

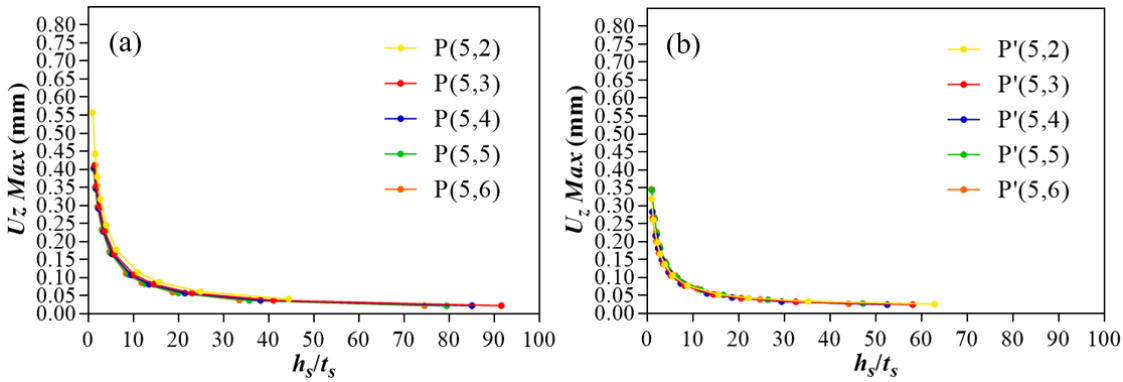

Figure 24. ϕ = 0.3 - Group D: (a) stiffeners at 0 °; (b) stiffeners at 45 °.

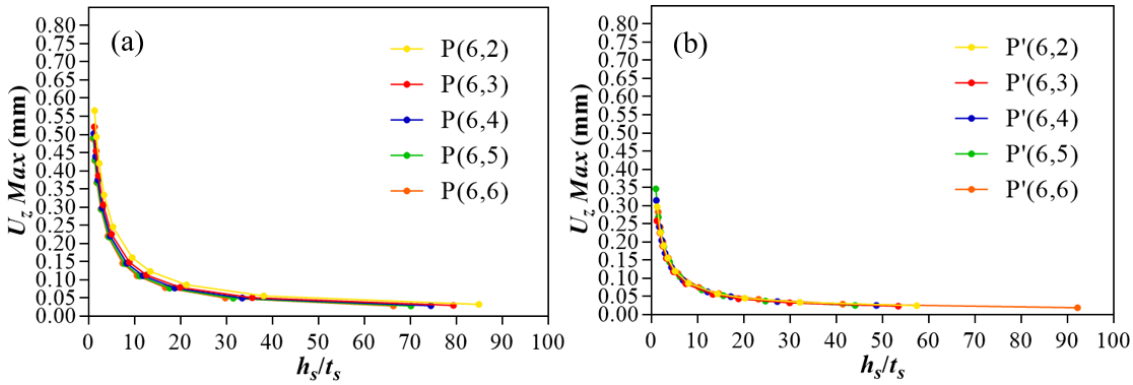

Figure 25. ϕ = 0.3 - Group A: (a) stiffeners at 0 °; (b) stiffeners at 45 °.

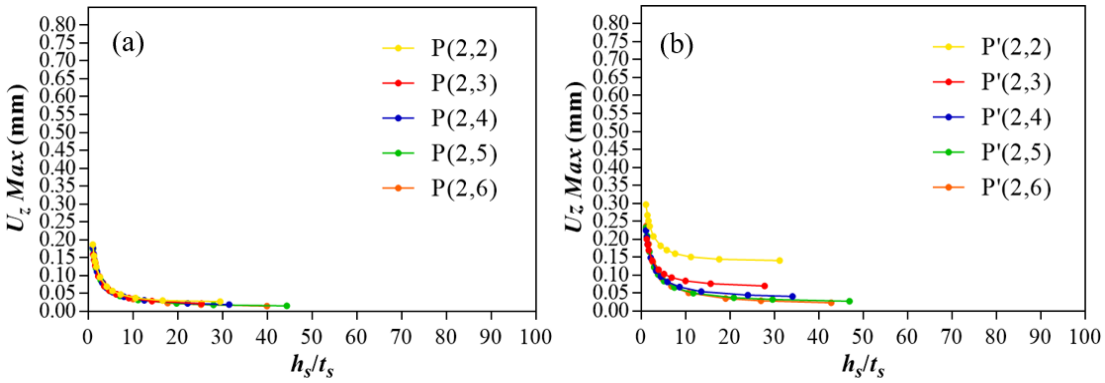

Figure 26. ϕ= 0.4 Group A: (a) stiffeners at 0 °; (b) stiffeners at 45 °.

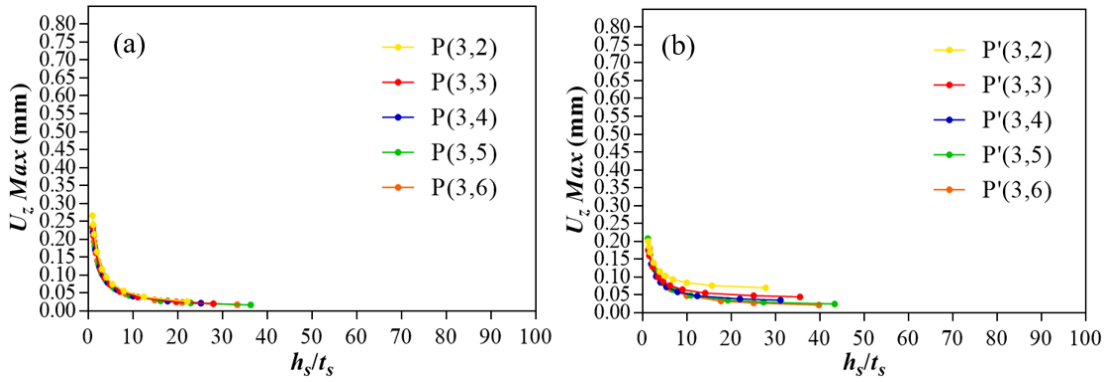

Figure 27. ϕ = 0.4 - Group B: (a) stiffeners at 0 °; (b) stiffeners at 45 °.

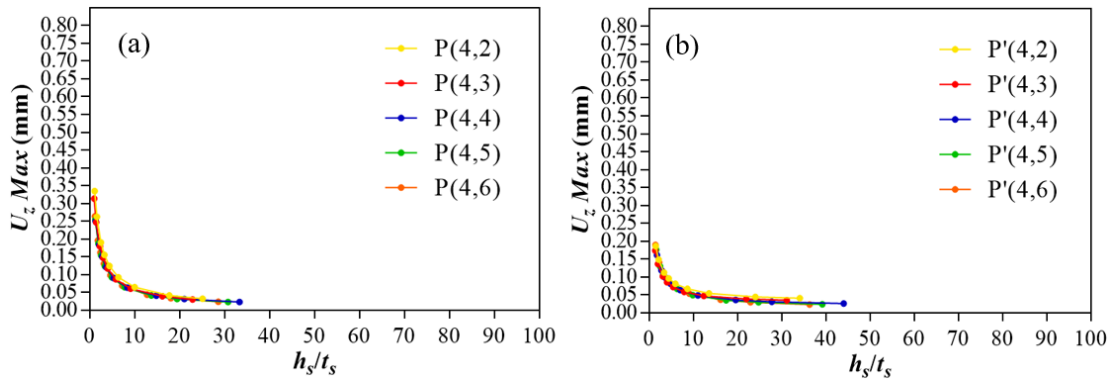

Figure 28. ϕ = 0.4 - Group C: (a) stiffeners at 0 °; (b) stiffeners at 45 °.

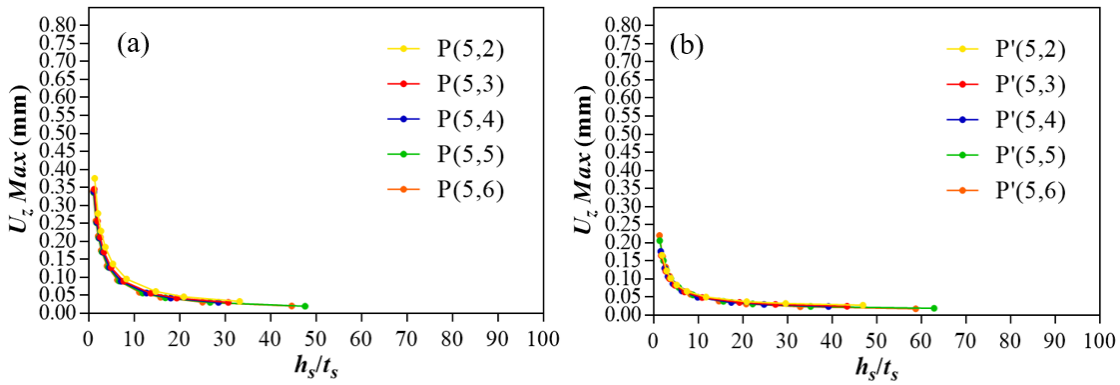

Figure 29. ϕ = 0.4 - Group D: (a) stiffeners at 0 °; (b) stiffeners at 45 °.

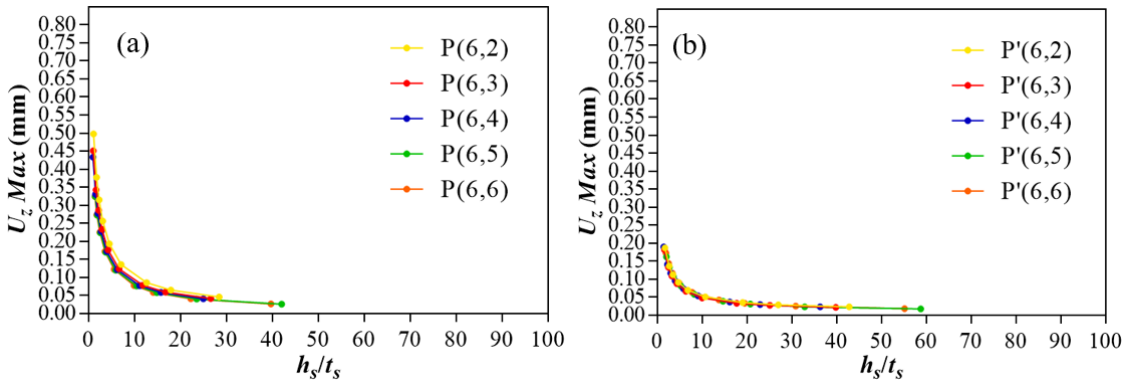

Figure 30. ϕ = 0.4 - Group E: (a) stiffeners at 0 °; (b) stiffeners at 45 °.

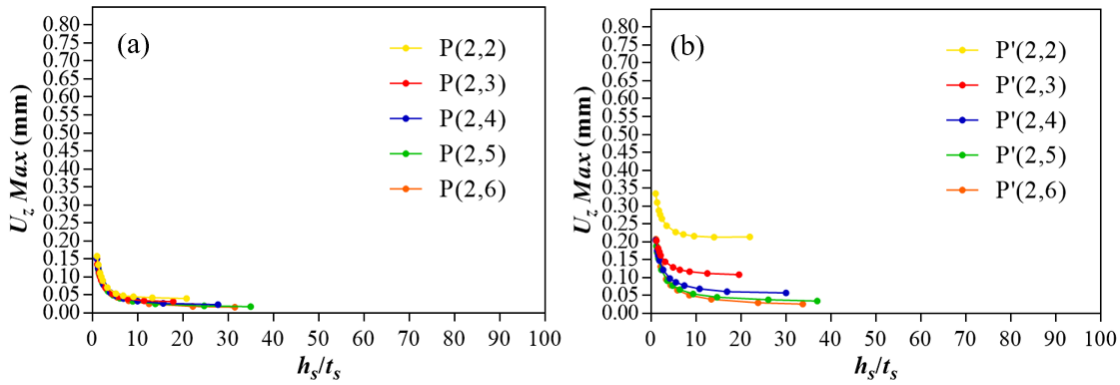

Figure 31. ϕ = 0.5 - Group A: (a) stiffeners at 0 °; (b) stiffeners at 45 °.

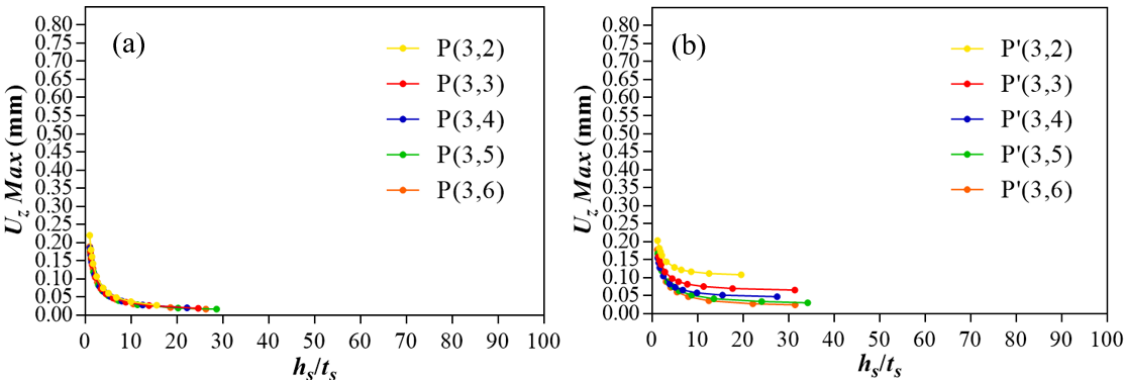

Figure 32. ϕ = 0.5 - Group B: (a) stiffeners at 0 °; (b) stiffeners at 45 °.

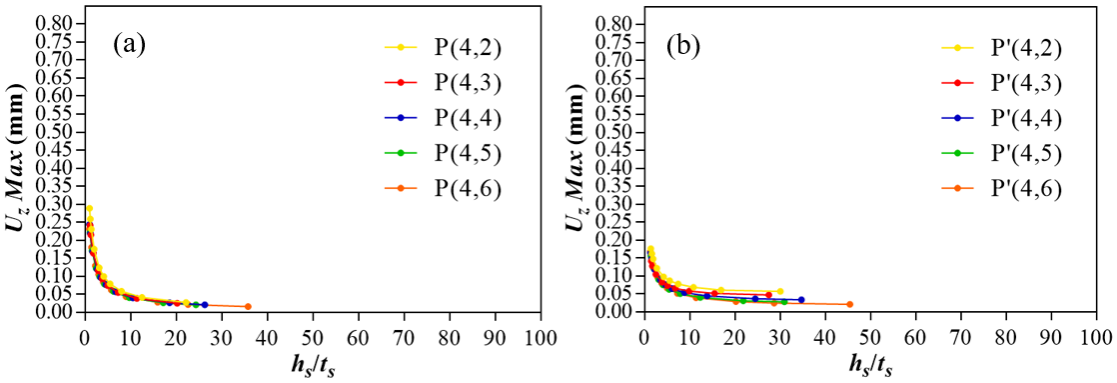

Figure 33. ϕ = 0.5 - Group C: (a) stiffeners at 0 °; (b) stiffeners at 45 °.

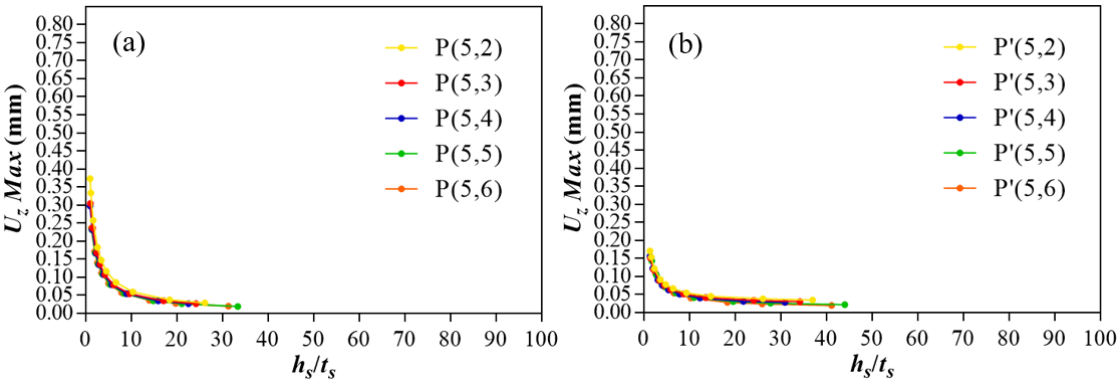

Figure 34. ϕ = 0.5 - Group D: (a) stiffeners at 0 °; (b) stiffeners at 45 °.

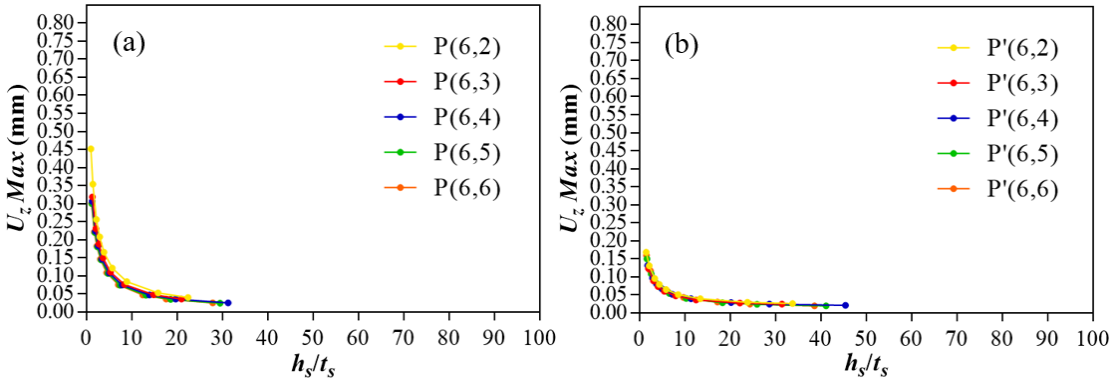

Figure 35. ϕ = 0.5- Group E: (a) stiffeners at 0 °; (b) stiffeners at 45 °.

Then, from the Figs. 11 to 35, the results for the stiffened plates that achieved the lowest maximum deflections are presented in bar graphs, considering the two stiffeners orientations (0 ° and 45 °), for each ϕ value (0.1 to 0.5), following the group division previously established (see Fig. 6). These results are shown in Figs. 36 to 40, respectively, for ϕ = 0.1 to 0.5.

It is worth to emphasize that the comparison of the results was performed between equivalent plates, i.e., with the same ϕ value, thickness and amounts of stiffeners in the *x*-*x*' and *y*-*y*' directions, being the stiffeners orientation the only differential. Thereby, it was possible to observe the direct influence of this degree of freedom on the stiffened plates behavior.

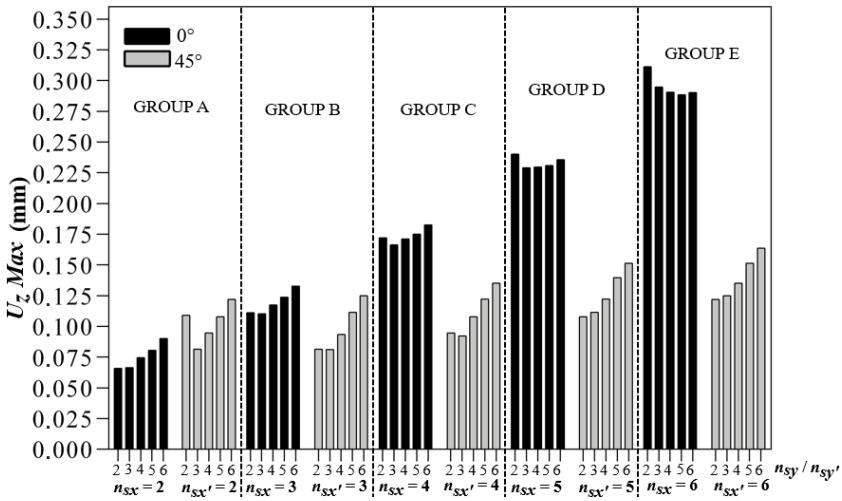

Figure 36. Results for ϕ = 0.1.

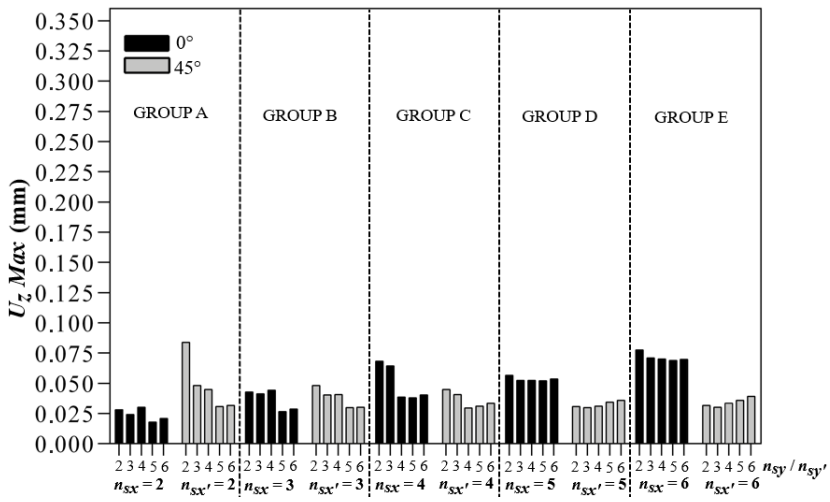

Figure 37. Results for ϕ = 0.2.

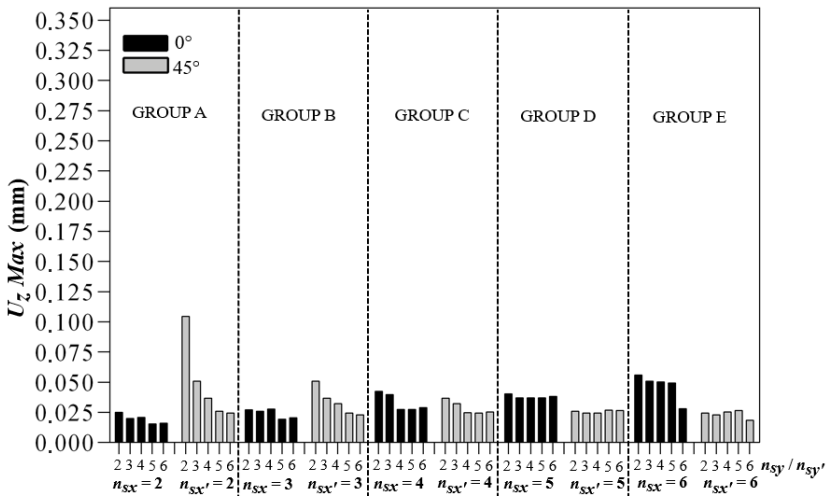

Figure 38. Results for ϕ = 0.3.

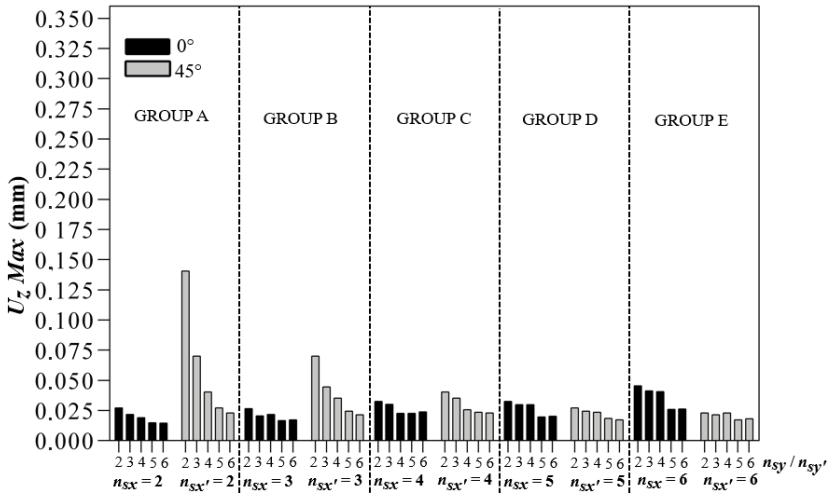

Figure 39. Results for ϕ = 0.4.

Observing the results of ϕ = 0.1 (Fig. 36), one can note that, excepting Group A, the plates with stiffeners oriented at 45 ° showed lower deflections than the plates with stiffeners oriented at 0 °. Taking the Group B as reference, the plate that reached the lowest maximum deflection was P'(3,3) with h_s/t_s = 56.091 and U_{zMax} = 0.0811 mm, presents a reduction of 26.50 % in comparison to the plate P(3,3) with h_s/t_s = 44.090, which registered U_zMax = 0.1103 mm. In turn, with respect to percentage differences, the largest one occurred between the plates P'(6,2) with h_s/t_s = 42.650 which presented U_{zMax} = 0.1220 mm and P(6,2) with h_s/t_s = 28.331 and U_zMax = 0.3113 mm, meaning a reduction of 60.81 % in favor of the plate with stiffeners oriented at 45 °.

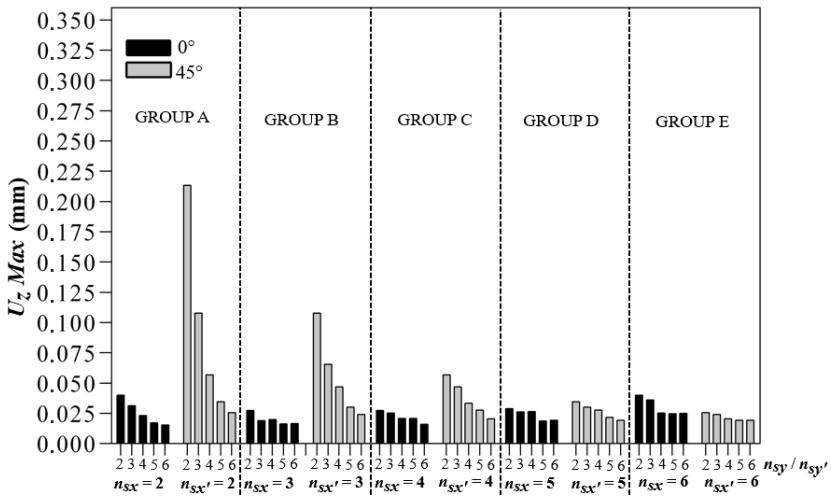

Figure 40. Results for ϕ = 0.5.

Regarding to the volumetric fraction ϕ = 0.2 (Fig. 37), it was noted that in a general way the maximum deflections tend to be smaller compared to values of ϕ = 0.1 (see Fig. 36). This is justified by the fact that a greater amount of material was destined to design of the stiffeners. It was also noted that the plates with stiffeners oriented at 45 ° become more advantageous as from Group C; standing out the plate P'(4,4) with h_s/t_s = 87.652 that presented the lowest maximum deflection U_zMax = 0.0297 mm, a minimization of 22.98 % compared to the plate P(4,4) with h_s/t_s = 66.206, which showed U_zMax = 0.0385 mm. However, the widest percentage reduction in maximum deflection favorable to the plate with stiffeners at 45 °, it was presented by the plate P'(6,2) and h_s/t_s = 85.301 with U_zMax = 0.0316 mm, achieving a value 59.2 % lower than the U_zMax = 0.0775 mm of the plate P(6,2) with h_s/t_s = 56.662.

Concerning Fig. 38, which presents the results for ϕ = 0.3, it was perceptible a similar behavior to ϕ = 0.2 (see Fig. 37). In other words, from Group C all plates with stiffeners oriented at 45 ° have smaller maximum deflections in comparison to the plates with stiffeners oriented at 0 °. In relation to the best result for plates with stiffeners at 45 ° for ϕ = 0.3, the plate P'(6,6) with h_s/t_s = 92.275 achieved

U_zMax = 0.0186 mm, i.e., a maximum deflection 33.84 % smaller than the plate P(6,6) with h_s/t_s = 66.348 which reached U_zMax = 0.0282 mm. For illustration purposes, this reduction in the maximum deflection can be seen in Fig. 41. However, the biggest percentage difference happened between the plates P'(6,2) with h_s/t_s = 57.464 which registered U_zMax = 0.0245 mm and P(6,2) with h_s/t_s = 38.145 which presented U_zMax = 0.0559 mm, reaching a minimization of 56.10 % favorable to the plate with stiffeners at 45 °.

In its turn, for ϕ = 0.4 the Fig. 39 indicates that the mechanical behavior of the stiffened plates with stiffeners at 45 ° is majoritarily superior only in Groups D and E. The best result for the plate with stiffeners at 45 ° was to P'(6,5) with h_s/t_s = 58.778 and U_zMax = 0.0174 mm, representing a minimization of 32.96 % in the maximum deflection comparing to the P(6,5) plate with h_s/t_s = 42.067 and U_zMax = 0.0259 mm. Nevertheless, the larger achieved reduction in maximum deflection it was 47.78 % comparing the plate P'(6,2) with h_s/t_s = 42.873 and U_zMax = 0.0229 mm with the plate P(6,2) with h_s/t_s = 28.498 which presented U_zMax = 0.0454 mm.

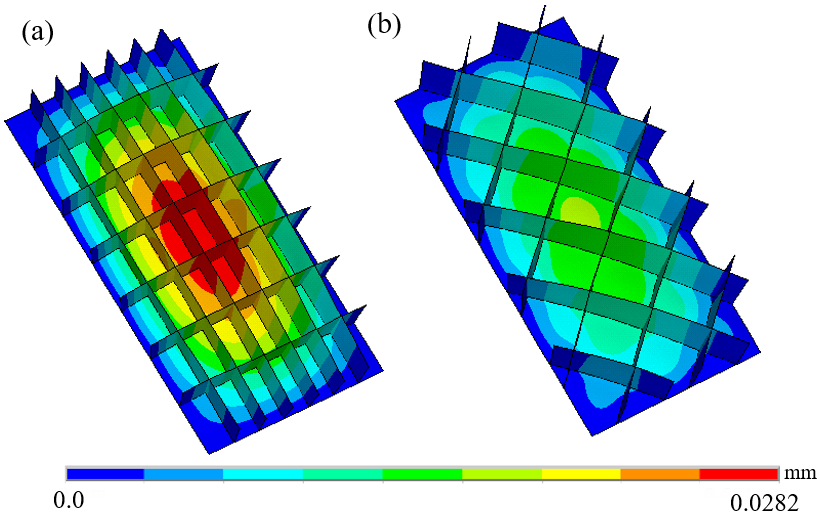

Figure 41. Deflection distribution: (a) P(4,5); (b) P'(4,5).

Finally, dealing with the volumetric fraction ϕ = 0.5 (Fig. 40), it was observed that the plates with stiffeners oriented at 45 ° have a superior mechanical behavior predominant only in Group E. For instance, the plate P'(6,5) with h_s/t_s = 41.177 and U_zMax = 0.0194 mm, that showed the lowest maximum deflection, achieved a reduction of 21.40 % in relation to the plate P(6,5) with h_s/t_s = 29.507 and U_zMax = 0.0247 mm. In addition, the largest percentage difference occurred when comparing the plate P'(6,2) with h_s/t_s = 33.801 and U_zMax = 0.0256 mm, which presented a reduction in the maximum deflection of 36.12 %, and the plate P(6,2) with h_s/t_s = 22.476 and U_zMax = 0.0401 mm.

Still observing Fig. 40, it was possible to notice an accentuated maximum deflection presented by the plate with stiffeners oriented at 45° P'(2,2), being observed this same behavior for the other ϕ values. This is due to the equidistant distribution of the stiffeners, which for the plates with stiffeners at 45 ° it was performed as a relation of the diagonals; while for the plates with stiffeners at 0 ° it was generated as a relation of the orthogonal edges. Hence, the plate P'(2,2) has a non-stiffened central area larger than the central area of plate P(2,2), concentrating the deflection field in this region, as shown in Fig. 42.

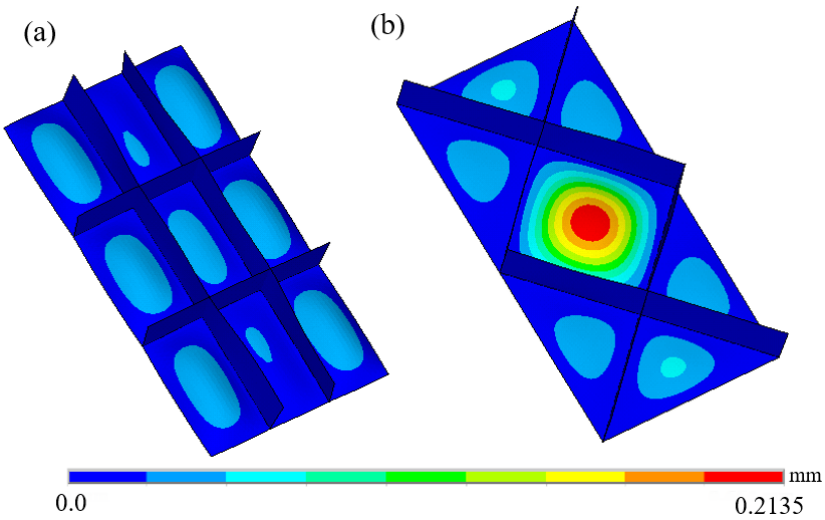

Figure 42. Deflection distribution: (a) P(2,2); (b) P'(2,2).

Analyzing Fig. 36 to 40, one can observe a tendency: as the volumetric fraction ϕ increases, the plates with stiffeners oriented at 45 ° began to show better mechanical behavior only for plates with larger amounts of stiffeners. When $\phi = 0.1$ (Fig. 36) plates with stiffeners at 45 ° are the best for the Groups B, C, D and E; when $\phi = 0.2$ (Fig. 37) and $\phi = 0.3$ (Fig. 38) for the Groups C, D and E; when $\phi = 0.4$ (Fig. 39) for the Groups D and E; and when $\phi = 0.5$ (see Fig. 40) just for Group E. This trend can be better observed in Fig. 43, where the best results per group were plotted for each volumetric fraction ϕ.

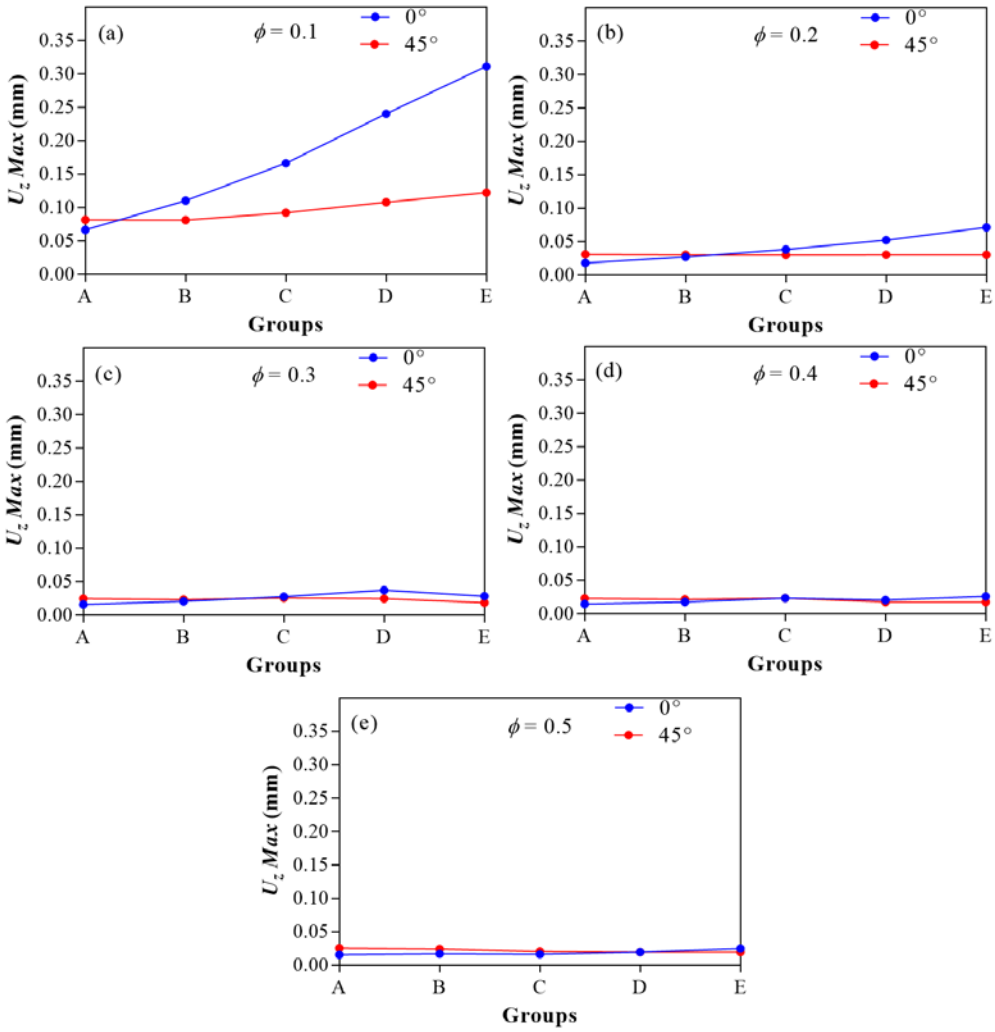

Figure 43. Best results per group: (a) $\phi = 0.1$; (b) $\phi = 0.2$; (c) $\phi = 0.3$; (d) $\phi = 0.4$; and (d) $\phi = 0.5$.

Fig. 44 presents the optimized results for each volumetric fraction ϕ considering just the groups A and E, i.e., the groups with the smallest and largest quantities of stiffeners, respectively. That way it was possible to observe which was previously stated, that plates with stiffeners oriented at 45 ° are more advantageous for large amounts of stiffeners.

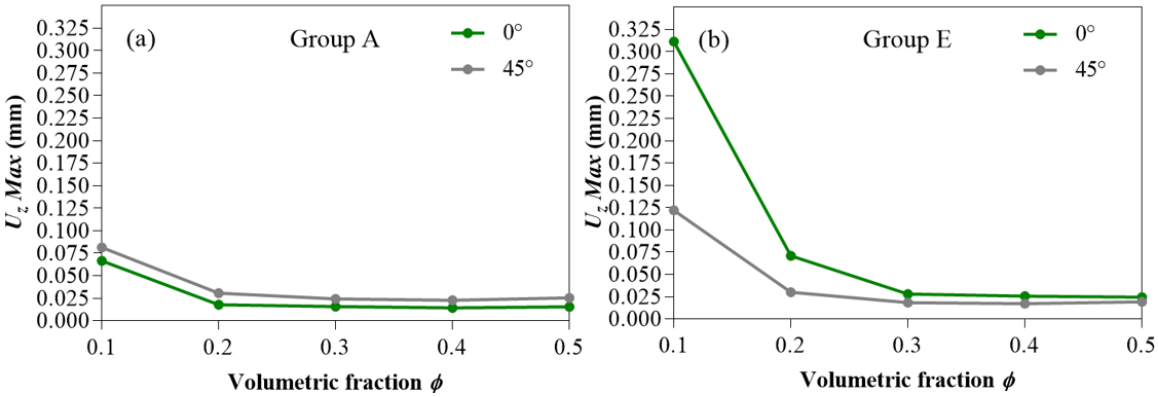

Figure 44. Optimized results: (a) Group A; (b) Group E.

Finally, Fig. 45 presents the maximum von Mises stress for the same stiffened plates of Fig. 44. The main purpose here is to show the stress level achieved by the studied structures through this representative sampling.

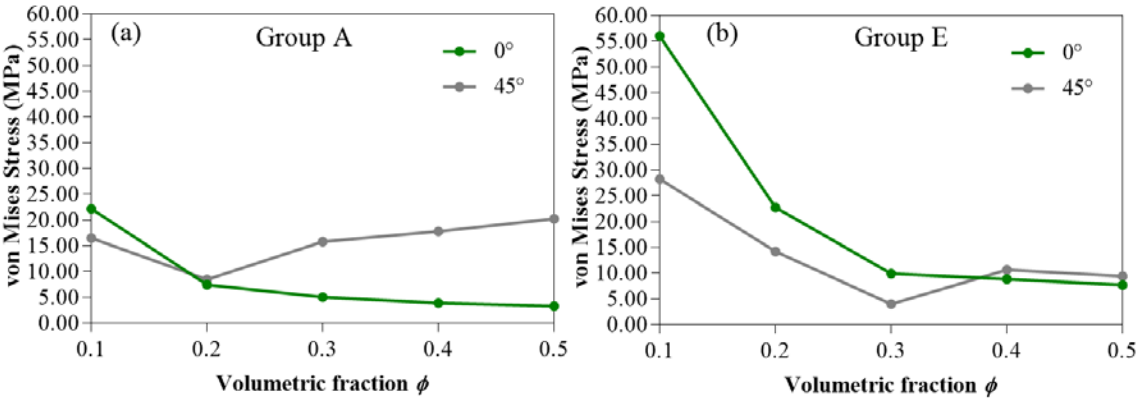

Figure 45. Maximum von Misses stress for the stiffened plates of Fig. 44.

From Fig. 45 one can note that the magnitude reached by the von Mises stress is considerably smaller than the steel yielding stress (250 MPa). For instance, the minimum factor of safety related to the steel yielding stress is around 4.5, obtained by the worst case, i.e., the one that achieved the maximum von Mises stress value (ϕ = 0.1, stiffeners oriented at 45 ° and Group E, in Fig. 45b).

Therefore, due to the low load magnitude of 10 kPa adopted for all cases, it is possible to affirm that the linear-elastic behavior adopted for the steel is an adequate approach. From this, the optimum geometric configurations obtained for the minimization of the maximum deflection can be used with higher values for the uniform transverse load, since the stress limit be not reached.

Another important aspect that emerged from Fig. 45 is that the optimized geometry defined when the maximum deflection is the performance parameter, as proposed in the present work, is not necessarily the same if the parameter performance is changed for the maximum von Mises stress.

4. Conclusion

Applying CDM, FEM and ES technique, it was possible to evaluate the behavior of different stiffened plate arrangements regarding the maximum deflection considering the stiffeners oriented at 0 ° and 45 °, aiming their geometric optimization.

Firstly, it was concluded that keeping constant the total material volume of a non-stiffened steel plate and transforming a portion of its material (fully deducted from the thickness) into stiffeners, it was possible to significantly improve the mechanical behavior, achieving reductions in the maximum deflection around 95 %. In addition, as already expected, it was observed that the variation of the h_s/t_s ratio causes a relevant influence on the rigidity of the plates, for both stiffeners oriented at 0° and stiffeners oriented at 45 °.

For most of the analyzed plate arrangements, orienting the stiffeners at 45 ° is more advantageous to reduce the maximum deflection compared to the plates with stiffeners oriented at 0 °, mainly for the values of ϕ = 0.1, 0.2 and 0.3, where it was possible to minimize the maximum deflection in the order of 60 % in some arrangements with stiffeners at 45°. The results also showed that, for larger percentages of material transformed into stiffeners (ϕ = 0.4 and 0.5), orienting stiffeners at 45 ° becomes viable for larger amounts of stiffeners.

It is important to emphasize that applying the ES technique on the search space, the optimal geometry that showed the lowest maximum deflection for plates with stiffeners at 45° was the plate $\mathrm{P}'(6,5)$ with h_s/t_s = 58.778 (having h_s = 279.193 mm and t_s = 4.75 mm) relative to ϕ = 0.4 (i.e. t_p = 12 mm), which showed U_zMax = 0.0174 mm.

In future works, it would be interesting to investigate other values of ϕ, as well as, other stiffeners orientations concerning the minimization of the maximum deflections and/or the maximum von Mises stress.

5. Acknowledgement

This work was performed with the support of the: *Coordenação de Aperfeiçoamento de Pessoal de Nível Superior – Brasil* (CAPES) – Finance Code 001, *Fundação de Amparo à Pesquisa do Estado do Rio Grande do Sul – Brasil* (FAPERGS) and *Conselho Nacional de Desenvolvimento Científico e Tecnológico – Brasil* (CNPq). Particularly, the authors L.A.O. Rocha, E.D. dos Santos and L.A. Isoldi thank to CNPq for their research grants (Processes: 307791/2019-0, 306024/2017-9 and 306012/2017-0, respectively).

References

1. Ventsel, E., Krauthammer, T. Thin Plates and Shells: Theory, Analysis and Applications. 1ª ed. Marcel Dekker: New York, 2001. DOI: 10.1201/9780203908723
2. Reddy, J.N. Theory and Analysis of Elastic Plates and Shells. 2ª ed., Boca Raton: CRC Press, 2007.
3. Szilard, R. Theories and applications of plate analysis: Classical numerical and engineering methods. 1ª ed., Wiley: Hoboken, 2004. DOI: 10.1002/97804701728722
4. Bedair, O.K. Analysis and Limit State Design of stiffened plates and shells: A world view. Applied Mechanics Reviews. 2009. 62(2). Pp. 01–16. DOI: 10.1115/1.3077137
5. Tyukalov, Yu. Calculation method of bending plates with assuming shear deformations. Magazine of Civil Engineering. 2019. 85(1). Pp. 107–122. DOI: 10.18720/MCE.85.9
6. Tyukalov, Yu. Finite element model of Reisner's plates in stresses. Magazine of Civil Engineering. 2019. 89(5). Pp. 61–78. DOI: 10.18720/MCE.89.6
7. Powell, G.H., Ogden, D.W. Analysis of orthotropic steel plate bridge decks. Journal of the Structural Division. 1969. 95. Pp. 909–921.
8. Rossow, M.P., Ibrahimkhail, A.K. Constraint method analysis of stiffened plates. Computers and Structures. 1978. 8(1). Pp. 51–60.
9. Mukhopadhyay, M., Satsangi, S.K. Isoparametric stiffened plate bending element for the analysis of ship's structure. Royal Institution of Naval Architects Transactions. 1984. 126. Pp. 141–151.
10. Kukreti, A.R., Cheraghi, E. Analysis procedure for stiffened plate systems using an energy approach. Computers & Structures. 1993. 46(4). Pp. 649–657.
11. Bedair, O.K. Analysis of stiffened plates under lateral loading using sequential quadratic programming (SQP). Computers & Structures. 1997. 62(1). Pp. 63–80. DOI: 10.1016/S0045-7949(96)00281-7
12. Tanaka, M., Matsumoto, T., Oida, S.A. Boundary Element Method Applied to the Elastostatic Bending Problem of Beam-Stiffened Plates. Engineering Analysis with Boundary Elements. 2000. 24(10). Pp. 751–758. DOI: 10.1016/S0955-7997(00)00057-6
13. Sapountzakis, E.J., Katsikadelis, J.T. Analysis of Plates Reinforced with Beams. Computational Mechanics. 2000. 26(1). Pp. 66–74. DOI: 10.1007/s004660000156
14. Singh, D.K., Duggal S.K., Pal, P. Analysis of Stiffened Plates using FEM – A Parametric Study. International Research Journal of Engineering and Technology. 2015. 2(4). Pp. 1650–1656.
15. Troina, G.S., Cunha, M.L., Pinto, V.T., Rocha, L.A.O., Dos Santos, E.D., Fragassa, C., Isoldi, L.A. Computational Modeling and Design Constructal Theory Applied to the Geometric Optimization of Thin Steel Plates with Stiffeners Subjected to Uniform Transverse Load. Metals. 2020. 10. Pp. 1–29. DOI: 10.3390/met10020220
16. Rappaz, M., Bellet M., Deville, M. Numerical Modeling in Materials Science and Engineering. Heidelberg: Springer, 2010. DOI: 10.1007/978-3-642-11821-0
17. Steinhauser, M.O. Computational Multiscale Modeling of Fluids and Solids. Heidelberg: Springer, 2008. DOI: 10.1007/978-3-540-75117-5
18. Ansys Academic Research Mechanical, Release 19, Help System, Element Reference, ANSYS, Inc.
19. Troina, G.S., de Queiroz, J.P.T.P., Cunha, M.L., Rocha, L.A.O., dos Santos E.D., Isoldi, L.A. Verificação de modelos computacionais para placas com enrijecedores submetidas a carregamento transversal uniforme. CEREUS. 2018. 5(2). Pp. 285–298. DOI: 10.18605/2175-7275/cereus.v10n2p285-298
20. Carrijo, E.C., Paiva, J.B., Giogo, J.S. (1999). A numerical and experimental study of stiffened plates in bending. Transactions on Modelling and Simulation. 1999. 22. Pp. 12–18. DOI: 10.2495/CMEM990021

21. Bejan, A., Zane, J.P. Design in Nature: How the Constructal Law governs evolution in biology, physics, technology, and social organizations. Doubleday: New York, 2012.
22. Reis, A.H. Constructal theory: from engineering to physics, and how flow systems develop shape and structure. Applied Mechanics Reviews. 2006. 59(5). Pp. 269–281. DOI: 10.1115/1.2204075
23. Bejan, A., Lorente, S. Design with Constructal Theory, Wiley: Hoboken, 2008. DOI: 10.1002/9780470432709
24. Dos Santos, E.D., Isoldi, L.A., Gomes, M.N., Rocha, L.A.O. The Constructal Design Applied to Renewable Energy Systems. In Rincón-Mejía. E & De las Heras. A (Ed.), Sustainable Energy Technologies 1ed. Pp. 63–87. Boca Raton: CRC Press – Taylor & Francis Group, 2017. DOI: 10.1201/9781315269979
25. Lorente, S., Lee, J., Bejan, A. The “flow of stresses” concept: the analogy between mechanical strength and heat convection. International Journal of Heat and Mass Transfer. 2010. 53. Pp. 2963–2968. DOI: 10.1016/j.ijheatmasstransfer.20-10.03.038
26. Isoldi, L.A., Real, M.V., Correia, A.L.G., Vaz, J., Dos Santos, E.D., Rocha, L.A.O. Flow of Stresses: Constructal Design of Perforated Plates Subjected to Tension or Buckling. In Rocha, L.A.O., Lorente, S., Bejan, A. (Ed.), Constructal Law and the Unifying Principle of Design – Understanding Complex Systems 1ed. Pp. 195–127. New York: Springer, 2013. DOI: 10.1007/978-1-4614-5049-8_12
27. Helbig, D., Da Silva, C.C.C., Real, M.V., Dos Santos, E.D., Isoldi, L.A., Rocha, L.A.O. Study About Buckling Phenomenon in Perforated Thin Steel Plates Employing Computational Modeling and Constructal Design Method. Latin American Journal of Solids and Structures. 2016. 13. Pp. 1912–1936. DOI: 10.1590/1679-78252893
28. Da Silva, C.C.C., Helbig, D., Cunha, M.L., Dos Santos, E.D., Rocha, L.A.O., Real, M.V., Isoldi, L.A. Numerical buckling analysis of thin steel plates with centered hexagonal perforation through constructal design method. Journal of the Brazilian Society of Mechanical Sciences and Engineering. 2019. 41(8). Pp. 309–1-309–18. DOI: 10.1007/s40430-019-1815-7
29. Lima, J.P.S., Rocha, L.A.O., Dos Santos, E.D., Real, M.V., Isoldi, L.A. Constructal design and numerical modeling applied to stiffened steel plates submitted to elasto-plastic buckling. Proceedings of the Romanian Academy Series A-Mathematics Physics Technical Sciences Information Science. 2018. 19. Pp. 195–200.
30. Lima, J.P.S., Cunha, M.L., dos Santos, E.D. Rocha, L.A.O., Real, M.V., Isoldi, L.A. Constructal Design for the ultimate buckling stress improvement of stiffened plates submitted to uniaxial compressive load. Engineering Structures. 2020. 203. 109883. DOI: 10.1016/j.engstruct.2019.109883
31. De Queiroz, J., Cunha, M.L., Pavlovic, A., Rocha, L.A.O, Dos Santos, E.D., Troina, G.S., Isoldi, L.A. Geometric Evaluation of Stiffened Steel Plates Subjected to Transverse Loading for Naval and Offshore Applications. Journal of Marine Science and Engineering. 2019. 7(1). Pp. 7–18. DOI: 10.3390/jmse7010007
32. Pinto, V.T., Cunha, M.L., Troina, G.S., Martins, K.L., dos Santos, E.D., Isoldi, L.A., Rocha, L.A.O. Constructal design applied to geometrical evaluation of rectangular plates with inclined stiffeners subjected to uniform transverse load. Research on Engineering Structures and Materials. 2019. 5. Pp. 379–392. DOI: 10.17515resm2019.118ms0215
33. Mardanpour, P., Izadpanahi, E., Rastkar, S., Lorente, S., Bejan, A. Constructal design of aircraft: flow of stresses and aeroelastic stability. AIAA Journal. 2019. DOI: 10.2514/1.J057183
34. Izadpanahi, E., Moshtaghzadeh, M., Radnezhad, H.R., Mardanpour, P. Constructal approach to design of wing cross-section for better flow of stresses. AIAA Journal. 2020. DOI: 10.2514/6.2020-0275

Contacts:

Vinicius Pinto, viniciustorreseng@gmail.com

Marcelo Cunha, marcelolamcunha@hotmail.com

Kaue Martins, leaodoparque@gmail.com

Luiz Rocha, luizor@unisinos.br

Elizaldo Dos Santos, elizaldosantos@furg.br

Liercio Isoldi, liercioisoldi@gmail.com

© Pinto, V., Cunha, M., Martins, K., Rocha, L., Dos Santos, E., Isoldi, L., 2021

Magazine of Civil Engineering

ISSN 2712-8172

journal homepage: http://engstroy.spbstu.ru/

DOI: 10.34910/MCE.103.11

Modeling the influence of input factors on foam concrete properties

K.D. Vu, S.I. Bazhenova*
National Research Moscow State Civil Engineering University, Moscow, Russia
** E-mail: sofia.bazhenova@gmail.com*

Keywords: optimization, concrete, mixtures, mechanical properties, cement, brick, silica fume

Abstract. The paper presents the use of blast furnace slag as a fine aggregate in foam concrete. Besides, the paper also presents the research results of the effect of the water-cement ratio and Silica fume on the mechanical properties of foam concrete. The absolute volume method was used to calculate the ratio of foam concrete mixture. Besides, the mechanical properties of foam concrete were determined at the age of 28 days. The method of Box-Wilson central composite design for two factors was used to predict the effect of the water-cement ratio and Silica fume on foam concrete properties. The results showed that the proposed regression equations of this mathematical model achieved an adequate prediction accuracy. Using computer programs obtained surface images of equations (10) and (12). Besides, the maximum value of the objective function was determined with compressive strength = 8.52 MPa and flexural strength = 1.21 MPa. This research result is a premise for studying foam concrete bricks to replace clay bricks in construction works.

1. Introduction

In scientific research, numerical methods and computer models used to predict specific properties are of particular importance [1–3]. Besides that, in concrete technology often uses mathematical methods to find the optimal concrete components for technological processes [4, 5].

Experiment planning is a procedure for selecting the number and conditions of the experiments necessary and sufficient to obtain a mathematical model of the process [5–7].

The following should be kept in mind when planning experiments:

- Note to minimize the number of experiments.
- Assume that some factors remain unchanged.
- Research a few important factors affecting the properties of materials to plan experiments.

The studies [5, 8–10] shown that when planning an experiment. It is necessary to gather additional information about the input variables and object under study, employing the skills and knowledge obtained in previous studies. It is needed to collect additional information about the input variables and object under investigation, employing the skills and knowledge obtained in previous studies.

As known, foamed concrete is a highly aerated mortar, typically containing 30 to 80 % air bubbles by volume. It comprises Portland cement, water, fine aggregate, additives and mechanically produced foam. It has high workability, which allows it to flow and compact under its weight [11, 14].

When using foam concrete in construction, there are advantages [3, 11, 13].

- Low thermal conductivity.
- Little weight.
- Easy to transport.
- Ease of use.

Vu, K.D., Bazhenova, S.I. Modeling the influence of input factors on foam concrete properties. Magazine of Civil Engineering. 2021. 103(3). Article No. 10311. DOI: 10.34910/MCE.103.11

This work is licensed under a CC BY-NC 4.0

- Ease of processing. (Due to the low density, aerated concrete products are easily sawn with a conventional hacksaw if necessary, to shorten their size.)
- Long service life.
- Compressive strength and flexural strength decrease with increasing density.

Besides that, silica fume is the most popular material used in concrete to increase its strength. For this study, silica fume is replaced in the range of 0.05÷0.15 % the weight of cement [15].

According to the research results [14–18], the use of clay bricks as a fine aggregate in foam concrete improves the mechanical properties of foam concrete and protects the environment.

Besides, according to the previous research results, the author has studied foam concrete with a density of 900 kg/m^3 using a silica-fume additive, superplasticizer. The result is compressive strength at the age of 28 days, from 7 MPa to 8 MPa. Besides, according to the Vietnamese standard of clay bricks used for construction works, compressive strength is > 7.5 MPa and density = 1600 kg/m^3 [19].

Therefore, the overarching purpose of this study is to use the method of central composite design for two input factors to predict the effect of superplasticizer and silica-fume on compressive and flexural strength of foam concrete at 28 days of age with a density of 900 kg/m^3.

2. Materials and Methods

2.1. Materials

Portland cement (OPC) CEM I 42.5 N produced by the factory “But Son” (Vietnam) with ρ = 3.10 g/cm^3. Its chemical properties are presented in Table 1.

Quartz sand (QS) of the "Lo River" (Vietnam) was used as fine aggregate in concrete mixtures with ρ = 2.65 g/cm^3 and particle size from 0.14 mm to 1.25 mm.

Blast furnace slag (BFS) from the factory "Hoa Phat" (Vietnam) with ρ = 2.297 g/cm^3.

Table 1. Chemical composition of OPC, BFS and SF90.

Chemical components (wt. %)	Cement (OPC)	Blast furnace slag (BFS)	Silica fume (SF90)
SiO_2	22.42	36.02	90.78
Al_2O_3	5.31	13.44	2.22
Fe_2O_3	3.45	-	2.46
SO_3	-	0.15	-
K_2O	0.64	0.29	-
Na_2O	0.15	-	0.57
MgO	2.03	7.66	-
CaO	62.56	40.47	0.54
TiO_2	-	0.5	-
Loss on ignition (%)	3.44	1.47	3.43
Blaine fineness (cm^2/g)	3665	4560	10120

Silica fume SF-90 (SF90) (Vietnam) was used as a binder. The analysis results of the chemical compositions of both SF90 and BFS are presented in Table 1. Besides, the particle size distribution details of raw materials used are shown in Figure 1.

Superplasticizer SR 5000F SilkRoad (SR5000) (Korea), which reduces water consumption, was used as a plasticizing additive. Its density at a temperature of 25±5°C was 1.1 g/cm^3. The optimal dosage of the superplasticizer is 1.5 % of the mass of Portland cement, which makes it possible to reduce water consumption in concrete mixtures by 30 %.

EABASSOC foaming agent manufactured at the factory EABSSOC in the United Kingdom. The foaming additives have the following specifications:

+ Specific weight 1.02 g/cm^3.

+ Dosage rate 0.3-0.6 lit/m^3.

- Mixing water (W) conforming to standard requirements GOST 23732-2011 and TCVN 4506:2012 [20, 21].

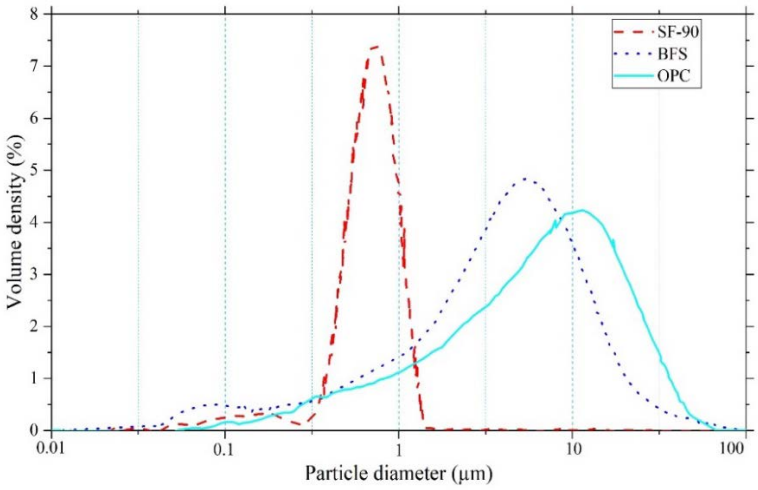

Figure 1. The particle size distribution of OPC, BFS and SF90.

The process of preparing test foam concrete samples is shown in Fig. 2.

Figure 2. The process of preparing foam concrete samples (from left to right, top to bottom).

2.2. Methods

The compressive strength and flexural strength of foam concrete at 28 days of age have been determined according to the Russian state standard GOST 10180-2012 [22].

On the one hand, this paper will analyze the chemical composition and the grain composition of BA and OPC by laser granulometry method on the device BT-9300Z (China). On the other hand, the calculation method of concrete mixture composition is applied by the absolute volume method of the Australian Standard [23].

The effect of Silica fume SF90, water-cement ratio to compressive strength and flexural strength of foam concrete have been identified by using the rotationally variable central compositional planning method for two factors.

3. Results and Discussion

3.1. Preliminary Determination components

In the present study, the mix proportions of foam concrete are given in Table 2. From the data of the study [15], the content of Portland cement is constant OPC of 350 kg/m3. Besides, SR5000 and SF90 have been used to increase strength and reduce water with ratio SR5000/OPC = 0.015, SF90/OPC = 0.1 [14, 24–25].

Table 2. Compositions of foam concrete mixtures.

Mix number	OPC (kg)	QS (kg)	BFS (kg)	SR5000 (kg)	SF90 (kg)	W (kg)	Foam (L)
FC-1	350	356	-	5.25	35	154	579.8
FC-2	350	-	356	5.25	35	154	558.5

Fig. 3 shows that the compressive and flexural strength of FC-2 is higher than the FC-1. In addition, the compressive strength at 28 days of FC-2 = 8.11 MPa > 7.5 MPa. Therefore, the author has used FC-2 to optimize the components by the experimental planning method.

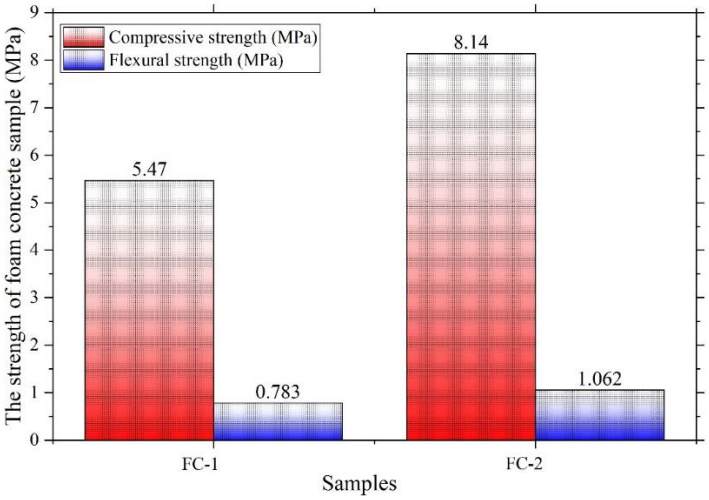

Figure 3. The compressive and flexural strength of foam concrete samples at 28 days.

3.2. Determine the optimal components

The factors that significantly affect the compressive and flexural strength are the W/OPC ratio, the amount of silica fume additive. According to research [15, 24, 26], the amount of silica fume additive in the range of 0.05÷0.15 is optimal. Additionally, based on the test results of this study, it is shown that the ratio of water-cement is in the range of 0.38÷0.42. The factors affecting the intensity of foam concrete were selected as below.

– x_1 – the rate of $\frac{W}{OPC}$ from 0.372 to 0.428;

– x_2 – the ratio of $\frac{SF90}{OPC}$ from 0.029 to 0.171.

Table 3. Values and ranges of influencing factors.

Factors		Levels of variation				
Variable coding	Real variable	-1.414	-1	0	+1	+1.414
x_1	$\frac{W}{OPC}$	0.372	0.38	0.40	0.42	0.428
x_2	$\frac{SF90}{OPC}$	0.029	0.05	0.10	0.15	0.171

Number of experiments needed N when second-order planning determined by the formula;

$$N = 2^k + 2*k + m \tag{1}$$

in which: k = 2 is number of input factors.

- m is the number of repeated experiments in the center, m = 5.
- $\Rightarrow N = 2^2 + 2\times2 + 5 = 13$.

The author used a second-order orthogonal central compositional plan to obtain a mathematical model. The results obtained during the experiment and the procedure for calculating the regression coefficients are given in Tables 4, 5, 6.

Table 4. Compositions of foam concrete according to the method of quadratic orthogonal experiments.

Nº	Real variable		Variable coding		Compositions of foam concrete mixture, kg/m³					
	$\frac{W}{OPC}$	$\frac{SF90}{OPC}$	x_1	x_2	OPC	BFS	SR5000	SF90	W	Foam (L)
1	0.42	0.15	+1	+1	350	354	3.5	47	144.90	564.56
2	0.38	0.15	-1	+1	350	364	3.5	47	135.10	570.10
3	0.42	0.05	+1	-1	350	379	3.5	23	144.90	565.29
4	0.38	0.05	-1	-1	350	389	3.5	23	135.10	570.83
5	0.428	0.1	+1.414	0	350	365	3.5	35	147.00	563.74
6	0.372	0.1	-1.414	0	350	379	3.5	35	133.00	571.65
7	0.4	0.171	0	+1.414	350	354	3.5	53	140.00	567.17
8	0.4	0.029	0	-1.414	350	389	3.5	18	140.00	568.22
9	0.4	0.1	0	0	350	372	3.5	35	140.00	567.70
10	0.4	0.1	0	0	350	372	3.5	35	140.00	567.70
11	0.4	0.1	0	0	350	372	3.5	35	140.00	567.70
12	0.4	0.1	0	0	350	372	3.5	35	140.00	567.70
13	0.4	0.1	0	0	350	372	3.5	35	140.00	567.70

Table 5. Calculation of regression equations for flexural strength at 28 days.

Nº	Variable coding					$\frac{W}{OPC}$	$\frac{SF90}{OPC}$	R_{fs}^{28}, MPa		$(Y_{1j}-\widehat{Y}_{1j})^2$	$(Y_{01j}-\widehat{Y}_{01j})^2$
	x_1	x_2	x_1^2	x_1x_2	x_2^2			Y_{1j}	$\widehat{Y}_{1j}$		
1	+1	+1	1	1	1	0.414	0.135	0.95	1.05	0.00938	-
2	-1	+1	1	-1	1	0.386	0.135	0.92	0.97	0.00228	-
3	+1	-1	1	-1	1	0.414	0.065	0.99	0.98	0.00007	-
4	-1	-1	1	1	1	0.386	0.065	0.93	0.9	0.00075	-
5	+1.414	0	2	0	0	0.42	0.1	1.1	1.05	0.00296	-
6	-1.414	0	2	0	0	0.38	0.1	0.94	0.93	0.00004	-
7	0	+1.414	0	0	2	0.4	0.15	1.1	1.01	0.00887	-
8	0	-1.414	0	0	2	0.4	0.05	0.88	0.91	0.00113	-
9	0	0	0	0	0	0.4	0.1	1.09	1.12	0.00078	0.0008
10	0	0	0	0	0	0.4	0.1	1.14	1.12	0.00048	0.0005
11	0	0	0	0	0	0.4	0.1	1.09	1.12	0.00078	0.0008
12	0	0	0	0	0	0.4	0.1	1.14	1.12	0.00048	0.0005
13	0	0	0	0	0	0.4	0.1	1.13	1.12	0.00014	0.0001
	$\sum(Y_{1j}-\widehat{Y}_{1j})^2 = 0.02816$								$\sum(Y_{01j}-\widehat{Y}_{01j})^2 = 0.0027$		

Table 6. Calculation of regression equations for compressive strength at 28 days.

Nº	Variable coding					$\frac{W}{OPC}$	$\frac{SF90}{OPC}$	R_{cs}^{28}, MPa		$(Y_{2j}-\widehat{Y}_{2j})^2$	$(Y_{02j}-\widehat{Y}_{02j})^2$
	x_1	x_2	x_1^2	x_1x_2	x_2^2			Y_{2j}	$\widehat{Y}_{2j}$		
1	+1	+1	1	1	1	0.414	0.135	7.15	7.86	0.50803	-
2	-1	+1	1	-1	1	0.386	0.135	7.36	7.62	0.07007	-
3	+1	-1	1	-1	1	0.414	0.065	7.6	7.31	0.08622	-
4	-1	-1	1	1	1	0.386	0.065	7.47	7.07	0.16135	-
5	+1.414	0	2	0	0	0.42	0.1	7.98	7.69	0.08477	-
6	-1.414	0	2	0	0	0.38	0.1	7.25	7.35	0.01045	-
7	0	+1.414	0	0	2	0.4	0.15	8.49	7.8	0.47072	-

Nº	Variable coding					$\frac{W}{OPC}$	$\frac{SF90}{OPC}$	R_{cs}^{28}, MPa		$(Y_{2j}-\widehat{Y}_{2j})^2$	$(Y_{02j}-\widehat{Y}_{02j})^2$
	x_1	x_2	x_1^2	x_1x_2	x_2^2			Y_{2j}	$\widehat{Y}_{2j}$		
8	0	-1.414	0	0	2	0.4	0.05	6.52	7.02	0.24717	-
9	0	0	0	0	0	0.4	0.1	8.37	8.48	0.01254	0.0125
10	0	0	0	0	0	0.4	0.1	8.76	8.48	0.07728	0.0773
11	0	0	0	0	0	0.4	0.1	8.21	8.48	0.07398	0.074
12	0	0	0	0	0	0.4	0.1	8.49	8.48	0.00006	0.0001
13	0	0	0	0	0	0.4	0.1	8.58	8.48	0.0096	0.0096
$\sum(Y_{2j}-\widehat{Y}_{2j})^2=1.8127$									$\sum(Y_{02j}-\widehat{Y}_{02j})^2=0.173$		

3.2.1. The calculation of the estimates of the coefficients

Base on the research [27], The coefficients of the regression equation, calculated by the formulas (2): The results are shown in Table 7.

$$b_j=\frac{\sum_{i=1}^{N}x_{ij}y_j}{\sum_{i=1}^{N}x_{ij}^2}\forall_j=\overline{1...n};\quad b_{ju}=\frac{\sum_{i=1}^{N}x_{ij}^2x_{ui}y_j}{\sum_{i=1}^{N}x_{ij}^2x_{ui}^2}\forall_{j,u}=\overline{1...n};j\neq u \tag{2}$$

Table 7. Coefficient of the quadratic regression equation.

	b_j / Y_j	b_0	b_1	b_2	b_{12}	b_{11}	b_{22}
Y_1	R_{fs}^{28}, MPa	1.118	0.040	0.033	-0.008	-0.064	-0.079
Y_2	R_{cs}^{28}, MPa	8.482	0.119	0.278	-0.085	-0.481	-0.536

Based on the calculation results, the following regression equations were obtained:

$$Y_1 = 1.118 + 0.040x_1 + 0.033x_2 - 0.008x_1^2 - 0.064x_2^2 - 0.079x_1x_2 \tag{3}$$

$$Y_2 = 8.482 + 0.119x_1 + 0.278x_2 - 0.481x_1^2 - 0.536x_2^2 - 0.085x_1x_2 \tag{4}$$

3.2.2. Check the coefficients of the regression equation (3) and (4)

Critical values for Cochran's test $G_c = G_Q(t_Q, n_1)$ was found from Table 3.2 of the Cochran distribution [28] depending on the values:

- Level of significance Q = 0.05.
- Degrees of freedom of the numerator $n_1 = m - 1 = 5 - 1 = 4$;
- $\Rightarrow t_{0,025}(4) = 2.7764$

Regression equations were determined by the formula:

$$t_{bj}=\frac{|b_j|}{s_{bj}} \tag{5}$$

The variance estimate of the regression coefficients of the equation S_{bj} was determined by the formula:

$$S_{bj}=\sqrt{\frac{s_{ll}^2}{\sum_{i=1}^{N}x_{ij}^2}} \tag{6}$$

in which: S^2_{ll} is the estimating observation-error variance, determined by the formula:

$$S_{ll}^2 = \frac{\sum_{j=1}^{m} (Y_{oj} - \widehat{Y}_o)^2}{m-1} \tag{7}$$

$$\widehat{Y_o} = \frac{1}{m}\sum_{j=1}^{m} Y_{oi} \tag{8}$$

in which:

m is the number of repeated experiments in the center, m = 5;

$\widehat{Y}_o$ is the average value of m experiments in the center;

Y_{oj} is the obtained value of the i-th experiment in the center.

For the regression equation (3):

$$\sum_{j=1}^{5} (Y_{01j} - \widehat{Y}_{01})^2 = 0.0027 \Rightarrow S_{1ll}^2 = \frac{0.0027}{5-1} = 0.00067 \tag{9}$$

The values of the student criterion for the test are given in Table 8.

Table 8. Student coefficients for checking the regression equation (3).

j	0	1	3	4	5	6
b_j	b_0	b_1	b_2	b_{12}	b_{11}	b_{22}
	1.118	0.040	0.033	-0.008	-0.064	-0.079
$\|b_j\|$	1.118	0.040	0.033	0.008	0.064	0.079
S_{bj}	0.012	0.009	0.009	0.013	0.010	0.010
t_{bj}	96.580	4.320	3.566	-0.580	-6.532	-8.059

After checking the coefficients, discarding negligible coefficients. We obtained the equation:

$$Y_1 = 1.118 + 0.040x_1 + 0.033x_2 - 0.064x_1^2 - 0.079x_2^2 \tag{10}$$

For the regression equation (4):

$$\sum_{j=1}^{5} (Y_{02j} - \widehat{Y}_{02j})^2 = 0.173 \Rightarrow S_{2ll}^2 = \frac{0.173}{5-1} = 0.043 \tag{11}$$

The values of the student criterion for the test are given in Table 9.

Table 9. Student coefficients for checking the regression equation (4).

j	0	1	3	4	5	6
b_j	b_0	b_1	b_2	b_{12}	b_{11}	b_{22}
	8.482	0.119	0.278	-0.085	-0.481	-0.536
$\|b_j\|$	8.482	0.119	0.278	0.085	0.481	0.536
S_{bj}	0.093	0.074	0.074	0.104	0.079	0.079
t_{bj}	91.073	1.617	3.778	-0.816	-6.083	-6.779

After checking the coefficients, discarding negligible coefficients. We obtained the equation:

$$Y_2 = 8.482 + 0.278x_2 - 0.481x_1^2 - 0.536x_2^2 \tag{12}$$

3.2.3. Check the adequacy of the experimental model

- Testing the Hypothesis of the Adequacy of the model is based on the calculations of the adequacy variance S^2_d (14) and Fisher's Criterion F_{pacc} (13):

$$F_{pacc} = \frac{S_d^2}{S_{ll}^2} \tag{13}$$

$$S_d^2 = \frac{\sum_{j=1}^{N} (Y_j - \widehat{Y}_j)^2}{N - m} \tag{14}$$

where S^2_{ll} is the estimating observation-error variance;

S^2_d is variance;

m is the number of repeated experiments in the center; m = 5.

Y_j is the observed value of the i-th experiment;

$\widehat{Y}_j$ is the values of a function obtained from an experiment following the i-th experiment;

F_Q, (v_1, v_2) from the Table 3.5 [28], at a significance level Q = 0.05; determined by the number of degrees of freedom $v_2 = N = m - 1 = 4$ and $v_1 = N - m = 13 - 5 = 8$. So, the value: $F_Q(8, 4) = 6.0410$.

For the regression equation (10):

$$\sum_{j=1}^{13} (Y_{ij} - \widehat{Y}_{1j})^2 = 0.02816 \Rightarrow S_{1d}^2 = \frac{0.02816}{13-5} = 0.00352 \text{ and } S_{1ll}^2 = 0.00067.$$

$$\Rightarrow F_{1pacc} = \frac{S_{1d}^2}{S_{1ll}^2} = \frac{0.0352}{0.00067} = 5.254 < F_{0.05}(8,4) = 6.0410.$$

For the regression equation (12):

$$\sum_{j=1}^{13} (Y_{2j} - \widehat{Y}_{2j})^2 = 1.8127 \Rightarrow S_{2d}^2 = \frac{1.8127}{13-5} = 0.226 \text{ and } S_{2ll}^2 = 0.043.$$

$$\Rightarrow F_{2pacc} = \frac{S_{2d}^2}{S_{2ll}^2} = \frac{0.2266}{0.043} = 5.286 < F_{0.05}(8,4) = 6.0410$$

Therefore, equation (10) and (12) satisfy the condition $F_{pacc} < F_{tab}$.

Response surfaces for the regression equations (10) and (12) are presented in Fig. 4 and 5.

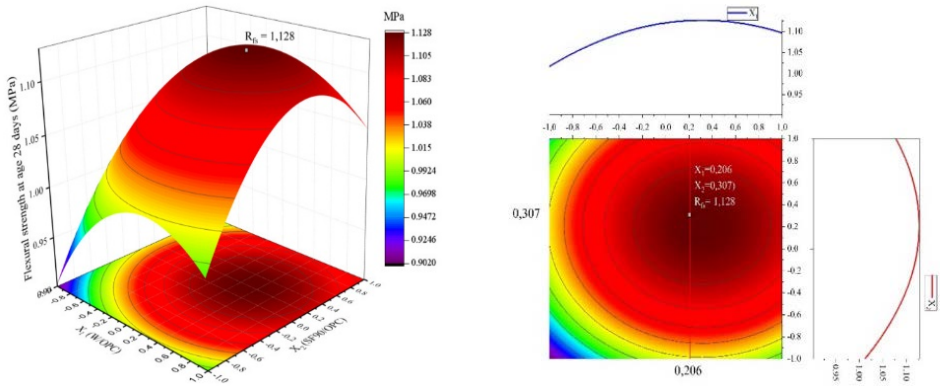

Figure 4. Second-order surface equation (10).

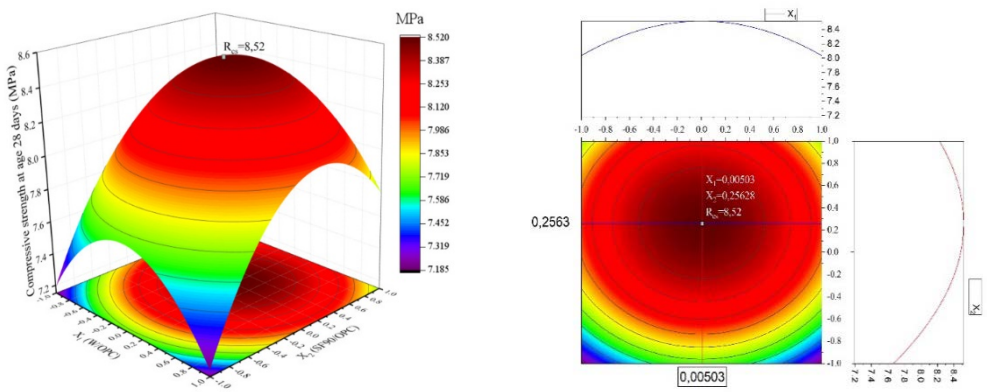

Figure 5. Second-order surface equation (12).

3.2.4. Search for the maximum value of the second-order regression equation and selection of the optimal composition

The first case:

When x_1 = 0.206, x_2 = 0.307 and flexural strength R_{fs} = 1.128 MPa.

Replacement: x_1 = 0.206, x_2 = 0.307 into the equation (10) $\Rightarrow R_{cs}$ = 8.495 MPa.

The second case:

When x_1 = 0.00503, x_2 = 0.25628 and compressive strength R_{cs} = 8.52 MPa.

Replacement: x_1 = 0.00503, x_2 = 0.25628 into the equation (12) $\Rightarrow R_{fs}$ = 1.21 MPa.

Thus, the most optimal value: x_1 = 0.00503 and x_2 = 0.25628.

- $$\Rightarrow \frac{W}{OPC} = \left(\frac{W}{OPC}\right)_0 + 0.02*x_1^{opt} = 0.40 + 0.02*0.00503 = 0.4001;$$

$$\Rightarrow \frac{SF90}{OPC} = \left(\frac{SF90}{OPC}\right)_0 + 0.05*x_2^{opt} = 0.1 + 0.05*0.25628 = 0.1128.$$

Thus, the optimal composition of the foam concrete is presented in Table 10.

Table 10. The optimal composition of the foam concrete mixture to obtain maximum compressive strength and flexural strength.

N°	The ratio of raw materials		Foamed concrete mix compositions, kg/m^3					
	$\frac{W}{OPC}$	$\frac{SF90}{OPC}$	OPC	BFS	SR5000	SF90	W	Foam (L)
1	0.4001	0.1128	350	367	3.5	39	140.0	567.4

4. Conclusions and future work

Based on the analysis of the data obtained from the experiment, the following conclusions can be drawn:

1. Based on test results, preliminary components have been identified to optimize components.

2. Static processing of the results, performed by mathematical methods for planning experiments to optimize the composition of the designed foam concrete, with a certain probability and the number of retests. The foam concrete samples are then compared with the results obtained by various methods.

3. The obtained second-order regression equations (10) and 12) describe the dependence of compressive strength and flexural strength of foam concrete at 28 days of standard hardness x_1 = 0.00503 and x_2 = 0.25628.

4. Using computer programs obtained surface images of equations (10) and (12), as shown in Fig. 4, 5. Besides, the maximum value of the objective function was determined.

5. The optimal composition of the foam concrete mix with the highest compressive strength and flexural strength are presented in Table 10.

6. The paper's result is the basis for designing foam concrete bricks to replace clay bricks in Vietnam.

References

1. Williams, H.P. Model Building in Mathematical Programming 2013. 411p.
2. Trong, C.N., Xuan, B.L. Reducing temperature difference in mass concrete by surface insulation. Magazine of Civil Engineering. 2019. 4(88). Pp. 70–79. DOI: 10.18720/MCE.88.7
3. Lam, T.V., Vu, D.T., Dien, V.K., Bulgakov, B.I., Korol, E.A. Properties and thermal insulation performance of lightweight concrete. Magazine of Civil Engineering. 2018. (8). Pp. 173–191. DOI: 10.18720/MCE.84.17
4. Wang, B., Xia, X., Zhang, J. A multi-objective optimization model for the life-cycle cost analysis and retrofitting planning of buildings. Energy and Buildings. 2014. 77. Pp. 227–235. DOI: 10.1016/j.enbuild.2014.03.025
5. Aniskin, N., Nguyen, T. Influence factors on the temperature field in a mass concrete. E3S Web of Conferences. 2019. 05021(97). Pp. 9. DOI: //doi.org/10.1051/e3sconf/20199705021
6. Dvorkin, L., Bezusyak, A., Lushnikova, N., Ribakov, Y. Using mathematical modeling for design of self compacting high strength concrete with metakaolin admixture. Construction and Building Materials. 2012. 37. Pp. 851–864. DOI: 10.1016/j.conbuildmat.2012.04.019
7. Sergeyevich, A.A. The mathematical theory of experimental design and planning an experiment in communication technology. Information Society Technologies. 2012. 8. Pp. 3–5.
8. Song, L., AbouRizk, S.M. Virtual shop model for experimental planning of steel fabrication projects. Journal of Computing in Civil Engineering. 2006. 20(5). Pp. 308–316. DOI: 10.1061/(asce)0887-3801(2006)20:5(308)
9. Pavlovna, A.T. Experiment Planning Methodology. Collection of laboratory works for students of the specialty. 2006. 35 p.
10. Chuc, N.T., Bui, A.K. Evaluation of the impact of parameter inputs of concrete mix on the. Structural integrity and life. 2019. 19(1). Pp. 8–12.
11. Steshenko, A.B., Kudyakov, A.I. Cement based foam concrete with aluminosilicate microspheres for monolithic construction. Magazine of Civil Engineering. 2018. 8(84). Pp. 86–96. DOI: 10.18720/MCE.84.9
12. Rybakov, V.A., Kozinetc, K.G., Vatin, N.I., Velichkin, V.Z., Korsun, V.I. Lightweight steel concrete structures technology with foam fiber-cement sheets. Magazine of Civil Engineering. 2018. 6(82). Pp. 103–111. DOI: 10.18720/MCE.82.10
13. Gökçe, H.S., Hatungimana, D., Ramyar, K. Effect of fly ash and silica fume on hardened properties of foam concrete. Construction and Building Materials. 2019. 194. DOI: 10.1016/j.conbuildmat.2018.11.036
14. Dien, V.K., Ly, N.C., Lam, T.V., Bazhenova, S.I. Foamed concrete containing various amounts of organic-mineral additives. Journal of Physics: Conference Series. 2020. 1425. Pp. 10. DOI: 10.1088/1742-6596/1425/1/012199
15. Vu, K.D., Bazhenova, S.I., T.V.L. The effect of mineral additives, fly ash, blast furnace slag on the mechanical properties of foam concrete. Stroitelstvo i Rekonstruktsiya. 2020. 2 (88). Pp. 25–34. URL: DOI. 10.33979/2073-7416-2020-88-2-25-34
16. Oren, O.H., Gholampour, A., Gencel, O., Ozbakkaloglu, T. Physical and mechanical properties of foam concretes containing granulated blast furnace slag as fine aggregate. Construction and Building Materials. 2020. 238. Pp. 117774. DOI: 10.1016/j.conbuildmat.2019.117774.
17. Bejan, G., Bărbuță, M., Vizitiu, R., Ștefan Burlacu, A. Lightweight Concrete with Waste - Review. Procedia Manufacturing. 2020. 46. Pp. 136–143. DOI: 10.1016/j.promfg.2020.03.021
18. Lesovik, V., Voronov, V., Glagolev, E., Fediuk, R., Alaskhanov, A., Amran, Y.H.M., Murali, G., Baranov, A. Improving the behaviors of foam concrete through the use of composite binder. Journal of Building Engineering. 2020. 31. Pp. 1–29. DOI: 10.1016/j.jobe.2020.101414
19. Hollow clay bricks. Vietnam standard. TCVN 1450-2009. 2009. 9 p.
20. Water for concrete and mortar – Technical speccification. Standard Vietnam. TCVN – 4506:2012. 2012. 7 p.
21. Water for concrete and mortar. Technical conditions. Standard Russian. GOST-23732-2011. 2012. 21 p.
22. Concrete Methods for determining the strength of the control samples. Standard Russian. GOST-10180-2012. 2013. 36 p.
23. Methods of testing concrete. Australian Standard. AS 1012.21994. 17 p.
24. Falliano, D., De Domenico, D., Ricciardi, G., Gugliandolo, E. Experimental investigation on the compressive strength of foamed concrete: Effect of curing conditions, cement type, foaming agent and dry density. Construction and Building Materials. 2018. 165. Pp. 735–749. DOI: 10.1016/j.conbuildmat.2017.12.241
25. Barabanshchikov Yu.G., Arkharova A.A., T.M.V. About the effect of superplasticizer on the effectiveness of anti-shrink additives. Magazine of Civil Engineering. 2014. 7. Pp. 23–30. DOI: 10.5862/MCE.51.3
26. Rassokhin, A.S., Haemek, M., Rassokhin, A.A.S. Silica fumes of different types for high – performance fine – grained concrete. Magazine of Civil Engineering. 2018. 2(78). Pp. 151–160. DOI: 10.18720/MCE.78.12
27. Bazhenov, Yu.M. Concrete technology. ASV 2011. 524 p.
28. Bol'shev, L.N., Math Statistics Tables. Moscow 1983. 416 p.

Contacts:

Kim Dien Vu, kimdienxdtb@gmail.com

Sofya Bazhenova, sofia.bazhenova@gmail.com

© Vu, K.D., Bazhenova, S.I., 2021

Magazine of Civil Engineering

ISSN 2712-8172

journal homepage: http://engstroy.spbstu.ru/

DOI: 10.34910/MCE.103.12

Thermal mode of a room with integrated regulation of cooling systems

O.D. Samarin
National Research Moscow State University of Civil Engineering, Moscow, Russia
** E-mail: samarin-oleg@mail.ru*

Keywords: microclimate, temperature, heat balance, heat gain, regulation, integral algorithm, transmission coefficient, civil engineering, building, construction industry

Abstract. An air-conditioned room with automatic regulation of the climate systems serving it using complex control algorithms is one of the most difficult objects for calculating non-stationary thermal regime, so to date, this method is insufficiently studied. At the same time, such objects are typical when organizing the internal microclimate of civil buildings. In this paper, we consider the mathematical formulation and solution of the problem of changing the temperature of internal air in a room equipped with automated local cooling systems and a background supply ventilation system under variable thermal influences. The main equations connecting the most important components of the heat flow in the room are analyzed. The dependence on time for the deviation of the room air temperature from the setpoint is presented, and the expression for the moment of time at which the maximum temperature deviation is observed, with a jump-like change in the heat flow from heat sources in the case of regulating the equipment of local cooling systems according to the integral law. Calculations were performed to confirm the analytical solution obtained using a finite-difference approximation of the differential equations of heat balance and heat transfer on the example of one of the currently existing residential buildings in the climatic conditions of Moscow, taking into account the structural characteristics of the building and the thermal properties of its enclosing structures. It is noted that the greatest deviation of the temperature from the setpoint (dynamic control error) in the first approximation is inversely proportional to the cubic root of the transmission coefficient of the regulator, as well as the moment of time for which this deviation is observed. The obtained relations are proposed to be used for an analytical assessment of the non-stationary thermal regime of an air-conditioned room served by local cooling systems equipped with an automation system with an integral law of regulation, to check the conditions of human comfort and safety, as well as to determine the required parameters of the regulator.

1. Introduction

The proposed publication studies the change in the indoor air temperature in a room equipped with automated local cooling systems and a background supply ventilation system under the conditions of variable thermal effects.

The necessity to maintain a set of indoor microclimate parameters in the range determined by human comfort conditions or ensuring technological process is primarily associated with health and safety requirements. In practice, hygrothermal regime stabilization is carried out primarily through the automatic regulation and control by climate systems, taking into account the heat resistance of buildings themselves. At the same time, since the thermal effects on the premises and their heat loss are found to be variable in almost all cases, this task is of a significantly dynamic nature.

The problem of calculating the temperature in air-conditioned rooms with the emergence of thermal disturbances has long been studied. Barring some simplified analytical solutions to this problem, given in the reference and educational literature and mainly related to insulated enclosure structures in the building cooling mode a during an emergency shutdown of heat supply or with periodic thermal disturbances without taking into account the overall heat equilibrium of the room, we can note more complex works recently

Samarin, O.D. Thermal mode of a room with integrated regulation of cooling systems. Magazine of Civil Engineering. 2021. 103(3). Article No. 10312. DOI: 10.34910/MCE.103.12

This work is licensed under a CC BY-NC 4.0

appeared, for example [1], however, their results often prove difficult to use in engineering calculations because of their considerable complexity. At the same time, using numerical methods for studying dynamic modes and their modeling is becoming increasingly widespread. In this regard, the following publications [2–3], are of particular interest and approaches of this kind are now especially incident to foreign studies, of which we can name such fairly distinctive works as [4–6]. However, various solution options are related to specific types of facilities used in limited areas and operating in special conditions, for example, for underground pipelines [7], in the presence of changes in phase [8] or for ventilated facades integrated with natural ventilation systems [9]. We should also mention one of the previous publications of the author [10], where a reasonably simple solution for the temperature-wave propagation in a thick-walled cylinder was obtained. In addition, the authors of certain works in this area are rather focused on solving the inverse problem – determining the thermal and physical characteristics of a material based on a study of temperature fluctuations [11–13], or using thermographic methods [14]. There are works [15–20] devoted to modeling processes in the room as a whole. A sufficiently accurate analytical solution for calculating temperature fluctuations is given in [15], however, it applies only to enclosure structures, and [16] considers a remarkably detailed simulation-type multiparameter numerical model, but it refers to the cold season with heating. Publications [17–20] also possess a certain integrity, in particular, [17–18] relate to the use of fuzzy logic principles in the organization of microclimate management, and [19–20] are more focused on the methods of automatic control theory, but their results are quite complicated for using them in engineering practice. Finally, there are also works related to the general principles of building engineering systems management and energy saving in these conditions, for example, [21–23], but due to their generality, they also do not contain specific dependencies of interest to us.

The author in [24] managed to obtain an analytical solution to the problem of lowering the temperature in the room during an emergency shutdown of heat supply using the heat equilibrium differential equation for the room as a whole. However, it remains advisable to conduct studies for other cases where such an equation lends itself to integration, especially if regular air conditioning systems equipped with the necessary equipment for their automatic regulation are functioning in the room, which allows maintaining internal meteorological parameters in the required range.

Although proportional control units are the most simply arranged, they are known to have a drawback, which may be significant under certain circumstances, namely, a non-zero steady-state error of maintaining the controlled parameter. Therefore, preference in a number of situations is given to control algorithms with an integral component, where the control action is proportional to the sum of the accumulated deviation from the onset of thermal disturbance and the control process is carried out until this deviation is completely eliminated.

At the same time, a situation where stabilization of the indoor air and fences temperature occurs through the local cooling systems, for example, such as “chiller-fan coil” or split systems, employing complete recirculation of the air used and thus not participating in the general air balance of the room, or even with the help of panel-radiant cooling systems, the most common of which are cooled ceilings, is quite common. There, a mechanical supply system plays mainly a sanitary and hygienic role, providing the necessary cleanliness of the internal air, and in cases where it ensures cooling of the supply, it is done primarily so as not to increase the heat load on local cooling systems due to the inflow of high temperature air into the room. In this case, it will be shown that, if switching to the regulation of the inflow temperature and in the absence of local cooling systems, the corresponding solution will be a special case of a more general one, directly considered in this paper.

Thus, the relevance of the proposed study lies in the need to search for sufficiently accurate and physically justified dependences on the time of the change in the temperature of the indoor air in a room cooled with local automated systems at the same time acceptable for engineering use, taking into account the amount of heat input, room heat resistance and control unit characteristics, as well as the relationship of these characteristics with the maximum temperature deviation from a given value. The results obtained may be applicable to a very wide range of facilities of this type.

The aim of the paper is to develop methods for calculating the dynamic thermal regime of a room where local automated cooling systems are operated in the presence of a background unregulated inflow. The objectives of the study are:

- compilation of the basic system of differential equations describing the heat equilibrium, heat transmission and heat exchange in a room air-conditioned with automated climate systems;
- construction of an analytical solution of this equation with abrupt thermal disturbance and regulation of cooling systems according to the integral law;
- obtaining analytical dependences for the maximum deviation of the room temperature from the set point and for the point in time when this deviation is observed, and their confirmation based on a comparison of theoretical results with the data of programmed generation.

2. Methods

The equation of convective heat balance for indoor air within the framework of its single-are model can be shown here as follows:

$$Q_{in} + G_s c_a \left(t_s - t_{in}\right) \Big/ 3.6 - Q_c - B\sqrt{\tau}\,\frac{dt_{in}}{d\tau} = 0\,, \tag{1}$$

Where Q_{in} is the sensible heat inflow in the room air from sources, W; τ is time interval, s, from the moment of the beginning of variable thermal effect; G_s is mass flow rate, kg/h, which is usually considered as equal to the value of the flow rate G_{ex} due to the almost instantaneous stationary state of the air equilibrium of the room compared to the heat equilibrium; c_a is specific heat of air equal to 1.005 kJ/(kg K); t_{in} is indoor air temperature, °C; t_s is inflow temperature, °C. Equation (1), compared with that presented in [24], contains an additional term of Q_c, representing the value of the regulated heat flow, W, from local cooling systems, which is designed to compensate for heat input. For the same reason, it is now assumed in (1) that t_s = const.

As in [19], parameter B in expression (1) is calculated by the formula:

$$B = \sum\left[A_m \sqrt{\lambda c \rho}\right]. \tag{2}$$

Here λ, c and ρ are the thermal conductivity, W/(m K), specific heat, J/(kg K), and the density of the material of the layer of the i-th massive fence facing the inside of the room, respectively, for example, of external and internal walls and partitions, as well as floors; A_m is area of each of the enclosure structures listed, m^2.

If the value of t_{in} is automatically supported by a control unit implementing a continuous integral law with the necessary change in the value of Q_c, the additional constraint equation the most conveniently written in this form:

$$\frac{dQ_c}{d\tau} = K_c\left(t_{in} - t_{in.0}\right). \tag{3}$$

Here, K_c is the equivalent transfer ratio of the automated system, W/(K s), over the channel $t_{in} \rightarrow$ derivative of Q_c". Using the concept of excess temperature $\theta_{in} = t_{in} - t_{in.0}$, where $t_{in.0}$ is a controlled level of t_{in}, or the so-called control point, and differentiating (1) term by term by τ for the possibility of substituting expressions (3) there, we can write (1) in the canonical form:

$$\frac{d^2\theta_{in}}{d\tau^2} + \left(\frac{1}{2\tau} + \frac{C}{\sqrt{\tau}}\right)\frac{d\theta_{in}}{d\tau} + \frac{D}{\sqrt{\tau}}\theta_{in} = 0\,. \tag{4}$$

The parameter of C, s$^{-1/2}$, can be determined by the formula:

$$C = \frac{G_s c_a}{3.6B}\,. \tag{5}$$

It is easy to see that differential equation (4) refers to linear homogeneous equations of the second order, albeit with variable coefficients, as a result of which the simplest solution methods like operation variants cannot be directly applied to it. However, if we use substitution $z = \sqrt{\tau}$, it is reduced to a somewhat simpler form in which one of the terms containing the first derivative is gone:

$$\frac{d^2\theta_{in}}{dz^2} + 2C\frac{d\theta_{in}}{dz} + 4zD\theta_{in} = 0\,, \tag{6}$$

where $D = K_c/B$, s$^{-3/2}$.

Generally speaking, this equation may be solved analytically, and it is the most easily found in the form of a series expansion in powers of z by the method of undetermined coefficients. Moreover, as initial

conditions at $\tau = 0$, we have $\theta_0 = 0$ and, obviously, $d\theta_{in}/dz = 2Q_{in}/B$, since at the initial moment of time for a given law of control in (1), only the first and last terms will be non-zero. In this case, the desired function is recorded in the following form:

$$\theta(z) = \frac{2Q_{in}z}{B}\left[\begin{array}{l} 1 - Cz + \frac{2}{3}C^2z^2 - \frac{1}{3}\left(C^3 + D\right)z^3 + \frac{1}{15}C\left(2C^3 + D\right)z^4 - \\ -\frac{1}{45}C^2\left(2C^3 + 3D\right)z^5 + \frac{1}{315}\left(4C^6 + 16C^3D + 10D^2\right)z^6 - \ldots \end{array}\right]. \quad (7)$$

Note that the parameter of D, which directly includes the quantity K_c, appears only with members of the series, starting with z^4, i.e. τ^2. It is easy to verify that for not very large τ and z values, respectively, the series convergence is rather fast.

At the same time, it can be obtained that in the limiting case of $D = 0$, i.e. if the automatic control system does not function, we have the following instead of (6):

$$\frac{d^2\theta_{in}}{dz^2} + 2C\frac{d\theta_{in}}{dz} = 0. \quad (8)$$

By substitution $X = \frac{d\theta_{in}}{dz}$ this equation is reduced to an equation of the first order with separable variables, from which we obtain the following taking into account the initial conditions and the expression for parameter of C:

$$\theta_{in} = \frac{3.6Q_{in}}{G_s c_a}\left(1 - exp\left[-\frac{2G_s c_a}{B}\sqrt{\tau}\right]\right). \quad (9)$$

It is easy to verify that the first three terms in the decomposition of solution (9) into the Taylor series in in the vicinity of the point $\tau = 0$ coincide with those for (7) therefore, (9) is indeed an asymptotic approximation for (7) at $D \to 0$. Moreover, from the same decomposition it follows that for small τ, dependence (9) will be equivalent to the following:

$$\theta_{in} = \frac{2Q_{in}}{B}\sqrt{\tau}. \quad (10)$$

As in other cases considered earlier, this coincides with the formula for the natural change in temperature in the room with no automatic control. At the same time, at $\tau \to \infty$ the expression (9) gives us $\theta_{in} \to \frac{3.6Q_{in}}{G_s c_a}$, which corresponds to the steady state during the operation of a mechanical ventilation system with a constant inflow temperature.

When the automatic control system is in operation, the value of θ_{in} reaches its peak value, and then approaches zero again, as it should. The moment where $\theta_{in} = \theta_{max}$, can be determined by calculating the derivative of $d\theta_{in}/dz$ and equate it to zero. From (7) we obtain the following decomposition:

$$\frac{d\theta(z)}{dz} = \frac{2Q_{in}}{B}\left[1 - 2Cz + 2C^2z^2 - \frac{4}{3}\left(C^3 + D\right)z^3 + \frac{1}{3}C\left(2C^3 + D\right)z^4 - \frac{2}{15}C^2\left(2C^3 + 3D\right)z^5 + \ldots\right]. \quad (11)$$

It is easy to see that this series also converges rather quickly. Since obviously $\frac{2Q_{in}}{B} \neq 0$, for $d\theta_{in}/dz = 0$ expressions in brackets must be equal to zero.

3. Results and Discussion

For clarity, we give an example of calculating the value of t_{in} by formula (7) in the room with the parameters of B = 12000 W c$^{1/2}$/K; C = 0.01 s$^{-1/2}$ (corresponding to G_s = 430 kg/h) and K_c = 0.25 W/(K s), from which D = K_c/B = 2.083 10^{-5}, s$^{-3/2}$. When calculating, the initial level of $t_{in.0}$ was taken equal to +20 °C, a jump in heat gain (design cooling load) Q_{in} = 500 W, and the value of B was determined taking into account the actual thermal and technical characteristics of building materials in the building and the geometry of the room. The dimensions of the room and its layout with some of the symbols used are shown in Fig. 1. The area is 14 m^2, inner structures made of reinforced concrete with density 1200 kg/m^3 and a total area of 64 m^2, which accounted for half, since it is assumed that the neighboring rooms are in similar conditions, and the influence of temperature is on both sides, the outer wall of lightweight concrete with a density of 500 kg/m^3 and a 7 m^2 with window with an area of 1.8 m^2.

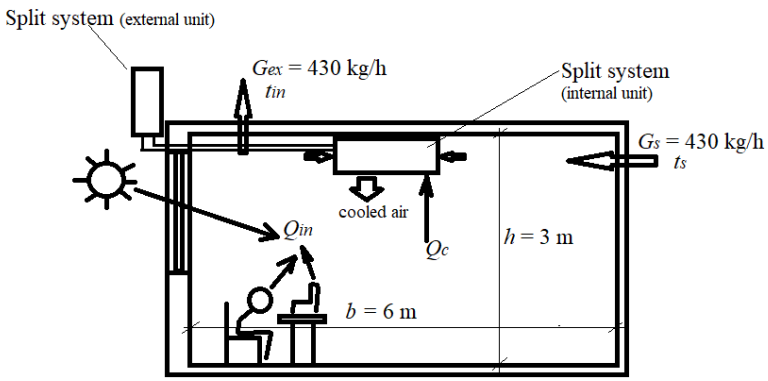

Figure 1. The scheme design of the room.

The corresponding graph is shown in Fig. 2 by a solid line. For comparison, the dotted line shows the results of numerical simulation for the same conditions using the computer program developed by the author and based on a direct solution of the system of differential equations of dynamic heat transmission in fences and heat exchange on their surfaces [24].

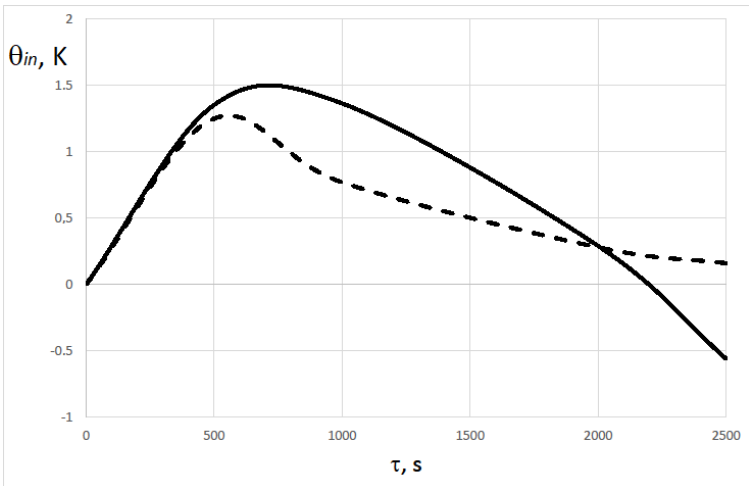

Figure 2. Dependence of θ_{in} Time dependence for the design room (solid line – according to the formula (7), dotted line – numerical calculation).

It is easy to notice that the coincidence of the data of numerical calculation and expression (11) is quite satisfactory, especially at the initial moments of time, at least from the viewpoint of the maximum deviation t_{in} and the time when it takes place. In the future, the calculation of (11) begins to give somewhat overestimated, and later, on the contrary, underestimated results, especially for bigger τ, when the curve under the conditions when using integral control should asymptotically tend to zero, which is reflected in the results of numerical calculation. It seems that the restrictions used in writing the original equation (1) are already beginning to affect here, namely, the assumption that the temperature wave does not have time to penetrate to the outer surface of the fence or to its axis of symmetry. However, since we are primarily interested in the value and moment of the greatest temperature deviation, the solution can be considered satisfactory.

The reliability of the obtained result was confirmed by a full-scale experiment for the same room for which the graphs in Fig. 2 were obtained. In this case, the jump in heat gain was simulated by switching on a convective electric heater of the appropriate power. It should only be borne in mind that in this case, in contrast to the comparison with the software calculation, which is focused on the simultaneous flow of similar processes in all neighboring areas, to construct the theoretical curve for (7), you need to take twice the value B = 24000 W $c^{1/2}$/K, since the temperature wave in the fences will propagate only in one direction. To compensate for heat surpluses, an internal split-system unit was used, which is regulated positionally, but due to the high frequency of switching on and off, this regulation is close to integral. The value of K_c in this case was 0.5 W/(K s), so the parameter D remains equal to 2.083 10^{-5}, $s^{-3/2}$. Fig. 3 shows the solid line graph of the internal temperature deviation calculated from (7), the dotted line shows the experimental data. It is easy to see that given the measurement accuracy of 0.1 degrees, the match is quite good.

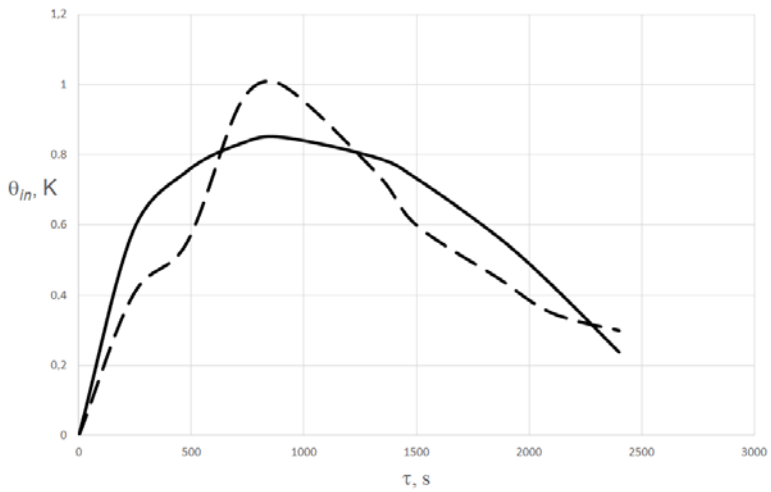

Figure 3. Dependence of θ_{in} Time dependence for the design room (solid line – according to the formula (7), dotted line – experiment).

It should be borne in mind that, based on the structure of equation (11), which includes two parameters of C and D, fairly simple formulas for θ_{max} and the corresponding level of z in this mode, are not obtained so easily. However, if we hold only the first terms containing C and D in (11), we can find the approximate dependence for z in the following form following linearization:

$$z = z_0\left(1-\frac{1}{1+Nz_0}\right), \tag{12}$$

where $z_0 = \frac{0.956}{\sqrt[3]{D}}$ is the value of z at $\theta = \theta_{max}$ and C = 0, obtained by dimensional analysis [25]; $N = 1.82\frac{\sqrt[3]{D^2}}{C}$ is the correction related to the emergence of unregulated inflows. Let us note that when substituting z_0 in (7) we can obtain that the value of θ_{max} must also be inversely proportional to the parameter of D raised to the power of 1/3. In the conditions of our example, we find z_0 = 34.7 $s^{1/2}$ and N = 0.14, therefore, z = 28.7 $s^{1/2}$, or τ = 824 s, which closely enough coincides with that shown in Fig. 2. Obviously, for G_s and, consequently non-zero C, the both values of θ_{max} and z will be lower than in the absence of background air exchange.

At the same time, it is easy to verify that, for C = 0, only terms with powers of z equal to 1, 4, 7, etc. remain in the decomposition (7) and thus, such a solution will be another limiting variant (7), being fair if there is no unregulated temperature inflow. In physical terms, this will mean replacing the regulated local cooling system with the direct maintenance of the internal microclimate by regulating the temperature of the influx of the central air conditioning system. From expression (12) it follows that in this case z_0 and, evidently, θ_{max} increase, i.e. the addition of unregulated flow increases the room's own heat resistance. It can also be noted that the general nature of dependence (7), shown in Fig. 2, is similar to the results obtained, in particular, by the authors of [16–17] under similar initial conditions, and the concept of the approach considered in the present paper as a whole, the obtained temperature deviations are of the same

order as those given in publications [26–27] in similar modes, and a number of elements of the mathematical formulation and solution of the problem under study are close to the data contained in [3], [15], [18] and some other works, therefore, the results of this study may be considered fairly reliable and reasonable.

4. Conclusions

1. It is shown that the analytical solution obtained in the paper describing the change in the value of tin in a room employing a background unregulated inflow and automated local cooling systems, provided that they are regulated according to the integral law, describes quite well the real process of heating or cooling for an abrupt change in heat supply, in any case, at the values of τ which are not too large.

2. It is noted that, as in other regulation modes, the dependence for tin has an asymptotically exponential character, however, unlike solutions showing the behavior of the indoor temperature for lengthy moments of time, the argument of the exponential function now contains the value $\sqrt{\tau}$ in explicit form, but not that of τ.

3. It is found that the largest deviation of tin from the set point (dynamic control error) is proportional to the magnitude of the thermal disturbance and, as a first approximation, inversely proportional to the regulator transfer ratio raised to the power of 1/3, as the point in time for which this deviation is observed.

4. It is proved that, other factors being equal, this deviation while maintaining tin due to the regulation of local cooling systems, will be lower than with a direct change in the temperature of the inflow in the central air conditioning system, since unregulated inflow increases the room's own heat resistance.

5. It is proposed to apply the ratios obtained in the paper for the analytical assessment of the dynamic thermal regime of an air-conditioned room employing local cooling systems equipped with an automation system with an integral law of control, in order to verify the conditions of human comfort and safety, as well as to determine the required parameters of the control unit.

References

1. Rafalskaya, T.A. Reliability and controllability of systems of centralized heat supply. Eastern Europe-an Scientific Journal. 2016. 2. Pp. 228–235. DOI: 10.12851/EESJ201604C06ART10
2. Malyavina, E.G. Rashchet tempa ostyvaniya pomeshcheniya posle otklyucheniya teplosnabzheniya [Calculation of the rate of cooling of a room after turning off the heat supply]. Promyshlennoe i grazhdanskoe stroitel 'stvo [Industrial and Civil Engineering]. 2015. 2. Pp. 55–58. URL: http://pgs1923.ru/ru/index.php?m=4&y=2015&v=02&p=00&r=14 (date of treatment: 07.05.2020). (rus)
3. Doroshenko, A.V. Imitacionnaya termodinamicheskaya model' zdaniya [Simulation thermodynamic model of the building]. BST: Byulleten' stroitel'noy tekhniki [Bulletin of construction equipment]. 2017. 12. Pp. 42–43. URL: https://elibrary.ru/item.asp?id=30598682 (date of treatment: 07.05.2020). (rus)
4. De Rosa, M., Bianco, V., Scarpa, F., Tagliafico, L.A. Modelling of energy consumption in buildings: an assessment of static and dynamic models. Russian Journal of Construction Science and Technology. 2016. V. 2. 1. Pp. 12–24. DOI: 10.15826/rjcst.2016.1.002
5. Liu, C.-S. An integral equation method to recover non-additive and non-separable heat source without initial temperature. International Journal of Heat and Mass Transfer. 2016. Vol. 97. Pp. 943–953. DOI: 10.1016/j.ijheatmasstransfer.2016.03.003
6. Horikiri, K., Yao, Y., Yao, J. Modelling conjugate flow and heat transfer in a ventilated room for indoor thermal comfort assessment. Building and Environment. 2014. 77. Pp. 135–147. DOI: 10.1016/j.buildenv.2014.03.027
7. Bouhacina, B., Saim, R., Oztop, H.F. Numerical investigation of a novel tube design for the geothermal borehole heat exchanger, Applied Thermal Engineering. 2015. 79. Pp. 153–162. DOI: 10.1016/j.applthermaleng.2015.01.027
8. Vasilyev, G.P., Gornov, V.F., Peskov, N.V., Popov, M.P., Kolesova, M.V., Yurchenko, V.A. Ground moisture phase transitions: Accounting in BHE'S design. Magazine of Civil Engineering. 2017. 6. Pp. 102–117. DOI: 10.18720/MCE.74.9
9. Petrichenko, M.R., Nemova, D.V., Kotov, E.V., Tarasova, D.S., Sergeev, V.V. Ventilated façade integrated with the HVAC system for cold climate. Magazine of Civil Engineering. 2018. 1 (77). Pp. 47–58. DOI: 10.18720/MCE.77.5
10. Samarin, O.D. The periodic temperature oscillations in a cylindrical profile with a large thickness. Magazine of Civil Engineering. 2019. 85(1). Pp. 51–58. DOI: 10.18720/MCE.85.5
11. Sáez Blázquez, C., Farfán Martín, A., Martín Nieto, I., González–Aguilera, D. Measuring of thermal conductivities of soils and rocks to be used in the calculation of a geothermal installation. Energies. 2017. 10(6). Pp. 795. DOI: 10.3390/en10060795
12. Ozturk, A. Overall heat transfer coefficient of functionally graded hollow cylinder. Solid State Phenomena. 2017. 267 SSP. Pp. 177–181. DOI: 10.4028/www.scientific.net/SSP.267.177
13. Li, N., Chen, Q. Experimental study on heat transfer characteristics of interior walls under partial-space heating mode in hot summer and cold winter zone in China. Applied Thermal Engineering. 2019. Vol. 162. Pp. 114264. DOI: 10.1016/j.applthermaleng.2019.114264
14. Marino, B.M., Muñoz, N., Thomas, L.P. Estimation of the surface thermal resistances and heat loss by conduction using thermography. Applied Thermal Engineering. 2017. Vol. 114. Pp. 1213–1221. DOI: 10.1016/j.applthermaleng.2016.12.033
15. Tarasova (Andreeva), D.S., Petritchenko, M.R. Building quasi-stationary thermal behavior. Magazine of Civil Engineering. 2017. 4 (72). Pp. 28–35. DOI: 10.18720/MCE.72.4
16. Bilous, I.Yu., Deshko, V.I., Sukhodub, I.O. Building inside air temperature parametric study. Magazine of Civil Engineering. 2016. 8 (68). Pp. 65–75. DOI: 10.5862/MCE.68.7

17. Faouzi, D., Bibi-Triki, N., Draoui, B., Abène, A. Modeling a fuzzy logic controller to simulate and op-timize the greenhouse microclimate management using Mathlab Simulink. International Journal of Mathematical Sciences and Computing. 2017. Vol. 3. 3. Pp. 12–27. DOI: 10.5815/ijmsc.2017.03.02
18. Latif, M., Nasir, A. Decentralized stochastic control for building energy and comfort management. Journal of Building Engineering. 2019. Vol. 24. Pp. 100739. DOI: 10.1016/j.jobe.2019.100739
19. Ryzhov, A., Ouerdane, H., Gryazina, E., Bischi, A., Turitsyn, K. Model predictive control of indoor microclimate: existing building stock comfort improvement. Energy Conversion and Management. 2019. Vol. 179. Pp. 219–228. DOI: 10.1016/j.enconman.2018.10.046
20. Serale, G., Capozzoli, A., Fiorentini, M., Bernardini, D., Bemporad, A. Model predictive control (MPC) for enhancing building and HVAC system energy efficiency: problem formulation, applications and opportunities. Energies. 2018. Vol. 11. 3. Pp. 631. DOI: 10.3390/en11030631
21. Belussi, L., Barozzi, B., Bellazzi, A., Danza, L., Devitofrancesco, A., Ghellere, M., Guazzi, G., Meroni, I., Salamone, F., Scamoni, F., Scrosati, C., Fanciulli, C. A review of performance of zero energy buildings and energy efficiency solutions. Journal of Building Engineering. 2019. Vol. 25. Pp. 100772. DOI: 10.1016/j.jobe.2019.100772
22. Sha, H., Xu, P., Yang, Z., Chen, Y., Tang J. Overview of computational intelligence for building energy system design. Renewable and Sustainable Energy Reviews. 2019. Vol. 108. Pp. 76–90. DOI: 10.1016/j.rser.2019.03.018
23. Kharchenko, V., Boyarchuk, A., Brezhnev, E., Andrashov, A., Ponochovnyi, Y. Monte-Carlo simulation and availability assessment of the smart building automation systems considering component failures and attacks on vulnerabilities. Advances in Intelligent Systems and Computing. 2019. Vol. 761. Pp. 270–280. DOI: 10.1007/978-3-319-91446-6_26
24. Samarin, O.D. Raschet ostyvaniya pomeshcheniy zdaniya v avariynykh rezhimakh dlya obespecheniya nadezhnosti ikh teplosnabzheniya [The calculation of cooling of building in emergency conditions to ensure reliability of their heating]. Vestnik MGSU [Papers of MSUCE]. 2019. Vol. 14. 4 (127). Pp. 496–501. DOI: 10.22227/1997-0935.2019.4.496-501. (rus)
25. Samarin, O.D., Lushin, K.I. Primenenie metoda analiza razmernostey v zadachakh teploperenosa i teploperedachi [Application of method of dimensional analysis in problems of heat transfer]. Ener-gosberezheniye i vodopodgotovka [Energy saving and water treatment]. 2020. 1. Pp. 33–36. (rus). URL: www.energija.ru/archive/ (date of treatment: 07.05.2020)
26. Gaujena, B., Borodinecs, A., Zemitis, J., Prozuments, A. Influence of building envelope thermal mass on heating design temperature. IOP Conference Series: Materials Science and Engineering. 2015. Vol. 96(1). Pp. 012031. DOI:10.1088/1757-899X/96/1/012031.
27. Odineca, T., Borodinecs, A., Korjakins, A., Zajecs, D. The impacts of the exterior glazed structures and orientation on the energy consumption of the building. IOP Conference Series: Earth and Envi-ronmental Science. 2019. Vol. 290(1). Pp. 012105. DOI: 10.1088/1755-1315/290/1/012105.

Contacts:

Oleg Samarin, samarin-oleg@mail.ru

© Samarin, O.D., 2021

Magazine of Civil Engineering

ISSN 2712-8172

journal homepage: http://engstroy.spbstu.ru/

DOI: 10.34910/MCE.103.13

Homogeneous pore distribution in foam concrete by two-stage foaming

R.E. Lukpanov, D.S. Dyussembinov, Ye.B. Utepov*, D.O. Bazarbayev, D.V. Tsygulyov, S.B. Yenkebayev, Zh.A. Shakhmov

Eurasian National University of L.N. Gumilyov, Nur-Sultan, Kazakhstan

**E-mail: utepov-elbek@mail.ru*

Keywords: concretes, pore size, foam, mortar, strength, mixtures

Abstract. The article addresses the issues of investigating the homogeneity of foam concrete produced by three methods: the classical method (CM), dry foam mineralization (DM), as well as the proposed method of two-stage foaming (TSF). The study is necessary due to the impact of the manufacturing process on the homogeneity degree of foam concrete. Therefore, the TSF method is aimed at improving the homogeneity of the material structure by evenly distributing the pores through the sequential foam introduction. The homogeneity of the materials produced by the three methods was evaluated by comparing the results of discrete (point and localized) strength testing over the entire volume of the foam concrete blocks, as well as the results of thermal conductivity measurements. The test results obtained gave an understanding of the degree of materials homogeneity, and confirmed the impact of the foam concrete manufacturing process on its quality. Thus, the most homogeneous material structure throughout the entire volume is observed in TSF specimens, as evidenced by the minimum deviations of particular values of strength and thermal conductivity, ranging from 4.19 % (in the analysis of thermal conductivity) to 6.71 % (in the analysis of strength), while the same indicators for CM specimens are 22.4 % and 48.35 %, and for DM specimens are 11.05 % and 19.21 %, respectively.

1. Introduction

The proposed method of production of non-autoclave foam concrete suggests two-stage foaming (hereinafter – TSF): the primary addition of a low-concentration mixture of foam is carried out at the stage of preparation of sand-cement mortar, which is followed by the addition of a high-concentration mixture of foam at the stage of production of a cellular concrete structure. TSF allows obtaining a product with a greater degree of homogeneity, and the reduction of the water-cement ratio reduces setting time. This provides an improvement in strength characteristics and is an additional factor for obtaining a homogeneous structure of the material.

The appearance of great interest in cellular concrete is due to its ability to combine relatively high strength with such physical-mechanical properties as thermal conductivity and frost resistance [1–6]. Important, in this context, can be technological ergonomics in the construction of building structures made of foam concrete (for example, in comparison with brick), as well as low density of the material [7–9]. Thus, a lot of compositions and technologies of cellular concrete production have appeared in the market, but the methods of foam concrete production using energy-saving non-autoclave technologies are of special interest [10–13].

Classically, aerated concrete is divided into aerated concrete and foam concrete [14, 15]. The main distinctive feature of these materials is their pore structure. Aerated concrete is produced by the introduction of gas-forming components that in the process of chemical reaction with a cement binder forms a gas emission, which enables the formation of interacting pores [16]. Foam concrete is produced by adding ready-made foam in the cement-sand mixture, which allows obtaining a closed pore system [17]. One of the most common issues of foam concrete manufacturers is the instability of the structure of the foam

Lukpanov, R.E., Dyussembinov, D.S., Utepov, Ye.B., Bazarbayev, D.O., Tsygulyov, D.V., Yenkebayev, S.B., Shakhmov, Zh.A. Homogeneous pore distribution in foam concrete by two-stage foaming. Magazine of Civil Engineering. 2021. 103(3). Article No. 10313. DOI: 10.34910/MCE.103.13

This work is licensed under a CC BY-NC 4.0

concrete mortar, shrinkage, uneven density of the material, and, as a consequence, unstable strength and thermal conductivity of the product. The reason for this shortcoming can be many factors, the main of which is a high water-cement ratio, which ultimately leads to heterogeneity of the material at its setting [1, 18].

To solve this problem, plasticizing additives are used. However, because plasticizing additives are surface-active substances (SAS), after decreasing the water-cement ratio, manufacturers of foam concrete faced another problem – shrinkage of the material due to the increasing time of setting under the influence of additives. This also leads to an uneven distribution of the pore structure of the material in the volume. To solve the problem of the quality of foam concrete material, many attempts have been made by using additives of curing accelerators in combination with plasticizers [19, 20]. But no significant result ensuring quality foam concrete has been achieved [21, 22].

A breakthrough solution in eliminating the problem of heterogeneity of foam concrete was the modernization of the technological process of its production. Instead of the classical method (hereinafter – CM) of foam concrete production [7, 23–27], which represents the cement-sand mixture with water and foam concentrate, the technology of foam concrete production by dry mineralization (hereinafter – DM) of foam was proposed [28]. The method of DM is the preparation of foam concrete by mechanical mixing of the dry cement-sand mixture with the foam. As a result of the application of the given technology several questions, concerning the quality of pore structure and density, have been solved. However, the problem of shrinkage of a material in the course of the setting remained unsolved. Despite this, the classical production method is still actively used in combination with various additives [28].

The analysis of CM and DM revealed the advantages and disadvantages of the methods. The disadvantage of CM is a high water-cement ratio, which leads to shrinkage of the material before setting. Besides, foam concrete obtained by CM has low strength and uneven density in the volume of the product. The decrease in strength is due to micro and macropores in the cement dough, which creates a weak skeleton. The disadvantages of the DM method include shrinkage of the material in the process of setting (as a result of partial destruction of the foam structure when combining the foam with dry components of the material), which leads to changes in the final geometric dimensions of the product. Partial destruction of the foam structure is accompanied by its stratification, which leads to the formation of a heterogeneous structure of the material [9, 18, 21, 22, 29].

The unsolved question of obtaining quality foam concrete has defined the goal of this study. Thus, it consists of developing an available technology of foam concrete production by the method of two-stage foaming. Achieving the goal should provide an improved pore structure of the material making the pore distribution more uniform, as well as improved physical-mechanical properties of the material due to the uniform distribution of the load-bearing skeleton structure.

The proposed method of TSF ensures maximum distribution of the foam concentrate over the entire specimen volume: the initial addition of a low-concentration foam mixture takes place at the sand-cement mortar preparation stage, thus improving its wettability and subsequent reduction of the water-cement ratio (reducing the quenching of the foam with water). Afterward, with the secondary addition of a highly concentrated mixture of foam at the stage of making the structure of cellular concrete, a decrease in the water-cement ratio allows to save the primary ratio of foam concentrate, facilitates the formation of a uniform structure of porous material.

The following tasks were set to achieve the goal:

- Testing the strength of foam concrete specimens obtained by CM, DM, and TSF in the laboratory according to [30].
- Measuring the thermal conductivity of foam concrete specimens obtained by CM, DM, and TSF in the laboratory according to [31].
- Comparative analysis of the results of laboratory tests and measurements.

The article presents the results of comparative analysis of methods of foam concrete production, namely the impact of the technological process of preparing the material on its quality, without assessing the possible impact of ingredients (additives to improve the physical-mechanical properties of materials).

For comparison with the proposed TSF method, considered two main methods of foam concrete production are widely used in practice such as CM and DM.

2. Methods

The research methodology includes the following stages:

- Preparation of foam concrete by comparable CM and DM methods;
- Preparation of foam concrete by the proposed method of TSF;

- Laboratory testing of foam concrete specimens;
- Analysis of results.

Preparation of foam concrete by comparable methods was carried out in laboratory conditions following the standard methods, specifications, and the requirements of the normative and technical documentation [14, 32, 33]. An important condition was to maintain the same composition of components and ingredients (additives) of prototypes for each method, as well as their dimensionality. The foam concrete compositions and the ratio of foam concentrate to aggregate are designed from the condition of obtaining the material density of D600 (600 kg/m^3) (Table 1). For each of the 3 methods (including the proposed one), 5 blocks were prepared.

Table 1. Composition of foam concrete of comparable methods.

Method	Cement, kg	Sand, kg	Water, l	Foam concentrate, l
TSF	310	270	124	1.2
CM	310	270	186	1.1
DM	310	270	155	1.2

The technological process of specimen preparation by TSF is shown in Fig. 1.

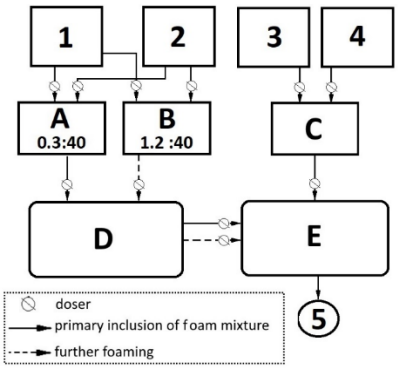

Figure 1. The technology of foam concrete preparation by the method of TSF: 1 – water; 2 – foam concentrate; 3 – cement; 4 – sand; 5 – finished product; A – the container for the low-concentrated mixture of the plasticizing additive of a foam concentrate in water 0.3:40 l, B – the container for a mixture of the modified foam concentrate in water 1.2:40 l, In – the cement-sand mixer, D – the foam generator, E – the mortar mixer.

The technological process consists of three stages. During production, a strict sequence of components must be followed (Fig. 1):

Stage 1: in a container (A) the foam concentrate (1) is thoroughly mixed with water (2), in ratio to water – 0.3:40 l; in parallel (independently) in a container (B) the foam concentrate (1) is thoroughly mixed with water (2), in water ratio – 1.2:40 l; in parallel in a container (C) the cement (3) is mixed with sand (4), in the ratio of cement to sand (1:3);

Stage 2: obtained in a container (A) mortar through the foam generator (C) is converted to foam and combined with cement and sand mixture from the container (D), in a mortar mixer (E);

Stage 3: The mortar obtained in a container (B) is converted to foam through the foam generator (C) and introduced into the mortar mixer (E).

After careful mixing in a mortar mixer, the resulting mortar (5) is poured into forms.

The main evaluation criterion of the quality of the material prepared by different methods is the degree of its homogeneity, or in other words, the even pore distribution in the structure of foam concrete over the entire volume. This indicator is directly related to the technology of foam concrete production. The resulting factors of material homogeneity can be attributed to the homogeneity of physical-mechanical properties of the material over the entire volume.

Evaluation of material homogeneity, through the evaluation of physical-mechanical properties, is reduced to the discrete measurement of physical-mechanical properties over the entire volume (mainly height) of the material of standard size (factory block): 20 cm height, 30 cm width, and 60 cm length. Cylindrical specimens with a height of 20 cm and a diameter of 6.4 mm, segmented by 2 cm in height, were used to assess the strength of the material (Fig. 2a). Also, for point assessment of the strength of factory sized specimen, conducted the tests of small-sized cubic specimens with the dimensions of 2×2×2 cm extracted continuously by height and selectively by the length and width of the factory specimen (Fig. 2b).

To assess the thermal conductivity of the material used the specimens in the form of a rectangular parallelepiped of standard size, selected in steps of 4 cm by the height of the specimen of factory size (Fig. 2c).

Figure 2. Specimens for determining the physical-mechanical properties of foam concrete.

The difference between testing the cylindrical and small specimens is that segments of a cylindrical specimen are tested simultaneously while small specimens are tested separately. In other words, testing cylindrical specimens is necessary to identify the weakest segments of the specimen by height, while testing small specimens will evaluate the distribution of strength characteristics over the entire volume of the material. In both cases, the analyses of the results reveal weaker locations, areas with maximum density, and generally assess the homogeneity of the material.

Assessment of the uniformity of foam concrete in height is due to the influence of gravitational forces on the heavy ingredients of the composition during the setting process (including excess water during foam delamination), leading to an uneven density of the material by volume.

Core cutting was carried out through a cylindrical crown with an electric drive, with an inner diameter of 6.5 mm. To reduce the impact of mechanical action on the skeleton structure, core extraction was carried out with maximum rotation and minimum movement of the crown. In total, 6 specimens were taken from each comparable foam block. The cylindrical and standard specimens were cut by string cutting at maximum rotational speeds to reduce the risk of disturbance of the material structure. Before testing, each element of the specimen was labeled.

The laboratory testing and measurement of foam concrete specimens included the following:

- Determining the strength of segmented cylindrical specimens using the Unconfined compression test (Fig. 3a);
- Determination of the strength of small cube-shaped specimens of material by Dynamic Mechanical Analysis (Fig. 3b);
- Determination of the thermal conductivity of standard specimens of material using the ITP MG-4 instrument (Fig. 3c).

Figure 3. Laboratory testing of foam concrete specimens.

Compressive strength tests on segmented cylindrical specimens were carried out on the “Press Automatic Pilot” equipment with a total compressive load of 500 kN, designed to determine the compressive strength of lightweight concrete and primer-cement specimens.

To evaluate the less robust part of the specimen within the height, segments of one specimen were tested simultaneously. Since the specimens have been mechanically subjected to cutting, the specimen surface has a roughness that can lead to a point transfer of normal stress at the contact edge of the segments. Therefore, for better distribution of normal stress, flexible gaskets [30] of nonwoven geotextile were used. The use of gaskets also simulates the tangential stresses at the contact edge of the segments, which are inherent to a solid, monolithic specimen, when compressed.

Testing was performed before the specimen failed, and strength measurements were made using two control measurements:

A – registration of the load value, at the destruction of at least one segment, to identify the weakest section by the height of the specimen;

B – recording the peak value of the load, to measure the maximum strength of the specimen as a product.

The tests of small specimens of cubic shape for assessing the distribution of strength properties of the material on the volume of specimens of comparable methods were conducted on specialized equipment called “Dynamic Mechanical Analysis”. The device is designed to study the properties of materials under the influence of periodic and constant loads of compression, bending, shearing, stretching of small specimens (height up to 3 cm). In total, 2250 specimens were tested.

To estimate the thermal conductivity and thermal resistance of the materials of the compared methods, specimens of standard sizes in the form of a rectangular prism were used. Measurements were carried out on the device ITP MG-4 on the principle of generation of a stationary heat flow passing through a flat specimen and directed perpendicular to the face edges of the specimen [31]. The heat flow is monitored automatically by the device. In total, 5 specimens of each method were tested, selected at the same distance within the block height (20 mm per step). The error of geometric dimensions of the specimens did not exceed ±0.1 mm. Before the test, to determine the density of the dry specimen, the

prototypes were dried to a constant mass, so that the mass change did not exceed 0.1 % during 30 minutes of observation.

The calculation of thermal conductivity λ (effective thermal conductivity) was performed according to Eq. (1), and thermal resistance R_H (in the stationary thermal mode) according to Eq. (2):

$$\lambda = \frac{H \cdot q}{T_h \cdot T_c}, \quad (1)$$

$$R_H = \frac{T_h - T_c}{q} - 2R_k, \quad (2)$$

where, λ is effective heat transfer, W/m °C;

R_H is the thermal resistance of the test specimen, m^2·°C/W;

R_k is the thermal resistance between the face of the specimen and the work surface of the instrument panel, m^2·°C/W;

H is the measured specimen thickness, mm;

q is the density of a stationary heat flux passing through a measured specimen, W/m^2;

T_h is the temperature of the hot edge of the measured specimen, °C;

T_c is the temperature of the cold edge of the measured specimen, °C.

3. Results and Discussion

3.1. Strength results of segmented cylindrical specimens by Unconfined compression test

Comparisons of the values of measurement A (identification of the weakest area within the height of the specimen) expressed by the relation of particular values of strength of TSF specimens with CM and DM are presented in Fig. 4. The presented linear functions have a close relation to the variables as the correlation coefficient in both cases is higher than 0.7. Proportionality coefficients show that the greatest convergence of strength values with TSF is observed in DM specimens (0.82 is closer to 1.0 than 0.66). According to the test results, the partial values of strength of the weakest segments of CM specimens vary from 0.61 to 0.93 MPa, which corresponds to the upper limit of foam concrete mark of D300. This means that all five CM specimens have weaker segments within the height, the density of which does not exceed 300 kg/m^3. Particular values of strength of the weakest segments of DM specimens vary from 1.52 to 1.73 MPa, which correspond to the average value of the strength of foam concrete mark of D400. The strength of TSF segments varies from 1.84 to 2.05 MPa, which corresponds to the upper limit of the strength of foam concrete mark of D400 and the average value of foam concrete mark of D500. The results of the study [34, 35], which aimed to assess the degree of homogeneity of foam concrete by measuring its density, showed that the density of the material depends on the setting time and methods of foam concrete preparation and varies on average from 10 to 25 %. In general, the particular values of density [34, 35] lie in a proportional range of obtained particular values of segmented specimens.

Comparing the standard deviations of the obtained results on the strength of three methods that are 0.129 for CM, 0.093 for DM, and 0.087 for TSF, it can be concluded that the greatest variation of the particular values of strength within the height is revealed for the DM specimens. The smallest standard deviation is observed in the TSF specimens, which indicates the maximum concentration of particular values of strength at the height around the arithmetic mean of the particular values.

In general, the results of the assessment showed that CM and DM specimens have a greater variation in height than TSF specimens. The weakest sections of the CM specimen turned mainly the two upper segments 9 and 10 (Fig. 5a), at an average load of 2 kN, which corresponds to a strength of 0.72 MPa. In the DM specimens the weakest sections are located in the upper part of the specimen, mainly the three upper segments 8, 9, and 10 (Fig. 5b), at an average load value of 4.5 kN, which corresponds to a strength of 1.62 MPa. No clear pattern of segment failure was found in the TSF specimens. Where the weakest was the lowest segment 4 (Fig. 5c), at an average load of 5.3 kN, which corresponds to a strength of 1.91 MPa.

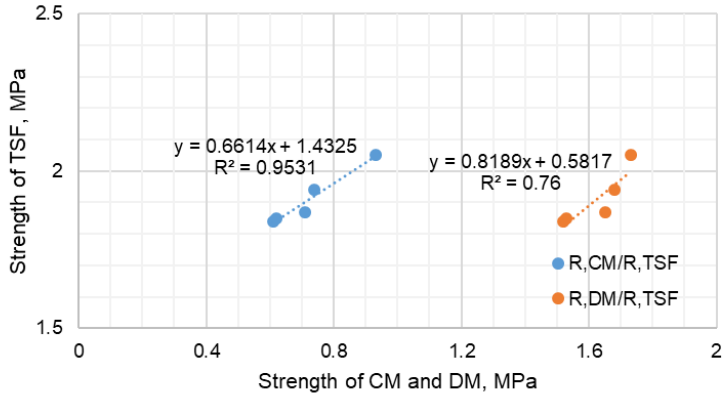

Figure 4. Temperature mode of concrete curing.

Figure 5. Weakest segments of specimens.

At the measurement B (maximum strength measurement) on the CM and partially DM specimens, the tests were continued after the upper segments were removed, otherwise, the peak load value would be limited by the failure of weak specimens due to their low strength value relative to other segments. In general, the maximum strength values of the three methods are close to each other. The average value of maximum strength of CM specimens was 3.2 MPa, which corresponds to the upper limit of the strength of foam concrete mark of D500 or the lower limit of the mark of D600. The DM and TSF specimens showed the strength of 2.5 MPa and 2.7 MPa respectively, which correspond to the average strength of the mark of D500. The obtained results of the maximum strength of CM specimens are due to the removal of weak segments, as well as changes in the ratio of the width of the specimen to its height, which led to data distortion.

Although the selection of foam concrete composition and the ratio of foam concentrate to aggregate is calculated from the condition of obtaining the material density of D600 (600 kg/m^3), the obtained specimens of comparable methods showed different results from the given values [36]. The resulting factor of distortion of the results is a non-standard dimensionality of specimens (due to the height of the standard block and the diameter of the core extractor) in comparison with the required test specimens regulated by the standards. Correction factors for the geometry of the specimens were also not taken into account, as the task of projecting the results of the specimen to the final construction product was not set in the analysis. The fact that the tested segmented cylindrical specimen does not have an integral structure also played a partial role, and since all specimens were tested under equal conditions, the results may vary from those of real values quantitatively, but not qualitatively. And since the task was to compare the results relative to each other, the quantitative factor has no principal importance, since the results are not expressed by particular values but by their ratio.

The results obtained from the tests of segmented cylindrical specimens gave an indirect idea of the degree of homogeneity of materials of the three compared production methods.

3.2. Dynamic Mechanical Analysis results for strength determination of small cube material specimens

The spread of the strength values by the height of the specimen of each compared method, aliquot to the height of an individual cube (2 cm), is shown in Table 2 below.

Table 2. Spreading of particular strength values by height.

Specimen No. (full height)	Particular values of strength, kgf/cm^2					
	CM		DM		TSF	
	Minimum	Maximum	Minimum	Maximum	Minimum	Maximum
10 (20 cm)	10.235	15.984	38.075	42.432	26.870	34.935
9 (18 cm)	13.885	24.253	38.342	44.583	28.944	37.384
8 (16 cm)	24.120	42.439	40.456	46.780	29.118	42.293
7 (14 cm)	31.786	44.328	42.359	48.467	37.881	44.277
6 (12 cm)	35.382	45.827	42.243	49.334	38.420	46.226
5 (10 cm)	38.340	48.105	42.589	49.015	38.318	47.986
4 (8 cm)	39.921	50.368	43.011	49.312	39.020	48.355
3 (6 cm)	42.334	54.492	43.516	50.016	40.267	50.417
2 (4 cm)	54.012	70.439	44.770	52.145	43.455	57.936
1 (2 cm)	77.228	91.870	46.342	54.211	48.171	61.939

According to the test results, particular values of strength of CM specimens vary from 10.235 kgf/cm^2 (≈0.98 MPa) to 91.87 kgf/cm^2 (≈9.60 MPa), DM specimens vary from 38.075 kgf/cm^2 (≈3.72 MPa) to 54.211 kgf/cm^2 (≈5.29 MPa), and TSF specimens vary from 26.87 kgf/cm^2 (≈2.65 MPa) to 61.939 kgf/cm^2 (≈6.10 MPa). According to the study of [37], the strength characteristics of foam concrete specimens of similar composition, on average, amounted to 50 kgf/cm^2, which does not contradict the results obtained and correspond to the average value of the range of CM, the upper value of the strength range of DM and TSF.

For visual comparison, the point strength results are presented in the form of color distribution [38] over 6 significant sections (from two opposite edges and the middle of the block in the transverse and longitudinal direction). Fig. 6 shows the comparison of strength in the planes C1 (in axes 1 – A÷O, Fig. 2b) and L1 (in axes A – 1÷30, Fig. 2b). Fig. 7 shows the comparison of strength in the planes C2 (16 – A÷O, Fig. 2b) and L2 (H – 1÷30, Fig. 2b). Fig. 8 shows the comparison of strength in the planes C3 (30 – A÷O, Fig. 2b) and L3 (1÷30, Fig. 2b). For the best comparative evaluation of each fragment (separate plane), a single-color scale of strength characteristics inherent in the most heterogeneous specimen (method) is given. Thus, the contrast of the scale and the planes under consideration will contribute to a better visual perception of the heterogeneity of the plane under consideration relative to the most heterogeneous specimen (method).

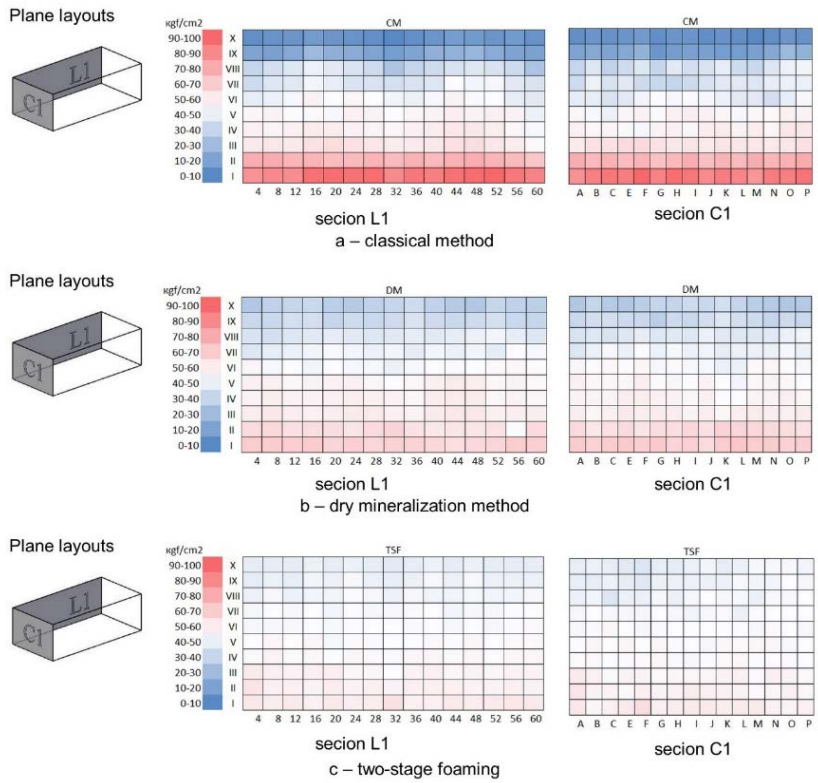

Figure 6. Color diagram of strength distribution in the cross-sections of C1 and L1 unit.

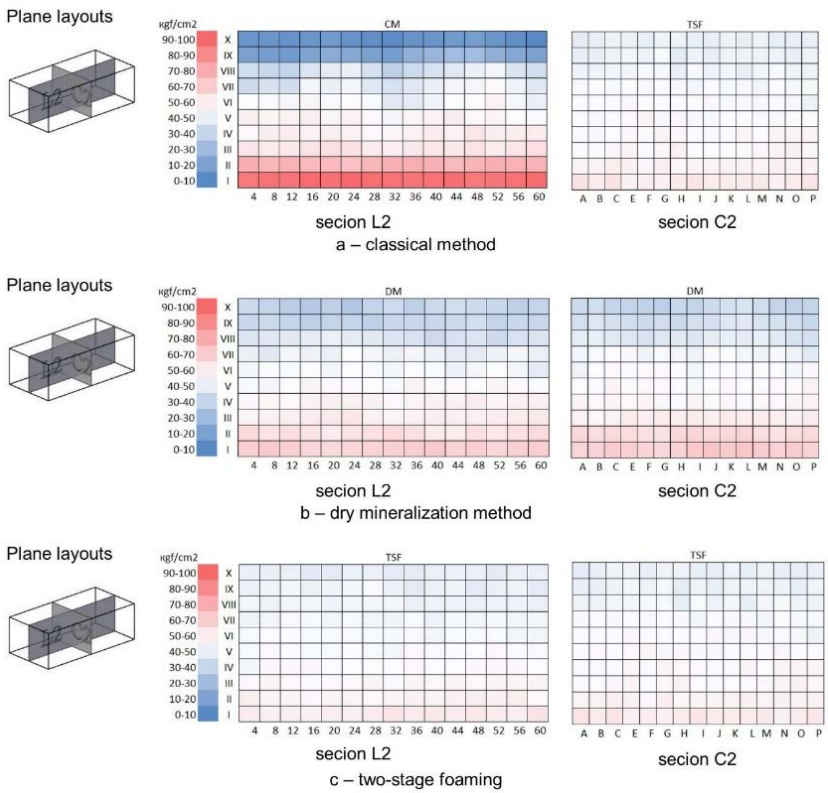

Figure 7. Color diagram of strength distribution in the cross-sections of C2 and L2 unit.

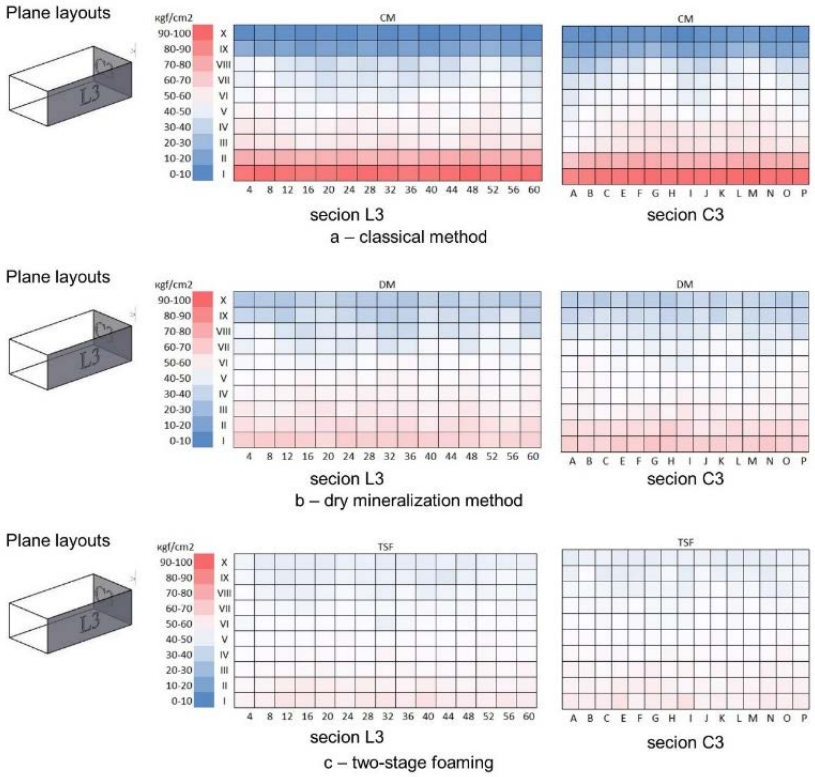

Figure 8. Color diagram of strength distribution in the cross-sections of C3 and L3 unit.

The difference of contrasts of color diagrams of strength distribution along transverse and longitudinal sections clearly shows the difference in the homogeneity of distribution of particular values of strength characteristics of compared methods of foam concrete production. The greatest contrast is observed at CM blocks (in all cross-sections), which testifies to the big dispersion of particular values of strength, therefore, the lowest homogeneity of the material. The greatest homogeneity is observed at blocks of TSF, which testifies to the smallest color contrast within the height of the section. The average degree of homogeneity is observed at DM blocks.

The average value of the minimum strength of CM specimens (all top specimens) is 13.25 kgf/cm^2 (1.30 MPa), and the average value of the maximum strength (all bottom specimens) is 87.9 kgf/cm^2 (8.62 MPa). The squared deviation of particular values of the upper specimens is 0.25, and of the lower specimens is 2.09. The variation coefficient or the deviations of particular values do not exceed 1.86 % of the average value for the upper specimens (an upper plane of the block) and 2.34 % – for the lower (lower plane of the block), which indicates a close relationship of particular values of the strength of all specimens within the plane of the considered height (horizontal plane). The statistical analysis of particular values of strength and standard deviations of DM specimens also showed close relation of particular values of strength within the limits of considered planes within the height. For the lower plane the deviation (variation coefficient) limit is 1.45 %, and for the upper plane is 1.68 %. In the case of the TSF method, the deviation limit for the lower plane is 0.59 %, and for the upper plane is 2.05 %.

This analysis allowed estimating the spread of these strength characteristics within two critical planes of the specimen (upper and lower planes of the foam concrete block) with minimum and maximum particular values of strength. The analysis showed a close relationship of the particular values within the plane of their location, excluding the assumption of random errors (since the number of particular values within one plane is 225 units), thus confirms the assumption of heterogeneity of the material in the transverse plane (in its height) and relatively good homogeneity in the horizontal plane.

A quantitative assessment of the material heterogeneity in height can be made by statistical processing of particular strength values in transverse planes perpendicular to the horizontal plane.

The average value of the transverse plane strength of CM specimens is 43.67 kgf/cm^2 (4.28 MPa), and the average value of squared deviations (within height) is 21.11. Hence, the deviations (variation coefficient) of particular values of strength from the arithmetic mean reach 48.35 %, which indicates a weak bond of particular values of strength within the transverse planes (values on the height of the specimen), as well as the heterogeneity of the material within height. The statistical analysis of particular values of strength and standard deviations of DM specimens showed closer relation of particular values of strength in transverse planes in comparison with CM. At the average value of strength equal to 44.54 kgf/cm^2 (4.37 MPa), the standard deviation was 8.56, and the deviation (variation coefficient) of particular values of strength within 19.21 %. The closest correlation of particular values of strength was found in TSF specimens, where the average value of strength was 43.42 kgf/cm^2 (4.25 MPa). With a standard deviation of 2.91, the deviations of the particular values of strength were within 6.71 %. Statistical analysis of the particular values of strength in transverse planes confirms the obvious heterogeneity of CM specimens concerning DM and TSF.

The results of the tests (point strength distribution of the material) generally correspond to the results of the strength testing of cylindrical specimens, confirming the general trend of strength distribution over the height at each of the 3 methods. Moreover, in contrast, they provide more accurate numerical values of strength over the entire volume of the specimen.

3.3. Results of the determination of the thermal conductivity of standard specimens

The results of measurements are presented in Fig. 9, and comparisons of particular values of measurements of TSF with CM and DM specimens are presented in Fig. 10.

Thermal resistance (R_H), m^2·°C/Wt — Efficient thermal conductivity (λ), Wt/m·°C

R_H	CM	DM	TSF	CM	DM	TSF	λ
0.14	0.140	0.139	0.158	0.103	0.110	0.137	0.10
0.16	0.143	0.159	0.163	0.132	0.137	0.139	0.12
0.19	0.165	0.164	0.163	0.142	0.140	0.137	0.15
0.21	0.165	0.171	0.158	0.145	0.144	0.141	0.17
0.23	0.234	0.164	0.174	0.190	0.148	0.143	0.19

Figure 9. Particular values of thermal conductivity and thermal resistance.

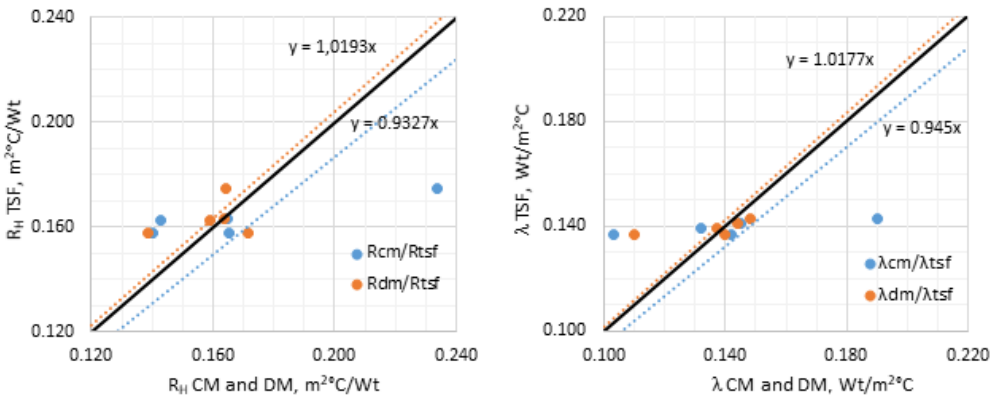

Figure 10. Comparisons of particular values of measurements.

Studies of [39] on the assessment of the thermal conductivity of foam concrete showed values comparable to those indicated in the article according to the density of specimens. The obtained results of thermal conductivity of specimens of three methods do not contradict these results. Thus, the thermal resistance values of CM specimens vary from 0.140 to 0.234 $m^2 \cdot °C/W$, of DM specimens from 0.139 to 0.171 $m^2 \cdot °C/W$, of TSF from 0.158 to 0.174 $m^2 \cdot °C/W$. Values of thermal conductivity of CM specimens vary from 0.103 to 0.190 $m^2 \cdot °C/W$, DM specimens from 0.110 to 0.148 $m^2 \cdot °C/W$, TSF – from 0.137 to 0.143 $m^2 \cdot °C/W$.

Statistical analysis of the data showed that the maximum deviation (variation coefficient) of particular values of thermal resistance (thermal conductivity) from the average for CM specimens is 22.4 % (22.0 %), and the lowest deviation for TSF specimens is 4.19 % (1.87 %). For DM specimens the deviation of thermal resistance is 7.8 %, and of thermal conductivity is 11.05 %.

Comparisons expressed by a linear function (Fig. 10) also indirectly indicate the degree of homogeneity in the structure of the specimens of compared methods. The most uniform distribution of the structure of foam concrete is observed in the specimens of TSF, and the smallest in the specimens of CM. The results of the assessment confirmed a greater dispersion of data within the height of CM and DM specimens, as compared with the specimens of TSF. The binding of the obtained thermal conductivity data to the mark of foam concrete showed the following: CM specimens are referred to the mark from the upper limit of D300 or the lower limit of D400 (upper specimens) to the average limit of D800 (lower specimens); DM specimens – from the average limit of D400 (upper specimens) to the average limit D600 (lower specimens); TSF specimens – from the upper limit of D500 (upper specimens) to the lower limit of D600 (lower specimens).

In general, the test results confirm the impact of the technological process on the homogeneity of the material, and as a consequence, the uneven distribution of its physical-mechanical properties over its volume. The results obtained have a similar trend (in terms of the distribution of physical-mechanical properties in the production of foam concrete) with the works of [34, 35, 37, 39, 40]. Nevertheless, the results obtained have creditable quantitative indicators and are more focused on a comparative evaluation of the TSF method.

4. Conclusion

1. A method for the production of foam concrete is proposed, which implies two stages of foaming: primary inclusion of a low-concentration foam mixture at the stage of preparation and secondary inclusion of a high-concentration foam mixture at the stage of producing a cellular concrete structure. Two-stage foaming provides a maximum distribution of the foam concentrate over the entire volume, as evidenced by the comparison of the results of laboratory measurements.

2. Although the selection of foam concrete composition and the ratio of foam concentrate to aggregate is designed from the condition of obtaining the material density of D600 (600 kg/m^3), the obtained specimens of comparable methods showed the results different from the given values: the density of CM by the height of specimens varies on average from 365.5 kgf/cm^3 to 840.1 kgf/cm^3, DM specimens from 528.3 kgf/cm^3 to 714.2 kgf/cm^3, and TSF specimens from 608.3 kgf/cm^3 to 669.5 kgf/cm^3.

3. Strength tests on small specimens showed that the greatest variety of particular strength values is observed in the transverse plane along with the height of the specimen. The total spread of particular strength values over the entire volume of the CM block amounted from 10 to 92 kgf/cm^2, DM block – from 38 to 54 kgf/cm^2, TSF block – from 27 to 62 kgf/cm^2. The strength values converted into a color chart (Fig. 6-8), clearly shows the different degree of homogeneity of the three methods.

4. Thermal conductivity tests on standard specimens confirmed a greater variation in the height of CM and DM specimens compared to TSF specimens, which is also an indirect assessment of material homogeneity.

5. Furthermore, the study results confirmed the impact of the technological process of foam concrete production on its quality. The proposed TSF production technology enables sufficiently even distribution of physical-mechanical properties of the material (strength and thermal conductivity) over its volume, which can be used as an indirect confirmation of the uniform distribution of the pore structure of the skeleton, and, consequently, improves the quality of the material as a construction product.

5. Acknowledgment

This research was funded by the Science Committee of the Ministry of Education and Science of the Republic of Kazakhstan (Grant No. AP08956209). The authors of the article express their great gratitude to the Research and Production Center of L.N. Gumilyov Eurasian National University “ENU-Lab” for the provided laboratory base for research work.

References

1. Raj, A., Sathyan, D., Mini, K.M. Physical and functional characteristics of foam concrete: A review. Construction and Building Materials. 2019. 221. Pp. 787–799. DOI: 10.1016/j.conbuildmat.2019.06.052
2. Vinith Kumar, N., Arunkumar, C., Srinivasa Senthil, S. Experimental Study on Mechanical and Thermal Behavior of Foamed Concrete. Materials Today: Proceedings. 2018. 5(2). Pp. 8753–8760. DOI: 10.1016/j.matpr.2017.12.302
3. Rybakov, V.A., Ananeva, I.A., Pichugin, E.D., Garifullin, M. Heat protective properties of enclosure structure from thin-wall profiles with foamed concrete. Magazine of Civil Engineering. 2020. 94(2). Pp. 11–20. DOI: 10.18720/MCE.94.2
4. Oren, O.H., Gholampour, A., Gencel, O., Ozbakkaloglu, T. Physical and mechanical properties of foam concretes containing granulated blast furnace slag as fine aggregate. Construction and Building Materials. 2020. 238. Pp. 117774. DOI: 10.1016/j.conbuildmat.2019.117774
5. Stolz, J., Boluk, Y., Bindiganavile, V. Mechanical, thermal and acoustic properties of cellular alkali activated fly ash concrete. Cement and Concrete Composites. 2018. 94. Pp. 24–32. DOI: 10.1016/j.cemconcomp.2018.08.004. URL: https://linkinghub.elsevier.com/retrieve/pii/S0958946517311277
6. Teltayev, B.B., Zhussupbekov, A., Shakhmov, Z., Suppes, E.A. Field Experimental Investigations of Freezing and Thawing of Highway Subgrade2020. Pp. 35–47.
7. Chica, L., Alzate, A. Cellular concrete review: New trends for application in construction. Construction and Building Materials. 2019. 200. Pp. 637–647. DOI: 10.1016/j.conbuildmat.2018.12.136
8. Hess, J.A., Kincl, L., Amasay, T., Wolfe, P. Ergonomic evaluation of masons laying concrete masonry units and autoclaved aerated concrete. Applied Ergonomics. 2010. 41(3). Pp. 477–483. DOI: 10.1016/j.apergo.2009.10.003
9. Richard, A. Experimental Production of Sustainable Lightweight Foamed Concrete. British Journal of Applied Science & Technology. 2013. 3(4). Pp. 994–1005. DOI: 10.9734/BJAST/2014/4242
10. Miruk, O. Development of cellular structure composites for energy efficient construction. Energy Procedia. 2017. 128. Pp. 469–476. DOI: 10.1016/j.egypro.2017.09.032
11. Siva, M., Ramamurthy, K., Dhamodharan, R. Development of a green foaming agent and its performance evaluation. Cement and Concrete Composites. 2017. 80. Pp. 245–257. DOI: 10.1016/j.cemconcomp.2017.03.012
12. Ren, C., Wang, W., Yao, Y., Wu, S., Qamar, Yao, X. Complementary use of industrial solid wastes to produce green materials and their role in CO_2 reduction. Journal of Cleaner Production. 2020. 252. Pp. 119840. DOI: 10.1016/j.jclepro.2019.119840
13. Vesova, L.M. Disperse Reinforcing Role in Producing Non-autoclaved Cellular Foam Concrete. Procedia Engineering. 2016. 150. Pp. 1587–1590. DOI: 10.1016/j.proeng.2016.07.126
14. Interstate standard GOST 25485-2019. Cellular concretes. General specifications. URL: https://www.russiangost.com/p-375403-gost-25485-2019.aspx (date of application: 28.02.2020).
15. Kurweti, A., Chandrakar, R. Specification and Quality Control of Light Weight Foam Concrete. International Journal of Engineering Development and Research. 2017. 5(2). Pp. 1932–1938. URL: https://www.ijedr.org/papers/IJEDR1702300.pdf
16. Hamad, A.J. Materials, Production, Properties and Application of Aerated Lightweight Concrete: Review. International Journal of Materials Science and Engineering. 2014. DOI: 10.12720/ijmse.2.2.152-157
17. Nguyen, T.T., Bui, H.H., Ngo, T.D., Nguyen, G.D., Kreher, M.U., Darve, F. A micromechanical investigation for the effects of pore size and its distribution on geopolymer foam concrete under uniaxial compression. Engineering Fracture Mechanics. 2019. 209. Pp. 228–244. DOI: 10.1016/j.engfracmech.2019.01.033
18. Hilal, A.A., Thom, N.H., Dawson, A.R. Failure Mechanism of Foamed Concrete Made with/without Additives and Lightweight Aggregate. Journal of Advanced Concrete Technology. 2016. 14(9). Pp. 511–520. DOI: 10.3151/jact.14.511
19. Makul, N. Modern sustainable cement and concrete composites: Review of current status, challenges and guidelines. Sustainable Materials and Technologies. 2020. 25. Pp. e00155. DOI: 10.1016/j.susmat.2020.e00155
20. Yang, Y., Zhou, Q., Deng, Y., Lin, J. Reinforcement effects of multi-scale hybrid fiber on flexural and fracture behaviors of ultra-low-weight foamed cement-based composites. Cement and Concrete Composites. 2020. 108. Pp. 103509. DOI: 10.1016/j.cemconcomp.2019.103509
21. Sun, C., Zhu, Y., Guo, J., Zhang, Y., Sun, G. Effects of foaming agent type on the workability, drying shrinkage, frost resistance and pore distribution of foamed concrete. Construction and Building Materials. 2018. 186. Pp. 833–839. DOI: 10.1016/j.conbuildmat.2018.08.019.
22. Nambiar, E.K.K., Ramamurthy, K. Shrinkage Behavior of Foam Concrete. Journal of Materials in Civil Engineering. 2009. 21(11). Pp. 631–636. DOI: 10.1061/(ASCE)0899-1561(2009)21:11(631)

23. Vardhan, R., Chandel, S., Sakale, R. Study of Cellular Light Weight Concrete. IJSRD -International Journal for Scientific Research & Development. 2016. 4(7). Pp. 1–6.
24. Amran, Y.H.M., Farzadnia, N., Abang Ali, A.A. Properties and applications of foamed concrete; a review. Construction and Building Materials. 2015. 101. Pp. 990–1005. DOI: 10.1016/j.conbuildmat.2015.10.112
25. Dunton, H.R., Rez, D.H. Apparatus and method to produce foam, and foamed concrete. US302887A. 1989.
26. Vine-Lott, K. Apparatus and method for producing foamed materials. US5102228A. 1989.
27. Ramamurthy, K., Kunhanandan Nambiar, E.K., Indu Siva Ranjani, G. A classification of studies on properties of foam concrete. Cement and Concrete Composites. 2009. 31(6). Pp. 388–396. DOI: 10.1016/j.cemconcomp.2009.04.006
28. Bartenjeva, E., Mashkin, N. Technological parameters influence on the non-autoclaved foam concrete characteristics. AIP Conference Proceedings. 1800(1). American Institute of Physics Inc., 2017. Pp. 020012.
29. Raj, B., Sathyan, D., Madhavan, M.K., Raj, A. Mechanical and durability properties of hybrid fiber reinforced foam concrete. Construction and Building Materials. 2020. 245. Pp. 118373. DOI: 10.1016/j.conbuildmat.2020.118373
30. Interstate standard GOST 8462-85. Wall materials. Methods for determination of ultimate compressive and bending strength.
31. Interstate standard GOST 7076-99. Building materials and products. Method of determination of steady-state thermal conductivity and thermal resistance.
32. Stroy-Beton. Technological Regulations for the manufacture of heat-insulating and structural-heat-insulating products made of non-autoclaved foam concrete. 2004. URL: https://www.ibeton.ru/download.php?to=pic/38-54.rar&id=4 (date of application: 11.03.2020).
33. Interstate Standard GOST 21520-89. Small-sized wall blocks of cellular concrete. Specifications.
34. Kozłowski, M., Kadela, M. Mechanical Characterization of Lightweight Foamed Concrete. Advances in Materials Science and Engineering. 2018. 2018. Pp. 1–8. DOI: 10.1155/2018/6801258.
35. Fu, Y., Wang, X., Wang, L., Li, Y. Foam Concrete: A State-of-the-Art and State-of-the-Practice Review. Advances in Materials Science and Engineering. 2020. 2020. Pp. 1–25. DOI: 10.1155/2020/6153602
36. Interstate standard GOST 12730.1-78. Concretes. Methods of determination of density.
37. Falliano, D., De Domenico, D., Ricciardi, G., Gugliandolo, E. Key factors affecting the compressive strength of foamed concrete. IOP Conference Series: Materials Science and Engineering. 2018. 431. Pp. 062009. DOI: 10.1088/1757-899X/431/6/062009
38. Utepov, Y.B., Khudaibergenov, O.A., Kabdush, Y.B., Kazkeev, A.B. Prototyping an embedded wireless sensor for monitoring reinforced concrete structures. Computers and Concrete. 2019. 24(2). Pp. 95–102. DOI: 10.12989/cac.2019.24.2.095
39. Baranova, A., Ryabkov, I. Investigation of thermal conductivity of non-autoclaved foam concrete based on microsilica. IOP Conference Series: Materials Science and Engineering. 2019. 667. Pp. 012010. DOI: 10.1088/1757-899X/667/1/012010
40. Steshenko, A.B., Kudyakov, A.I. Cement based foam concrete with aluminosilicate microspheres for monolithic construction. Magazine of Civil Engineering. 2018. 84(8). Pp. 86–96. DOI: 10.18720/MCE.84.9

Contacts:

Rauan Lukpanov, Rauan_82@mail.ru

Duman Dyussembinov, dusembinov@mail.ru

Yelbek Utepov, utepov-elbek@mail.ru

Daniyar Bazarbayev, phdd84@mail.ru

Denis Tsygulyov, denis_riza_72@mail.ru

Serik Yenkebayev, yenkebayev-serik@mail.ru

Zhanbolat Shakhmov, zhanbolat8624@mail.ru

© Lukpanov, R.E., Dyussembinov, D.S., Utepov, Ye.B., Bazarbayev, D.O., Tsygulyov, D.V., Yenkebayev, S.B., Shakhmov, Zh.A., 2021

Magazine of Civil Engineering

ISSN 2712-8172

journal homepage: http://engstroy.spbstu.ru/

DOI: 10.34910/MCE.103.14

Plastic shrinkage of concrete modified by metakaolin

K. Usanova*, Yu.G. Barabanshchikov, A.V. Krasova, S.V. Akimov, S.V. Belyaeva
Peter the Great St. Petersburg Polytechnic University, St. Petersburg, Russia
**E-mail:* plml@mail.ru

Keywords: cement, concrete, heat release, heat of hydration, plastic shrinkage, early age shrinkage, autogenous shrinkage, superplasticizer, metakaolin, concrete mixtures, concrete additives, cracks

Abstract. The subject of research is concrete containing a polycarboxylate superplasticizer admixture and metakaolin. The effect of water-cement ratio, superplasticizer, and metakaolin on plastic shrinkage of cement paste was investigated. Two types of cement are also compared. One of them was alite-aluminate cement (cement *A*). Another one was belite-celite cement (cement *B*). If the water-cement ratio is increased, then the plastic shrinkage of samples with both cements develops more intensively and achieves higher values. However, the w/c ratio affects the shrinkage of the cement *A* more. For the first 8 hours, the cement *A* shrinkage is 1.71–5.21 mm/m at W/C = 0.2–0.35. For cement *B*, the corresponding values are 0.953–2.63 mm/m. The cement *A*'s plastic shrinkage is 1.51–1.98 times higher than cement *B*'s plastic shrinkage. If polycarboxylate superplasticizer content is increased, then the shrinkage of both cements increases significantly due to the release of part of physically bound water and its evaporation. The addition of the superplasticizer increases the shrinkage of the cement *A* by an average of 40 %, and the shrinkage of cement B by approximately twice. Simultaneously, the shrinkage of two cements becomes approximately equal due to the same rate of interaction of water with the cement, limited by the diffusion of water through the polycarboxylate adsorption film. Selective capacity of polycarboxylate concerning two types of cement is shown. The alite-aluminate cement gives the same shrinkage as the belite-celite cement, with a 1.89 times higher superplasticizer content. Replacing part of the cement by metakaolin reduces the initial shrinkage, however, not so significantly as the other two factors. If the metakaolin content in the binder is increased, then the shrinkage of both cements decreases. More noticeable is the effect of metakaolin on the cement *A*. The shrinkage of the cement *B* has not changed much.

1. Introduction

One of the main problems of concrete pouring is ensuring the crack resistance of concrete during its hardening. Uneven and restrained deformations cause cracks in hardening concrete. They develop due to shrinkage and heat release of concrete [1]. A specific area of concern is the early-age cracking of self-compacting concrete, which is an extremely fluid mix with a high content of powdered additives and superplasticizers [2]. The plastic shrinkage reviewed in [3–5].

It is known that the self-compacting concrete requires a careful combination of the various components of the mixture. For this reason, much attention needs to be paid to the influence of additives and powdered fillers on the early shrinkage of concrete [6–10]. Results [11] show that shrinkage depends on the mineral admixture type and more particularly on the developed microstructure. Replacing 15% of Portland cement by metakaolin increases the plastic state's shrinkage and decreases it significantly at the hardened state in free drying conditions. A study [12] showed that concrete mixtures blended with mineral admixtures (silica fume, microsilica or fly ash) also had more plastic cracks but below average crack compared to plain Portland cement.

An important role in early shrinkage was the water-cement ratio. According to [13], a low water-cement ratio could cause large shrinkage. The experimental results showed that an increasing the water-cement ratio in the range from 0.13 to 0.24 reduced the chemical and autogenous shrinkage after 8-10

Usanova, K., Barabanshchikov, Yu.G., Krasova, A.V., Akimov, S.V., Belyaeva, S.V. Plastic shrinkage of concrete modified by metakaolin. Magazine of Civil Engineering. 2021. 103(3). Article No. 10314. DOI: 10.34910/MCE.103.14

This work is licensed under a CC BY-NC 4.0

hours of hardening. With further hardening in air, starting from 42 hours from mixing and up to 28 days, shrinkage, on the contrary, increased at an increase in W/C. Moreover, air shrinkage was less than plastic shrinkage. Minimizing the autogenous shrinkage of concrete was an important task. The way to solve this was the use of low-heat belite types of cement and shrink-resistant additives [14–16].

The use of mineral fillers to reduce creep and shrinkage was well known [17–23]. According to [24], fly ash could significantly reduce early age autogenic shrinkage, while silica fume caused an increase in the autogenic shrinkage. The effect of mineral fillers was related to their quantity and fineness of grinding. If the specific surface area of fly ash was above 4000 cm^2/g, then the autogenous shrinkage increased at an increasing amount of additive. A mixture of fly ash and slag significantly reduced the autogenous shrinkage and concrete creep [25]. If more than 20% of the cement was replaced by fly ash, then the shrinkage decrease was not so significant. The influence of the slag on early age shrinkage, on the contrary, was more noticeable when replacing cement above 20%. A mixture of fly ash and slag had lower shrinkage than only ash had [26].

The study [27] showed that limestone filler with a large specific surface area increased autogenous shrinkage, reduced the rate of water evaporation, and increased plastic cracking of self-compacting concrete.

On the other hand, fillers reduced concrete bleeding, which [27, 28] significantly reduced cracking, as shown in [27]. The addition of 10 % of water reduced the cracks' length, and a decrease in the amount of superplasticizer reduced the cracking width of the concrete mixture.

The study of various fillers used as partially replacing cement showed [29] that the shrinkage depends on the type of mineral additive and, in particular, on the fineness of grinding. Replacing 15% of Portland cement by metakaolin increased the plastic shrinkage and significantly reduced it in the hardened concrete if air drying was used [30]. The fillers from waste marble and ceramic tiles increased the resistance to cracking of early age concrete, tested at temperatures of 25 and 40 °C, and the presence and absence of wind (ventilation) [31].

In addition to mineral additives, superplasticizers have a great effect on the concrete mixture. They can significantly improve the quality and characteristics of the mixture; regulate the concrete setting and its hardening [32–35].

In [36], two kinds of naphthalene compounded superplasticizers were tested. One was a retarder for concrete, and the other one was an early strength-air entraining-retarding superplasticizer. The use of this mixture had a positive effect not only on strength but also on the shrinkage of cement paste, mortar, and concrete. In [37], the effect of naphthalene based plasticizers, polycarboxylate superplasticizer, a retarding component, and shrinkage-reducing admixtures on concrete creep was studied. The results showed that polycarboxylates can significantly reduce the shrinkage and the creep of concrete compared to the naphthalene based plasticizers. The shrinkage-reducing admixtures also reduced the concrete creep. However, in [38], a mixture modified with a superplasticizer suddenly cracked, and the air-entraining admixture significantly reduced shrinkage.

As the literature review shows, the results of various studies can be contradictory. Therefore, a separate study is required to evaluate specific cases.

The subject of research is concrete containing a polycarboxylate superplasticizer admixture and metakaolin.

The objective of the work is a comparison of concretes from two cements with different capacity of reaction. The plastic shrinkage is analyzed. The water-cement ratio, the polycarboxylate superplasticizer content, and the metakaolin content are varied.

2. Materials and Methods

2.1. Testing laboratory

Concrete mixtures were tested in the laboratory of Peter the Great St. Petersburg Polytechnic University (Russian Federation).

2.2. Materials

The mixtures were tested using two types of cement produced by Holsim (Rus) LLC.

1. Cement *A*: Portland cement without mineral additives based on clinker of normalized composition.

2. Cement *B*: class G oil well Portland cement without additives. It is high-sulfate-resistant cement. API Specification 10A 24 Edition: API Well Cement Class G at Grade HSR.

The physical and mechanical properties of two types of cement are presented in Table 1.

Table 1. Physical and mechanical properties of two types of cement.

Properties	Cement *A*	Cement *B*
Blaine fineness [cm^2/g]	3488	3027
Normal consistency [%]	27.0	26.5
Initial setting time [min]	177	212
Final setting time [min]	245	466
Soundness Test on Cement	sound cement	sound cement
Compressive strength [MPa] at the age:		
3 days	44.9	32.2
28 days	61.2	50.8
Flexural strength [MPa] at the age:		
3 days	5.7	3.5
28 days	7.4	5.9

Chemical composition and mineralogical composition of the cements are presented in Table 2.

Table 2. Chemical composition and mineralogical composition of the cements.

Type of cement	Chemical composition [%]								Mineralogical composition [%]				
	SiO_2	Al_2O_3	Fe_2O_3	CaO	MgO	SO_3	K_2O	Na_2O	C_3S	C_2S	C_3A	C_4AF	CaO_{free}
Cement A	20.7	4.6	3.5	65.0	1.2	2.9	0.8	0.2	73.0	8.1	5.2	12.0	0.5
Cement B	20.9	4.1	4.9	64.4	1.1	2.5	0.5	0.2	65.0	12.5	2.6	15.7	0.3

The concrete mixes contained additives produced by MC Bauhemi LLC: MC-PowerFlow PF 7951 polycarboxylate superplasticizer and powdered metakaolin produced under the trade name Centrilit NC.

These cements were tested for heat release in concrete.

The concrete composition is shown in Table 3.

Table 3. Concrete composition.

Ingredient	Content [kg/m^3]
Cement	365
Sand with fineness modulus of 1.6	810
Crushed stone with a fraction of 5-20 mm	1040
Water	181
Additive Centrilit NC	10.95
superplasticizer MC-PowerFlow PF 7951	1.64
Total	2409

2.3. Plastic shrinkage measurement

Cement paste samples in rectangular plastic containers with dimensions 90×50×25 mm were made to determine plastic shrinkage. The upper edge of the samples was in contact with the room air. The relative air humidity was 30–32 % and a temperature of 22–24 ºC. Water evaporated through this upper edge of the samples during the experiment. The other faces were in contact with the walls of the containers.

The MIR-12 microscope measured the plastic shrinkage by marks applied to the sample's exposed surface (see Fig. 1). The gauge length was 50 mm. Measurements started 10 minutes after mixing of the cement and ended after 24 hours.

Figure 1. Measuring microscope.

2.4. Heat release of concrete measurement

The heat release of concrete was determined by the semi-adiabatic method by EN 196-9:2010 Methods of testing cement. Part 9: Heat of hydration. Semi adiabatic method. The initial temperature was 20 ºC. The sample was placed in a glass Dewar flask (thermos). It had a high thermal resistance due to the silvering flask surfaces and a vacuum between two glass layers. However, heat exchange between the sample and the surroundings was not completely excluded. Part of the heat generated by cement Q_1 was consumed to increase the sample's temperature, and the other one Q_2 was scattered into the environment with a constant temperature.

Total heat release Q generated by cement during the hydration is composed of two parts:

$$Q=Q_1+Q_2.$$

The heat Q_1 is proportional to the increase in the temperature of the sample t_x relative to the initial temperature of the sample t_0 with a proportionality coefficient equal to the specific heat capacity C_t [J/ºC] of all heated parts of the calorimeter:

$$Q_1=C_t(t_x-t_0).$$

The specific heat capacity C_t of all heated parts of the calorimeter was determined experimentally for every calorimeter.

The heat Q_2 is the heat loss to the surroundings, and this heat loss determined by the heat conductivity coefficient α. The heat conductivity coefficient α is the amount of heat loss from the body in 1 c of time from 1 m^2 surface area with a temperature difference between the body's surface and the surroundings of 1 °C. Since the thermos' contact area with the surrounding S is constant value for this thermos, the heat conductivity constant of the calorimeter $Q_c = \alpha S$ (W/°C) was used. The Qc value was determined experimentally.

The heat Q_2 was determined by the formula:

$$Q_2 = Q_c \int_0^{\tau} (t_x - t_n)\, d\tau,$$

where τ is time and $t_n = const$ is environment temperature.

The integration over time was replaced by summing over the area F_x. These areas were enclosed between the curve $t_x=f(\tau)$ and the line $t_n = const$. Hence

$$Q_2=Q_kF_x.$$

The heat Q was the amount of heat generated by unit volume of concrete during its hardening. The value of the heat Q depended on the cement content C in concrete. Therefore, the results of the experimental measurement of heat release are presented further in the article in the form of heat release per unit mass of cement:

$$q=Q/C.$$

The heat release of the same concrete mixture tested in different thermoses was not the same. The reason for this is the different Q_k values for different thermoses and, accordingly, the samples' measured temperatures.

The experimental results were recalculated for the isothermal hardening mode at a temperature of 20 ºC

$$\frac{v_1}{v_2} = \frac{\tau_2}{\tau_1} = f_t = const$$

for the correct comparison of different cements.

The characteristical temperature difference ε was used further in the article to present the experimental data. The characteristical temperature difference ε is related to the temperature function by the following formula:

$$f_t = 2\frac{t_1 - t_2}{\varepsilon},$$

where f_t is temperature function. If t_1-t_2=ε, then f_t=2; this means if the temperature rises by ε degrees, the rate of heat release will double.

The hypothesis on the ratio of the heat release rate was used to determine the temperature function f_t. According to the hypothesis, the heat release rates $v=dQ/d\tau$ and corresponding terms τ_1 and τ_2 remains constant at moments of equal heat release at $Q_1 = Q_2$:

$$v_1 v_2 = \tau_2 \tau_1 = f_t = const.$$

The value of ε is obtained from experimental data on the heat release of concrete at three (not less) temperatures. It is established that the characteristic temperature difference ε is not constant, but depends on temperature.

This dependence is approximated by the linear function $\varepsilon = k_t + l$, where k≈0.13; l≈8 are empirical characteristics of the process.

2.5. Flexural strength and compressive strength measurement

The compressive strength of concrete was determined on cubes with a size of 70.7×70.7×70.7 mm according to Russian State Standard GOST 10180-2012 “Concretes. Methods for strength determination using reference specimens”. The test results of the concrete specimens for the compressive strength at the age of 3 and 28 days are presented in Table 4.

The flexural strength was determined on beams of a square section with a size of 40×40×160 mm according to Russian State Standard GOST 310.4-81 “Cements. Methods of bending and compression strength determination”. The test results of the concrete specimens for the flexural strength at the age of 3 and 28 days are presented in Table 4.

3. Results and Discussion

The effects of the water-cement ratio, polycarboxylate superplasticizer MC-PowerFlow PF 7951, and metakaolin additive Centrilit NC on plastic shrinkage of cement paste were investigated. Two types of cements were compared. One of them was an alite-aluminate cement (cement *A*), and the other one was a belite-celite cement (cement *B*).

The manufacturing environment makes it possible to protect concrete from water evaporation only a few hours after concrete pouring when the concrete acquires some initial strength necessary for workers to walk on it. For this reason, the air-hardening of cement is used in the study.

The reaction capacity of cements is evaluated by the value of heat release per unit mass of cement.

Figure 2 show the results of determining the heat release per unit mass of cement q.

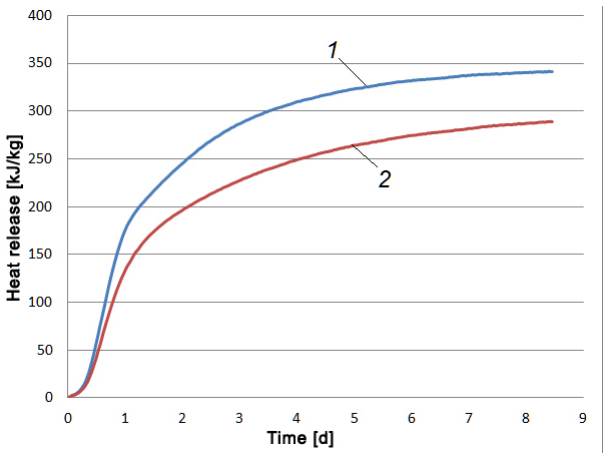

Figure 2. The specific heat release per unit mass of cement *q*: 1 is cement *A*, 2 is cement *B*.

The Figure 2 shows that the cement *A* generates a greater amount of heat by any period and has a higher heat release rate in the initial period of hardening than the cement *B*. This ratio of heat releases is consistent with cements' strength characteristics and with differences in their mineralogical composition. In contrast to cement *B*, the cement *A* has an increased amount of tricalcium aluminate C_3A and tricalcium silicate C_3S. Therefore, cement *A* has accelerated hydration and hardening. However, after about 5 days, the heat release rates of cements begin to change oppositely. The angle of arrival to curve 1 becomes slightly less than the angle of arrival to curve 2. The ratio of angles suggests that the difference in the strength of two cements in the later stages of hardening will not be so significant. This suggestion is partially confirmed by the ratio in cements' strength for the ages of 3 and 28 days (see Table 4).

Table 4. Ratio R_{cA}/R_{cB} ultimate strengths of cement A and cement B.

Age of cement samples	R_{cA}/R_{cB}	
	Flexural strength	Compressive strength
3	1.63	1.39
28	1.25	1.20

As can be seen from Table 4, the ratio R_{cA}/R_{cB} decreases with age.

The results of determining the plastic shrinkage of cement *A* and cement *B* depending on the water-cement ratio are presented in Figure 3.

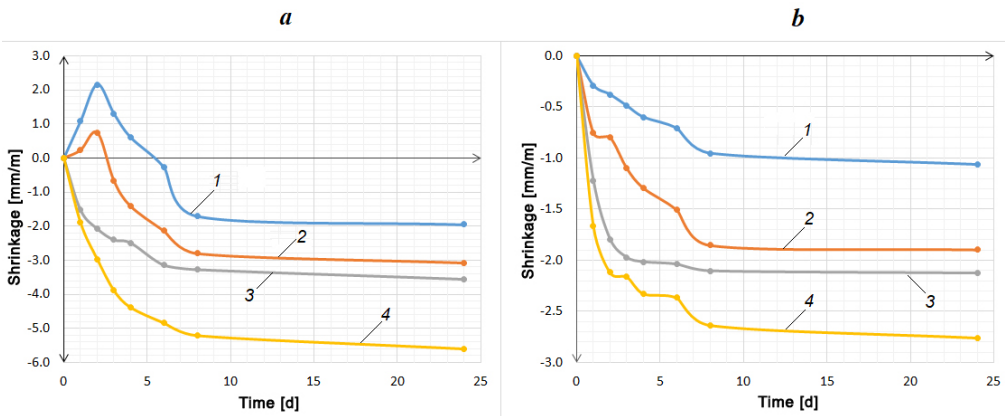

Figure 3. The plastic shrinkage of cement pastes *A* (a) and *B* (b) at water-cement ratio: 1 is 0.20; 2 is 0.25; 3 is 0.30; 4 is 0.35.

As shown in Figure 3, if the W/C ratio is increased, then the samples' shrinkage develops more intensively and reaches higher values. The plastic shrinkage ends after about 8 hours, which almost corresponds to the final set of cement. After that, shrinkage occurs in the set cement paste. For the first 8 hours, the cement *A* shrinkage is 1.71–5.21 mm/m, and for the next 16 hours, it is only 0.247–0.392 mm/m, depending on the W/C ratio. For the cement *B*, the corresponding values are 0.953–2.63 and 0.022–0.123 mm/m. Hence, cement A's plastic shrinkage is 1.51–1.98 times higher than cement *B*'s plastic shrinkage. This plastic shrinkages rates are logical due to the difference in the

mineralogical composition of cements. Unlike cement *B*, the cement *A* is characterized by a 2 times higher content of C_3A and 12% higher content of C_3S.

In addition to high initial shrinkage, the difference between the cement *A* and the cement *B* is a significant expansion during the first three hours at W/C = 0.20–0.25. This difference in the shrinkages is also due to its chemical and mineralogical composition, which leads to the formation of an increased amount of hydrated calcium sulfoaluminate. The cement samples with a W/C = 0.30–0.35 have no expansion due to the high shrinkage that compensates for the expansion.

The results of determining the plastic shrinkage of cement *A* and cement *B* depending on the polycarboxylate superplasticizer content at a constant W/C = 0.25 are presented in Figure 4.

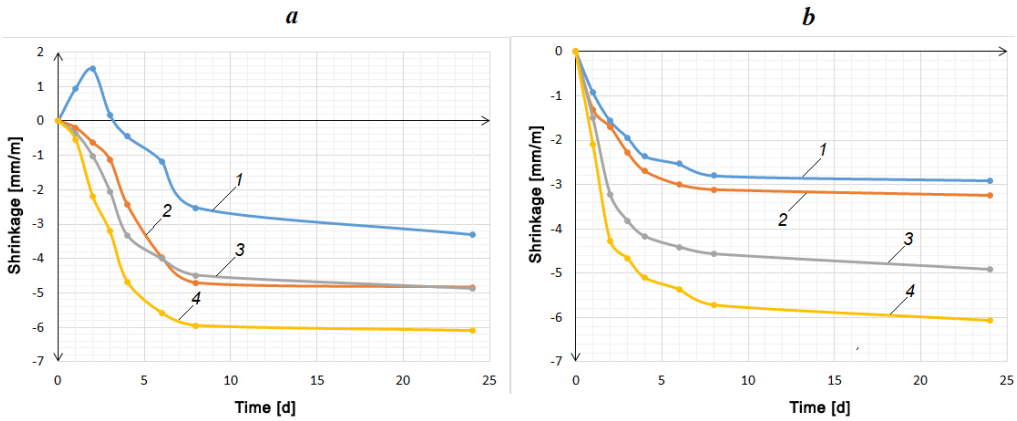

Figure 4. The plastic shrinkage of cement pastes A (a) and B (b) with the superplasticizer content as a percentage by mass of cement:
1 is 0.2; 2 is 0.4; 3 is 0.6; 4 is 0.8.

The addition of the superplasticizer MC-PowerFlow PF 7951 increases the shrinkage of the cement *A* by an average of 40%, and the shrinkage of the cement *B* by approximately twice, when compared to the cement paste without admixture. In this case, the order of the shrinkage values of the two cements is approximately equal. There is an assumption that equalizing the shrinkage of two cements is associated with two things. The first of these is the peptization of particles. The second one is the water-repellent effect of the screening adsorption layers of polycarboxylate on cement grains. Thus, the rate of interaction of water with cement is equally limited by water diffusion through the film. If the admixture content increases, then the shrinkage of cements also increases. This increasing due to the release of part of physically bound water. Water goes into a weakly bound or free state. This state allows it to evaporate more easily and allows solid particles to come close.

A normal consistency test was conducted to determine the effect of metakaolin additive Centrilit NC on the plastic shrinkage. Metakaolin was introduced instead of cement. The total amount of the solid component remained constant.

The results of determining the plastic shrinkage of cements depending on the metakaolin content are presented in Figure 5.

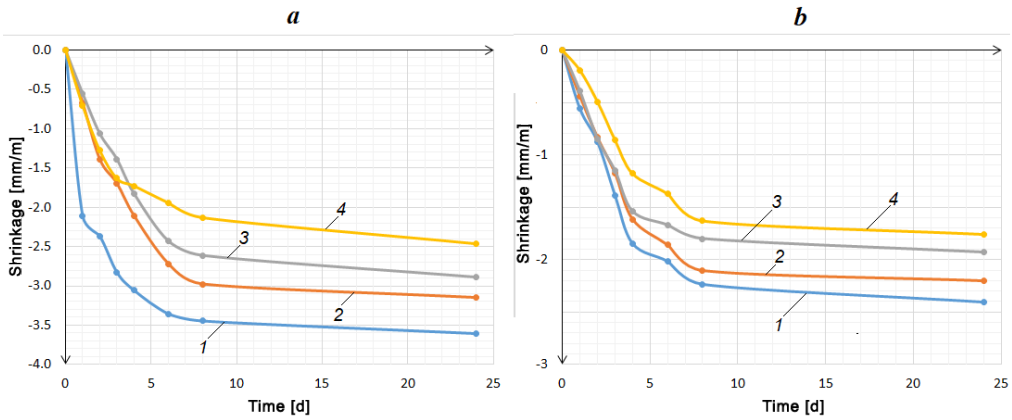

Figure 5. The plastic shrinkage of cement pastes *A* (a) and *B* (b) with the metakaolin content as a percentage by mass of binder (cement and metakaolin):
***1* is 5; *2* is 10; *3* is 15; *4* is 20.**

There is no expansion of cement *A* test in this case, as in previous experiments, possibly because of metakaolin's pozzolanic effect. Replacing part of the cement by metakaolin reduces the initial shrinkage, however, not so significantly. More noticeable is the effect of metakaolin on the cement *A*. The shrinkage of the cement *B* has not changed much. If the metakaolin content in the binder is increased, then the shrinkage of both cements decreases.

Figure 6 shows that metakaolin, replacing part of the cement, reduces plastic shrinkage the more, the higher its content. The shrinkage trend continues for both cements, but faster for cement *A*. Plastic shrinkage is reduced, starting from 10 % metakaolin content, compared to normal consistency mix without additives.

Figure 6 shows a histogram of shrinkage values for the first 8 hours for all testes.

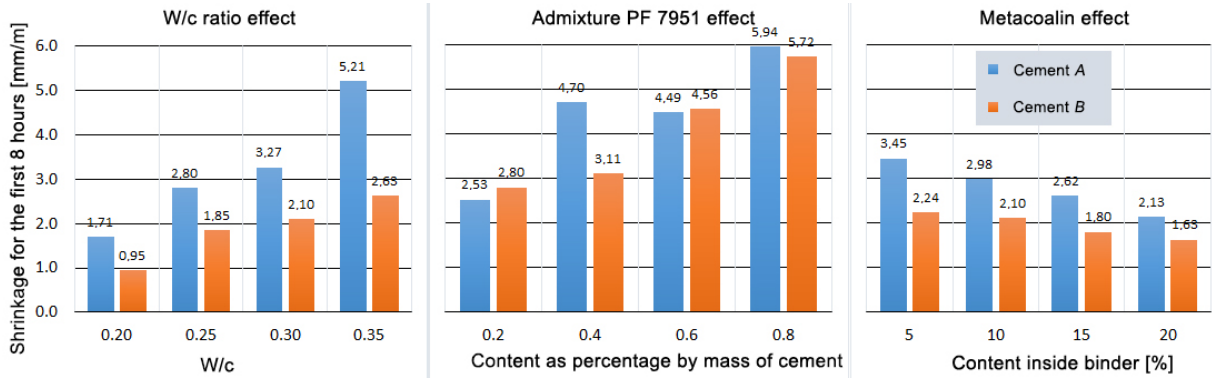

Figure 6. Histograms of shrinkage values for the first 8 hours.

The histogram shows that two factors are essential for plastic shrinkage in air, which are the water-cement ratio and the polycarboxylate superplasticizer content. Both factors affect the amount of free water in the cement paste. A significant part of the shrinkage is due to the water evaporation.

An analysis showing the superplasticizer's contribution to plastic shrinkage compared to the equivalent amount of evaporation water is performed below. Two dependences of plastic shrinkage ε are plotted on one graph. The first dependence is ε on the W/C ratio of cement without additive. The second one is the dependence of ε on the additive D content at W/C = 0.25. Since the values of W/C and D have the same numbers, it is convenient to use a single scale along the abscissa axis, using it both in one and in the other case.

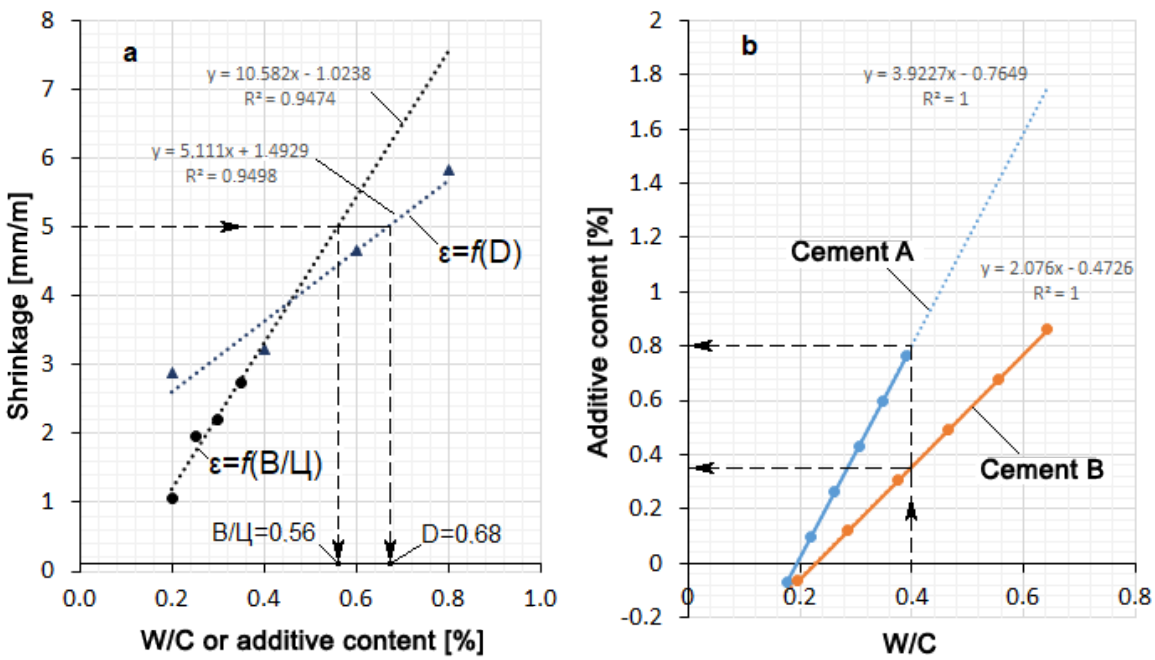

Figure 7. a. Linear approximation of shrinkage dependencies: ε in the function of W/C of mix without additive and ε in the function of superplasticizer content D at W/C=0.25 (cement *B*); b. correlation between W/C of normal consistency mix without additives and the superplasticizer content at W/C =0.25, causing the same plastic shrinkage.

Both dependences give a linear correlation with the coefficient of determination R^2 = 0.95 (Figure 7a). According to the graphs in Figure 7a, we find the values of W/C and D, giving the same plastic shrinkage. For example, for shrinkage, 5 mm/m, we find W/C=0.56 and D=0.68. That is, the initial shrinkage of the cement paste equal to 5 mm/m can be obtained in two ways: 1) preparing of the mix with W/C =0.56; 2) preparing the mix with W/C =0.25 and adding a superplasticizer in the amount of 0.68% of the cement mass. For any shrinkage value, a corresponding pair of W/C and D values can be found. Figure 7b shows the correlation between W/C and *D* for the two types of cement. This diagram gives an infinite series of W/C and D values associated with the same plastic shrinkage. So the shrinkage of the mix with W/C=0.4 can be obtained at W/C=0.25 using a superplasticizer. In the case of cement *A*, 0.8% of the superplasticizer by cement weight must be added, and in the case of cement *B*, 0.36% of the superplasticizer by cement weight must be added. At a linear correlation, the slopes or $dD/d\ (W/C)$ ratio for cements *A* and *B* remains constant, equal to 3.923/2.076 = 1.89. This constant ratio means that cement A requires the addition of a superplasticizer (to compensate for the decrease in W/C) 1.89 times more than cement *B*, regardless of the value of the shrinkage deformation.

The selectivity of polycarboxylates for plasticizing cementitious compositions is well known. In this case, it manifested itself in relation to the initial shrinkage.

4. Conclusions

1. Based on the experimental research, the influence of three factors (water-cement ratio, superplasticizer MC-PowerFlow PF 7951 content, and content of metakaolin as a partial replacement of cement) on the initial shrinkage of Portland cement and high-sulfate-resistant cement is established.

2. The tested cements vary significantly in their activity, both in terms of strength (structure formation) and heat release (hydration of cement), which is determined by their chemical and mineralogical composition. According to the mineralogical composition, the first cement is the alite-aluminate cement, and the second one is the belite-celite cement.

3. If W/C ratio is increased, then the shrinkage of the samples develops more intensively and reaches higher values. The W/C ratio has a greater effect on shrinkage of cement *A*. For the first 8 hours, the cement *A* shrinkage is 1.71–5.21 mm/m at W/C = 0.2–0.35. For cement *B*, the corresponding values are 0.953–2.63 mm/m. The plastic shrinkage of cement *A* is 1.51–1.98 times higher than cement *B*'s plastic shrinkage. In addition to high initial shrinkage, the cement *A* has a significant expansion of up to 2.2 mm/m during the first three hours at W/C = 0.20–0.25.

4. If superplasticizer PF 7951 content is increased, then the shrinkage of both cements increases significantly. This is due to the release of part of physically bound water and its evaporation. The addition of the superplasticizer MC-PowerFlow PF 7951 increases the shrinkage of the cement *A* by an average of 40%, and the shrinkage of the cement *B* by approximately twice. At the same time, the values of shrinkage of two cements become approximately equal. This is due to the same rate of interaction of water with the cement, limited by the diffusion of water through the polycarboxylate adsorption film.

Selective capacity of polycarboxylate in relation to two types of cement is shown. The alite-aluminate cement gives the same shrinkage as the belite-celite cement, with a 1.89 times higher superplasticizer content.

5. Replacing part of the cement by metakaolin reduces the initial shrinkage, however, not so significantly as the other two factors. If the metakaolin content in the binder is increased, then the shrinkage of both cements decreases. More noticeable is the effect of metakaolin on the cement *A*. The shrinkage of the cement *B* has not changed much.

Further research on this topic may be experimental studies of the influence of these factors on the initial shrinkage of cold-bonded fly ash aggregate concrete. Fly ash can be used as an additive in the mix [39] or as a large aggregate [40]. If the presoaked aggregate is added to the concrete mix, this will create “internal curing” for the concrete and reduce cracks caused by the heat release [41].

5. Acknowledgement

Reported study was funded by RFBR, project number No. 20-33-90015.

References

1. Struchkova, A.Y., Barabanshchikov, Y.G., Semenov, K.S., Shaibakova, A.A.: Heat dissipation of cement and calculation of crack resistance of concrete massifs. Magazine Civil Engineering. 2018. 78(2). Pp. 128–135. DOI: 10.18720/MCE.78.10
2. José Oliveira, M., Ribeiro, A.B., Branco, F.G. Combined effect of expansive and shrinkage reducing admixtures to control autogenous shrinkage in self-compacting concrete. Construction and Building Materials. 2014. 52. Pp. 267–275. DOI: 10.1016/j.conbuildmat.2013.11.033
3. Ghoddousi, P., Abbasi, A.M., Shahrokhinasab, E., Abedin, M. Prediction of plastic shrinkage cracking of self-compacting concrete. 2019. Advances in Civil Engineering. DOI: 10.1155/2019/1296248
4. Ghourchian, S., Wyrzykowski, M., Plamondon, M., Lura, P. On the mechanism of plastic shrinkage cracking in fresh cementitious materials. Cement and Concrete Research. 2019. 115. Pp. 251–263. DOI: 10.1016/j.cemconres.2018.10.015
5. Wu, L., Farzadnia, N., Shi, C., Zhang, Z., Wang, H. Autogenous shrinkage of high performance concrete: A review. Construction and Building Materials. 2017. 149. Pp. 62–75. DOI: 10.1016/j.conbuildmat.2017.05.064
6. Corinaldesi, V. Combined effect of expansive, shrinkage reducing and hydrophobic admixtures for durable self–compacting concrete. Construction and Building Materials. 2012. 36. Pp. 758–764. DOI: 10.1016/j.conbuildmat.2012.04.129
7. Maia, L., Figueiras, H., Nunes, S., Azenha, M., Figueiras, J. Influence of shrinkage reducing admixtures on distinct SCC mix compositions. Construction and Building Materials. 2012. 35. Pp. 304–312. DOI: 10.1016/j.conbuildmat.2012.02.033
8. Güneyisi, E., Gesolu, M., Özbay, E. Strength and drying shrinkage properties of self-compacting concretes incorporating multi-system blended mineral admixtures. Construction and Building Materials 2010. 24. Pp. 1878–1887. DOI: 10.1016/j.conbuildmat.2010.04.015
9. Yang, K., Zhong, M., Magee, B., Yang, C., Wang, C., Zhu, X., Zhang, Z. Investigation of effects of Portland cement fineness and alkali content on concrete plastic shrinkage cracking. Construction and Building Materials. 2017. 144. Pp. 279–290. DOI: 10.1016/j.conbuildmat.2017.03.130
10. Al-Amoudi, O.S.B., Maslehuddin, M., Shameem, M., Ibrahim, M. Shrinkage of plain and silica fume cement concrete under hot weather. Cement and Concrete Composites. 2007. 29. Pp. 690–699. DOI: 10.1016/j.cemconcomp.2007.05.006
11. Niknezhad, D., Kamali-Bernard, S., Garand, C. Influence of Mineral Admixtures (Metakaolin, Slag, Fly Ash) on the Plastic, Free, and Restrained Shrinkage of SCCs. CONCREEP 10. 2015. Pp. 1157–1166. DOI: 10.1061/9780784479346.138
12. Rashad, A.M. Plastic and dry shrinkages cracking of blended white cement concrete. Silic. Ind. 2009. 74. Pp. 353–361.
13. Ye, B., Zhang, Y., Han, J., Pan, P. Effect of water to binder ratio and sand to binder ratio on shrinkage and mechanical properties of High-strength Engineered Cementitious Composite. Construction and Building Materials 2019. 226. Pp. 899–909. DOI: 10.1016/j.conbuildmat.2019.07.303
14. Yoo, D.Y., Banthia, N., Yoon, Y.S. Effectiveness of shrinkage-reducing admixture in reducing autogenous shrinkage stress of ultra-high-performance fiber-reinforced concrete. Cement and Concrete Composites. 2015. 64. Pp. 27–36. DOI: 10.1016/j.cemconcomp.2015.09.005
15. Lecomte, A., Vulcano-Greullet, N., Steichen, C., Scharfe, G. The risk of cracking of fine hydraulic mixtures. Cement and Concrete Research. 2003. 33. Pp. 1983–1997. DOI: 10.1016/S0008-8846(03)00221-7
16. Barabanshchikov, Y.G., Arkharova, A.A., Ternovskii, M.V. On the influence on the efficiency of anti-shrinkage additives superplasticizer. Magazine Civil Engineering. 2014. 7(51). Pp. 23–30. DOI: 10.5862/MCE.51.3
17. Liu, J., Sun, W., Miao, C., Liu, J. Effect of mineral admixtures on drying and autogenous shrinkage of concrete with low water-to-binder ratio. Dongnan Daxue Xuebao (Ziran Kexue Ban)/Journal Southeast Univ. (Natural Sci. Ed.). 2009. 39. Pp. 580–585. DOI: 10.3969/j.issn.1001-0505.2009.03.030
18. Williams, A., Markandeya, A., Stetsko, Y., Riding, K., Zayed, A. Cracking potential and temperature sensitivity of metakaolin concrete. Construction and Building Materials. 2016. 120. Pp. 172–180. DOI: 10.1016/j.conbuildmat.2016.05.087
19. Wang, X., Zheng, J. Influence of compounded mineral admixtures on shrinkage and early-age cracking behaviors of concrete. Advanced Materials Research. 2012. 450–451. Pp. 738–742. DOI: 10.4028/www.scientific.net/AMR.450-451.738
20. Barluenga, G., Puentes, J., Palomar, I., Rio, O. Early age drying shrinkage evaluation of self-compacting concretes and pastes with mineral additions. CONCREEP 10. 2015. Pp. 1514–1523. DOI: 10.1061/9780784479346.177
21. Klyuev, S.V., Klyuev, A.V., Shorstova, E.S. The micro silicon additive effects on the fine-grassed concrete properties for 3-D additive technologies. Materials Science Forum. 2019. 974. Pp. 131–135. DOI: 10.4028/www.scientific.net/MSF.974.131
22. Taskin, A., Fediuk, R., Grebenyuk, I., Elkin, O., Kholodov, A. Effective cement binders on fly and slag waste from heat power industry of the Primorsky krai, Russian Federation. International Journal of Scientific and Technology Research. 2020. 9. Pp. 3509–3512.
23. Barabanshchikov, Y., Usanova, K., Akimov, S., Uhanov, A., Kalachev, A. Influence of Electrostatic Precipitator Ash “Zolest-Bet” and Silica Fume on Sulfate Resistance of Portland Cement. Materials (Basel). 2020. 13. 4917. DOI: 10.3390/ma13214917
24. Xie, L. Influence of mineral admixtures on early-age autogenous shrinkage of high-performance concrete. Applied Mechanics and Materials. 2014. 457–458. Pp. 318–322. DOI: 10.4028/www.scientific.net/AMM.457-458.318
25. He, Z., Qian, C., Gao, X. The autogenous shrinkage and creep characteristics of concrete with modified admixtures. Advanced Science Letters. 2012. 12. Pp. 402–406. DOI: 10.1166/asl.2012.2759
26. Zhang, L., Lai, J., Qian, X., Hu, D. Influence of mineral admixtures on early shrinkage of ordinary concrete. Advanced Materials Research. 2012. 450–451. Pp. 135–139. DOI: 10.4028/www.scientific.net/AMR.450-451.135
27. Esping, O. Effect of limestone filler BET(H2O)-area on the fresh and hardened properties of self-compacting concrete. Cement and Concrete Research. 2008. 38. Pp. 938–944. DOI: 10.1016/j.cemconres.2008.03.010
28. Yakoubi, I., Aggoun, S., Ait Aider, H., Houari, H. The influence of bleeding, extra water and superplasticizer on the SCC plastic shrinkage cracking: Case of hot weather. Journal of Adhesion Science and Technology. 2016. 30. Pp. 2596–2618. DOI: 10.1080/01694243.2016.1189869
29. Niknezhad, D., Kamali-Bernard, S., Garand, C. Influence of Mineral Admixtures (Metakaolin, Slag, Fly Ash) on the Plastic, Free, and Restrained Shrinkage of SCCs. CONCREEP 10. 2015. Pp. 1157–1166. DOI: 10.1061/9780784479346.138
30. Markandeya, A., Mapa, D.G., Fincan, M., Shanahan, N., Stetsko, Y.P., Riding, K.A., Zayed, A. Chemical shrinkage and cracking resilience of metakaolin concrete. ACI Materials Journal. 2019. 116. Pp. 99–106. DOI: 10.14359/51716714

31. Tennich, M., Ouezdou, M. Ben, Kallel, A. Thermal effect of marble and tile fillers on self-compacting concrete behavior in the fresh state and at early age. Journal of Building Engineering. 2018. 20. Pp. 1–7. DOI: 10.1016/j.jobe.2018.06.015
32. Vatin, N.I., Barabanshchikov, Y.G., Komarinskiy, M. V., Smirnov, S.I. Modification of the cast concrete mixture by air-entraining agents. Magazine Civil Engineering. 12015. 56(4). DOI: 10.5862/MCE.56.1
33. Ibragimov, R., Fediuk, R. Improving the early strength of concrete: Effect of mechanochemical activation of the cementitious suspension and using of various superplasticizers. Construction and Building Materials. 2019. 226. Pp. 839–848. DOI: 10.1016/j.conbuildmat.2019.07.313
34. Alfimova, N.I., Shadskiy, E.E., Lesovik, R. V., Ageeva, M.S. Organic-mineral modifier on the basis of volcanogenic-sedimentary rocks. International Journal of Applied Engineering Research. 2015. 10. Pp. 45131–45136.
35. Shepelenko, T.S., Sarkisov, U.S., Gorlenko, N.P., Tsvetkov, N.A., Zubkova, O.A. Structure-forming processes of cement composites, modified by sucrose additions. Magazine of Civil Engineering. 2016. 66(6). Pp. 3–11. DOI: 10.5862/MCE.66.1
36. Wang, Y., Yan, H. Effect of naphthalene compounded superplasticizer on strength and shrinkage of ready-mixed concrete. Applied Mechanics and Materials. 2012. 174–177. Pp. 488–495. DOI: 10.4028/www.scientific.net/AMM.174-177.488
37. Zhang, Y., Qian, C.X., Zhao, F., He, Z.H., Qu, J., Guo, J.Q., Danzinger, M. Influence regularities of chemical admixtures on creep. Gongneng Cailiao/Journal Funct. Mater. 2013. 44. Pp. 1620–1623. DOI: 10.3969/j.issn.1001-9731.2013.11.023
38. Kronlöf, A., Leivo, M., Sipari, P. Experimental study on the basic phenomena of shrinkage and cracking of fresh mortar. Cement and Concrete Research. 1995. 25. Pp. 1747–1754. DOI: 10.1016/0008-8846(95)00170-0
39. Fediuk, R.S., Yushin, A.M. The use of fly ash the thermal power plants in the construction. IOP Conference Series: Materials Science and Engineering. 2015. 93. DOI: 10.1088/1757-899X/93/1/012070
40. Usanova, K.Y. Properties of Cold-Bonded Fly Ash Lightweight Aggregate Concretes. Lecture Notes in Civil Engineering. 2020. 70. Pp. 507–516. DOI: 10.1007/978-3-030-42351-3_44
41. Usanova, K., Barabanshchikov, Y.G. Cold-bonded fly ash aggregate concrete. Magazine of Civil Engineering. 2020. 95. Pp. 104–118. DOI: 10.18720/MCE.95.10.

Contacts:

Kseniia Usanova, plml@mail.ru
Yuriy Barabanshchikov, ugb@mail.ru
Anastasiya Krasova, krasova-nastya14@mail.ru
Stanislav Akimov, akimov_sv@spbstu.ru
Svetlana Belyaeva, belyaeva_sv@spbstu.ru

© Usanova, K.,Barabanshchikov, Yu.G.,Krasova, A.V.,Akimov, S.V.,Belyaeva, S.V., 2021

Федеральное государственное автономное образовательное учреждение высшего образования
Санкт-Петербургский политехнический университет Петра Великого

ПОЛИТЕХ
Санкт-Петербургский политехнический университет Петра Великого

Инженерно-строительный институт
Центр дополнительных профессиональных программ

195251, г. Санкт-Петербург, Политехническая ул., 29, тел/факс: 552-94-60, www.stroikursi.spbstu.ru, stroikursi@mail.ru

Приглашает специалистов проектных и строительных организаций, не имеющих базового профильного высшего образования на курсы профессиональной переподготовки (от 500 часов) по направлению «Строительство» по программам:

П-01 «Промышленное и гражданское строительство»

Программа включает учебные разделы:

- ***Основы строительного дела***
- ***Инженерное оборудование зданий и сооружений***
- ***Технология и контроль качества строительства***
- ***Основы проектирования зданий и сооружений***
- ***Автоматизация проектных работ с использованием AutoCAD***
- ***Автоматизация сметного дела в строительстве***
- ***Управление строительной организацией***
- ***Управление инвестиционно-строительными проектами. Выполнение функций технического заказчика***

П-02 «Экономика и управление в строительстве»

Программа включает учебные разделы:

- ***Основы строительного дела***
- ***Инженерное оборудование зданий и сооружений***
- ***Технология и контроль качества строительства***
- ***Управление инвестиционно-строительными проектами. Выполнение функций технического заказчика и генерального подрядчика***
- ***Управление строительной организацией***
- ***Экономика и ценообразование в строительстве***
- ***Управление строительной организацией***
- ***Организация, управление и планирование в строительстве***
- ***Автоматизация сметного дела в строительстве***

П-03 «Инженерные системы зданий и сооружений»

Программа включает учебные разделы:

- ***Основы механики жидкости и газа***
- ***Инженерное оборудование зданий и сооружений***
- ***Проектирование, монтаж и эксплуатация систем вентиляции и кондиционирования***
- ***Проектирование, монтаж и эксплуатация систем отопления и теплоснабжения***
- ***Проектирование, монтаж и эксплуатация систем водоснабжения и водоотведения***
- ***Автоматизация проектных работ с использованием AutoCAD***
- ***Электроснабжение и электрооборудование объектов***

П-04 «Проектирование и конструирование зданий и сооружений»

Программа включает учебные разделы:

- ***Основы сопротивления материалов и механики стержневых систем***
- ***Проектирование и расчет оснований и фундаментов зданий и сооружений***
- ***Проектирование и расчет железобетонных конструкций***
- ***Проектирование и расчет металлических конструкций***
- ***Проектирование зданий и сооружений с использованием AutoCAD***
- ***Расчет строительных конструкций с использованием SCAD Office***

П-05 «Контроль качества строительства»

Программа включает учебные разделы:

- ***Основы строительного дела***
- ***Инженерное оборудование зданий и сооружений***
- ***Технология и контроль качества строительства***
- ***Проектирование и расчет железобетонных конструкций***
- ***Проектирование и расчет металлических конструкций***
- ***Обследование строительных конструкций зданий и сооружений***
- ***Выполнение функций технического заказчика и генерального подрядчика***

По окончании курса слушателю выдается диплом о профессиональной переподготовке установленного образца, дающий право на ведение профессиональной деятельности